

A STRAIN SPACE MULTIPLE MECHANISM MODEL  
FOR CYCLIC BEHAVIOR OF SAND  
AND ITS APPLICATION

By

Susumu IAI

May 1991

Earthquake Engineering Research Group  
Port and Harbour Research Institute  
Ministry of Transport, JAPAN

A STRAIN SPACE MULTIPLE MECHANISM MODEL  
FOR CYCLIC BEHAVIOR OF SAND  
AND ITS APPLICATION

By

Susumu IAI

MAY 1991

## CONTENTS

ABSTRACT . . . . .	iv
ACKNOWLEDGMENT . . . . .	vi
NOTATION . . . . .	xi
 1. INTRODUCTION . . . . .	 1
1.1 General . . . . .	1
1.2 Review of Previous Studies . . . . .	2
1.2.1 Cyclic Mobility as Identified through Laboratory Studies . . . . .	2
1.2.2 Previous Studies on Modeling of Cyclic Mobility . . . . .	7
1.3 Objectives . . . . .	21
1.4 Scope . . . . .	22
References . . . . .	24
 2. MODELING OF CYCLIC MOBILITY . . . . .	 29
2.1 Generalized Plasticity Theory in Strain Space . . . . .	29
2.2 Decomposition into Simple Mechanisms . . . . .	33
2.2.1 Transformation . . . . .	34
2.2.2 Volumetric Mechanism . . . . .	36
2.2.3 Shear Mechanism . . . . .	38
2.2.4 Incremental Relation . . . . .	39
2.3 Integrated Formulation . . . . .	42
2.4 Undrained Stress Path . . . . .	45
2.4.1 Effective Mean Stress Change . . . . .	45
2.4.2 Liquefaction Front . . . . .	47
2.4.3 Shear Work Correlation . . . . .	51
2.4.4 Threshold Limit . . . . .	55
2.5 Virtual Simple Shear Mechanism . . . . .	61
2.5.1 Initial Loading . . . . .	61
2.5.2 Memory of Loading History . . . . .	62
2.5.3 Unloading from the Initial Loading . . . . .	65
2.5.4 Reloading . . . . .	71
2.6 Shear Mechanism . . . . .	73
2.6.1 Shear Strength and Reference Strain . . . . .	73
2.6.2 Hysteretic Damping Factor for Hysteresis Loop . . . . .	75
2.7 Numerical Robustness . . . . .	82
2.7.1 Problems . . . . .	82
2.7.2 A Simple Scheme . . . . .	86
2.8 Summary . . . . .	90
References . . . . .	92
 3. ANALYSIS WITH SINGLE SOIL ELEMENT . . . . .	 96
3.1 Procedure for Numerical Analysis . . . . .	96
3.2 Procedure for Parameter Identification . . . . .	97
3.3 Analysis with Initially Isotropic Consolidation Condition . . . . .	100
3.4 Analysis with Initially Anisotropic Consolidation Condition . . . . .	105
3.4.1 Analysis with Bulging Constrained . . . . .	108
3.4.2 Analysis with Bulging Unconstrained . . . . .	111
3.5 Effect of Initial Mean Effective Stress . . . . .	115
3.6 Applicability to Soil Element Analysis . . . . .	119
References . . . . .	120

4. ONE DIMENSIONAL ANALYSIS OF LEVEL GROUND . . . . .	122
4.1 Shaking Table Tests . . . . .	122
4.1.1 Outline of Model Tests . . . . .	122
4.1.2 Shaking Table and Container . . . . .	123
4.1.3 Instrumentation . . . . .	125
4.1.4 Properties of Sand . . . . .	131
4.1.5 Model Preparation . . . . .	137
4.1.6 Initial Densities and Other Properties of Model Ground . . . . .	143
4.1.7 Input Motion . . . . .	146
4.2 Results of the Model Tests . . . . .	153
4.2.1 Results for Sinusoidal Input Motion . . . . .	153
4.2.2 Results for Earthquake Input Motion . . . . .	163
4.3 Soil Parameter Identification . . . . .	171
4.3.1 Parameters for Shear . . . . .	171
4.3.2 Parameters for Volume Change . . . . .	176
4.4 Analysis of Level Model Ground . . . . .	181
4.4.1 Response to Sinusoidal Input Motion . . . . .	181
4.4.2 Response to Earthquake Input Motion . . . . .	195
4.5 Applicability to Level Ground Analysis . . . . .	201
References . . . . .	203
 5. TWO DIMENSIONAL ANALYSIS OF SHEET PILE QUAY WALLS . . . . .	204
5.1 Earthquake and Damage . . . . .	205
5.1.1 1983 Nihonkai-Chubu Earthquake . . . . .	205
5.1.2 Damage at Akita Port . . . . .	210
5.2 Modeling of Soils, Structures and Sea . . . . .	225
5.2.1 Modeling of Soils at Akita Port . . . . .	225
5.2.2 Modeling of Structures and Soil Structure Interface . . . . .	233
5.2.3 Modeling of Sea Water . . . . .	234
5.3 Initial and Boundary Conditions and Input Motion . . . . .	234
5.3.1 Static Analysis with Gravity . . . . .	234
5.3.2 Boundary Conditions . . . . .	236
5.3.3 Input Motion and Time Integration . . . . .	239
5.4 Analysis of a Damaged Quay Wall . . . . .	242
5.4.1 Earthquake Response and Deformation . . . . .	242
5.4.2 Earth Pressure and Bending Moment . . . . .	248
5.4.3 Comparison between Observed and Computed Results . . . . .	254
5.5 Mechanism of Deformation . . . . .	254
5.5.1 Stress and Strain in front of Sheet Pile . . . . .	255
5.5.2 Stress and Strain behind Sheet Pile . . . . .	256
5.5.3 Stress and Strain in the middle of the Ground . . . . .	261
5.5.4 Stress and Strain in front of Anchor . . . . .	264
5.5.5 Initial Stress and Residual Deformation . . . . .	269
5.6 Analysis of a Quay Wall without Damage . . . . .	271
5.6.1 Earthquake Response and Deformation . . . . .	271
5.6.2 Earth Pressure and Bending Moment . . . . .	275
5.6.3 Comparison between Observed and Computed Results . . . . .	280
5.7 Applicability to Quay Wall Analysis . . . . .	280
References . . . . .	283
 6. CONCLUSIONS . . . . .	285

APPENDIX A	EXTENSION TO THREE DIMENSIONS	288
A.1	Coordinate Transformation	288
A.2	Virtual Two Dimensional Shear Mechanisms	292
A.3	Incremental Constitutive Equation in Three Dimensions	294
A.4	Objectivity	297
A.5	Relation among One, Two and Three Dimensional Models	301
	Notation for the Appendix A	302
	References	304
APPENDIX B	COMPARISON WITH THE STRESS DILATANCY RELATION	
		305
	References	312

## ABSTRACT

Two modes have been identified in the earthquake induced damage to soil structures and foundations associated with excess pore water pressure rise in saturated sand. One involves complete flow failure due to reduction in soil strength of saturated sand. This mode of damage is essentially analyzed with a simple static approach by comparing post-earthquake residual strength of sand with initial stress due to gravity. The other involves limited, but often large, amount of deformation due to significant reduction in soil stiffness but without involving mechanism of failure in soil. The mechanism inducing this mode of damage is called cyclic mobility. The cyclic mobility occurring in the loose sand is often called "liquefaction" in practice but in the present study the mechanism which does not involve the failure in soil will be called cyclic mobility. The cyclic mobility, often called liquefaction, plays a significant role in earthquake induced deformation in soil structures and foundations as often revealed in the case histories during past earthquakes.

In assessing amount of earthquake induced deformation in soil structures and foundations, a simple but physically feasible model is needed for representing essential features of cyclic mobility. Many approaches have been proposed for modeling of cyclic mobility but, up to the present, none of the proposals seem to be so successful as to be readily applicable in practice of soil dynamics and earthquake engineering. The main problems widely seen in the previous studies are (1) inadequate modeling of initially anisotropically consolidated soil and (2) numerical

vulnerability associated with the stress path in the vicinity of the failure line.

An attempt is made in this study to solve these problems. The proposed model is of a generalized plasticity type defined in the strain space. The concept of multiple mechanism is used as a vehicle for decomposing the complex mechanism into a set of simple mechanisms defined in one dimensional space. Each virtual simple shear mechanism is assumed to follow a hyperbolic relation in the virtual stress and strain space. These virtual simple shear mechanisms play a key role in idealizing the soil behavior under the initially anisotropic consolidation condition.

In order to overcome the numerical difficulty, a simple scheme is proposed; modeling of cyclic mobility, not as a yielding process, but as a process in which the scale of the shear strain is gradually enlarged as the effective stress path approaches the failure line. To define the "distance" to the failure line, the concept of "liquefaction front" is introduced in the effective stress space as an envelope of current stress points. The liquefaction front, originating from the envelope of initial effective stress points, gradually approaches the failure line as the cyclic mobility proceeds as a function of plastic shear work. The liquefaction front is used to define plastic volumetric strain as well as to define the scale for enlarging shear strain.

Mathematical formulation of the present model results in incremental as well as integrated constitutive equations. In particular, the tangent stiffness matrix in the incremental relation becomes symmetric, ensuring the efficiency in the

numerical analysis, whereas the integrated constitutive relation serves as a guide, ensuring the convergence on the physically feasible stress strain relation. Number of the parameters of the present model is ten; two for elastic behavior, two for plastic shear, and the rest for dilatancy.

Numerical analysis with a single soil element indicates that the present model, under undrained cyclic loading condition, is capable of representing the rapid as well as gradual increases in the shear strain amplitude greater than several percent in the manner consistent with the laboratory data.

According to the present approach, actual simple shear mobilizes most of the virtual simple shear mechanisms but obviously degree of the mobilization depends on the directions of the virtual mechanisms. The virtual mechanism most significantly mobilized is the one which is oriented to the direction of the actual simple shear. Anisotropic consolidation mainly mobilizes the virtual simple shear mechanisms oriented to or close to the compression shear mode but does not have a significant influence on the virtual simple shear mechanisms oriented close to horizontal direction. When the cyclic simple shear begins in the horizontal direction, the latter group of virtual mechanisms are the main mechanisms being mobilized. Thus the behavior of soil under cyclic simple shear loading with bulging of soil constrained as in the level ground is not affected by the initial anisotropic consolidation conditions if the initial mean effective stress is kept the same. This is consistent with the laboratory findings.

When the bulging of the soil is not constrained, the results



of the single element analysis show the limit in decreasing value of effective mean stress and the gradual settlement with bulging in the soil element, suggesting reasonable applicability in the two dimensional analysis of soil structures and foundations.

In order to examine the overall applicability of the present model in the level ground analysis, shaking table tests are conducted and analyzed with the present model. The model ground in the present study has dimensions of about 2 meters in diameter and height, contained in a stack of 64 aluminum rings. Three series of shaking table tests are reported in the present study; two of them are shaken with a sinusoidal input motion, the rest with an earthquake input motion. Excess pore water pressures, accelerations and displacements are measured. The results of the analysis indicate a fundamental applicability of the present model in the one dimensional analysis of level ground.

In order to examine the applicability of the present model in the two dimensional analysis, a case study is conducted on the performance of sheet pile quay walls during 1983 Nihonkai-Chubu Earthquake of magnitude 7.7. Quay walls with and without damage are analyzed of which water depth is 10 meters. The damaged quay wall displaced about 1.5 meters toward sea due to the cyclic mobility in the backfill sand, exhibiting yielding in the steel sheet pile at 6 meters below the water level. The quay wall without damage was constructed by excavation without backfilling.

The results of the analysis of the damaged quay wall are consistent with the observed deformation and the observed yielding of the sheet pile. The results of the analysis are also consistent with the observed performance of the quay wall without

damage. Thus the present approach is capable of differentiating seriously large deformation (i.e. damage) from negligibly small deformation (i.e. non damage) of quay walls during earthquakes.

The analysis also provides a full understanding on the mechanism of deformation of quay walls during earthquakes. Though very complex stress paths are involved in the soil deformation, e.g. with rotation of principal stress axes due to Rayleigh wave generated by the soil-structure interaction, fundamental mechanism inducing residual deformation is the existence of initial stress and its release in accordance with the cyclic mobility. In particular, principal strains are gradually induced mainly in the principal axes directions of initial stresses.

## ACKNOWLEDGMENTS

This research was initiated when the 1983 Nihonkai-Chubu Earthquake of magnitude 7.7 hit northern Japan, causing serious damage to port structures. The author wishes to express his sincere gratitude to Professor Kenji Ishihara of Tokyo University for his guidance and encouragement. The author also wishes to express his sincere gratitude to Professor Ikuo Towhata for his advice and encouragement, and for his friendship. Sincere gratitude is also due to Professors Fumio Tatsuoka, Masahiko Isobe and Hideyuki Horii of Tokyo University for their advice.

The sincere gratitude is also due to Dr. Hajime Tsuchida, former Director General of the Port and Harbour Research Institute, and other members and colleagues of the Port and Harbour Research Institute. In particular, the author wishes to express his utmost gratitude to Dr. Masaki Kobayashi, Chief of the Soil Mechanics Laboratory of the Port and Harbour Research Institute, for his advice upon the constitutive equations and computer programming. The author also wishes to express his gratitude to Professor W. D. Liam Finn of the University of British Columbia, Canada, for his continuing advice and encouragement.

Special thanks are due to Mr. Katsuhiko Koizumi, former member of the Earthquake Resistant Structures Laboratory of the Port and Harbour Research Institute, for his elaborate assistance in the shaking table tests and to Mr. Tomohiro Kameoka, member of the Geotechnical Earthquake Engineering Laboratory of the Port and Harbour Research Institute, for his devoted assistance in the

x

numerical analysis. Mr. Yasuo Matsunaga and Mr. Takeshi Urakami, members of the Geotechnical Earthquake Engineering Laboratory of the Port and Harbour Research Institute, also assisted in the final stage of preparing the manuscript. The author wishes to express his gratitude to all of them.

## NOTATION

a, b and c : scaling parameters for virtual simple shear mechanism

$B = [0.5K_a/(-\sigma_{ma}')^{0.5}]^2$  : factor for volumetric relation

$c_1$  : parameter for specifying the level of threshold limit in liquefaction resistance curve

[D] : tangential stiffness matrix

$[D_{L/U}^{(i)}]$  : tangential stiffness matrix for mechanism i at loading and unloading

$\{e\}^T = \{(\epsilon_x + \epsilon_y) \quad (\epsilon_x - \epsilon_y) \quad \gamma_{xy}\}$  : transformed strain

$\{e_p\}^T = \{\epsilon_p \quad 0 \quad 0\}$  : additional volumetric strain of plastic nature in transformed space; compression negative

f and g : normalized hyperbolic relation and its tangent stiffness

G : secant shear modulus

$G_0$  : shear modulus measured at strain level of  $10^{-6}$

$G_{m0}$  : initial shear modulus at  $\sigma_m' = \sigma_{m0}'$

$G_m^*$  : shear modulus used for computing plastic shear work

$G_m$  : shear modulus at the current effective mean stress  $\sigma_m'$

$G_{t1}$ ,  $G_{t2}$  and  $G_{t3}$  : factors for tangent stiffness

H : hysteretic damping factor observed in the laboratory

$\tilde{H}$  : hysteretic damping factor generated by the present model

$H_{L/U}$  : hardening function in plasticity theory

$H_m$  : limiting value of hysteretic damping factor

h : hysteretic damping factor which should be generated in the virtual simple shear

$\tilde{h}$  : hysteretic damping factor generated by the present model

in the virtual simple shear

$h_v$  : limiting value of virtual hysteretic damping factor

$I$  : number of the multiple virtual mechanisms for shear

$K$  : elastic tangent bulk modulus of soil skeleton

$K_a$  : value of  $K$  at  $\sigma'_m = \sigma'_{ma}$

$K_f$  : bulk modulus of pore water

$K_0$  : coefficient of earth pressure ( $= \sigma'_x / \sigma'_y$ )

$\{l^{(i)}\}$  and  $\{l_{L/U}^{(i)}\}$  : transformed vectors of  $\{n^{(i)}\}$  and  $\{n_{L/U}^{(i)}\}$

$m_1 = \sin \phi'_f$  : inclination of failure line

$m_2 = \sin \phi'_p$  : inclination of phase transformation line

$m_3 = 0.67m_2$  : auxiliary parameter for defining the liquefaction front

$n_{ij}$  : loading/unloading direction tensor

$n_{L/Uij}$  : direction tensor of plastic strain increment

$\{n^{(i)}\}$  : loading/unloading direction vector for mechanism  $i$

$\{n_{L/U}^{(i)}\}$  : direction vectors of stress increments for mechanism  $i$  at loading and unloading

$n$  : porosity of soil skeleton

$p$  : excess pore water pressure; compression positive

$p_1, p_2, w_1$  and  $S_1$  : material parameters for defining cumulative dilatancy

$Q^{(i)}$  : virtual shear stress per unit angle  $\theta$  for mechanism  $i$

$Q_B^{(i)}$  : virtual simple shear stress amplitude per unit angle  $\theta$

$Q_v$  : virtual shear strength per unit angle  $\theta$

$r$  : state variable equivalent to  $\tau / (-\sigma'_{m0})$

$R$  : correction factor for cumulative shear work in dilative zone

$R_{L/U}^{(i)}$  : tangential stiffness modulus for mechanism  $i$  at loading

and unloading

- $S$  : state variable equivalent to  $\sigma_m'/\sigma_{m0}'$
- $S_0$  : liquefaction front parameter
- $S_w$  : a parameter for correction factor  $R$
- $\{s'\}^T = \{(\sigma_x' + \sigma_y')/2 \quad (\sigma_x' - \sigma_y')/2 \quad \tau_{xy}\}$  : transformed stress
- $t$  : time coordinate
- $[T_\epsilon]$  : transformation matrix for strain
- $[T_\sigma]$  : transformation matrix for stress
- $U_n$  : normal component of displacement of the solid-water boundary
- $u$  and  $v$  : displacements in  $x$  and  $y$  directions
- $W$  : equivalent elastic strain energy
- $\Delta W$  : hysteretic damping energy
- $W_n$  : factor for normalization of shear work
- $W_s$  : plastic shear work
- $W_{st}$  : total shear work
- $W_{se}$  : elastic shear work
- $W^{(i)}$  : equivalent elastic virtual strain energy for mechanism  $i$
- $\Delta W^{(i)}$  : hysteretic damping energy of virtual mechanism  $i$
- $w$  : normalized shear work
- $x, y$  and  $z$  : space coordinates
- $\alpha$  and  $\beta$  : coefficients for specifying Rayleigh damping; i.e. coefficients for mass matrix and stiffness matrix
- $\gamma$  : shear strain amplitude measured at drained cyclic loading
- $\gamma^{(i)}$  : virtual simple shear strain for mechanism  $i$
- $\gamma_{m0}$  : initial reference strain
- $\gamma_m$  : reference strain
- $\gamma_v$  : virtual reference strain

$\gamma_{xyB}$  : amplitude of simple shear strain

$\gamma_{(i)B}$  : amplitude of virtual simple shear strain for mechanism i

$\gamma_{0.5}$  : shear strain amplitude at  $G/G_0 = 0.5$

$\delta$  : threshold value for loading criterion

$\epsilon_a$  : axial strain amplitude at triaxial cyclic testing

$\epsilon_{ij}$  : strain tensor

$\{\epsilon\}^T = \{ \epsilon_x \quad \epsilon_y \quad \gamma_{xy} \}$  : strain vector

$\{\epsilon_p\}$  : volumetric strain of plastic nature; compression negative

$\epsilon_e$  : elastic volumetric strain; compression negative

$\epsilon_{e0}$  : initial elastic volumetric strain; compression negative

$\theta$  : a parameter in Wilson's  $\theta$  scheme for time integration

$\theta_i = (i-1)\Delta\theta$  : angle for virtual shear mechanism i in  $(\epsilon_x - \epsilon_y) - \gamma_{xy}$  plane

$\Delta\theta = \pi/I$

$\xi_h$  : a parameter for damping factor similar to virtual reference strain

$\xi$  and  $\eta$  : normalized virtual strain and stress

$\xi'$  and  $\eta'$  : normalized virtual strain and stress scaled by factors a, b and c for adjusting the hysteresis loop

$\xi_B$  and  $\eta_B$  : coordinates of reversal point in the normalized space

$\xi_r$  and  $\eta_r$  : coordinates of reversal point

$\rho$  : density of water

$\sigma_1, \sigma_2, \sigma_3$  : principal stresses; compression positive

$\sigma_c'$  : initial confining pressure at triaxial cyclic testing; compression positive

$\sigma_{ij}$  : stress tensor

$\{\sigma'\}^T = \{ \sigma_x' \quad \sigma_y' \quad \tau_{xy} \}$  : effective stress vector

$\{\sigma',^{(i)}\}$  : virtual stress for mechanism i



$\sigma_m' = (\sigma_x' + \sigma_y')/2$  : mean effective stress; compression negative

$\sigma_{m0}'$  : initial mean effective stress; compression negative

$\tau = (\sigma_1' - \sigma_3')/2$  : deviatoric stress

$\tau_D$  : deviatoric stress amplitude in triaxial cyclic testing

$\tau_m$  : shear strength

$\tau_{m0}$  : initial shear strength

$\phi_f'$  : shear resistance angle

$\phi_p'$  : phase transformation angle

## CHAPTER 1

### INTRODUCTION

#### 1.1 General

Two modes have been identified in the earthquake induced damage to soil structures and foundations associated with excess pore water pressure rise in saturated cohesionless soil. One involves complete flow failure due to reduction in saturated soil strength. This mode of damage is essentially analyzed with a simple static approach within a framework of the critical state concept (Castro, 1975); the analysis is done by comparing post-earthquake residual strength of soil with initial stress due to gravity.

The other involves limited, but often large, amount of deformation due to significant reduction in soil stiffness but without involving mechanism of failure in soil. The mechanism inducing this mode of damage is called cyclic mobility.

In practice, the cyclic mobility occurring in loose cohesionless soil is often called 'liquefaction,' which is distinguished from the 'cyclic mobility' occurring in dense cohesionless soil. The distinction is made by such observation that the former cyclic mobility produces 'rapid growth' in strain amplitude under undrained cyclic loading whereas the latter produces 'slow growth' in strain amplitude. In the present study, both phenomena will be called cyclic mobility as long as the mechanism does not involve the flow failure of soil.

For estimating amount of deformation due to the cyclic

mobility, dynamic analysis is needed based on a simple but physically feasible modeling of cyclic mobility. Many approaches have been proposed for modeling of cyclic mobility but, up to the present, none of the proposals seem to be so successful as to be readily applicable in practice of the soil dynamics and the earthquake engineering as will be shown in the next section.

## 1.2 Review of Previous Studies

### 1.2.1 Cyclic Mobility as Identified through Laboratory Studies

Essential features of the cyclic mobility as identified through the previous laboratory studies may be summarized as follows. First of all, when saturated cohesionless soils are tested in the laboratory under the undrained cyclic loading condition, such stress paths and stress-strain curves as shown in Figs. 1.1 and 1.2 (after Ishihara, 1985) are usually observed. As cyclic loading goes on, the stress path approaches from a initial stress point to the failure lines, as shown in Figs. 1.1(a) and 1.2(a), and eventually converges on a certain limiting stress path in the vicinity of the failure lines. The stress-strain curve, however, does not converge on a closed hysteresis loop; the shear strain rapidly increases in looser sand as shown in Fig. 1.1(b) or gradually and continually increases in denser sand as shown in Fig. 1.2(b). Obviously the shear strain increases beyond several percent. This is important to note for modeling of cyclic mobility.

It is a common practice in the soil dynamics and the earthquake engineering that resistance against 'liquefaction' of

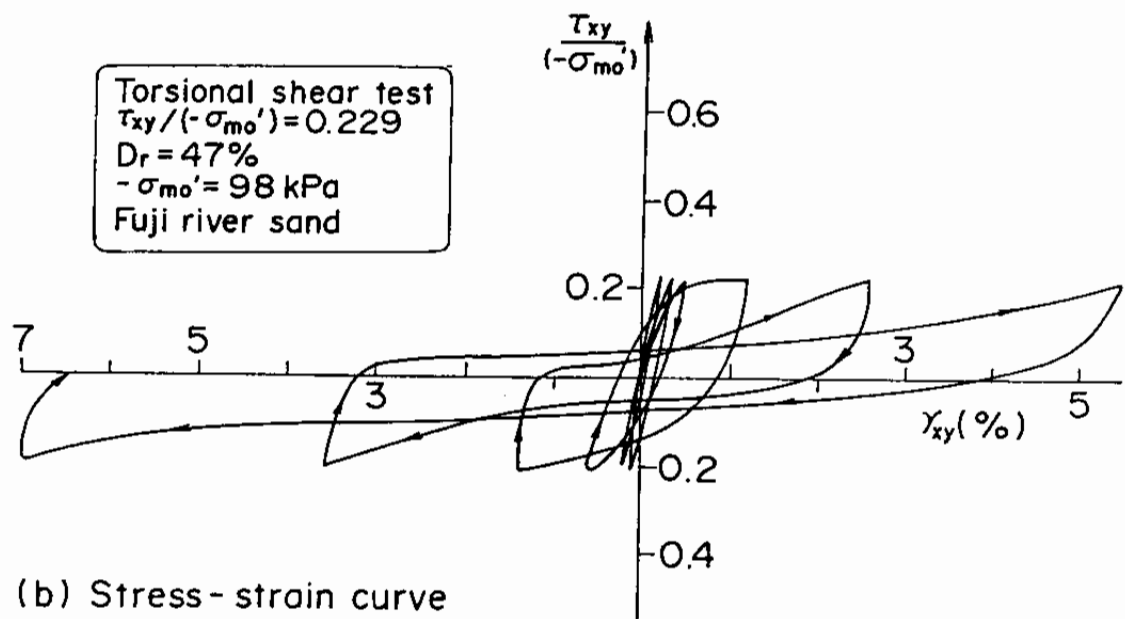
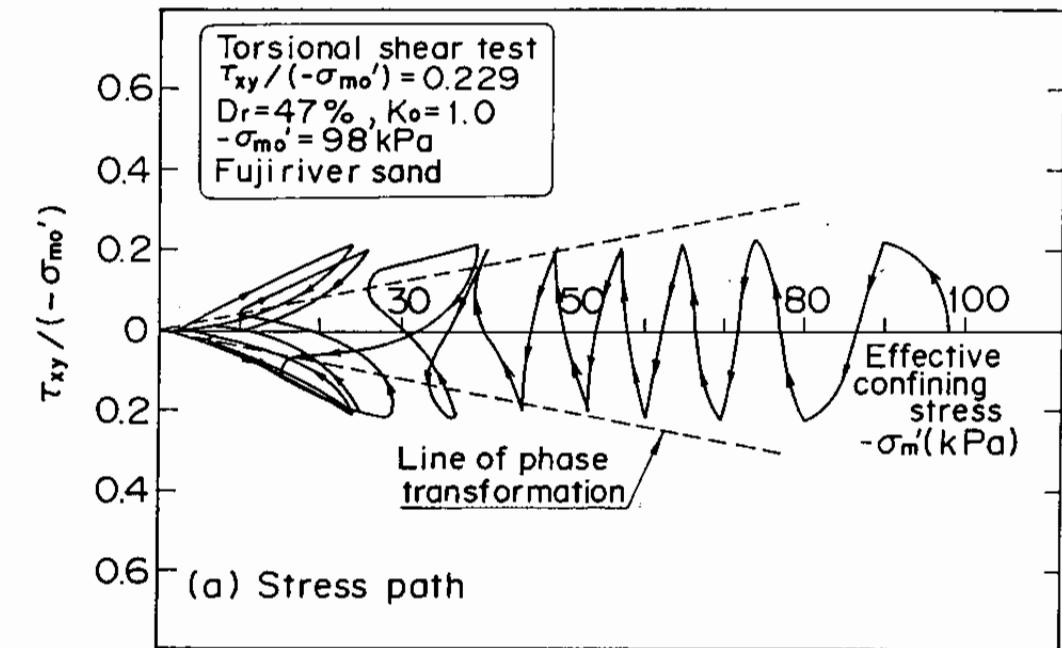


Fig. 1.1 Stress path and stress-strain curve for loose sand obtained from the cyclic torsion shear test (after Ishihara, 1985)

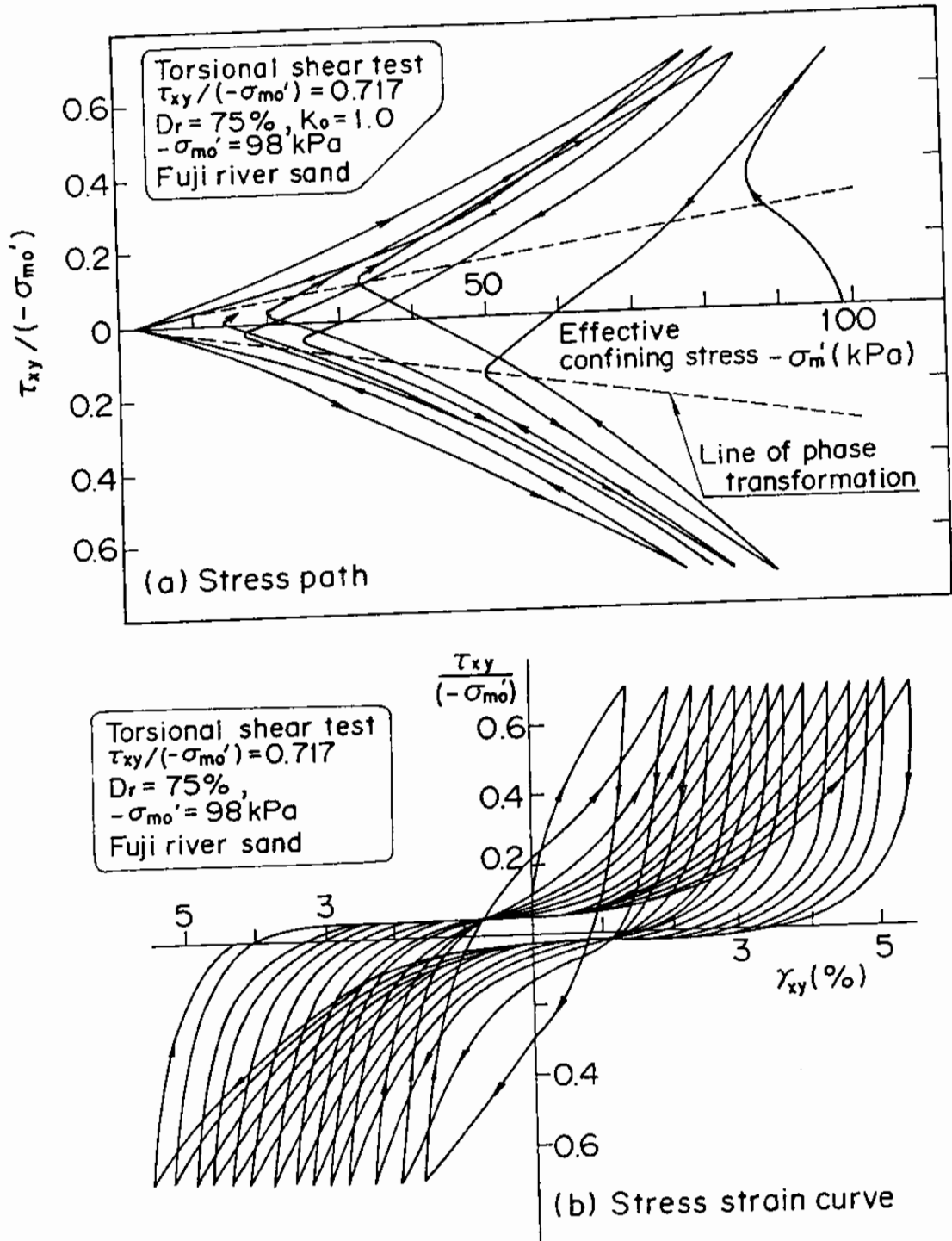


Fig. 1.2 Stress path and stress-strain curve for dense sand obtained from the cyclic torsion shear test (after Ishihara, 1985)

cyclic mobility is defined in reference to the state of achieving 5 percent shear strain in double amplitude. To be more specific, the 'liquefaction resistance' is defined by the ratio of shear stress amplitude over initial confining stress to achieve the aforementioned state. The stress ratio depends on number of cycles of loading and hence the liquefaction resistance is represented as a relation between the shear stress ratio and the number of cycles of loading.

Initial anisotropic consolidation condition, specified by the ratio  $K_0$  of horizontal over vertical normal stresses at an initial stress state, affects the liquefaction resistance obtained with simple shear testing as shown in Fig. 1.3 if the initial vertical effective stress is used for defining the shear stress ratio (Ishihara, et al, 1977). If, on behalf of the initial vertical effective stress, the initial mean effective stress is used for defining the shear stress ratio, the liquefaction resistance becomes independent of initial  $K_0$  value. This is also one of the important properties of sand in the cyclic mobility.

It is also to be noted in Fig. 1.3 that a threshold limit exists in the stress ratio below which the 'liquefaction' will never be achieved even if number of cycles of loading is increased up to more than one hundred.

Simple shear testing of sand with initial  $K_0$  consolidation condition reveals the effect of principal stress axes rotation. Two important properties are recognized in cohesionless soil undergoing principal stress axes rotation as follows;

- (1) the rotation of principal stress axes results in greater

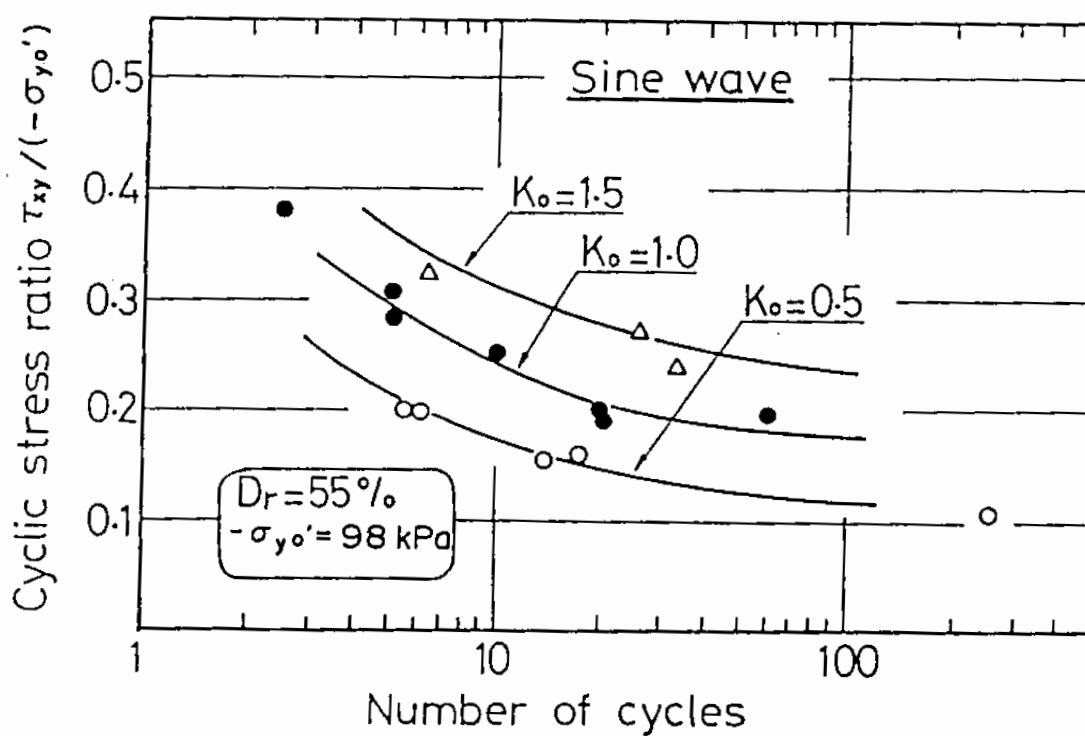


Fig. 1.3 Effect of  $K_0$  condition on liquefaction resistance (after Ishihara et al, 1977)

amount of excess pore water pressure rise under undrained condition (Ishihara and Towhata, 1983), and

- (2) direction of principal strain increment does not coincide with that of principal stress (Miura et al., 1986a).

Deformation properties of cohesionless soil under drained cyclic loading condition are also important for modeling of cyclic mobility if the model is to be applied in practice for differentiating significantly large deformation from very small deformation of soil structures and foundations. The mechanism associated with the very small deformation often involves only a small amount of excess pore water pressure rise, being effectively the same as that of drained condition.

The deformation properties of sand under drained condition are studied in terms of a secant shear modulus and a hysteretic damping factor as defined in Fig. 1.4. The secant shear modulus and the hysteretic damping factor depend on shear strain amplitude. Typical laboratory results are shown in Fig. 1.5 (Kong et al, 1986; Iwasaki et al, 1978). In this figure, the factor  $\gamma_{0.5}$  for normalizing the shear strain amplitude is the shear strain amplitude at  $G/G_0 = 0.5$ . The unique relations are recognized between  $G/G_0$  and  $\gamma/\gamma_{0.5}$  and between  $h$  and  $G/G_0$ , which are independent of the confining pressures.

### 1.2.2 Previous Studies on Modeling of Cyclic Mobility

Many attempts have been made for modeling of cyclic mobility. The models proposed out of those attempts are from time to time modified for incorporating additional capability of representing the complex but essential features of soil behavior



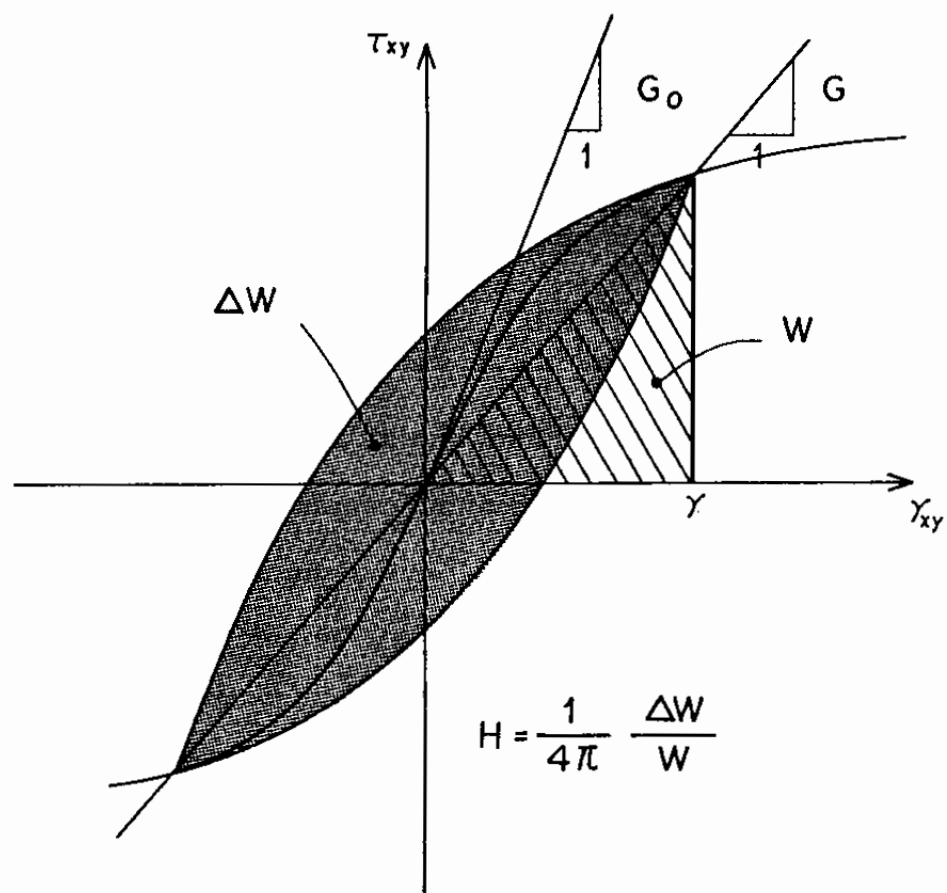
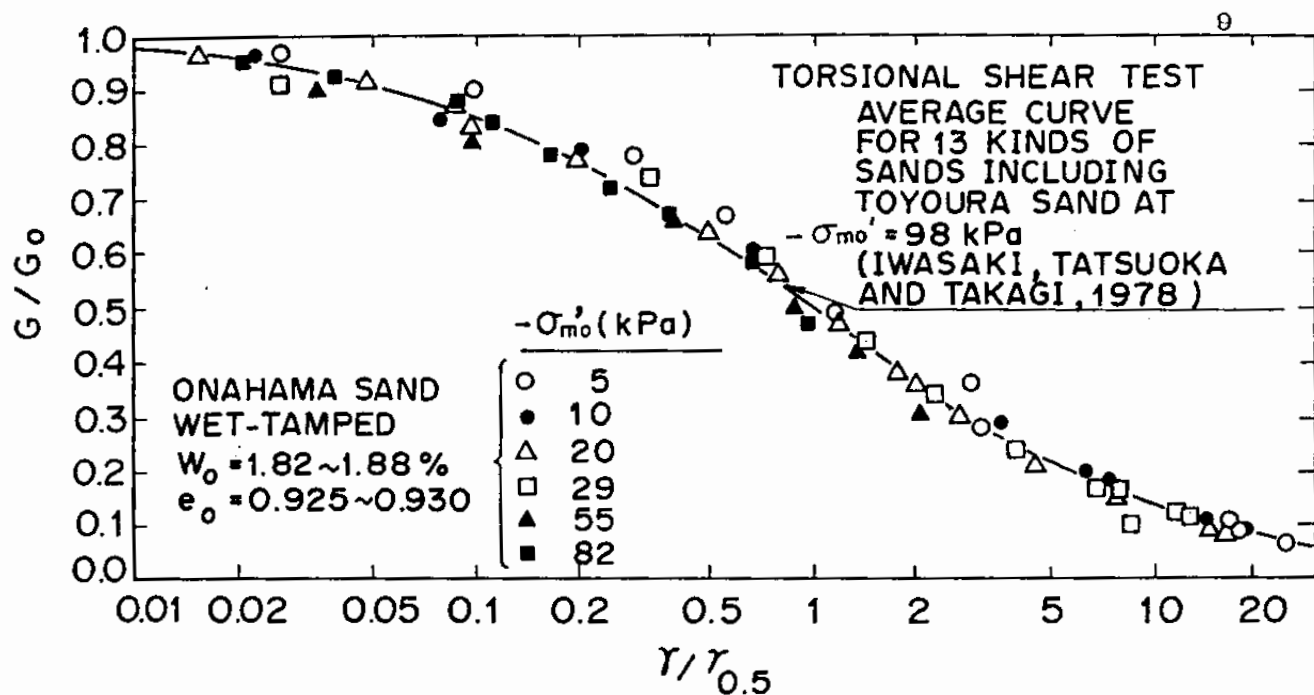
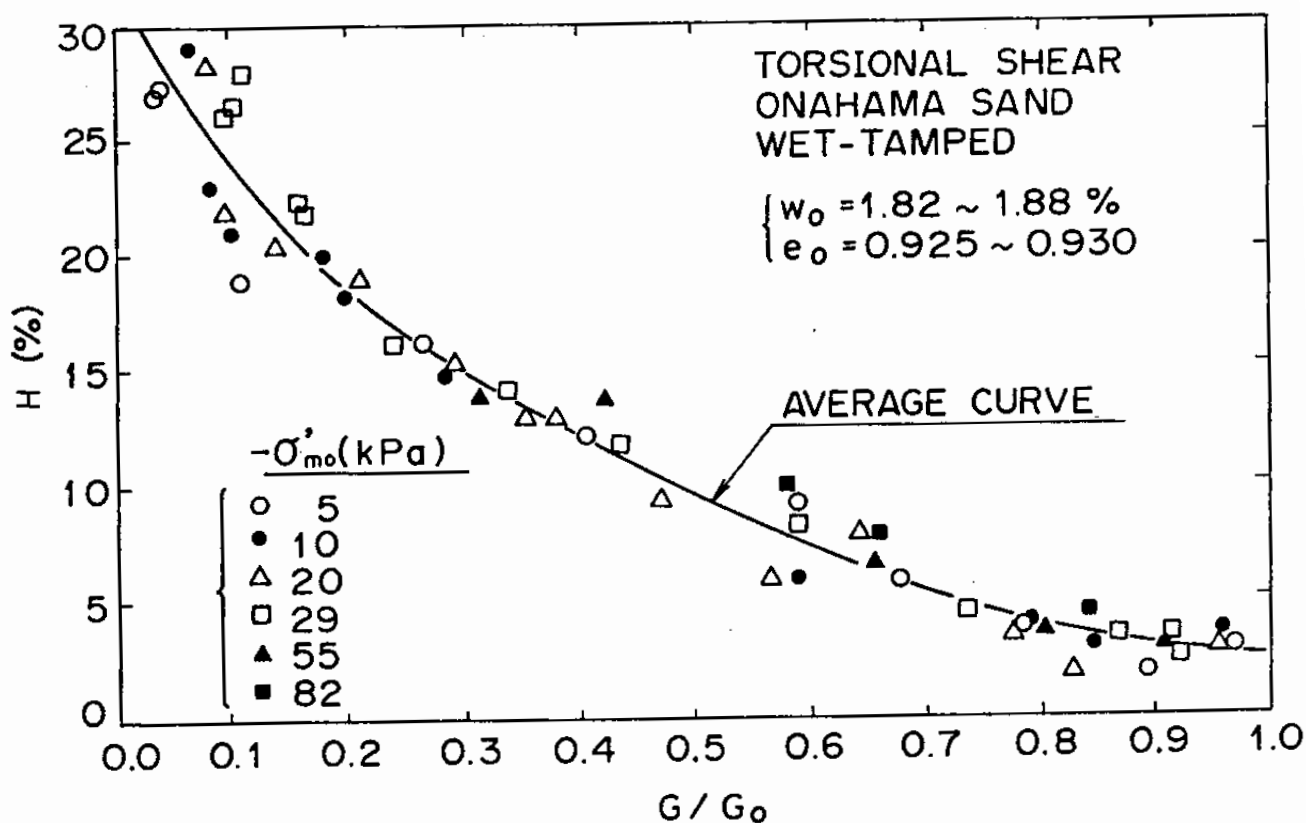


Fig. 1.4 Secant shear modulus and hysteretic damping factor



(a) Normalized secant shear modulus (after Kong et al., 1986;  
Iwasaki et al., 1978)



(b) Hysteretic damping factor (after Kong et al., 1986)

Fig. 1.5 Deformation properties of sands under the drained  
condition

summarized in the previous subsection. Their up-to-date capability in representing the cyclic mobility can be seen in the joint study conducted at the Japanese Society of Soil Mechanics and Foundation Engineering (Ishihara et al, 1989). In this study the participants were asked to present computed results with the model which they believe to be the best at present. Several outputs were asked for computation. As one of the outputs asked for computation, stress paths and stress-strain relations of soil under undrained cyclic loading were computed under initial consolidation conditions with  $K_0 = 1.0$  and  $0.5$ . This provides a good opportunity for evaluating fundamental capability of the existing approaches.

A question raised at this occasion is how to idealize the undrained cyclic behavior of sand with initially anisotropic consolidation. The experimental evidence suggests, as mentioned earlier, that cyclic behavior of sand should not be affected by the initial  $K_0$  condition if the initial effective mean stress is kept the same. Amplitude of cyclic change in deviatoric stress  $\tau = (\sigma_1' - \sigma_3')/2$ , however, is significantly affected by the initial  $K_0$  value as illustrated in Fig. 1.6; i.e. the greater the initial deviatoric stress is, the smaller becomes the amplitude of cyclic change in deviatoric stress.

Seven models were examined on this opportunity. Three models among others represent up-to-date versions of a conventional approach for modeling of soil behavior under cyclic loading. In these models a theoretical framework is given by the plasticity theory, which will be briefly reviewed below.

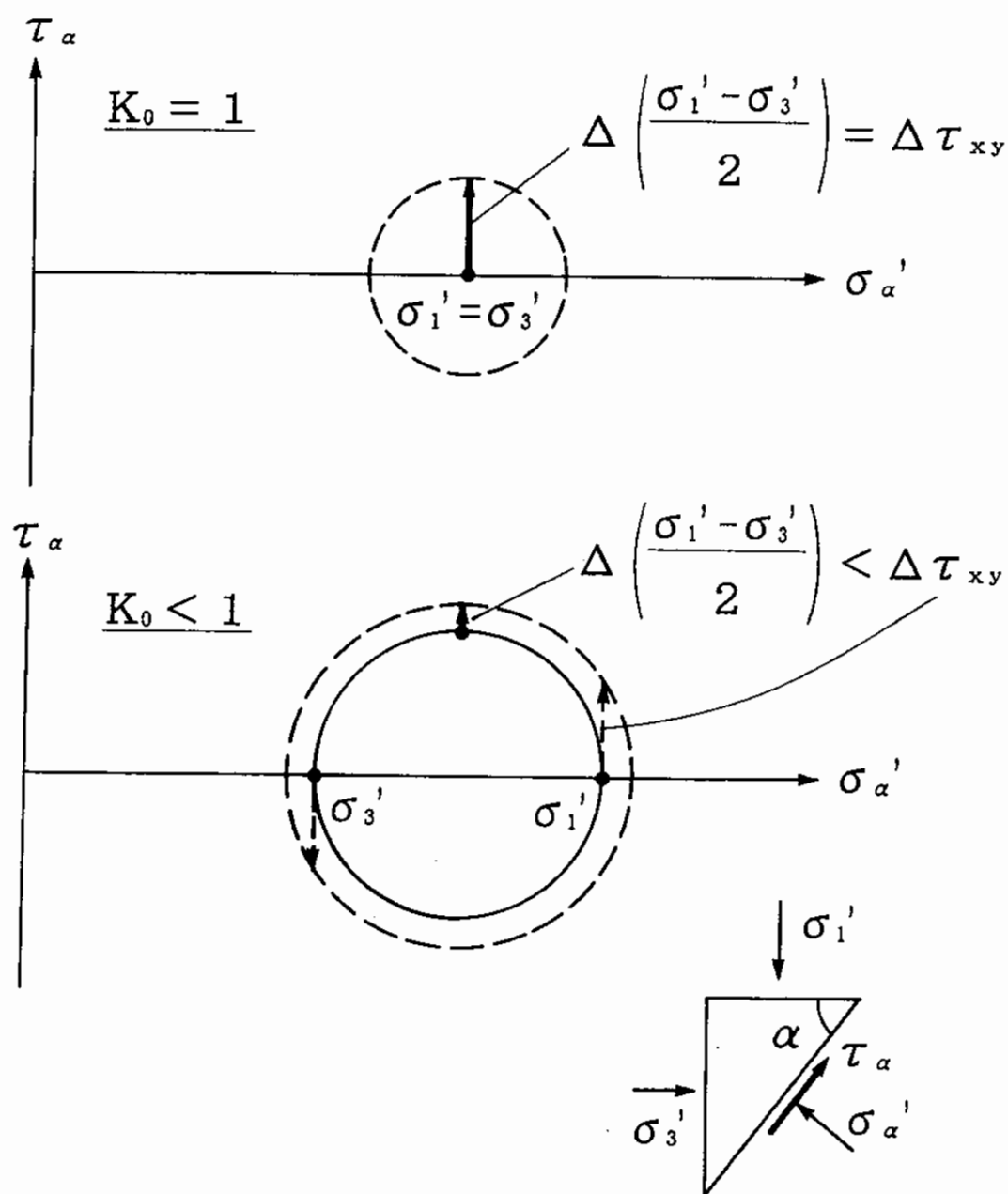


Fig. 1.6 Cyclic deviatoric stress amplitude at initially isotropic and anisotropic stress conditions under the same cyclic simple shear loading

## (1) Brief review on plasticity theory

The plasticity theory consists of the following concepts;

- a) direction  $n_{ij}$  which differentiates loading from unloading (i.e. reversal loading) in stress space,
- b) direction  $n_{L/Uij}$ , called flow rule, which defines direction of strain increment  $d\epsilon_{ij}^p$  in plastic deformation associated with stress increment  $d\sigma_{ij}$ , and
- c) a scalar function  $H_{L/U}$ , called hardening function, which defines magnitude of strain increment in plastic deformation.

With these concepts, behavior of soil under cyclic loading is represented through such relations as

$$d\epsilon_{ij}^p = H_L (n_{ij} d\sigma_{ij}) n_{Lij} \quad (\text{if } n_{ij} d\sigma_{ij} > 0) \quad (\text{loading}) \quad (1.1)$$

$$d\epsilon_{ij}^p = 0 \quad (\text{if } n_{ij} d\sigma_{ij} = 0) \quad (\text{neutral}) \quad (1.2)$$

$$d\epsilon_{ij}^p = H_U (n_{ij} d\sigma_{ij}) n_{Uij} \quad (\text{if } n_{ij} d\sigma_{ij} < 0) \quad (\text{unloading}) \quad (1.3)$$

The direction for loading/unloading is in general specified as an outward normal to a loading surface defined in stress space. Similarly the direction for strain increment is specified with a plastic potential, the hardening function  $H_{L/U}$  specified with deformation and translation of the loading surface in stress space. In recent years, however, both of the directions and the hardening function are often directly specified in the stress space.

The virtue of the plasticity theory is to assure the

uniqueness of strain increment induced by arbitrary stress increment; i.e. strain increment does not 'jump' in the vicinity of the neutral direction. This is confirmed with Eqs. (1.1) through (1.3) because, when  $n_{ij}d\sigma_{ij}$  is equal to or close to zero, these equations indeed demand that strain increment be equal to or close to zero.

## (2) Up-to-date studies along the conventional approach

Within the framework of plasticity theory, the three approaches mentioned earlier can be summarized as shown in Table 1.1. Pastor-Zienkiewicz model (Pastor and Zienkiewicz, 1986), hereafter called P-Z model, is the most conventional approach among them. The loading surface is defined in the principal stress space, of which dimension is three and of which coordinates are specified by three principal stresses ( $\sigma_1$ ,  $\sigma_2$ ,  $\sigma_3$ ). The loading surface deforms and translates with the current principal stress and with its history in the principal stress space. Cam Clay model (Schofield and Wroth, 1968) is the origin of P-Z model.

Kabilamany-Ishihara model (Kabilamany and Ishihara, 1990), hereafter called K-I model, uses the concept of multiple mechanism defined in the principal stress space. Each mechanism is defined in the two dimensional stress space each of which is defined with two out of three principal stresses. The loading surface is defined for each mechanism in the two dimensional principal stress space. The theoretical framework of the multiple mechanism was originally presented by Koiter (1949). Though K-I model is often called Multi-Mechanism model, the model consists

Table 1.1 Up-to-date models along the conventional approach

Model Name	Loading Surface	Flow Rule	Hardening function
P-Z model	Cam Clay Type	Cam Clay Type	hyperbolic
K-I model	$q_k/p_k = \text{const.}$	Cam Clay Type	hyperbolic
Nishi model	$\eta^* = \text{const.}$	Cam Clay Type	hyperbolic

$$\eta^* = \sqrt{(\eta_{11} - \eta_{110})(\eta_{11} - \eta_{110})}$$

$$\eta_{11} = S_{11} / \sigma_m'$$

$S_{11}$  deviatoric stress tensor

$$p_k = (\sigma_i + \sigma_j) / 2, \quad q_k = (\sigma_i - \sigma_j) / 2$$

of only four principal mechanisms; three aforementioned principal mechanisms with an isotropic volumetric mechanism. In this context, the author suggests this type of models be called 'Principal-Mechanism model'. K-I model differs from P-Z model because the multiple mechanism concept is involved but it shares such a common feature that the model is defined in the principal stress space.

Nishi model (Nishi and Kanatani, 1990) differs from those two because the model uses the relative stress in reference to initial or most recent reversal stress point defined in the general stress space of which dimension is six and of which coordinates are specified by six stress components ( $\sigma_{11}$ ,  $\sigma_{22}$ ,  $\sigma_{33}$ ,  $\sigma_{12}$ ,  $\sigma_{23}$ ,  $\sigma_{31}$ ). The relative stress is then converted to a stress point in the principal stress space, of which dimension is three, and the loading surface is accordingly defined. A major breakthrough in defining the relative stress in six dimensional stress space was made by Sekiguchi and Ohta (1977), of which origin is again Cam-Clay model.

The results from these models for undrained cyclic loading test are shown in Figs. 1.7 through 1.9. P-Z model, as shown in Fig. 1.7, shows a closed stress path once the stress path touches the phase transformation line. The stress-strain relation also becomes a closed loop. Moreover the stress path becomes dependent on the initial  $K_0$  condition though the same shear stress ratio defined with the initial mean effective stress is applied. One may have to admit that none of these results are consistent with the properties of soil identified through the laboratory studies mentioned in the previous subsection.



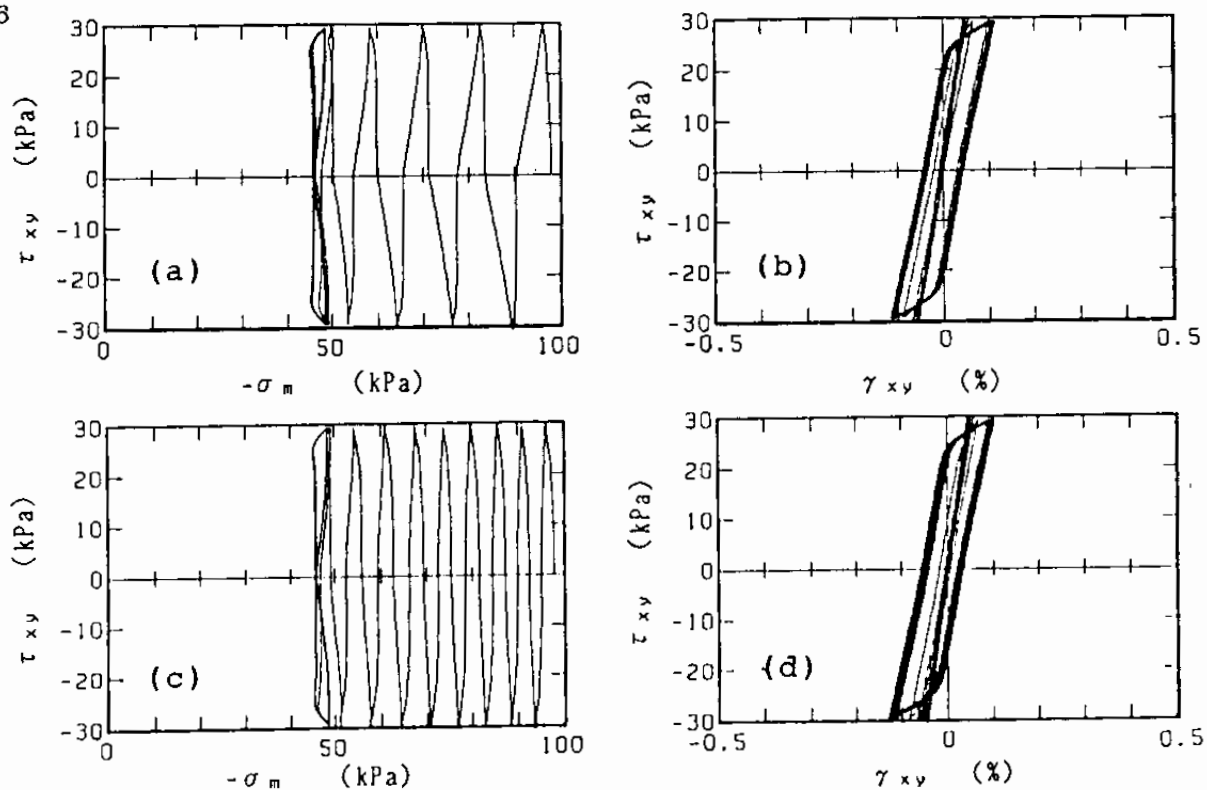


Fig. 1.7 Computed results by P-Z model (after Shiomi, 1989)

(a)(b)  $K_0 = 1.0$ ; (c)(d)  $K_0 = 0.5$

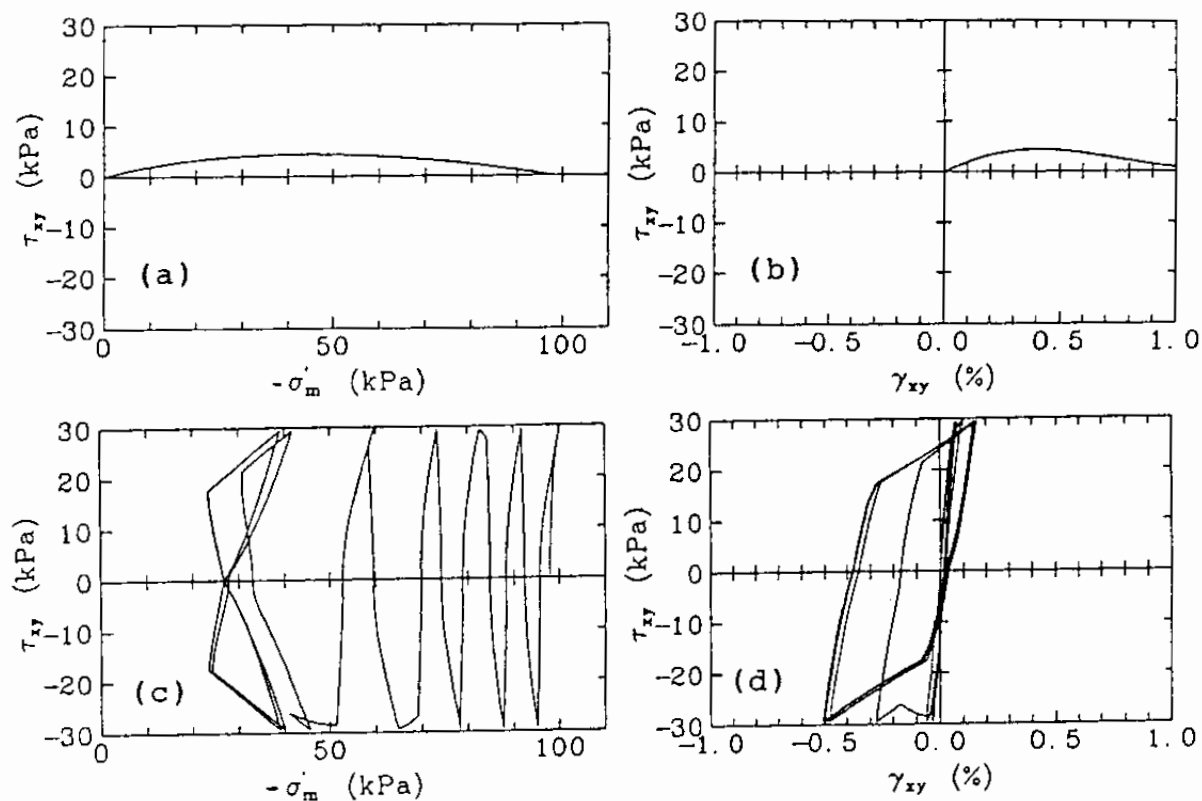


Fig. 1.8 Computed results by K-I model (after Yoshida et al,

1989), (a)(b)  $K_0 = 1.0$ ; (c)(d)  $K_0 = 0.5$

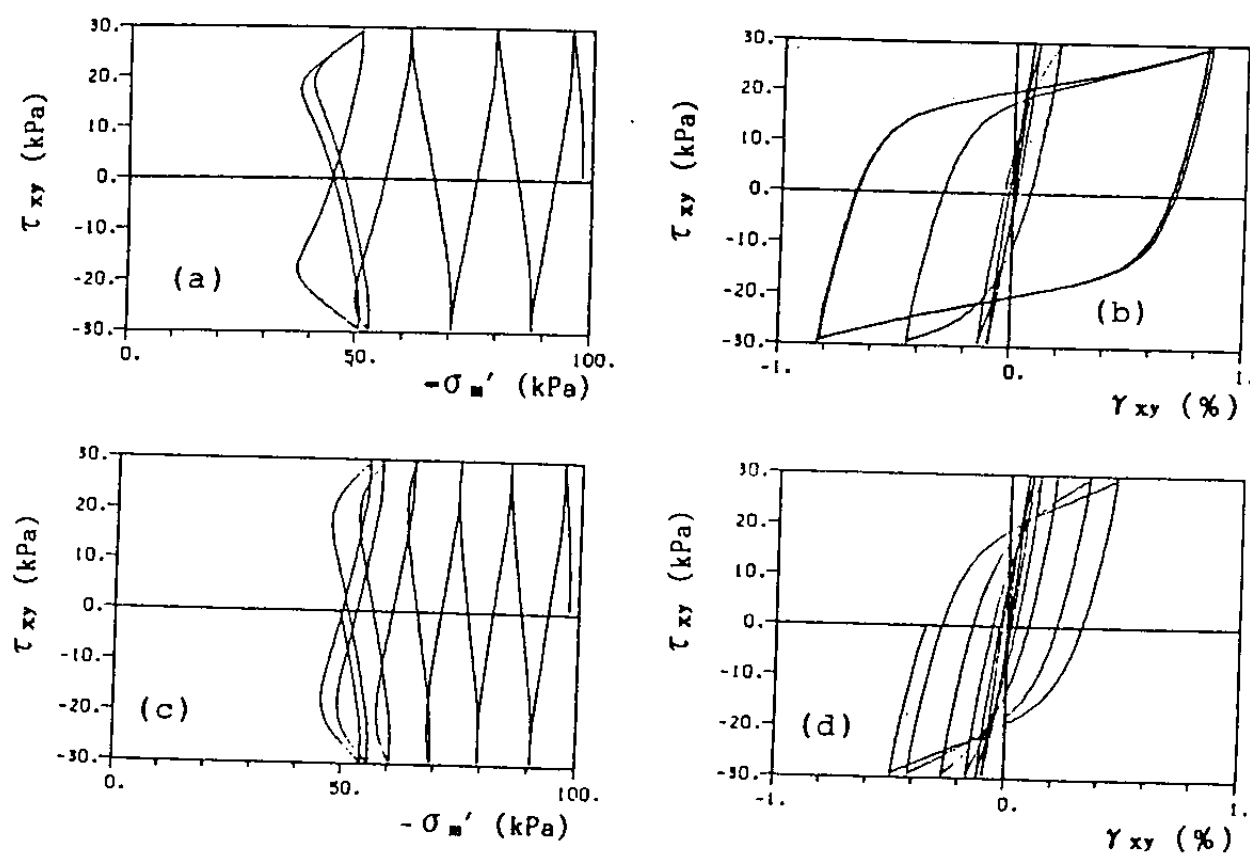


Fig. 1.9 Computed results by Nishi model (after Nishi and Kanatani, 1989), (a)(b)  $K_0 = 1.0$ ; (c)(d)  $K_0 = 0.5$

K-I model, as shown in Fig. 1.8, shows stronger influence of initial  $K_0$  condition and the stress-strain relation becomes a closed loop when  $K_0 = 0.5$ . One may have to admit again that these results are inconsistent with those identified in the laboratory studies.

Nishi model, too, shows closed loops for stress path and stress-strain relation as shown in Fig. 1.9. Dependence on the initial  $K_0$  condition is less obvious than in the results from the other models, being more consistent with those identified in the laboratory studies.

Though a certain improvement is seen in Nishi model, the results presented in Figs. 1.7 through 1.9 indicate that more work is needed for modeling of the cyclic mobility. There are many other models which can be broadly categorized with one of the three; e.g. the model by Sato et al(1981) is categorized with P-Z model, the one by Aubry et al.(1982) with K-I model, and the one by Poorooshasb and Pietruszczak (1986) with Nishi model, among others. They seem to share a common problem as seen earlier when they are to represent the cyclic mobility.

### (3) Prospect of multiple mechanism approach

In contrast to the up-to-date versions of the conventional approach reviewed so far, the approach proposed by Towhata and Ishihara(1985) offers prospect of more direct interpretation on the effect of initial  $K_0$  condition. A theoretical framework for this approach is similar to that for the multiple mechanism presented by Koiter(1949). Towhata and Ishihara (1985) postulate that actual simple shear mechanism is associated with multiple

virtual simple shear mechanisms oriented in arbitrary directions. Each virtual simple shear mechanism is represented by an inelastic spring defined in deviatoric stress and strain space, as shown in Fig. 1.10, in which each spring represents one dimensional virtual stress strain relation in the virtual simple shear.

According to their approach, the value of  $K_0$  affects many of the virtual simple shear modes, especially does the virtual simple shear mechanism of compression mode oriented in the vertical direction, but it does not affect the one in the horizontal direction. During actual simple shear, the virtual simple shear mechanism in the horizontal direction plays a major role. In consequence, the value of  $K_0$  does not have a significant influence on the actual simple shear behavior of soil if the same simple shear stress and the same effective mean stress is used in the simple shear testing of soil. Thus, this approach offers a very simple and transparent interpretation of actual simple shear mechanism.

It is, however, not readily applicable for modeling of the cyclic mobility at the existing level of development. The existing capability of the model as presented by Towhata and Ishihara (1985), shown in Fig. 1.11, indicates more work is necessary for physically feasible modeling of the cyclic mobility.

A similar approach, which will be broadly categorized in this study as multiple mechanism approach, was originally proposed for modeling of clayey soil by Calladine (1971). Since then, the prospect of the multiple mechanism approach for

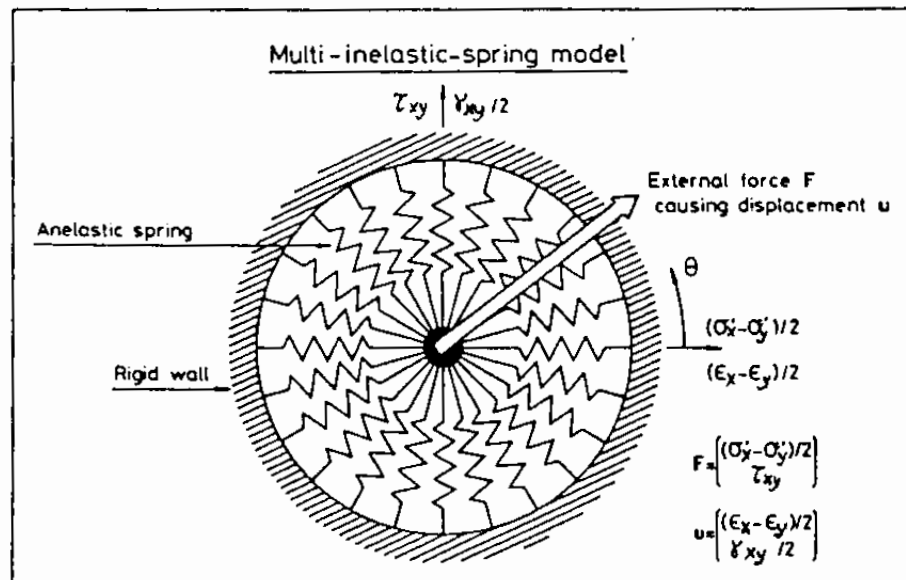


Fig. 1.10 Multi inelastic spring model (after Towhata and Ishihara, 1985)

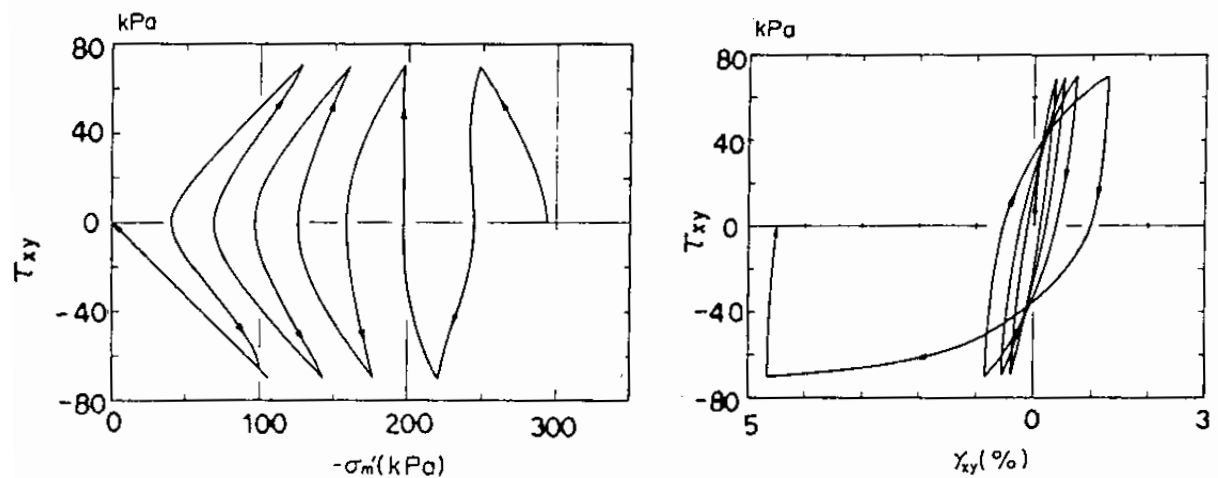


Fig. 1.11 Computed results by Multi inelastic spring model (after Towhata and Ishihara, 1985)

modeling the effect of principal stress axes rotation has attracted considerable attention from the soil engineers such as Pande and Sharma (1983), Miura et al (1986b), Bazant (1986), Pietruszczak and Pande (1987) and Chang (1989) among others. The capability for modeling of cyclic mobility along this line of studies, however, is not yet known at present.

### 1.3 Objectives

With keeping in mind the need in practice to estimate amount of deformation induced in soil structures and foundations due to the cyclic mobility, the objective of the present study is to develop a simple and physically feasible model for the cyclic mobility. If a model for the cyclic mobility can be of any use in practice of the soil dynamics and the earthquake engineering, the model may have to be able to simulate the rapid or gradual increase in shear strain ranging from about one to ten percent, from which cracks, settlements and other deformation of major consequence initiate. Such a large shear strain, as shown in Figs. 1.1 and 1.2, is generated only when the effective stress path becomes very close to the failure lines. This causes difficulty in numerical analysis because a very small error contained in the computed effective stress causes a very large error in the computed strains, sometimes causing divergence in the solution process. In the present study, an attempt is made toward achieving numerical robustness.

In addition to the numerical robustness, the model may have to satisfy the following requirements as indicated by the

laboratory studies mentioned earlier;

- (1) physically feasible shape of hysteresis loop during cyclic mobility,
- (2) physically feasible generation of pore pressures under undrained cyclic loading condition,
- (3) rapid or gradual increase in shear strain amplitude greater than several percent during cyclic mobility,
- (4) physically feasible relation between the amplitude of cyclic loading and the number of cycles required to cause specified strain amplitude under undrained condition; in particular the existence of threshold limit,
- (5) physically feasible modeling of initially anisotropically consolidated soil, and
- (6) physically feasible dependence of secant shear modulus and hysteretic damping factor on shear strain amplitude under drained cyclic loading condition such as shown in Fig. 1.5.

In the present study, such an attempt is made as to satisfy all of these requirements for modeling of cyclic mobility. With practical application in mind, the model to be developed in this study is of two dimensional nature. Extension to three dimensions, nevertheless, is not very difficult as shown in the APPENDIX A.

#### 1.4 Scope

The scope of the present study is as follows.

First of all, a model for representing cyclic mobility is developed in Chapter 2 along the line of thought originally

developed by Towhata and Ishihara (1985). Though they developed the original model without the vehicle of the plasticity theory, the model is reconstructed in this study within the framework of the plasticity theory defined in strain space. This is believed to give a more transparent theoretical structure in the formulation than the physical image of multiple springs presented in the original study. Concept of the multiple mechanism is fully utilized for decomposing the complex mechanism into simple mechanisms.

The model performance is then examined in Chapter 3 by using a single element in finite element approximation. Undrained cyclic torsion test results are numerically analyzed under three kinds of initial and boundary conditions; one with initially isotropic stress condition, another with initially  $K_0 = 0.5$  condition and with keeping the bulging constrained as a boundary condition for displacement, and the last with initially  $K_0 = 0.5$  condition and keeping the  $K_0$  value constant as a stress boundary condition but without constraint on the bulging. In addition effect is examined of initial confining pressure.

Applicability of the present model in practice of level ground analysis is examined in Chapter 4 by conducting one dimensional analysis. Shaking table tests of sand deposits are conducted with a container made of a stack of 64 aluminum rings and the results of the model tests are analyzed with the present model.

Applicability of the present model for estimating amount of deformation of soil structures and foundations is then examined in Chapter 5 by conducting two dimensional analysis. Case history



data of anchored steel sheet pile quay walls during 1983 Nihonkai-Chubu Earthquake are used for the analysis. Quay walls with and without damage are analyzed for examining the capability of the present model in differentiating seriously large deformation from insignificantly small deformation.

The conclusions obtained from the present study are presented in the final chapter.

## References

- (1) Aubry, D., Hujeux, J.C., Lassoudiere, F. and Meimon, Y. (1982) : "A double memory model with multiple mechanisms for cyclic soil behaviour," in Dungar, Pande and Studer (eds), Numerical Models in Geomechanics, A.A.Balkema, (International Symposium on Numerical Models in Geomechanics, Zurich), pp.3-13
- (2) Bazant, Z.P. (1986) : "Microplane model for strain-controlled inelastic behaviour," in Desai and Gallagher (eds), Mechanics of Engineering Materials, John Wiley & Sons, pp.45-59
- (3) Calladine, C.R. (1971) : "A microstructural view of the mechanical properties of saturated clay," Geotechnique, Vol.21, No.4, pp.391-415
- (4) Castro, G. (1975) : "Liquefaction and cyclic mobility of saturated sand," Journal of Geotechnical Engineering Division, ASCE, Vol.101, No.GT6, pp.55-569
- (5) Chang, C.S. (1989) : "Micromechanical approach to constitutive modelling for granular soils based on slip

- mechanism," in Saada and Bianchini (eds), Constitutive Equations for Granular Non-Cohesive Soils, A.A.Balkema, (Proceedings of the International Workshop on Constitutive Equations for Granular Non-Cohesive Soils, Cleveland), pp.183-200
- (6) Ishihara, K. (1985) : "Stability of natural deposits during earthquakes," Proceedings of 11th International Conference on Soil Mechanics and Foundation Engineering, San Francisco, Vol.1, pp.327-376
- (7) Ishihara, K., Iwamoto, S., Yasuda, S. and Takatsu, H. (1977) : "Liquefaction of anisotropically consolidated sand," Proceedings of 9th International Conference on Soil Mechanics and Foundation Engineering, Tokyo, Vol.2, pp.261-264
- (8) Ishihara, K. and Towhata, I. (1983) : "Sand response to cyclic rotation of principal stress directions as induced by wave loads," Soils and Foundations, Vol.23, No.4, pp.11-26
- (9) Ishihara, K. et al (1989) : "Effective stress analysis of level ground and soil structures," Research Committee Report, Proceedings of the Symposium on Seismic Performance of Level Ground and Soil Structures, Japanese Society of Soil Mechanics and Foundation Engineering, pp.50-136 (in Japanese)
- (10) Iwasaki, T., Tatsuoka, F. and Takagi, Y. (1978) : "Shear moduli of sands under cyclic torsional shear loading," Soils and Foundations, Vol.18, No.1, pp.39-56
- (11) Kabilamany, K. and Ishihara, K. (1990) : "Stress dilatancy

- and hardening laws for rigid granular model of sand," Soil Dynamics and Earthquake Engineering, Vol.9, No.2, pp.66-77
- (12) Koiter, W.T.(1953) : "Stress-strain relations, uniqueness and variational theorems for elastic-plastic materials with a singular yield surface," Quarterly of Applied Mathematics, Vol.11, pp.350-354
- (13) Kong, X.J., Tatsuoka, F. and Pradhan, T.B.S. (1986) : "Dynamic deformation properties of sand at extremely low pressures," Proceedings of 7th Japan Earthquake Engineering Symposium, pp.631-636
- (14) Miura, K., Miura, S. and Toki, S. (1986a) : "Deformation behavior of anisotropic dense sand under principal stress axes rotation," Soils and Foundations, Vol.26, No.1, pp.36-52
- (15) Miura, K., Toki, S. and Miura, S. (1986b) : "Deformation prediction for anisotropic sand during the rotation of principal stress axes," Soils and Foundations, Vol.26, No.3, pp.42-56
- (16) Nishi, K. and Kanatani, M. (1989) : "Analysis by NAFSS," in Ishihara et al., Research Committee Report, "Effective stress analysis of level ground and soil structures," Proceedings of the Symposium on Seismic Performance of Level Ground and Soil Structures, Japanese Society of Soil Mechanics and Foundation Engineering, pp.114-123 (in Japanese)
- (17) Nishi, K. and Kanatani, M. (1990) : "Constitutive relations for sand under cyclic loading based on elasto-plasticity theory," Soils and Foundations, Vol.30, No.2, pp.43-59

- (18) Pande G.N. and Sharma, K.G.(1983) : "Multilaminate model of clays; a numerical evaluation of the influence of rotation of principal stress axes," International Journal of Numerical and Analytical Methods in Geomechanics, Vol.7, pp.397-418
- (19) Pastor, M. and Zienkiewicz, O.C. (1986): "A generalized plasticity, Hierarchical model for sand under monotonic and cyclic loading," Proceedings of 2nd International Symposium on Numerical Models in Geomechanics, Ghent, pp.131-150
- (20) Pietruszczak, S. and Pande, G.N (1987): "Multilaminate framework of soil models; plasticity formulation," International Journal of Numerical and Analytical Methods in Geomechanics, Vol.11, pp.651-658
- (21) Poorooshasb, H.B. and Pietruszczak, S. (1986) : "A generalized flow theory for sand," Soils and Foundations, Vol.26, No.2, pp.1-15
- (22) Sato, T., Shibata, T. and Kosaka, M. (1981) : "Dynamic behaviour and liquefaction of saturated sandy soil," in Pande and Zienkiewicz (eds), Soils under Cyclic and Transient Loading, A.A.Balkema, (Proceedings of the International Symposium on Soils under Cyclic and Transient Loading, Swansea), pp.523-532
- (23) Schofield, A.N. and Wroth, C.P. (1968) : Critical State Soil Mechanics, McGraw-Hill, London
- (24) Sekiguchi, H. and Ohta, H. (1977) : "Induced anisotropy and time dependency in clay," Proceedings of 9th International Conference on Soil Mechanics and Foundation Engineering, Tokyo, Specialty Session No.9, Constitutive equations of

soils, pp.163-175

- (25) Shiomi, T. (1989) : "Analysis by Pastor-Zienkiewicz model," in Ishihara et al., Research Committee Report, "Effective stress analysis of level ground and soil structures," Proceedings of the Symposium on Seismic Performance of Level Ground and Soil Structures, Japanese Society of Soil Mechanics and Foundation Engineering, pp.104-113 (in Japanese)
- (26) Towhata and Ishihara (1985) : "Modelling soil behaviour under principal stress axes rotation," Proceedings of 5th International Conference on Numerical Methods in Geomechanics, Nagoya, Vol.1, pp.523-530
- (27) Yoshida, N., Tsujino, S. and Ishihara, K. (1989) : "Analysis by Multi-mechanism model," in Ishihara et al., Research Committee Report, "Effective stress analysis of level ground and soil structures," Proceedings of the Symposium on Seismic Performance of Level Ground and Soil Structures, Japanese Society of Soil Mechanics and Foundation Engineering, pp.74-83 (in Japanese)

## CHAPTER 2

### MODELING OF CYCLIC MOBILITY

#### 2.1 Generalized Plasticity Theory in Strain Space

Behavior of saturated cohesionless soil is defined in terms of effective stress and strain. If vector-matrix notation is used, the effective stress increment  $\{d\sigma'\}$  and the strain increment  $\{d\epsilon\}$  are related to each other through the tangential stiffness matrix  $[D]$  as

$$\{d\sigma'\} = [D]\{d\epsilon\} \quad (2.1)$$

In general the value of  $[D]$  depends on the state and the history of effective stress and strain.

At each stage of deformation process under transient and cyclic loads, a direction is introduced which differentiates loading from unloading (i.e. reversal loading). Commonly adopted practice is to define a direction in the stress space as reviewed in the previous chapter but, in the present study, the direction  $\{n\}$  is introduced in the strain space as suggested by Mroz and Norris (1982).

Loading and unloading in the strain space are specified by comparing direction of strain increment vector  $\{d\epsilon\}$  with the direction  $\{n\}$ . If the direction of  $\{d\epsilon\}$  is on the same side as the vector  $\{n\}$  is pointing to, it is loading. If it is on the opposite side, unloading. If the direction of  $\{d\epsilon\}$  is perpendicular to the direction  $\{n\}$ , it is neutral. Thus, the

loading criterion in the strain space is specified by sign of  $\{n\}^T\{d\epsilon\}$ :

$$\begin{aligned} \text{loading} & \quad \text{if } \{n\}^T\{d\epsilon\} > 0, \\ \text{unloading} & \quad \text{if } \{n\}^T\{d\epsilon\} < 0, \text{ and} \\ \text{neutral} & \quad \text{if } \{n\}^T\{d\epsilon\} = 0. \end{aligned}$$

Dependence of material behavior on the direction is specified by introducing two tangential stiffness matrix  $[D_L]$  and  $[D_U]$ , one for loading and the other for unloading, as

$$\begin{aligned} \{d\sigma'\} &= [D_L]\{d\epsilon\} \quad \text{if } \{n\}^T\{d\epsilon\} > 0 \\ \{d\sigma'\} &= [D_U]\{d\epsilon\} \quad \text{if } \{n\}^T\{d\epsilon\} < 0 \end{aligned} \quad (2.2)$$

Uniqueness of the stress increment requires that when  $\{n\}^T\{d\epsilon\} = 0$  both loading and unloading moduli be identical (i.e.  $[D_L] = [D_U]$ ) and hence the behavior be locally elastic. This requirement, called continuity condition, imposes an essential constraint on  $[D_{L/U}]$ , giving the specific formulation for  $[D_{L/U}]$ , such that

$$\begin{aligned} [D_L] &= [D_e] + R_L\{n_L\}\{n\}^T \\ [D_U] &= [D_e] + R_U\{n_U\}\{n\}^T \end{aligned} \quad (2.3)$$

in which  $[D_e]$  is elastic stiffness matrix,  $\{n_{L/U}\}$  are arbitrarily specified vectors defining directions of stress increment and the scalars  $R_{L/U}$  define magnitudes of stress increment per unit strain increment along the direction  $\{n\}$  (i.e. per unit value of

$\{n\}^T\{d\epsilon\}$ ). These meanings of  $\{n_{L/U}\}$  and  $R_{L/U}$  are easily understood if Eq.(2.3) is substituted into Eq.(2.2); it is seen that the direction vector  $\{n\}$  is always acting on the strain increment vector  $\{d\epsilon\}$  to produce an inner product  $\{n\}^T\{d\epsilon\}$ , which is nothing but a scalar, and hence  $\{n_{L/U}\}$  are directions of stress increment and  $R_{L/U}$  define the magnitudes.

As mentioned earlier, commonly adopted practice is to define a direction in the stress space. In this approach, strain increment  $\{d\epsilon\}$  is generated from stress increment  $\{d\sigma\}$ , whereas in the strain space approach as in the present study, stress increment  $\{d\sigma\}$  is generated from strain increment  $\{d\epsilon\}$ . This is summarized in Table 2.1. Both approaches are equivalent with each other (Mroz and Norris, 1982) but, when the multiple mechanism are considered as will be discussed later, the strain space approach is very efficient in computation because stiffness matrix is obtained by simple summation.

Models of this type shown in Eqs.(2.2) and (2.3) can be generalized further by considering that deformation of material is produced by  $I+1$  separate mechanisms with  $i = 0, \dots, I$ , all of which are subjected to the same state and the same history of strain. In this approach the increment of effective stress is written by

$$\{d\sigma'\} = \sum_{i=0}^I \{d\sigma'^{(i)}\} \quad (2.4)$$

and is related to the increment of strain by

$$\{d\sigma'\} = \sum_{i=0}^I [D^{(i)}]\{d\epsilon\} \quad (2.5)$$



Table 2.1 Comparison of Stress Space and Strain Space Plasticity Theories

	Stress Space Plasticity (Conventional Approach)	Strain Space Plasticity
Basic Con- cept	$\{d\epsilon\}$ is generated by $\{d\sigma'\}$	$\{d\sigma'\}$ is generated by $\{d\epsilon\}$
Single Mecha- nism Model	$\{d\epsilon\} = H_{L/U} \{n_{L/U}\} \{n\}^T \{d\sigma'\}$	$\{d\sigma'\} = R_{L/U} \{n_{L/U}\} \{n\}^T \{d\epsilon\}$
Multi- ple Mecha- nism Model	$\{d\epsilon\} = \sum_i H_{L/U}^{(i)} \{n_{L/U}^{(i)}\} \{n^{(i)}\}^T \{d\sigma'\}$	$\{d\sigma'\} = \sum_i R_{L/U}^{(i)} \{n_{L/U}^{(i)}\} \{n^{(i)}\}^T \{d\epsilon\}$

----- present study

Dependence of material behavior on the direction of loading is separately defined for each mechanism, such that

$$\begin{aligned} \{d\sigma^{(i)}\} &= [D_L^{(i)}]\{d\epsilon\} & \text{if } \{n^{(i)}\}^T\{d\epsilon\} > 0 \\ \{d\sigma^{(i)}\} &= [D_U^{(i)}]\{d\epsilon\} & \text{if } \{n^{(i)}\}^T\{d\epsilon\} < 0 \end{aligned} \quad (2.6)$$

The continuity condition requires that the tangent moduli for each mechanism be given by

$$\begin{aligned} [D_L^{(i)}] &= [D_e^{(i)}] + R_L^{(i)}\{n_L^{(i)}\}\{n^{(i)}\}^T \\ [D_U^{(i)}] &= [D_e^{(i)}] + R_U^{(i)}\{n_U^{(i)}\}\{n^{(i)}\}^T \end{aligned} \quad (2.7)$$

Thus, the constitutive relation is given by

$$\{d\sigma'\} = \sum_{i=0}^I ([D_e^{(i)}] + R_{L/U}^{(i)}\{n_{L/U}^{(i)}\}\{n^{(i)}\}^T)\{d\epsilon\} \quad (2.8)$$

in which L/U is determined for each mechanism by Eq.(2.6).

To summarize, the material behavior can fully be described if one prescribes  $[D_e^{(i)}]$ ,  $\{n^{(i)}\}$ ,  $\{n_{L/U}^{(i)}\}$  and  $R_{L/U}^{(i)}$  for all mechanisms at all states and histories of the material behavior.

In the following discussion, the elastic matrix  $[D_e^{(i)}]$  will be omitted for ensuring simplicity in the formulation. The constitutive relation in this study is thus simply given by

$$\{d\sigma'\} = \sum_{i=0}^I R_{L/U}^{(i)}\{n_{L/U}^{(i)}\}\{n^{(i)}\}^T\{d\epsilon\} \quad (2.9)$$

## 2.2 Decomposition into Simple Mechanisms

In attempting to construct the model for cyclic mobility with practical application in mind, the author limits himself, throughout the following discussion, to the two dimensional behavior of soil under the plane strain condition. Thus, the components of the effective stress and the strain vectors are given by

$$\{\sigma'\}^T = \{ \sigma_x' \quad \sigma_y' \quad \tau_{xy} \} \quad (2.10)$$

$$\{\epsilon\}^T = \{ \epsilon_x \quad \epsilon_y \quad \gamma_{xy} \} \quad (2.11)$$

in which compressive stress and contractive strain will be assumed negative and the strains will be given from displacements  $u$  and  $v$  in  $x$  and  $y$  directions by

$$\epsilon_x = \frac{\partial u}{\partial x} \quad , \quad \epsilon_y = \frac{\partial v}{\partial y} \quad , \quad \gamma_{xy} = \frac{\partial u}{\partial y} + \frac{\partial v}{\partial x} \quad (2.12)$$

It is assumed in the following discussion that  $\sigma_z'$  can be approximated by  $(\sigma_x' + \sigma_y')/2$ .

### 2.2.1 Transformation

The first step for developing the model is to decompose the mechanism of cyclic mobility into two mechanisms; one being the mechanism of cumulative pore pressure build up with occasional recovery of mean effective stress, the other the mechanism of shear deformation without volume change.

This type of decomposition is most conveniently done if one at first transforms the effective stress and the strain vectors into the vectors with components of volumetric nature and

shearing nature. In particular, the effective stress vector is transformed as

$$\{s'\} = [T_\sigma]\{\sigma'\} \quad (2.13)$$

in which

$$\{s'\}^T = \{ (\sigma'_x + \sigma'_y)/2 \quad (\sigma'_x - \sigma'_y)/2 \quad \tau_{xy} \} \quad (2.14)$$

$$[T_\sigma] = \begin{bmatrix} 1/2 & 1/2 & 0 \\ 1/2 & -1/2 & 0 \\ 0 & 0 & 1 \end{bmatrix} \quad (2.15)$$

and the strain vector is transformed as

$$\{e\} = [T_\epsilon]\{\epsilon\} \quad (2.16)$$

in which

$$\{e\}^T = \{ (\epsilon_x + \epsilon_y) \quad (\epsilon_x - \epsilon_y) \quad \gamma_{xy} \} \quad (2.17)$$

$$[T_\epsilon] = \begin{bmatrix} 1 & 1 & 0 \\ 1 & -1 & 0 \\ 0 & 0 & 1 \end{bmatrix} \quad (2.18)$$

It is to be noted that  $[T_\sigma]$  and  $[T_\epsilon]$  are related with each other by

$$[T_\sigma]^T = [T_\epsilon]^{-1} \quad (2.19)$$

By using Eqs.(2.13), (2.16) and (2.19), the constitutive relation in Eq.(2.9) is rewritten as

$$\{ds'\} = \sum_{i=0}^I R_{L/U}^{(i)} [T_\sigma] \{n_{L/U}^{(i)}\} \{n^{(i)}\}^T [T_\sigma]^T \{de\} \quad (2.20)$$

If one defines the direction vectors in the transformed space by writing

$$\begin{aligned} \{l_{L/U}^{(i)}\} &= [T_\sigma] \{n_{L/U}^{(i)}\} \\ \{l^{(i)}\} &= [T_\sigma] \{n^{(i)}\} \end{aligned} \quad (2.21)$$

then Eq.(2.20) is rewritten as

$$\{ds'\} = \sum_{i=0}^I R_{L/U}^{(i)} \{l_{L/U}^{(i)}\} \{l^{(i)}\}^T \{de\} \quad (2.22)$$

Equations (2.9) and (2.22) are the dual representation of a constitutive relation and, if one prescribes  $R_{L/U}^{(i)}$ ,  $\{l_{L/U}^{(i)}\}$  and  $\{l^{(i)}\}$  for Eq.(2.22) in the transformed space,  $\{n_{L/U}^{(i)}\}$  and  $\{n^{(i)}\}$  will readily be given in the original space by Eqs.(2.19) and (2.21) and consequently Eq.(2.9) is completely specified.

### 2.2.2 Volumetric Mechanism

With Eq.(2.22) in hand, the first mechanism (i.e. the mechanism for  $i = 0$ ) will be defined for representing the cumulative pore pressure build up with occasional recovery of mean effective stress. For modeling such a mechanism, the author takes the approach similar, in principle, to that taken for densification model (Zienkiewicz et al, 1978). This approach has

the advantage of simplicity and of the most direct use of the laboratory data obtained under the undrained cyclic loading condition. In this approach, one needs simply to include an additional strain  $\{e_p\}$  of volumetric nature into the mechanism for  $i = 0$  in Eq.(2.22) by writing

$$\{ds',^{(0)}\} = R_{L/U}^{(0)} \{l_{L/U}^{(0)}\} \{l^{(0)}\}^T (\{de\} - \{de_p\}) \quad (2.23)$$

in which  $\{de_p\}$  will be independently determined.

Since the mean effective stress and the volumetric strain are the first components of  $\{s'\}$  and  $\{e\}$ , the direction vectors in Eq.(2.23) are given by

$$\{l_L^{(0)}\}^T = \{l_U^{(0)}\}^T = \{l^{(0)}\}^T = \{ 1 \ 0 \ 0 \} \quad (2.24)$$

with the additional volumetric strain given by

$$\{e_p\}^T = \{ \epsilon_p \ 0 \ 0 \} \quad (2.25)$$

The additional volumetric strain  $\{e_p\}$  is further assumed to represent whole part of the plastic volumetric strain generated by the transient and cyclic loads. Then the strain increment  $\{l^{(0)}\}^T (\{de\} - \{de_p\})$  in Eq.(2.23) becomes elastic so that the moduli  $R_{L/U}^{(0)}$  in Eq.(2.23) should represent elastic volumetric behavior, i.e.

$$K = R_L^{(0)} = R_U^{(0)} \quad (2.26)$$

in which  $K$  is elastic tangent bulk modulus of soil skeleton, often called rebound modulus. The laboratory data suggest that, for cohesionless soil,  $K$  is given by a power function of effective mean stress, approximately given by

$$K = K_a (\sigma'_m / \sigma'_{ma})^{0.5} \quad (2.27)$$

in which  $\sigma'_m$  : effective mean stress =  $(\sigma'_x + \sigma'_y)/2$ ;  $K_a$  : elastic tangent bulk modulus of soil skeleton at  $\sigma'_m = \sigma'_{ma}$ .

### 2.2.3 Shear Mechanism

The frame work for the first mechanism thus defined, the second mechanism will be defined for representing the shear deformation without volume change. For modeling such a mechanism, the author adopts the approach similar to that proposed by Towhata and Ishihara (1985a). This approach has the advantage of representing soil behavior under principal stress axes rotation. This approach, at the same time, has the advantage of simplicity by decomposing the complex mechanism into a set of such simple mechanisms as those defined in one dimensional space.

In this approach, one needs to mobilize  $I$  mechanisms for  $i = 1, \dots, I$  out of Eq.(2.22), as a tool for decomposition, by writing

$$\sum_{i=1}^I \{ds^{(i)}\} = \sum_{i=1}^I R_{L/0}^{(i)} \{l_{L/0}^{(i)}\} \{l^{(i)}\}^T \{de\} \quad (2.28)$$

The mechanism  $i$  represents a one dimensional stress strain relation defined in a virtual simple shear which is, in concept,

mobilized at the angle  $\theta_i/2 + \pi/4$  relative to x axis; e.g. the mechanism with  $\theta_i = 0$  represents a virtual compression mode, that with  $\theta_i = \pi/2$  a virtual simple shear mode in the x axis direction as shown in Fig. 2.1. The angle  $\theta_i$  for mechanism i is given so that all the possible directions for mobilization are approximately represented by those of I mechanisms, such that

$$\theta_i = (i-1)\Delta\theta \quad (\text{for } i = 1, \dots, I) \quad (2.29)$$

in which  $\Delta\theta = \pi/I$ .

The above definition of mechanism i demands, as shown in Fig. 2.1, that the direction vectors in Eq.(2.28) be given by

$$\{l_L^{(i)}\}^T = \{l_U^{(i)}\}^T = \{l^{(i)}\}^T = \{ 0 \quad \cos\theta_i \quad \sin\theta_i \} \quad (\text{for } i = 1, \dots, I) \quad (2.30)$$

with  $R_{L/U}^{(i)}$  representing tangent shear moduli which will be given as a function of virtual simple shear strain for mechanism i ( i.e.  $\{l^{(i)}\}^T\{e\}$  ) and of its history.

#### 2.2.4 Incremental Relation

If the expressions for the mechanisms given by Eqs.(2.23) and (2.28) are combined, a relation which corresponds to Eq.(2.22) is given by

$$\{ds'\} = K\{l^{(0)}\}\{l^{(0)}\}^T(\{de\} - \{de_p\}) + \sum_{i=1}^I R_{L/U}^{(i)}\{l^{(i)}\}\{l^{(i)}\}^T\{de\} \quad (2.31)$$

in which modulus K is defined by Eq.(2.27), the direction vectors



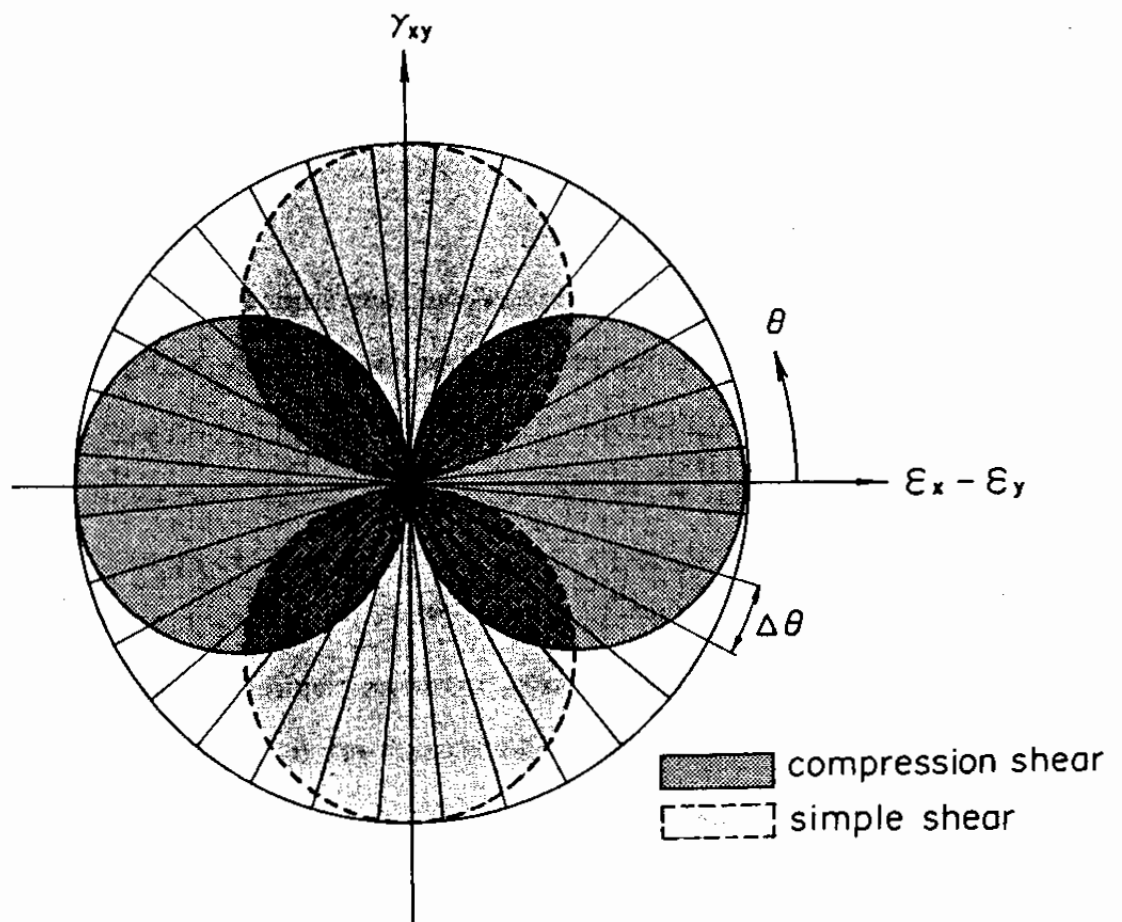


Fig. 2.1 Schematic figure for multiple simple shear mechanisms; pairs of circles indicate mobilized virtual shear strain in positive and negative modes of compression shear (solid lines with darker hatch) and simple shear (broken lines with lighter hatch)

by Eqs.(2.24) and (2.30).

As mentioned earlier, the constitutive relation in Eq.(2.31) is back-transformed into the original representation corresponding to Eq.(2.9) as

$$\{d\sigma'\} = K\{n^{(0)}\}\{n^{(0)}\}^T(\{d\epsilon\} - \{d\epsilon_p\}) + \sum_{i=1}^I R_{L/U}^{(i)}\{n^{(i)}\}\{n^{(i)}\}^T\{d\epsilon\} \quad (2.32)$$

in which the volumetric strain increment  $\{d\epsilon_p\}$  of plastic nature is given, by using the relations in Eqs.(2.16) and (2.19), as

$$\{d\epsilon_p\} = [T_\sigma]^T\{d\epsilon_p\} \quad (2.33)$$

and the direction vectors in the original space  $\{n^{(i)}\}$  are given by Eqs.(2.19) and (2.21) by

$$\{n^{(0)}\}^T = \{ 1 \quad 1 \quad 0 \} \quad (2.34)$$

$$\{n^{(i)}\}^T = \{ \cos\theta_i \quad -\cos\theta_i \quad \sin\theta_i \} \quad (\text{for } i = 1, \dots, I) \quad (2.35)$$

Because  $\{n^{(i)}\}^T\{d\epsilon_p\} = 0$  for  $i = 1, \dots, I$ , Eq.(2.32) is rewritten as

$$\{d\sigma'\} = [D](\{d\epsilon\} - \{d\epsilon_p\}) \quad (2.36)$$

in which

$$[D] = K\{n^{(0)}\}\{n^{(0)}\}^T + \sum_{i=1}^I R_{L/U}^{(i)}\{n^{(i)}\}\{n^{(i)}\}^T \quad (2.37)$$

If these relations are more explicitly written down for

practical application in mind, it is given as follows.

$$\begin{Bmatrix} d\sigma_x' \\ d\sigma_y' \\ d\tau_{xy} \end{Bmatrix} = [D] \begin{Bmatrix} d\epsilon_x \\ d\epsilon_y \\ d\gamma_{xy} \end{Bmatrix} - \begin{Bmatrix} 1 \\ 1 \\ 0 \end{Bmatrix} K_a \left( \frac{\sigma_m}{\sigma_{ma}} \right)^{0.5} d\epsilon_p \quad (2.38)$$

with

$$\begin{aligned} [D] = K_a \left( \frac{\sigma_m}{\sigma_{ma}} \right)^{0.5} & \begin{bmatrix} 1 & 1 & 0 \\ 1 & 1 & 0 \\ 0 & 0 & 0 \end{bmatrix} + G_{t1} \begin{bmatrix} 1 & -1 & 0 \\ -1 & 1 & 0 \\ 0 & 0 & 0 \end{bmatrix} \\ & + G_{t2} \begin{bmatrix} 0 & 0 & 1 \\ 0 & 0 & -1 \\ 1 & -1 & 0 \end{bmatrix} + G_{t3} \begin{bmatrix} 0 & 0 & 0 \\ 0 & 0 & 0 \\ 0 & 0 & 1 \end{bmatrix} \end{aligned} \quad (2.39)$$

in which

$$G_{t1} = \sum_{i=1}^I R_{L/U}^{(i)} \cos^2 \theta_i \quad (2.40)$$

$$G_{t2} = \sum_{i=1}^I R_{L/U}^{(i)} \cos \theta_i \sin \theta_i \quad (2.41)$$

$$G_{t3} = \sum_{i=1}^I R_{L/U}^{(i)} \sin^2 \theta_i \quad (2.42)$$

As expected from the associative manner with which the direction vectors are chosen ( i.e.  $\{n_{L/U}^{(i)}\} = \{n^{(i)}\}$ ), the stiffness matrix  $[D]$  is symmetric, giving the advantage of efficient solution.

### 2.3 Integrated Formulation

The decomposition into one dimensional mechanisms in

Eq.(2.32) provides a salient feature in the present approach; the incremental relation can be integrated so that a direct relation can be specified between effective stress and strain. Such integration can be done one by one with respect to each variable defined for each mechanism.

The mechanism  $i = 0$  in Eq.(2.31) can be rewritten as

$$d\sigma_m' = K_a(\sigma_m'/\sigma_{ma}')^{0.5}d\epsilon_e \quad (2.43)$$

in which elastic volumetric strain increment  $d\epsilon_e$  is defined by

$$d\epsilon_e = \{l^{(0)}\}^T(\{de\} - \{de_p\}) \quad (2.44)$$

Integration of Eq.(2.43) into the compressive side ( i.e. into the negative side) with the initial conditions that  $\epsilon_e = 0$  when  $\sigma_m' = 0$  yields

$$\sigma_m' = -B(-\epsilon_e)^2 \quad (2.45)$$

in which

$$B = [0.5K_a/(-\sigma_{ma}')^{0.5}]^2 \quad (2.46)$$

$$\epsilon_e = \epsilon_x + \epsilon_y - \epsilon_p \quad (2.47)$$

The integrated result can be written back in the multiple mechanism formulation similar to Eq.(2.23) as

$$\{s'^{(0)}\} = -B(-\epsilon_e)^2\{l^{(0)}\} \quad (2.48)$$

The transformation back to the original space by using Eqs.(2.13) and (2.21) yields

$$\{\sigma^{(0)}\} = -B(-\epsilon_e)^2 \{n^{(0)}\} \quad (2.49)$$

This is the integrated relation for the mechanism  $i = 0$ .

The rest of the mechanisms  $i = 1, \dots, I$  are integrated by introducing a virtual shear strain for each mechanism  $i$  by

$$\begin{aligned} \gamma^{(i)} &= \{l^{(i)}\}^T \{e\} \\ &= (\epsilon_x - \epsilon_y) \cos \theta_i + \gamma_{xy} \sin \theta_i \end{aligned} \quad (2.50)$$

and by introducing a scalar function  $Q^{(i)}(\gamma^{(i)})$  defined so that its first order derivative  $\frac{dQ^{(i)}}{d\gamma^{(i)}}$  represents the virtual tangent shear moduli per unit angle of  $\theta$  by

$$R_{L/U}^{(i)} = \frac{dQ^{(i)}}{d\gamma^{(i)}} \Delta\theta \quad (2.51)$$

in which  $\Delta\theta = \pi/I$ . The value of  $Q^{(i)}$  generally depends on the history of  $\gamma^{(i)}$ . Analogously to the integration of mechanism  $i = 0$ , the mechanisms  $i = 1, \dots, I$  in Eq.(2.31) are rewritten by using Eqs.(2.50) and (2.51) as

$$\{ds^{(i)}\} = \frac{dQ^{(i)}}{d\gamma^{(i)}} \Delta\theta d\gamma^{(i)} \{l^{(i)}\} \quad (2.52)$$

Integration of Eq.(2.52) yields

$$\{s^{(i)}\} = Q^{(i)}(\gamma^{(i)}) \Delta\theta \{l^{(i)}\} \quad (2.53)$$

The transformation back to the original space by using Eqs.(2.13) and (2.21) yields

$$\{\sigma^{(i)}\} = Q^{(i)}(\gamma^{(i)})\Delta\theta\{n^{(i)}\} \quad (2.54)$$

From Eqs.(2.47), (2.49) and (2.54), one obtains the integrated formulation for the stress and strain relation as

$$\{\sigma'\} = -B[\epsilon_p - (\epsilon_x + \epsilon_y)]^2\{n^{(0)}\} + \sum_{i=1}^I Q^{(i)}(\gamma^{(i)})\Delta\theta\{n^{(i)}\} \quad (2.55)$$

in which, as mentioned earlier, the value of the function  $Q^{(i)}(\gamma^{(i)})$  generally depends on the value as well as the history of the variable  $\gamma^{(i)}$ . The function  $Q^{(i)}$  can be interpreted as virtual shear stress per unit angle  $\theta$  for mechanism  $i$ .

Now that incremental as well as integrated relations for modeling cyclic mobility are obtained in the previous and the present sections, it only remains to define the volumetric strain  $\epsilon_p$  of plastic nature and the function  $Q^{(i)}(\gamma^{(i)})$  for representing the virtual simple shear mechanism.

## 2.4 Undrained Stress Path

### 2.4.1 Effective Mean Stress Change

General understanding on the cyclic mobility of saturated cohesionless soil is that transient or cyclic loading induces soil particle rearrangement causing, under the drained condition, volumetric shrinkage. Such a rearrangement causes, under the undrained condition, loss in effective mean stress and increase

in pore water pressure.

In order to formulate this relation, let us consider the mechanism of undrained behavior of cohesionless soil. For simplicity, let us assume that the volumetric strain  $\epsilon_p$  of plastic nature is zero at the initial condition. The initial elastic volumetric strain  $\epsilon_{e0}$  is related to the initial effective mean stress  $\sigma_{m0}'$  via Eq.(2.45) as

$$\sigma_{m0}' = -B(-\epsilon_{e0})^2 \quad (2.56)$$

Under constant total mean stress with the undrained condition, the volumetric strain induced by the change in the effective stress is only due to the volumetric strain of pore water, such that

$$\epsilon_e + \epsilon_p - \epsilon_{e0} = (n/K_f)(\sigma_{m0}' - \sigma_m') \quad (2.57)$$

in which  $n$  and  $K_f$  are the porosity of soil skeleton and the bulk modulus of pore water. Elimination of  $\epsilon_e$  from Eq.(2.57) by using Eq.(2.45) yields

$$\epsilon_p = (n/K_f)(\sigma_{m0}' - \sigma_m') + [\sigma_m'/(-B)]^{0.5} + \epsilon_{e0} \quad (2.58)$$

Whereas the volumetric strain  $\epsilon_p$  of plastic nature is needed to be specified in Eq.(2.55), common practice in the soil dynamics and the earthquake engineering is to measure pore water pressure change or, equivalently, to measure the change in the effective mean stress under the undrained cyclic loading

condition. Since one quantity is related to the other by Eq.(2.58), the measurable quantity, i.e. the undrained effective stress change under constant total confining pressure, will be used in the following formulation.

#### 2.4.2 Liquefaction Front

Several attempts have been made for modeling the effective stress paths for cyclic mobility, such as shown in Figs. 1.1(a) and 1.2(a), under the undrained cyclic loading condition. Pender (1980), paying due attention to the critical state, adopted a parabolic function. Ishihara and Towhata (1982), paying due attention to the yield loci and phase transformation line, adopted a combination of a parabolic and a hyperbolic functions. Yamazaki et al (1985), paying due attention to the envelope of stress points specified by equally accumulated shear work, adopted a hyperbolic function.

In the present study, the author postulates that the phase transformation line and the envelope of stress points at equal shear work are two of the key concepts for modeling effective stress path associated with the cyclic mobility. The phase transformation line as defined by Ishihara et al (1975) is a straight line differentiating the dilative zone in the stress space from the contractive zone as indicated by broken lines in Figs. 1.1(a) and 1.2(a). The envelope of stress points at equal shear work as defined by Towhata and Ishihara (1985b) is represented by a contour, as shown in Fig. 2.2, defined in the stress space at which cumulative shear work is equal to a specified value. As the shear work is accumulated by cyclic shear



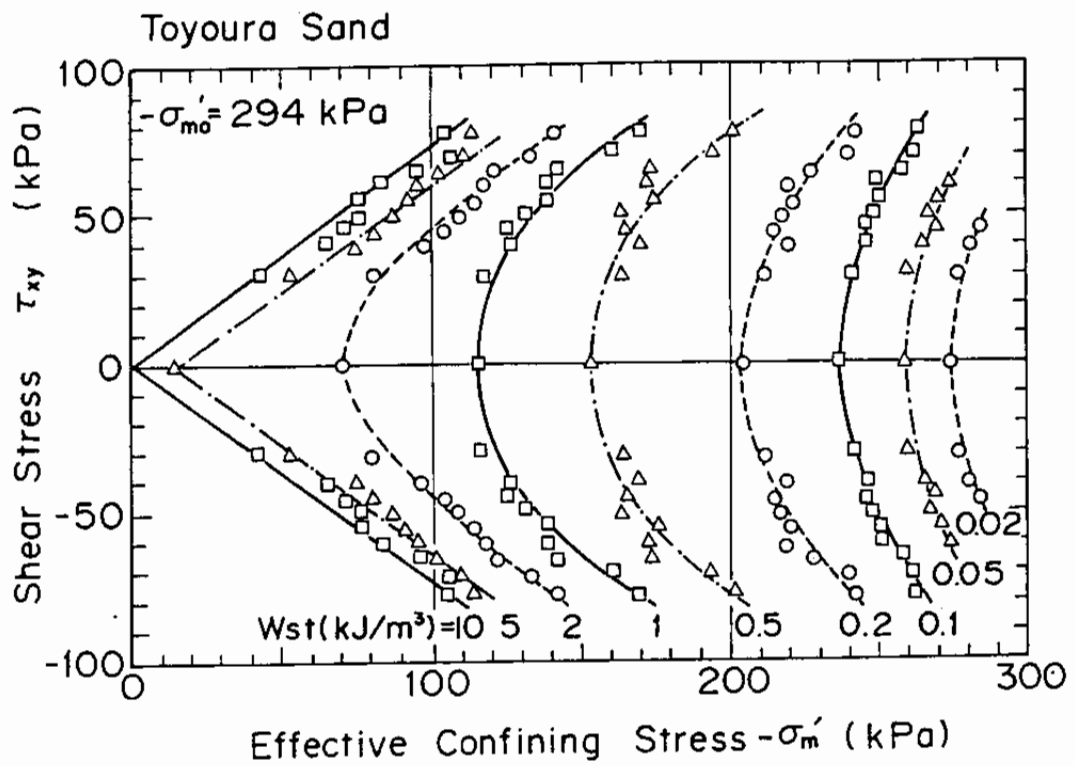


Fig. 2.2 Envelope of stress points at equal cumulative shear work  
(after Towhata and Ishihara, 1985b)

under the undrained condition, the envelope of stress points at equal shear work gradually moves from the initial envelope to the failure line. Such an envelope, being one of the key concepts for modeling cyclic mobility, will be called "liquefaction front" in the following discussion.

In order to generalize the formulation of liquefaction front, the liquefaction front will be defined in the normalized stress space defined with the effective mean stress ratio  $S = \sigma'_m / \sigma'_{m0}$  and the deviatoric stress ratio  $r = \tau / (-\sigma'_{m0})$ , in which  $\sigma'_{m0} = (\sigma'_{x0} + \sigma'_{y0}) / 2$  is the initial effective mean stress and the deviatoric stress is defined by  $\tau = (\sigma'_1 - \sigma'_3) / 2 = \sqrt{\tau_{xy}^2 + [(\sigma'_x - \sigma'_y) / 2]^2}$ . In principle the shape of the liquefaction front may be approximated by two segments of straight lines in the stress space as indicated by the broken line segments in Fig. 2.3; one being the segment of a vertical line defined in the contractive zone, the other being the segment of a line parallel to the failure line defined in the dilative zone. In practice, however, a smooth transition from one zone to the other is necessary for assuring easy and reliable numerical solution. Consequently, the shape of the liquefaction front will be approximated, as shown in Fig. 2.3, by the following function:

where

equation

$$\begin{aligned} S &= S_0 & (\text{if } r < r_3) \\ S &= S_2 + \sqrt{(S_0 - S_2)^2 + [(r - r_3) / m_1]^2} & (\text{if } r > r_3) \end{aligned} \quad (2.59)$$

where

and

in which

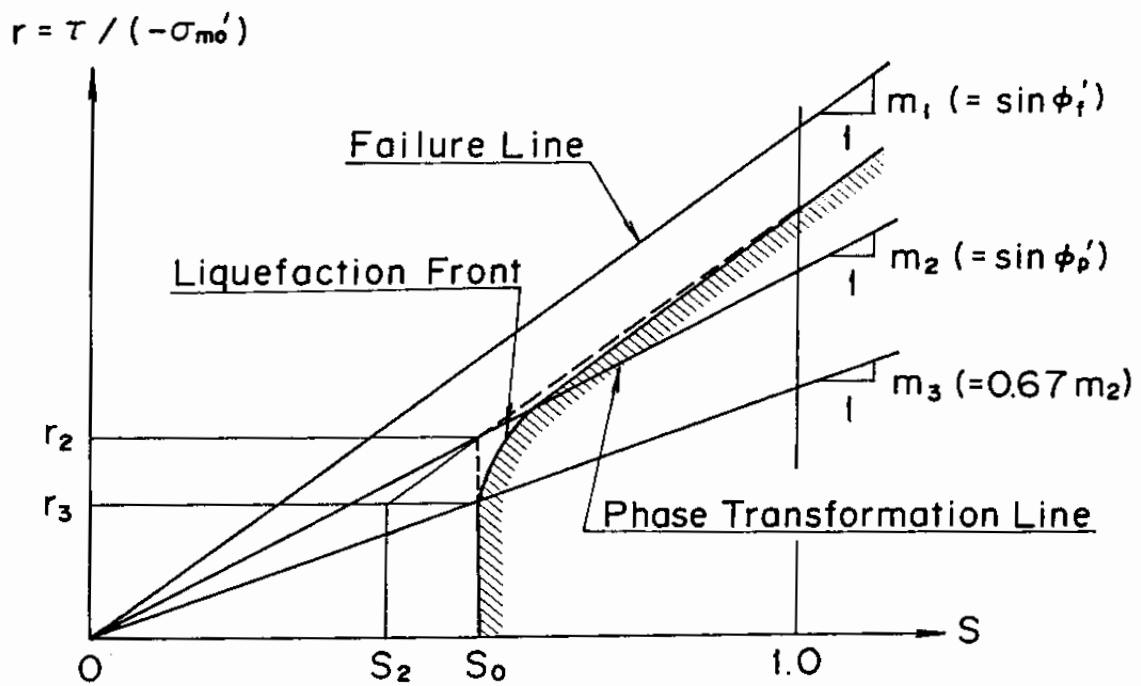


Fig. 2.3 Schematic figure of liquefaction front, state variable  $S$  and shear stress ratio  $r$

$$r_2 = m_2 S_0 \quad (2.60)$$

$$r_3 = m_3 S_0 \quad (2.61)$$

$$S_2 = S_0 - (r_2 - r_3)/m_1 \quad (2.62)$$

and  $S_0$  : a parameter to be defined by a function of shear work;  
 $m_1$  : inclination of the failure line, defined by the shear resistance angle  $\phi_f'$  as  $m_1 = \sin\phi_f'$ ;  $m_2$  : inclination of the phase transformation line, defined by the phase transformation angle  $\phi_p'$  as  $m_2 = \sin\phi_p'$ ; and  $m_3 = 0.67m_2$ . The auxiliary parameter  $m_3$ , introduced for ensuring the smooth transition from one zone to the other, is determined as a balance of the smoothness and the physically feasible stress path shape.

In this formulation, the parameter  $S_0$ , hereafter called "liquefaction front parameter," may well be interpreted as a measure which defines the state of the cyclic mobility; e.g.  $S_0 = 1.0$  being the initial stress state if  $r < m_3$ ,  $S_0 = 0$  being the limiting state at which failure occurs due to the cyclic mobility.

At a certain boundary value problem, initial shear stress ratio can be very high so that  $r > m_3$ . In such a case, the initial value of the liquefaction front parameter  $S_0$  should be determined from the initial value of  $r$  by solving the second equation in Eq.(2.59) with  $S = 1.0$ . The initial value of  $S_0$  is easily obtained as a solution of second order polynomial equation.

#### 2.4.3 Shear Work Correlation

The liquefaction front parameter  $S_0$  is given by a function

of shear work. Towhata and Ishihara (1985b) obtained the correlation between the shear work and the excess pore water pressure such as shown in Fig. 2.4 and concluded that the correlation is independent of the shear stress paths with or without the rotation of principal stress axes. This correlation is generalized by defining a relation between the liquefaction front parameter  $S_0$  and the normalized shear work defined by

$$w = W_s / W_n \quad (2.63)$$

The factor for normalization  $W_n$  is given by

$$W_n = \tau_{m0} \gamma_{m0} / 2 \quad (2.64)$$

in which  $\tau_{m0}$  and  $\gamma_{m0}$  are the shear strength of soil at the drained condition and the reference strain of soil at the initial effective mean stress  $\sigma_{m0}'$ . To be more specific, they are defined with the initial shear modulus  $G_{m0}$  as

$$\tau_{m0} = (-\sigma_{m0}') \sin \phi_f' \quad (2.65)$$

$$\gamma_{m0}' = \tau_{m0} / G_{m0} \quad (2.66)$$

The initial shear modulus of cohesionless soil is known to be given by a power function of effective mean stress, approximately given by

$$G_{m0} = G_{ma} (\sigma_{m0}' / \sigma_{ma}')^{0.5} \quad (2.67)$$

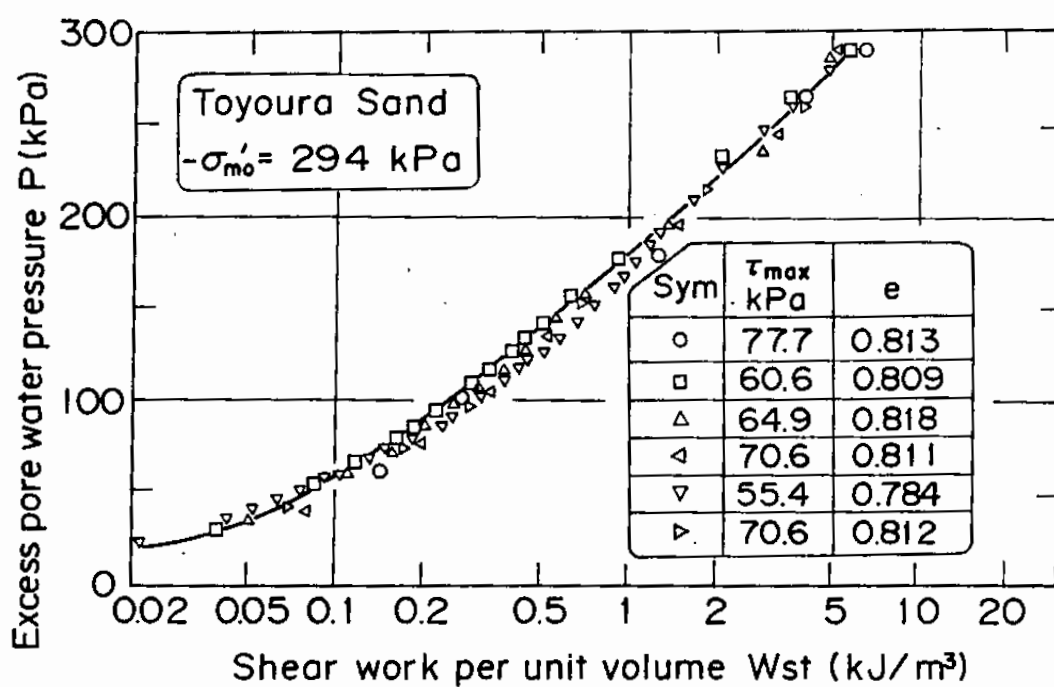


Fig. 2.4 Correlation between shear work and excess pore water pressure (after Towhata and Ishihara, 1985b)

in which  $G_{ma}$  : initial shear modulus at  $\sigma_{m0}' = \sigma_{ma}'$ .

With such a normalization for shear work as shown in Eq.(2.63), the correlation between the liquefaction parameter and the normalized shear work can be empirically modeled based on the following consideration:

- (1) Certain laboratory studies indicate a "break" at  $S_0 = 0.4$  (Zienkiewicz et al, 1978) from which the behavior of soil drastically change. It would be desirable to express the correlation with two functions; one defined for  $S_0 > 0.4$ , the other for  $S_0 < 0.4$ . Thus, at least two parameters are necessary.
- (2) In order to fit the model to a set of soils with various degree of liquefaction resistance, it would be desirable to have a parameter which can control, over the entire zone of  $S_0$ , the contribution of normalized shear work. This adds one parameter.
- (3) In the limiting case  $S_0$  should not become zero if stable simulation of cyclic mobility is needed. This indicates use of a small parameter is needed as the limiting value for  $S_0$ . This adds another parameter.

Based on the above consideration, such a correlation with four parameters is given between the liquefaction front parameter and the normalized shear work as

$$\begin{aligned} S_0 &= 1 - 0.6(w/w_1)^{p_1} && (\text{if } w < w_1) \\ S_0 &= (0.4 - S_1)(w_1/w)^{p_2} + S_1 && (\text{if } w > w_1) \end{aligned} \quad (2.68)$$

in which  $S_1$ ,  $w_1$ ,  $p_1$  and  $p_2$  are the material parameters which

characterize the cyclic mobility of the cohesionless soil. Several examples represented by this equation is shown in Fig. 2.5.

#### 2.4.4 Threshold Limit

In obtaining the shear work correlation, Towhata and Ishihara (1985b) used total shear work defined by

$$dW_{st} = [(\sigma'_x - \sigma'_y)/2]d(\epsilon_x - \epsilon_y) + \tau_{xy}d\gamma_{xy} \quad (2.69)$$

It is assumed in Eq.(2.69) that  $dW_{st}$  is always positive so that, if the right hand side of this equation should take a negative value, its absolute is taken. The use of the total shear work gave satisfactory correlation for the range of test data studied by Towhata and Ishihara (1985b). It is known, however, that there exists a threshold limit in the amplitude of cyclic shear strain or shear stress; for cyclic strain or stress below this threshold level, there is no pore water pressure build-up (e.g. Dobry et al, 1982). In order to incorporate such a factor of practical significance into the correlation in Eq.(2.68), the shear work which would be consumed by the threshold limit will be subtracted from the total shear work. Because the shear work consumed by the threshold limit may be closely related with the elastic shear work, it will be given by introducing a parameter  $c_1$  for specifying the threshold level as

$$c_1 dW_{se} = c_1 \left| \tau d(\tau/G_m^*) \right| \quad (2.70)$$



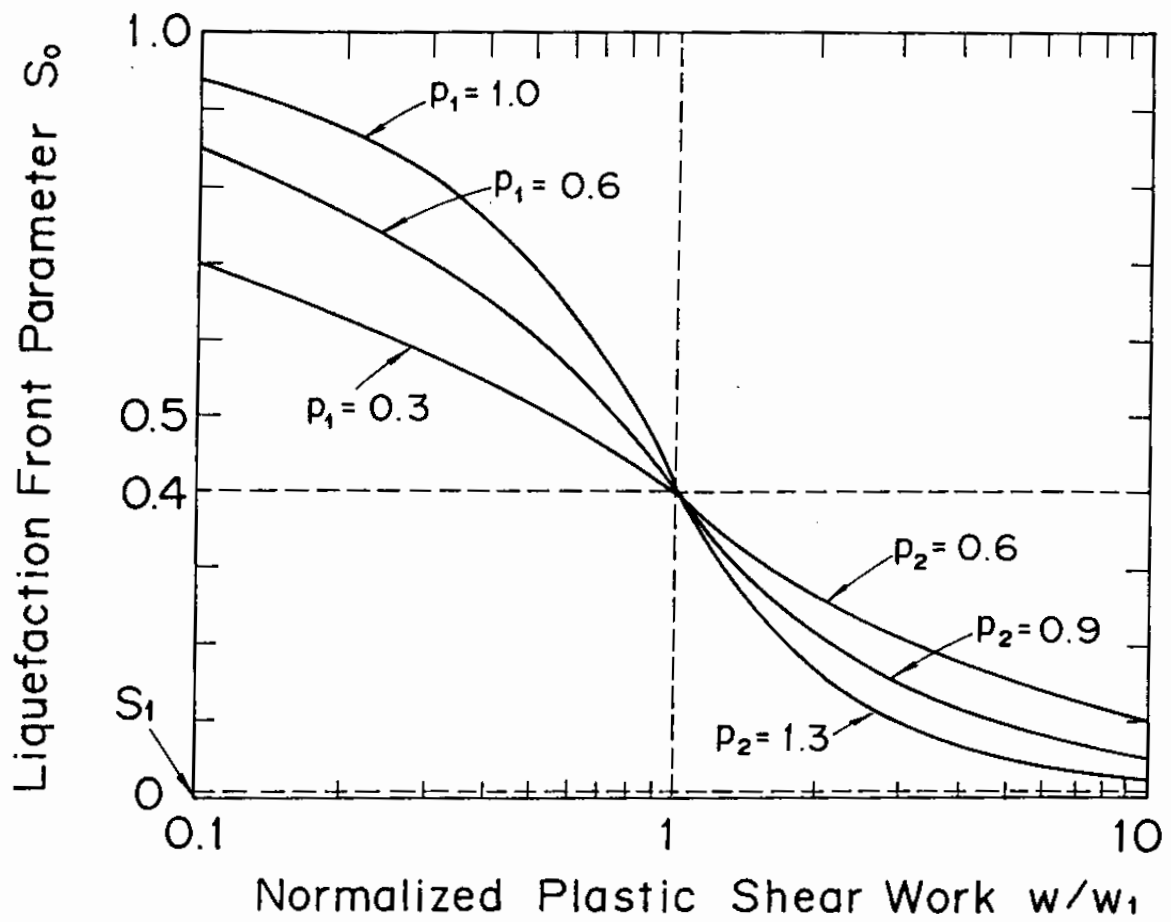


Fig. 2.5 Relation between normalized plastic shear work  $w$  and liquefaction front parameter  $S_0$

in which  $G_m^*$  : elastic modulus at effective mean stress  $\sigma_m'$  given by

$$G_m^* = G_{m0} (\sigma_m' / \sigma_{m0}')^{0.5} \quad (2.71)$$

Thus the shear work increment to be used for the shear work correlation in Eq.(2.68) with Eq.(2.63) is given by

$$dW_s = dW_{st} - c_1 dW_{se} \quad (2.72)$$

It is understood in Eq.(2.72) that, if the value of right hand side of the equation should become negative,  $dW_s$  will be assumed zero.

In general shear work induced by plastic strain is called plastic shear work. The shear work  $W_s$  defined in Eq.(2.72) is in its approximate sense the total shear work minus the elastic shear work. In the following discussion, the shear work  $W_s$  will be conveniently called "plastic shear work".

In the formulation presented so far, the plastic shear work always contributes to the progress of liquefaction whether the effective stress is in the dilative zone or the contractive zone. It is believed, however, that not all the plastic shear work induced in the dilative zone contributes to the progress of liquefaction. In a pragmatic sense this fact is already incorporated in the shear work correlation in Eq.(2.68). The author believes, however, that a certain explicit correction for shear work increment is needed for the dilative zone. Such a correction is achieved by introducing a correction factor  $R$  to

be multiplied with  $dW_s$  given by

$$R = (m_1 - r/S)/(m_1 - m_3) \quad (\text{if } r/S > m_3) \quad (2.73)$$

When  $S$  becomes small, however, the value of  $r/S$  becomes so sensitive to the small errors contained in the values of  $r$  and  $S$  that  $R$  given by Eq.(2.73) becomes numerically unreliable. Therefore, a measure is taken for small values of  $S$ , such that, if  $S < 0.4$ ,  $R$  is given by

$$R = (m_1 - r/0.4)/(m_1 - m_3) \quad (\text{if } r/0.4 > m_3) \quad (2.74)$$

An additional exception is imposed if the initial deviatoric stress ratio is so high that the initial value of  $S_0$  becomes less than 0.4. In this case, the value of 0.4 in Eq.(2.74) is replaced by  $S_w$  defined by

$$S_w = 0.4 + (\text{initial } S_0 - 0.4)S_0/(\text{initial } S_0) \quad (2.75)$$

A schematic figure is shown in Fig. 2.6 for the dilative zone to be affected by the correction factor  $R$ . The author admits that the correction factor introduced here complicates the formulation without so much of reasoning or laboratory data to rely on. The laboratory studies are urgently needed on the behavior of soil under cyclic loading with a static shear. It might be possible in future that this part of the modeling will be modified based on the future laboratory studies. In the meantime, as mentioned earlier, the most of the effect of the above correction might be

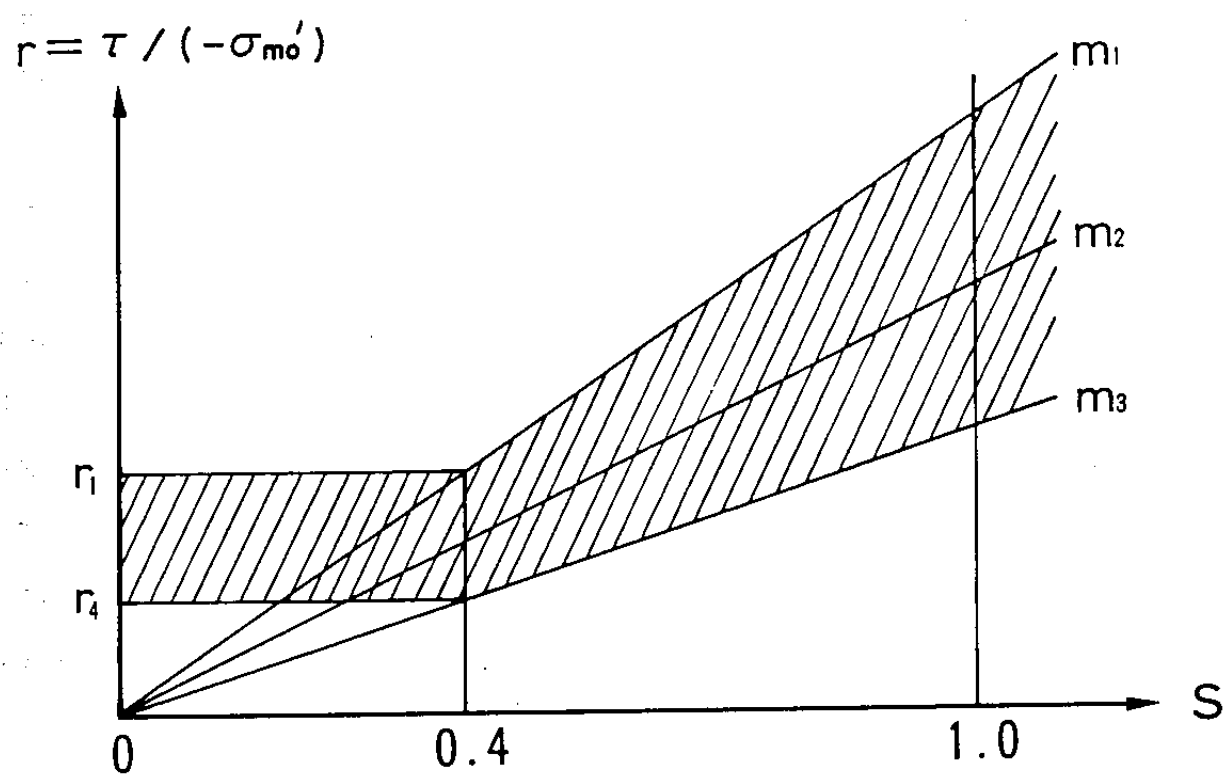


Fig. 2.6 Dilative zone to be affected by the correction factor  $R$

offset by the effect of the parameter  $p_2$  in Eq.(2.68). If an adverse effect should exist due to these correction factors, the effect might be minor.

At each stage of deformation process under transient and cyclic loads, increment in plastic shear work will be computed via Eq.(2.72) with the correction in Eqs.(2.73) through (2.75) if the current stress state is in the dilative zone. The accumulated plastic shear work  $W_s$  will then be normalized by Eq.(2.63) and substituted into Eq.(2.68), giving the liquefaction front parameter  $S_0$ . From the liquefaction front parameter  $S_0$  and the deviatoric stress ratio  $r$ , the effective mean stress ratio  $S$  will be obtained by Eq.(2.59). Finally, the effective mean stress ratio  $S$  is multiplied by initial mean effective stress  $\sigma_{m0}'$ , giving the volumetric strain  $\epsilon_p$  of plastic nature through Eq.(2.58).

In the discipline of soil mechanics, stress dilatancy relation has been well understood in a much more fundamental and simpler manner than the present approach; the ratio of plastic volumetric strain increment over plastic shear strain increment is governed by a function of relevant stress ratio with one parameter which corresponds to phase transformation angle (e.g. Rowe, 1962). Though in a pragmatic sense it is not necessary to refer to this fundamental relation in modeling of undrained cyclic behavior of sand as in the present study, the stress dilatancy relation is so well established and fundamental in the soil mechanics that it might be necessary to compare the present approach with it. The comparison is shown in APPENDIX B.

In closing this section, it should be cautioned that such

variables as  $\sigma_m'$  and  $S$  are used in this section in the context of undrained tests under constant total mean stress. Such tests are considered only as a means to establish the relation between the shear work and the volumetric strain  $\epsilon_p$  of plastic nature. Therefore, when those variables are computed from the plastic shear work as shown in this section, they should be regarded as the state variables rather than the real variables to be computed as a solution of boundary value problems.

## 2.5 Virtual Simple Shear Mechanism

### 2.5.1 Initial Loading

In defining the virtual tangent shear moduli  $R_{L/V}^{(i)}$  in Eq.(2.32) and the virtual shear stress  $Q^{(i)}(\gamma^{(i)})$  in Eq.(2.55), it is assumed that each virtual simple shear mechanism can be approximated by the one dimensional stress strain relation observed in the actual simple shear test. As a candidate for such one dimensional relation, the hyperbolic stress strain relation is adopted for the initial or the monotonic loading as

$$Q^{(i)}(\gamma^{(i)}) = [(\gamma^{(i)}/\gamma_v^{(i)})/(1 + |\gamma^{(i)}/\gamma_v^{(i)}|)]Q_v^{(i)} \quad (2.76)$$

in which  $Q_v^{(i)}$  : virtual shear strength for mechanism  $i$ ; and  $\gamma_v^{(i)}$  : virtual reference strain for mechanism  $i$ . For simplicity, inherent isotropy is assumed in the following discussion. Then, the hyperbolic relation is rewritten by

$$Q^{(i)}(\gamma^{(i)}) = [(\gamma^{(i)}/\gamma_v)/ (1 + |\gamma^{(i)}/\gamma_v|)]Q_v \quad (2.77)$$

in which  $Q_v$  : virtual shear strength and  $\gamma_v$  : virtual reference strain. By substituting Eq.(2.77) into Eq.(2.51), the virtual tangent shear moduli are obtained for the initial loading as

$$R_L^{(i)} = [1/(1 + |\gamma^{(i)}/\gamma_v|)^2] (Q_v/\gamma_v) \Delta\theta \quad (2.78)$$

It is to be noted in Eqs.(2.77) and (2.78) that, though inherent isotropy is assumed, the superscript (i) for the functions  $Q$  and  $R_L$  is retained because, once unloading becomes involved, its value will become dependent on the individual history of the virtual shear strain; i.e. the inherent isotropic material will exhibit stress induced anisotropy.

### 2.5.2 Memory of Loading History

To record the history of loading, it is postulated that the memory of loading history is registered in the normalized space defined by such variables as

$$\xi = \gamma^{(i)}/\gamma_v \quad (2.79)$$

$$\eta = Q^{(i)}/Q_v \quad (2.80)$$

In the above definition, the superscript (i) is omitted from  $\xi$  and  $\eta$  for simplicity but the following discussion is supposed to be applicable to each mechanism  $i = 1, \dots, I$ . According to this definition, the hyperbolic relation in Eq.(2.77) is rewritten in the normalized space as

$$\eta = \xi / (1 + |\xi|) \quad (2.81)$$

and the curve defined by Eq.(2.81) in the normalized space will be called back-bone curve.

It is postulated in this study that the memory of loading history, which affects the present and the future material behavior, is completely specified by only two points out of the previous loading history defined in the normalized space; one being the point on the back-bone curve of which  $|\xi|$  takes the maximum value of the previous loading history, the other being the most recent reversal point. As shown in Fig. 2.7, once unloading begins and  $|\xi|$  becomes less than the maximum value of  $|\xi|$  in the previous loading history, the point will either be directed to the memorized point on the back-bone curve or to its symmetrical image on the back-bone curve. When the loading continues beyond this point, the point will follow again the back-bone curve.

Thus, the formal definitions relevant to the loading processes are given as follows:

- (1) initial loading : the process which satisfies  $|\xi| = \max |\xi|$
- (2) unloading/reloading : the process which satisfies  $|\xi| < \max |\xi|$ 
  - a) unloading : the sign of  $d\xi$  is opposite to that of initial loading
  - b) reloading : the sing of  $d\xi$  is the same as that of initial loading
- (3) reversal point : a point at which  $d\xi$  changes its sign

Such formal definitions can be helpful for conceptual understanding of the present approach. It is to be noted that the



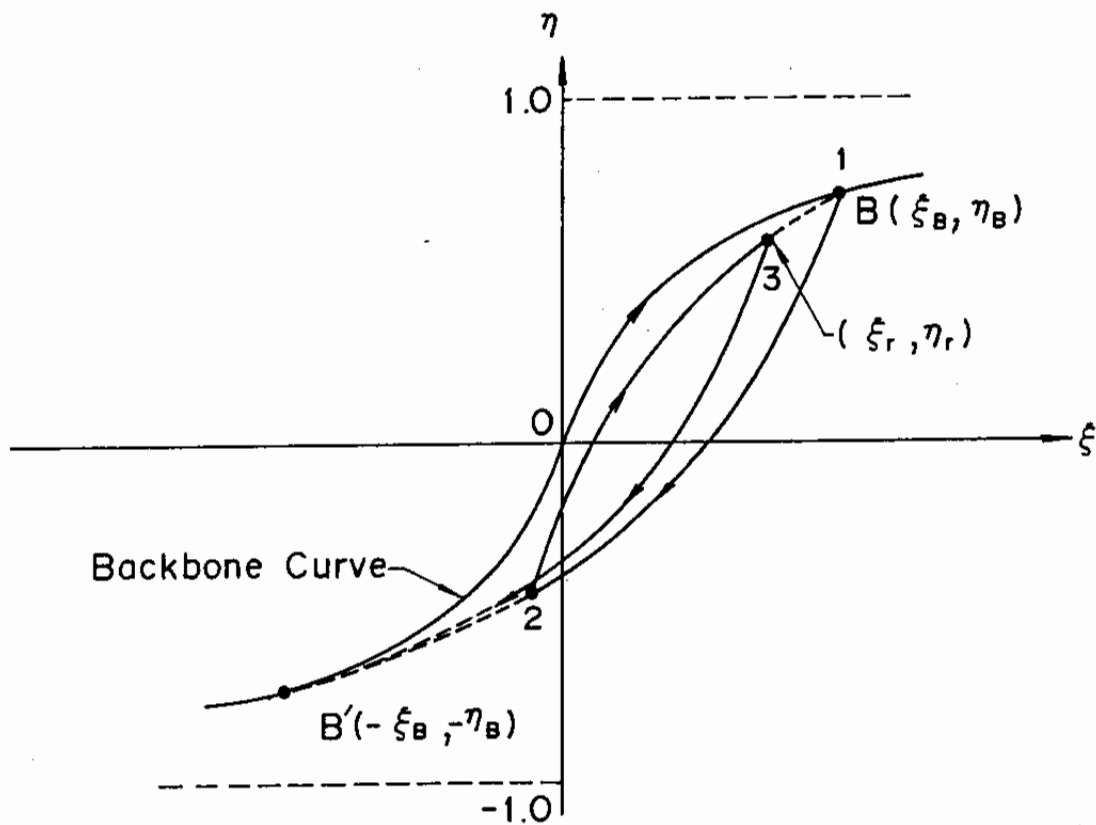


Fig. 2.7 Schematic figure of loading/unloading curves of the virtual simple shear mechanism in the normalized space

definitions given by  $d\xi$  are consistent with the definition given earlier in Eq.(2.6) for subscripts L/U for  $R^{(i)}$  based on the sign of  $\{n^{(i)}\}^T \{d\epsilon\} = (d\xi)\gamma_v$ .

In practice of numerical analysis, the following set of definitions might be much more useful;

- (1) initial loading : either of the following two;
  - a) the process which never experiences the unloading, or
  - b) the process which goes beyond the previously memorized reversal point or its symmetrical image on the back-bone curve
- (2) unloading/reloading : the process which begins after the reversal but which ends when the process goes either beyond the reversal point or its symmetrical image on the back-bone curve.
  - a) unloading : number of the reversals is odd by counting the reversal from the back-bone curve as one
  - b) reloading : number of the reversals is even by counting the reversal from the back-bone curve as one
- (3) reversal point : a point at which not only  $d\xi$  changes its sign from its previous loading process but also  $|d\xi|$  exceeds the threshold value  $\delta$ .

The threshold value  $\delta$ , similar to the small elastic region, is necessary for assuring stability in the numerical analysis; the value of the order of  $10^{-6}$  is satisfactory in practice.

### 2.5.3 Unloading from the Initial Loading

For representing the one dimensional stress strain relation during unloading and reloading, Masing's rule was often used (Finn et al, 1977; Ishihara and Towhata, 1982); i.e. if the initial loading curve is given by

$$\eta = f(\xi) \quad (2.82)$$

then the unloading and reloading curves are given by

$$(\eta - \eta_r)/2 = f[(\xi - \xi_r)/2] \quad (2.83)$$

in which  $\xi_r$  and  $\eta_r$  represent the coordinates of the reversal point. It is known, however, that Masing's rule when combined with the hyperbolic stress strain relation does not represent the physically feasible hysteresis loop when the amplitude of cyclic shear strain becomes as large as a few percent; at this strain level the hysteresis loop given by Masing's rule consumes about twice the energy as those observed in the laboratory tests (Ishihara, 1982).

Such a drawback can be corrected by introducing scaling parameters into the variables  $\xi$  and  $\eta$  (Ishihara et al, 1985). Let us defined the scaled variables by

$$\begin{aligned} \xi' &= \xi/a \\ \eta' &= \eta/b \end{aligned} \quad (2.84)$$

in which the scaling parameters  $a$  and  $b$  are determined by functions of  $\max |\xi|$  for the previous loading history.

Let us denote the coordinates of the reversal points on the back-bone curve as  $\xi_B$  and  $\eta_B$  and let us scale these coordinates in the similar manner as

$$\begin{aligned}\xi_B' &= \xi_B/a \\ \eta_B' &= \eta_B/b\end{aligned}\tag{2.85}$$

Using scaled coordinates in Eqs.(2.84) and (2.85), let us define a function for unloading curve from the back-bone curve by

$$(\eta' - \eta_B')/2 = f[(\xi' - \xi_B')/2]\tag{2.86}$$

in which the function  $f$  represents the hyperbolic relation given by

$$f(\xi) = \xi/(1 + |\xi|)\tag{2.87}$$

Because the curve defined by Eq.(2.86) should go through the symmetrical image of the reversal point, one obtains

$$-\eta_B' = f(-\xi_B')\tag{2.88}$$

whereas the reversal point is on the back-bone curve, such that

$$\eta_B = f(\xi_B)\tag{2.89}$$

Elimination of  $\eta_B$  from Eqs.(2.88) and (2.89) by using Eqs.(2.85) and (2.87) yields

$$b = (a + |\xi_B|) / (1 + |\xi_B|) \quad (2.90)$$

It is to be noted that strain level of cyclic loading is represented by  $|\xi_B|$ , which coincides with  $\max |\xi|$  for the previous loading history of transient and cyclic loading. In the following discussion  $|\xi_B|$  will be conveniently called strain level. Because the scaling parameter  $b$  is determined by Eq.(2.90) from the parameter  $a$  and the strain level  $|\xi_B|$ , it remains to define a function of strain level  $|\xi_B|$  for determining the scaling parameter  $a$ .

The energy consumed by the hysteresis loop is generally expressed by a relative value to the equivalent elastic energy; i.e. a hysteretic damping factor  $h$ . The definition of  $h$ , as briefly mentioned in the previous chapter, is given by

$$h = (1/4\pi)(\Delta W/W) \quad (2.91)$$

in which  $\Delta W$  is the damping energy, i.e. the area within the hysteresis loop shown in Fig. 2.8, and  $W$  is the equivalent elastic strain energy defined by

$$W = (1/2)\xi_B \eta_B \quad (2.92)$$

It is to be noted that the hysteretic damping factor  $h$  is independent of the normalization factors or scaling factors used for the stress and strain because effects of these factors are canceled by taking the ratio of  $\Delta W$  over  $W$  in Eq.(2.91). Therefore, the definition of the hysteretic damping factor given

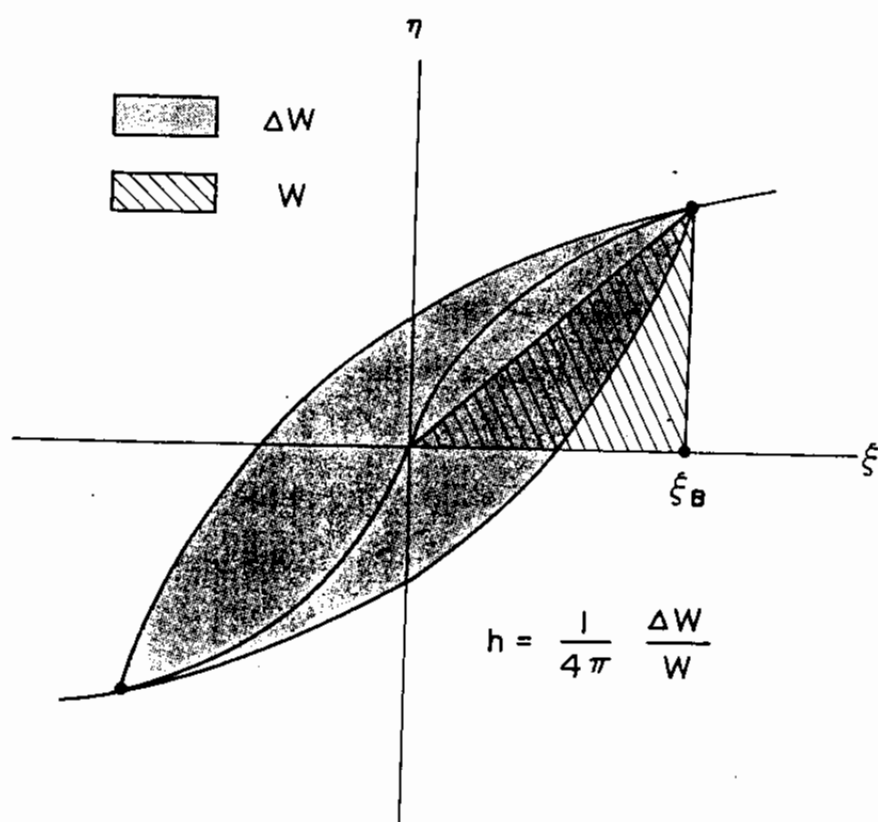


Fig. 2.8 Definition of hysteretic damping factor in the normalized space

in the stress strain space in the previous chapter in Fig. 1.4 is consistent with that given in the normalized space mentioned above.

As a candidate for the physically feasible hysteretic damping factor to be represented by each virtual simple shear mechanism, the hyperbolic function of strain level  $|\xi_B|$  is adopted as

$$h(|\xi_B|) = [|\xi_B/\xi_h|/(1 + |\xi_B/\xi_h|)]h_v \quad (2.93)$$

in which  $h_v$  : limiting value of virtual damping factor when virtual shear strain level is infinity; and  $\xi_h$  : a parameter similar to virtual reference strain.

Because the hysteresis loop defined by Eq.(2.86) produces the hysteretic damping factor  $\tilde{h}$  as (Ishihara, 1982)

$$\tilde{h}(|\xi_B'|) = (4/\pi)(1 + 1/|\xi_B'|)[1 - (1/|\xi_B'|)]\ln(1 + |\xi_B'|) - (2/\pi) \quad (2.94)$$

the scaling parameter  $a$  should be so determined as to produce the same value for  $\tilde{h}$  and  $h$  for the same strain level  $|\xi_B|$ , such that

$$\tilde{h}(|\xi_B/a|) = h(|\xi_B|) \quad (2.95)$$

Once unloading begins from the back-bone curve at the virtual normalized shear strain  $\xi_B$ , the scaling parameter  $a$  is determined by numerically solving Eq.(2.95) from the current strain level  $|\xi_B|$ . Then, the corresponding scaling parameter  $b$  is

determined by Eq.(2.90) and consequently the unloading curve is given by Eq.(2.86).

The unloading curve in Eq.(2.86) can be more explicitly written by converting the normalized variables  $\xi'$  and  $\eta'$  to the original variables  $\gamma^{(i)}$  and  $Q^{(i)}$ , such that

$$(Q^{(i)}/Q_v - \eta_b)/(2b) = f[(\gamma^{(i)}/\gamma_v - \xi_b)/(2a)] \quad (2.96)$$

in which the function  $f$  is defined by Eq.(2.87) and  $\xi_b$ ,  $\eta_b$ ,  $a$  and  $b$  are, as mentioned earlier, separately defined for each mechanism  $i = 1, \dots, I$ .

By substituting Eq.(2.96) into Eq.(2.51), the virtual tangent shear moduli are obtained for the unloading process from the initial loading as

$$R_v^{(i)} = g[(\gamma^{(i)}/\gamma_v - \xi_b)/(2a)](Q_v/\gamma_v)(b/a)\Delta\theta \quad (2.97)$$

in which the function  $g$  is the first order derivative of  $f$  in Eq.(2.87) and given by

$$g(\xi) = 1/(1 + |\xi|)^2 \quad (2.98)$$

#### 2.5.4 Reloading

For representing the one dimensional stress strain relation during reloading and re-unloading, a function similar to Eq.(2.86) is used for the interpolation between the two points in the normalized space; one is the most recent reversal point ( $\xi_r$ ,  $\eta_r$ ) at which the current reloading or re-unloading process



initiated, the other the most recent reversal point or its mirror image on the back-bone curve to which the current process is directed. The function is given by

$$(\eta' - \eta_r')/(2c) = f[(\xi' - \xi_r')/(2c)] \quad (2.99)$$

The scaling factor  $c$  is determined so that the curve defined by Eq.(2.99) goes through the most recent reversal point or its symmetrical image on the back-bone curve, such that

$$(\pm\eta_B' - \eta_r')/(2c) = f[(\pm\xi_B' - \xi_r')/(2c)] \quad (2.100)$$

in which the signs of  $\pm$  takes plus if reloading and minus if re-unloading. Solving Eq.(2.100) for  $c$  with the aid of Eq.(2.87), one obtains

$$c = (1/2) \left| \pm\xi_B' - \xi_r' \right| (\pm\eta_B' - \eta_r') / [(\pm\xi_B' - \xi_r') - (\pm\eta_B' - \eta_r')] \quad (2.101)$$

Explicit equations for  $Q^{(i)}$  and  $R_{L/U}^{(i)}$  similar to Eqs.(2.96) and (2.97) will be obtained if the scaling factors  $ac$  and  $bc$  are used on behalf of  $a$  and  $b$  in those equations and the coordinates of reversal point  $\xi_r$  and  $\eta_r$  are used on behalf of  $\xi_B$  and  $\eta_B$ . Thus, for reloading and re-unloading

$$(Q^{(i)}/Q_v - \eta_r)/(2bc) = f[(\gamma^{(i)}/\gamma_v - \xi_r)/(2ac)] \quad (2.102)$$

$$R_{L/U}^{(i)} = g[(\gamma^{(i)}/\gamma_v - \xi_r)/(2ac)] (Q_v/\gamma_v) (b/a) \Delta\theta \quad (2.103)$$

As mentioned earlier,  $\xi_r$ ,  $\eta_r$ ,  $a$ ,  $b$  and  $c$  are separately defined for each mechanism  $i = 1, \dots, I$ .

## 2.6 Shear Mechanism

In the previous section, four soil parameters were introduced for modeling the virtual simple shear mechanism; the virtual shear strength  $Q_v$  and the virtual reference strain  $\gamma_v$  in Eqs.(2.77) and (2.78), and the limiting value of hysteretic damping factor  $h_v$  for the virtual simple shear mechanism and a parameter  $\xi_h$  in Eq.(2.93). In the present section, it will be shown how those parameters for the virtual simple shear mechanism are related to the actual soil parameters which are measurable through the actual shearing process.

### 2.6.1 Shear Strength and Reference Strain

First of all, the virtual shear strength and the virtual reference strain in Eqs.(2.77) and (2.78) can readily be determined by such soil parameters as shear strength  $\tau_m$  and shear modulus  $G_m$  at small strain level. Following the approach by Towhata and Ishihara (1985a), let us consider a simple shear test under the drained and monotonic loading condition with the initially isotropic stress state. It is assumed that only non zero shear strain is  $\gamma_{xy}$ . When the shear strain is very small such that  $\gamma_{xy} = 0$ , the definition of the shear modulus  $G_m$  implies

$$d\tau_{xy} = G_m d\gamma_{xy} \quad (2.104)$$

whereas Eq.(2.78) yields

$$R_L^{(i)} = (Q_v/\gamma_v)\Delta\theta \quad (2.105)$$

Substitution of Eq.(2.105) into Eqs.(2.41) and (2.42) yields

$$\begin{aligned} G_{t2} &= 0 \\ G_{t3} &= (Q_v/\gamma_v) \sum_{i=1}^I \sin^2\theta_i \Delta\theta \end{aligned} \quad (2.106)$$

and, therefore, Eqs.(2.38) and (2.39) yield

$$d\tau_{xy} = [(Q_v/\gamma_v) \sum_{i=1}^I \sin^2\theta_i \Delta\theta] d\gamma_{xy} \quad (2.107)$$

Comparing Eqs.(2.104) and (2.107), one obtains

$$G_m = (Q_v/\gamma_v) \sum_{i=1}^I \sin^2\theta_i \gamma_{xy} \quad (2.108)$$

Similarly, when  $\gamma_{xy} = \infty$ , the definition of the shear strength  $\tau_m$  implies

$$\tau_{xy} = \tau_m \quad (2.109)$$

whereas Eq.(2.77) yields

$$Q^{(i)}(\infty) = Q_v \quad (2.110)$$

Substitution of Eq.(2.110) into Eq.(2.55) yields

$$\tau_{xy} = Q_v \sum_{i=1}^I \sin \theta_i \Delta \theta \quad (2.111)$$

Comparing Eqs.(2.109) and (2.111), one obtains

$$\tau_m = Q_v \sum_{i=1}^I \sin \theta_i \Delta \theta \quad (2.112)$$

From Eqs.(2.108) and (2.112), the virtual shear strength and the virtual reference strain are determined by

$$Q_v = \tau_m / \left( \sum_{i=1}^I \sin \theta_i \Delta \theta \right) \quad (2.113)$$

$$\gamma_v = (\tau_m / G_m) \left[ \left( \sum_{i=1}^I \sin^2 \theta_i \Delta \theta \right) / \left( \sum_{i=1}^I \sin \theta_i \Delta \theta \right) \right] \quad (2.114)$$

When number of multiple mechanisms  $I$  is increased to infinity, the limiting value in Eqs.(2.113) and (2.114) will be given by

$$Q_v^0 = \tau_m / 2 \quad (2.115)$$

$$\gamma_v^0 = \pi (\tau_m / G_m) \quad (2.116)$$

The relations in Eqs.(2.115) and (2.116) are consistent with the results obtained by Towhata and Ishihara (1985a).

### 2.6.2 Hysteretic Damping Factor for Hysteresis Loop

The soil parameters  $h_v$  and  $\xi_h$  for the virtual simple shear mechanism in Eq.(2.93) can readily be determined by such a measurable parameter as the hysteretic damping factor of actual simple shear measured as a function of shear strain amplitude level. In order to prove this, let us examine the behavior of the virtual shear mechanisms during the actual cyclic simple shear

under the drained condition. The amplitude of the shear strain will be denoted by  $\gamma_{xyB}$ .

(1) Equivalent elastic strain energy

When the unloading starts at the peak value of the strain, the shear strain will be given by

$$\gamma_{xy} = \gamma_{xyB} \quad (2.117)$$

so that the virtual simple shear strain amplitude is given by Eq.(2.50) as

$$\gamma_B^{(i)} = \gamma_{xyB} \sin \theta_i \quad (2.118)$$

and the corresponding virtual simple shear stress is given by Eq.(2.77) as

$$Q_B^{(i)} = Q^{(i)}(\gamma_B^{(i)}) \quad (2.119)$$

From this and Eq.(2.55), the actual simple shear stress amplitude is given by

$$\tau_{xyB} = \sum_{i=1}^I Q_B^{(i)} \sin \theta_i \Delta \theta \quad (2.120)$$

Therefore, the equivalent elastic strain energy for the cyclic loading process of shear strain amplitude  $\gamma_{xyB}$  is given by

$$W = (1/2) \left[ \sum_{i=1}^I Q_B^{(i)} \sin \theta_i \Delta \theta \right] \gamma_{xyB} \quad (2.121)$$

Rearranging this and using Eq.(2.118), one obtains

$$W = (1/2) \sum_{i=1}^I Q_B^{(i)} Y_B^{(i)} \Delta \theta \quad (2.122)$$

If the equivalent elastic virtual strain energy is defined by

$$W^{(i)} = (1/2) Q_B^{(i)} Y_B^{(i)} \quad (2.123)$$

the equivalent elastic strain energy in Eq.(2.122) is rewritten as

$$W = \sum_{i=1}^I W^{(i)} \Delta \theta \quad (2.124)$$

Thus, the equivalent elastic strain energy is obtained by summing up the equivalent elastic virtual strain energy.

## (2) Hysteretic damping energy

Similarly, the energy consumed by the actual hysteresis loop  $\Delta W$  is given by summing up the energy consumed by each stress contribution appearing in the right hand side of Eq.(2.120). In order to do the summation, some elaboration is necessary, First of all, let us go back to the definition of the hysteretic damping factor in Eq.(2.91) and write down the explicit equation for the equivalent damping energy  $\Delta W$ . As mentioned earlier, the hysteretic damping factor is defined irrespective of the scaling factors for the relevant variables.

Since the area within the hysteresis loop (in the actual stress and strain space) is twice the upper half of the area, one

obtains

$$\Delta W = 2 \int_{-|\delta_{xyB}|}^{|\delta_{xyB}|} [\tau_{xy} - (\tau_{xyB}/\gamma_{xyB})\gamma_{xy}] d\gamma_{xy} \quad (2.125)$$

The linear term, i.e.  $(\tau_{xyB}/\gamma_{xyB})\gamma_{xy}$  in the integral, will vanish upon integration so that

$$\Delta W = 2 \int_{-|\delta_{xyB}|}^{|\delta_{xyB}|} \tau_{xy} d\gamma_{xy} \quad (2.126)$$

In the manner similar to the derivation of Eqs.(2.117) through (2.120),  $\tau_{xy}$  is expressed by the virtual simple shear stress  $Q^{(i)}$  as

$$\tau_{xy} = \sum_{i=1}^I Q^{(i)} \sin\theta_i \Delta\theta \quad (2.127)$$

in which

$$Q^{(i)} = Q^{(i)}(\gamma^{(i)}) \quad (2.128)$$

$$\gamma^{(i)} = \gamma_{xy} \sin\theta_i \quad (2.129)$$

Substitution of Eq.(2.127) into Eq.(2.126) yields

$$\Delta W = 2 \int_{-|\delta_{xyB}|}^{|\delta_{xyB}|} \left[ \sum_{i=1}^I Q^{(i)} \sin\theta_i \Delta\theta \right] d\gamma_{xy} \quad (2.130)$$

Rearranging this equation, one obtains

$$\Delta W = 2 \sum_{i=1}^I \left[ \int_{-|\delta_{xyB}|}^{|\delta_{xyB}|} Q^{(i)} d\gamma_{xy} \sin\theta_i \Delta\theta \right] \quad (2.131)$$

The transformation of the variable for the integration from  $\gamma_{xy}$  to  $\gamma^{(i)} = \gamma_{xy} \sin \theta_i$  in Eq.(2.131) yields

$$\Delta W = 2 \sum_{i=1}^I \left[ \int_{-|\gamma_B^{(i)}|}^{|\gamma_B^{(i)}|} Q^{(i)} d\gamma^{(i)} \right] \Delta \theta \quad (2.132)$$

If, by the analogy to Eq.(2.126), the consumed energy by each virtual simple shear mechanism is defined as

$$\Delta W^{(i)} = 2 \int_{-|\gamma_B^{(i)}|}^{|\gamma_B^{(i)}|} Q^{(i)} d\gamma^{(i)} \quad (2.133)$$

then Eq.(2.132) will be rewritten as

$$\Delta W = \sum_{i=1}^I \Delta W^{(i)} \Delta \theta \quad (2.134)$$

Thus, the energy consumed by the actual hysteresis loop is given by summing up the energy consumed by each virtual simple shear mechanism.

### (3) Hysteretic damping factor produced by the present model

It remains to identify  $\Delta W^{(i)}$  with the hysteretic damping factor  $h$  defined in Eq.(2.91) for the virtual simple shear mechanism. Since the hysteretic damping factor  $h$  defined in Eq.(2.91) is irrespective of the scaling factors for the relevant variables, the factor  $h$  is equal to the ratio of the energies  $\Delta W^{(i)}$  over  $W^{(i)}$  defined by the variables with  $\gamma^{(i)}$  and  $Q^{(i)}$ , such that

$$h \left( \left| \gamma_B^{(i)} / \gamma_v \right| \right) = (1/4\pi) (\Delta W^{(i)} / W^{(i)}) \quad (2.135)$$



in which  $W^{(i)}$  and  $\Delta W^{(i)}$  are defined in Eqs.(2.123) and (2.133). Therefore,  $\Delta W^{(i)}$  is determined from  $h$  and  $W^{(i)}$  as

$$\Delta W^{(i)} = 4\pi h \left( \left| \gamma_B^{(i)} / \gamma_v \right| \right) W^{(i)} \quad (2.136)$$

Substitution of Eq.(2.136) into Eq.(2.134) yields

$$\Delta W = 4\pi \sum_{i=1}^I h \left( \left| \gamma_B^{(i)} / \gamma_v \right| \right) W^{(i)} \Delta \theta \quad (2.137)$$

From Eqs.(2.124) and (2.137), one finally obtains the hysteretic damping factor for the actual simple shear as

$$\widetilde{H} \left( \left| \gamma_{xyB} \right| \right) = \left[ \sum_{i=1}^I W^{(i)} h \left( \left| \gamma_B^{(i)} / \gamma_v \right| \right) \right] / \left[ \sum_{i=1}^I W^{(i)} \right] \quad (2.138)$$

in which  $W^{(i)}$  and  $\gamma_B^{(i)}$  are defined by Eqs.(2.123) and (2.118).

#### (4) Physically feasible hysteretic damping factor

Whereas the hysteretic damping factor given by the present model is thus identified, the actual hysteretic damping factor observed in the laboratory is known to be fairly closely approximated by the hyperbolic relation proposed by Hardin and Drnevich (1972), such that

$$H \left( \left| \gamma_{xyB} \right| \right) = \left[ \left| \gamma_{xyB} / \gamma_m \right| / (1 + \left| \gamma_{xyB} / \gamma_m \right|) \right] H_m \quad (2.139)$$

in which  $H_m$  is the hysteretic damping factor when the shear strain amplitude is infinity and  $\gamma_m$  is reference strain defined by

$$\gamma_m = \tau_m / G_m \quad (2.140)$$

From these measurable parameters  $H_m$  and  $\gamma_m$ , the parameters  $h_v$  and  $\xi_h$  for the virtual simple shear are determined as follows. First of all, when  $|\gamma_{xyB}|$  becomes infinity, the hysteretic damping factor produced by the present model through Eq.(2.138) becomes

$$\widetilde{H}(\infty) = h_v \quad (2.141)$$

whereas the hysteretic damping factor observed in the laboratory given by Eq.(2.139) becomes

$$H(\infty) = H_m \quad (2.142)$$

In order to represent the laboratory results in Eq.(2.139) by the present model in Eq.(2.138), it is necessary to satisfy that

$$\widetilde{H}(\infty) = H(\infty) \quad (2.143)$$

Consequently, from Eqs.(2.141) and (2.142), one obtains

$$h_v = H_m \quad (2.144)$$

The parameter  $\xi_h$  similar to virtual reference strain is numerically determined so that the hysteretic damping of the model  $\widetilde{H}$  is best fitted to the physically feasible damping  $H$ .

To summarize the discussions presented in this section, the

shear mechanism is completely defined by three soil parameters: i.e. the shear modulus at small strain level, the shear strength and the hysteretic damping factor at large shear strain. Once initial values are given by Eqs.(2.65) through (2.67) with the hysteretic damping factor at large shear strain level, the soil properties  $\tau_m$ ,  $G_m$  and  $\gamma_m$  during cyclic mobility are given in accordance with the current effective mean stress. How they should be given will be discussed in the next section.

## 2.7 Numerical Robustness

### 2.7.1 Problems

When the transient and cyclic loading begins, the excess pore water pressure will build up and the effective mean stress will decrease, changing the values of the shear strength and the shear modulus of soil. If the current values of the shear strength and the shear modulus are determined from the initial values by

$$\tau_m = \tau_{m0}(\sigma'_m / \sigma'_{m0}) \quad (2.145)$$

$$G_m = G_{m0}(\sigma'_m / \sigma'_{m0})^{0.5} \quad (2.146)$$

then they are consistent with the manner in which the initial values depend on the initial effective mean stress in Eqs.(2.65) and (2.67). The reference strain is defined by

$$\gamma_m = \tau_m / G_m \quad (2.147)$$

so that the reference strain corresponding to the formulation in Eqs.(2.145) and (2.146) is given by

$$\gamma_m = \gamma_{m0} (\sigma'_m / \sigma'_{m0})^{0.5} \quad (2.148)$$

The above formulation, though consistent with the Mohr-Coulomb's failure criterion, poses two problems.

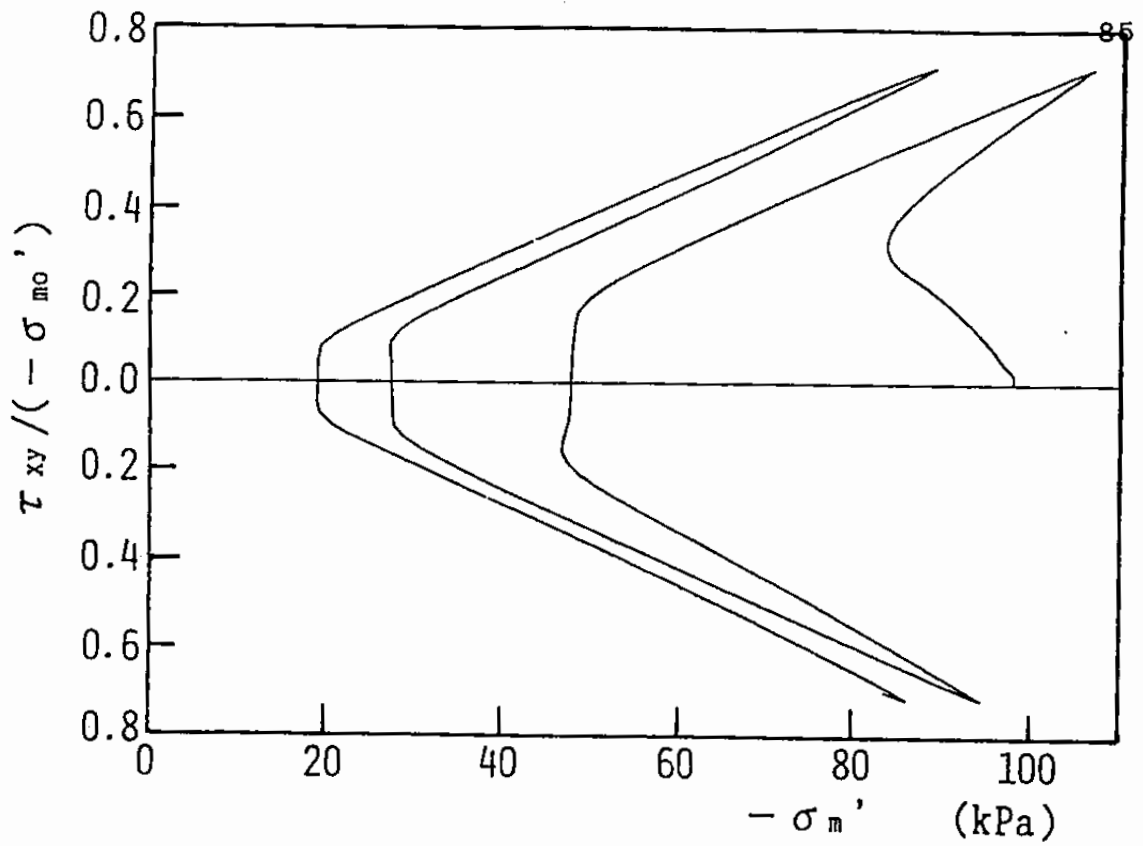
The first problem is the difficulty in the numerical analysis when the effective stress path during cyclic mobility becomes very close to the failure line. Whereas, in the static analysis, a computational artifice, such as introduction of virtual visco-plastic term (Zienkiewicz and Corneau, 1984), is available to overcome this problem, this is not the case in the dynamic analysis. A very small error contained in the computed effective stress causes a very large error in the computed strains, sometimes causing divergence in the solution process. This problem, common to most of the existing models, has been indeed the main obstacle to the two dimensional application of effective stress models in practice.

In practice, as mentioned in the previous chapter, meaningful prediction of induced deformation due to the cyclic mobility involves the shear strain ranging from about one to ten percent, from which cracks, settlement and other deformation of major consequence initiate. Such a large shear strain, as shown in Figs. 1.1 and 1.2, is generated only when the effective stress path becomes very close to the failure line. Whereas, in the vicinity of the failure line, the effective stress path apparently converges on a certain limiting stress path, the

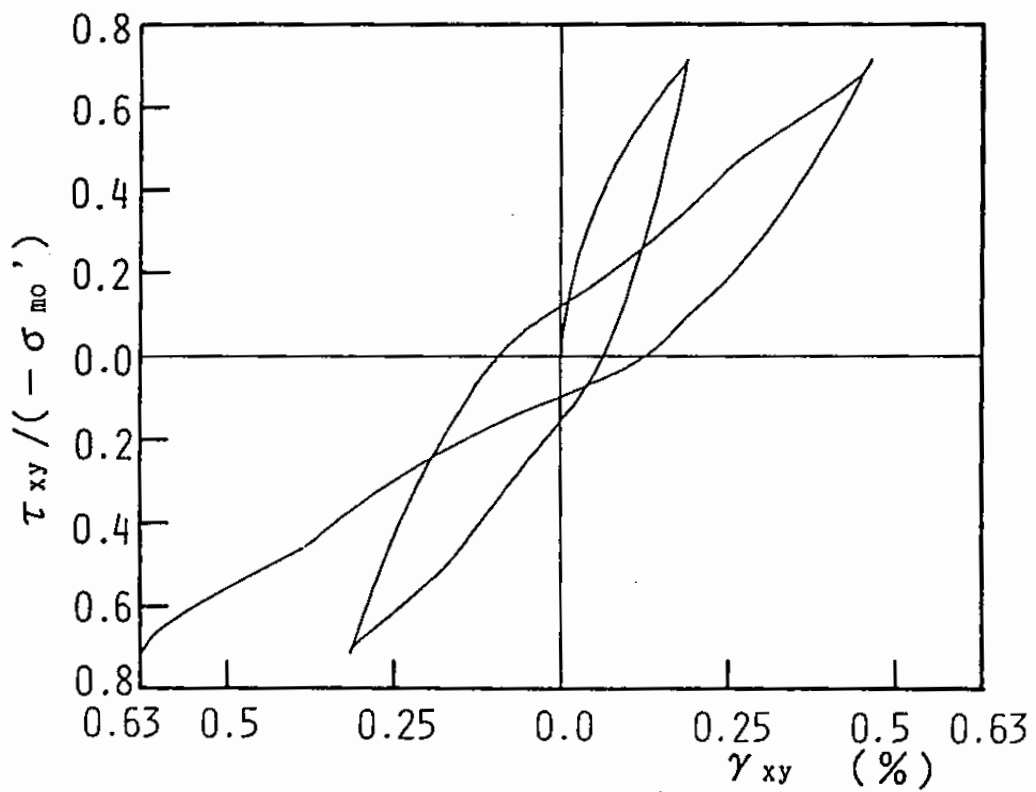
stress-strain curve does not converge on a closed hysteresis loop; the shear strain rapidly increases in loose sand as shown in Fig. 1.1 or gradually and continually increases in dense sand as shown in Fig. 1.2. As seen in the previous chapter, some of the existing models, which are successful in simulating the cyclic mobility in the numerically robust manner, do not seem to be very successful in simulating such increase in the shear strain; the stress-strain curve simulated by those models gradually converges on the limiting closed hysteresis loop at the shear strain level ranging from about one to ten percent.

The second problem arising from the formulation by Eqs.(2.145), (2.146) and (2.148) relates to the shape of the hysteresis loop for cyclic loading. The hysteresis loop simulated with this formulation is more of a convex nature even when the stress path is in dilative zone, as shown in Fig. 2.9, than that observed in the laboratory shown in Fig. 1.2. Two effects contribute to the stiffness of soil; as shown in Eqs.(2.78), (2.97) and (2.103), one being  $Q_v/\gamma_v$ , the other the function of  $\gamma^{(i)}/\gamma_v$ . Increasing  $(-\sigma'_m)$  produces increase in  $G_m$  and consequently increase in  $Q_v/\gamma_v$  by Eq.(2.108), producing a stiffening in soil. Increasing  $\gamma^{(i)}/\gamma_v$ , however, produces decrease in the stiffness, resulting in a softening in soil. Thus a mechanism is available for explaining a stiffening with increasing  $(-\sigma'_m)$  but its effect is too mild, resulting in the unusual hysteresis loop.

A scheme is necessary which (1) is numerically robust, (2) simulates the rapid or gradual increase in the shear strain ranging from about one to ten percent while the stress path gradually converges and (3) produces physically feasible shape



(a) Stress path



(b) Stress strain curve

Fig. 2.9 An example of problem in shape of hysteresis loop computed by the conventional scheme

in the hysteresis loop.

### 2.7.2 A Simple Scheme

A simple scheme for enhancing the numerical robustness is to introduce an additional strength  $\Delta\tau_m$  in the shear strength. Such a computational artifice is necessary only when the effective stress becomes close to the failure line. As a measure of the "distance" between the failure line and the current effective stress path, the liquefaction front parameter  $S_0$  in Eq.(2.68) is conveniently used. It is postulated that, when  $S_0 < 0.4$ , the additional strength is gradually increased in accordance with decrease in  $S_0$  as

$$\Delta\tau_m = \Delta r_m(-\sigma_{m0}') \quad (2.149)$$

in which

$$\Delta r_m = (m_1 - m_2)(0.4 - S_0) \quad (2.150)$$

In the above equation, the term  $(0.4 - S_0)$  represents the gradual increase and the difference between inclinations of the failure line and the phase transformation line  $m_1$  and  $m_2$  is conveniently chosen as magnitude of the additional shear strength.

Obviously the introduction of the additional shear strength produces an adverse effect on the shear strain amplitude; the shear strain of the order of few percent will never be achieved or if achieved will result in the closed hysteresis loop. For simulating the rapid or gradual increase in the shear strain

ranging from about one to ten percent, another scheme is necessary to overcome the undesirable effect.

Let us go back to examine the laboratory data shown in Figs. 1.1 and 1.2. If a closer look is directed to these data, it would be possible to recognize that the rapid or gradual increase in the shear strain amplitude, greater than about one percent, can be approximately simulated by rapidly or gradually enlarging the scale of shear strain axis. Such a scheme as enlarging the scale of shear strain is achieved by recognizing in Eqs.(2.77), (2.96) and (2.102) that the scale of shear strain is governed by the factor  $\gamma_v$ , which is proportional to the reference strain  $\gamma_m$  as understood from Eqs.(2.114) and (2.147). Thus, if the reference strain is gradually enlarged, the shear strain will be proportionally enlarged under the same cyclic loading. Because the change in the value of  $S_0$  becomes very small when  $S_0$  approaches zero, the reference strain should be very sensitive to the change in  $S_0$ . From this reasoning, it is postulated that when  $S_0 < 0.4$  the reference strain is inversely proportional to  $(S_0/0.4)$ , such that

$$\gamma_m \propto 1/(S_0/0.4) \quad (2.151)$$

For producing physically feasible shape in the hysteresis loop, it was pointed out earlier that the mechanism for a stiffening with increasing  $(-\sigma'_m)$  offers only too mild an effect; the shear modulus  $G_m$  should be more sensitive to the change in  $(-\sigma'_m)$ . From this reasoning, it is postulated that the current value of the shear modulus during cyclic mobility is proportional



to  $(\sigma_m'/\sigma_{m0}')$ , such that

$$G_m \propto (\sigma_m'/\sigma_{m0}') \quad (2.152)$$

From the conditions given by Eqs.(2.149) through (2.152), the formulation on behalf of Eqs.(2.145), (2.146) and (2.148) will be obtained as a simple scheme for the numerically robust simulation of the cyclic mobility. To begin with, when  $S_0 > 0.4$ , no correction is applied for the shear strength so that the shear strength is given by Eq.(2.145), such that

$$\tau_m = \tau_{m0}(\sigma_m'/\sigma_{m0}') \quad (\text{if } S_0 > 0.4) \quad (2.153)$$

From the condition in Eq.(2.152), the shear modulus during cyclic mobility is given by

$$G_m = G_{m0}(\sigma_m'/\sigma_{m0}') \quad (\text{if } S_0 > 0.4) \quad (2.154)$$

Thus, the reference strain is given by

$$\gamma_m = \gamma_{m0} \quad (\text{if } S_0 > 0.4) \quad (2.155)$$

When  $S_0 < 0.4$ , the factor  $\Delta\tau_m$  defined in Eqs.(2.149) and (2.150) should be added to the shear strength, such that

$$\tau_m = \tau_{m0}(\sigma_m'/\sigma_{m0}') + \Delta\tau_m \quad (\text{if } S_0 < 0.4) \quad (2.156)$$

From the condition in Eq.(2.151) and the relation in Eq.(2.155),

the reference strain is given by

$$\gamma_m = \gamma_{m0}/(S_0/0.4) \quad (\text{if } S_0 < 0.4) \quad (2.157)$$

Therefore, the shear modulus during cyclic mobility is given by

$$G_m = \tau_m/\gamma_m \quad (\text{if } S_0 < 0.4) \quad (2.158)$$

In theory when the liquefaction parameter  $S_0$  reaches the limiting value of  $S_1$  in Eq.(2.68), the hysteresis loop becomes a closed loop. Such limit, in practice, can be chosen so as to produce a shear strain amplitude of more than a hundred percent as the limiting case; then the existence of the limit does not cause a problem in practice. It is further to be noted that in the present scheme the liquefaction front parameter  $S_0$  serving as a scaling factor for the shear strain amplitude is determined by a function of cumulative plastic shear work so that the computed shear strain is insensitive against sporadically arising, if any, errors during the computation process.

The present scheme is further simplified under the undrained condition. Under the undrained condition, the state variable  $S$  in Eq.(2.59) is approximately equal to  $(\sigma'_m/\sigma'_{m0})$ . If it is realized that, after all, the relations in Eqs.(2.153) through (2.158) are a computational artifice which approximates the relations in reality, it can be justified to use further approximation that  $S$  is used on behalf of  $(\sigma'_m/\sigma'_{m0})$  in Eqs.(153) through (158). The use of the state variable  $S$  further enhances the efficiency and the stability of the numerical solution

because  $S$  is directly determined from the accumulated plastic shear work and the shear stress ratio. Such an efficient scheme is given by the following equations : when  $S_0 > 0.4$ , it is given by

$$\tau_m = \tau_{m0} S \quad (2.159)$$

$$G_m = \tau_m / \gamma_{m0} \quad (2.160)$$

$$\gamma_m = \gamma_{m0} \quad (2.161)$$

and, when  $S_0 < 0.4$ , it is given by

$$\tau_m = \tau_{m0} S + \Delta\tau_m \quad (2.162)$$

$$G_m = \tau_m / \gamma_m \quad (2.163)$$

$$\gamma_m = \gamma_{m0} / (S_0 / 0.4) \quad (2.164)$$

in which  $\Delta\tau_m$  is defined in Eqs.(2.149) and (2.150).

It is to be noted that the scheme for enlarging the scale of shear strain is applicable only for the process in which  $S_0$  monotonically decreases such as the undrained or partially but mildly drained condition. For the process in which  $S_0$  involves increasing as well as decreasing processes, it would be necessary to introduce an additional scheme for appropriately memorizing the effect of the previous history of  $S_0$ . To develop such a scheme is beyond the scope of the present study.

## 2.8 Summary

An attempt is made for modeling cyclic mobility of saturated cohesionless soil. The proposed concept is of a generalized

plasticity type defined in the strain space. The concept of multiple mechanism is used as a vehicle for decomposing the complex mechanism into a set of simple mechanisms defined in one dimensional space.

Incremental as well as integrated constitutive relations are obtained. In particular, the tangent stiffness matrix in the incremental relation becomes symmetric, ensuring the efficiency in the numerical analysis, whereas the integrated constitutive relation serves as a guide, ensuring the convergence on the physically feasible stress strain relation.

Each virtual simple shear mechanism is assumed to follow a hyperbolic relation in the virtual stress and strain space. The hysteresis is given by Masing's rule with a modification. In order to represent the appropriate hysteresis damping factor observed in the laboratory test during drained cyclic loading, such a conventional tool as Masing's rule is not applicable in the large shear strain level. In the present study, this problem is overcome by introducing appropriate scaling factors for the virtual simple shear stress and strain.

Difficulty is known to exist in the numerical analysis of the cyclic mobility when the effective stress path becomes very close to the failure line. In order to overcome such difficulty, a simple scheme is proposed; modeling of cyclic mobility, not as a yielding process, but as a process in which the scale of the shear strain is gradually enlarged as the effective stress path approaches failure line.

To define the "distance" to the failure line, the concept of liquefaction front is introduced in the effective stress

space. The liquefaction front, originating from the envelope of initial effective stress points, gradually approaches the failure line as the cyclic mobility proceeds. The liquefaction front is used to define the volumetric strain of plastic nature as well as to define the scale for enlarging shear strain.

The soil parameters of the present model are summarized in Table 2.2. Number of the parameters for the proposed model is ten if two obvious parameters, i.e. porosity of soil skeleton and bulk modulus of pore water, are omitted in counting number of the parameters. In particular, two parameters, i.e. the shear and the rebound moduli, specify the elastic behavior of soil. The rest of eight specify the plastic behavior; two parameters, i.e. the effective shear resistance angle and the hysteretic damping factor at large shear strain level, specify shear behavior of soil, the others, i.e. the phase transformation angle and the five parameters, specify the dilatancy of soil.

## References

- (1) Dobry, R., Ladd, R.S., Yokel, F.Y., Chung, R.M. and Powell, D. (1982) : "Prediction of pore water pressure buildup and liquefaction of sands during earthquakes by the cyclic strain method," NBS Building Science Series 138, National Bureau of Standards, U.S. Department of Commerce, 150p.
- (2) Finn, W.D.L., Lee, K.W. and Martin, G.R. (1977) : "An effective stress model for liquefaction," Journal of the Geotechnical Engineering Division, ASCE, Vol.103, No.GT6,

Table 2.2 Parameters for the present model

Parameters	Type of Mechanism		Typical Name
$K_a$	Elastic	Volumetric	Rebound modulus
$G_{ma}$	Elastic	Shear	Shear modulus
$p_1$	Plastic	Dilatancy	Empirical parameter
$p_2$	Plastic	Dilatancy	Empirical parameter
$w_1$	Plastic	Dilatancy	Empirical parameter
$s_1$	Plastic	Dilatancy	Empirical parameter
$c_1$	Plastic	Dilatancy	Empirical parameter
$\phi_f'$	Plastic	Shear	Shear resistance angle
$\phi_p'$	Plastic	Dilatancy	Phase Transformation angle
$H_m$	Plastic	Shear	Hysteretic damping factor at large shear strain level
$n$			porosity
$K_f$			compressibility coefficient of water

pp.517-533

- (3) Hardin, B.O. and Drnevich, V.P. (1972) : "Shear modulus and damping of soils : design equation and curves," Journal of Soil Mechanics and Foundation Division, ASCE, Vol.98, No.SM7, pp.667-692
- (4) Ishihara, K. (1982) : "Evaluation of soil properties for use in earthquake response analysis," Proceedings of International Symposium on Numerical Models in Geomechanics, Zurich, pp.237-259
- (5) Ishihara, K., Tatsuoka, F. and Yasuda, S. (1975) : "Undrained deformation and liquefaction of sand under cyclic stresses," Soils and Foundations, Vol.15, No.1, pp.29-44
- (6) Ishihara, K. and Towhata, I. (1982) : "Dynamic response analysis of level ground based on the effective stress method," in Pande, G.N. and Zienkiewicz, O.C. (eds), Soil Mechanics - Transient and Cyclic Loads, John Wiley and Sons, pp.133-172
- (7) Ishihara, K., Yoshida, N. and Tsujino, S. (1985) : "Modelling of stress-strain relations of soils in cyclic loading," Proceedings of 5th Conference on Numerical Methods in Geomechanics, Nagoya, Vol.1, pp.373-380
- (8) Mroz, Z. and Norris, V.A. (1982) : "Elastoplastic and viscoplastic constitutive models for soils," in Pande, G.N. and Zienkiewicz, O.C. (eds). Soil Mechanics - Transient and Cyclic Loads, Chapter 8, John Wiley and Sons, pp.173 - 217
- (9) Pender, M.J. (1980) : "Cyclic mobility - a critical state model," Proceedings of International Symposium on Soils

under Cyclic and Transient Loading, Swansea, Vol.1, pp.325-333

- (10) Rowe, P.W. (1969) : "The stress dilatancy relation for static equilibrium of an assembly of particles in contact," Proc. Roy. Soc., London, Series A, Vol.269, pp.500-527
- (11) Towhata, I. and Ishihara, K. (1985a) : "Modelling soil behaviour under principal stress axes rotation," Proceedings of 5th International Conference on Numerical Methods in Geomechanics, Nagoya, Vol.1, pp.523-530
- (12) Towhata, I. and Ishihara, K. (1985b) : "Shear work and pore water pressure in undrained shear," Soils and Foundations, Vol.25, No.3, pp.73-84
- (13) Yamazaki, F., Towhata, I. and Ishihara, K. (1985) : "Numerical model for liquefaction problem under multi-directional shearing on horizontal plane," Proceedings of 5th International Conference on Numerical Methods in Geomechanics, Nagoya, Vol.1, pp.399-406
- (14) Zienkiewicz, O.C., Chang, C.T. and Hinton, E. (1978) : "Non-linear seismic response and liquefaction," International Journal for Numerical and Analytical Methods in Geomechanics, Vol.2, pp.381-404
- (15) Zienkiewicz, O.C. and Corneau, I.C. (1984) : "Viscoplasticity - plasticity and creep in elastic solids - a unified numerical solution approach," International Journal for Numerical Methods in Engineering, Vol.8, pp.821-845



## CHAPTER 3

### ANALYSIS WITH SINGLE SOIL ELEMENT

#### 3.1 Procedure for Numerical Analysis

The model presented in the previous chapter is coded into a finite element computer program and is used for examining overall performance of the present approach. The most basic performance of the present approach is examined in this chapter by using a single soil element. In the analysis, the basic equations for a porous saturated material are used with the undrained condition (Zienkiewicz and Bettess, 1982).

Basic steps in the computation are (1) to compute the displacement increment from the nodal force increment by using the incremental relation in Eq.(2.38) and (2) to compute the nodal force from the computed displacement by using the integrated relation in Eq.(2.55). Convergence to the stress strain relation given by Eq.(2.55) is ensured by use of correction force as well as iteration. The scheme in Eqs.(2.159) through (2.164) is used for ensuring the numerical robustness. All the results to be presented in this study are computed as a solution of a stress controlled boundary value problem by using one element. Thus, the numerical robustness of the model is more critically examined in the present study than in the commonly adopted practice of strain controlled computation.

### 3.2 Procedure for Parameter Identification

When the analysis is conducted with the present model, ten parameters should be specified, as mentioned in the previous chapter, in addition to the two obvious parameters of bulk modulus of pore water  $K_f$  and porosity of soil skeleton  $n$ . In particular, the shear mechanism is shown to be completely specified by three soil parameters; shear modulus  $G_{sa}$  in Eq.(2.67), effective shear resistance angle  $\phi_f'$  in Eq.(2.65), and hysteretic damping factor at large shear strain level  $H_m$  in Eq.(2.139). In addition to these parameters, there are five parameters defining the mechanism of dilatancy; i.e.  $S_1$ ,  $w_1$ ,  $p_1$ ,  $p_2$  and  $c_1$  appearing in Eqs.(2.68) and (2.72). Though there are two more parameters such as phase transformation angle  $\phi_p'$  appearing in Eqs.(2.59) through (2.62) and bulk moduli of soil skeleton  $K_a$  in Eqs.(2.27) and (2.46), they are so well defined that no more explanation would be necessary. Given the soil parameters for shear mechanism  $G_{sa}$ ,  $\phi_f'$ ,  $H_m$  as well as the well defined parameters  $\phi_p'$ ,  $K_a$ ,  $K_f$ , and  $n$ , the five parameters  $S_1$ ,  $w_1$ ,  $p_1$ ,  $p_2$ , and  $c_1$  for defining the cumulative volumetric strain of plastic nature are determined from undrained cyclic loading test results as follows.

- 1) First of all, the test data, commonly available in the practice of soil dynamics, should be provided for representing (i) a liquefaction resistance curve (i.e. the cyclic shear stress ratio vs. the number of the cyclic loading  $N_1$  required to cause shear strain of 5 percent in

double amplitude), (ii) an envelope of an excess pore water pressure generation curve such as shown in Fig. 3.1 by a broken line and (iii) an envelope of shear strain amplitude such as shown in Fig. 3.2 by broken lines.

- 2) The parameter  $S_1$  takes small positive value of about 0.005 so that  $S_0$  will never be zero. In such a special case as the stress strain curve should become a closed loop during the cyclic mobility,  $S_1$  can take a larger value and can be determined in a try and error manner.
- 3) The parameter  $c_1$  for specifying the threshold level is temporarily fixed to 1.0 as the first guess. The value of  $c_1$  will later be modified in a try and error manner. The modification in the value of  $c_1$ , however, does not have a great influence upon the cyclic mobility when the shear stress ratio is much higher than the threshold level. Therefore, with  $c_1 = 1.0$ , the rest of the parameters  $w_1$ ,  $p_1$  and  $p_2$  are determined by the following steps from the test results with a relatively large shear stress ratio.
- 4) The parameters  $w_1$  and  $p_1$  are determined in a try and error manner from the excess pore water pressure generation curve. In particular, the portion of the curve for  $p/(-\sigma'_{m0}) < 0.6$  is used, in which  $p$  denotes excess pore water pressure. Because  $w_1$  is not significantly influenced by variation in  $p_1$ , the parameter  $w_1$  is at first determined with an appropriate guess of  $p_1$ . The value of  $p_1$  ranges from about 0.4 to 0.7. With the determined value of  $w_1$ , the value of  $p_1$  is determined. In general the greater  $w_1$  is, and the greater  $p_1$  is, the more slowly the pore water pressure rises

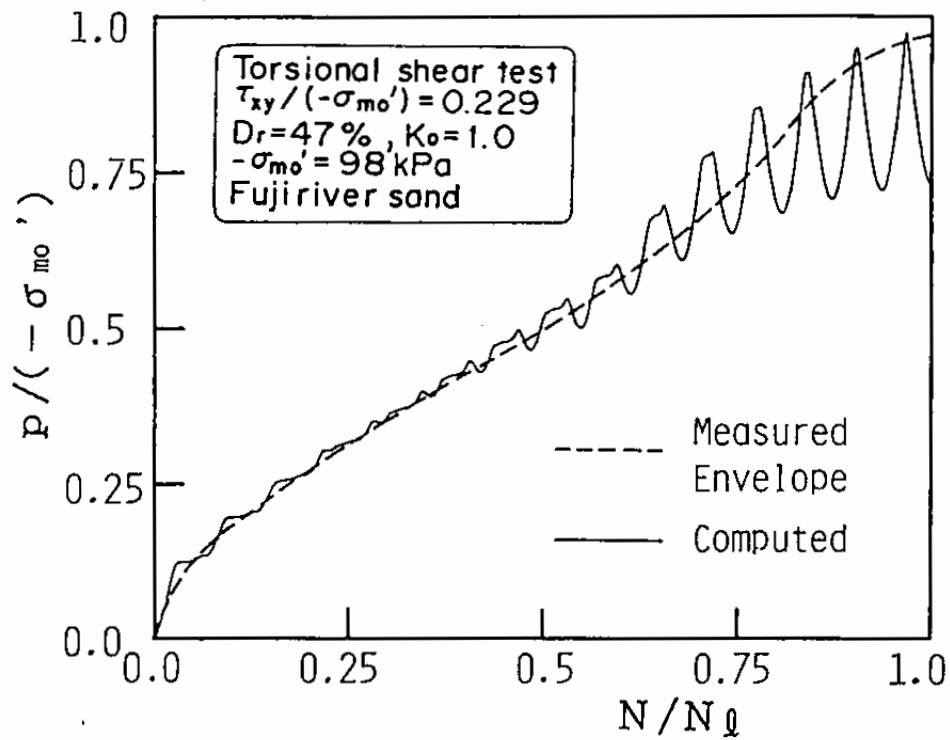


Fig. 3.1 Excess pore water pressure generation curve in cyclic torsion shear test for loose sand

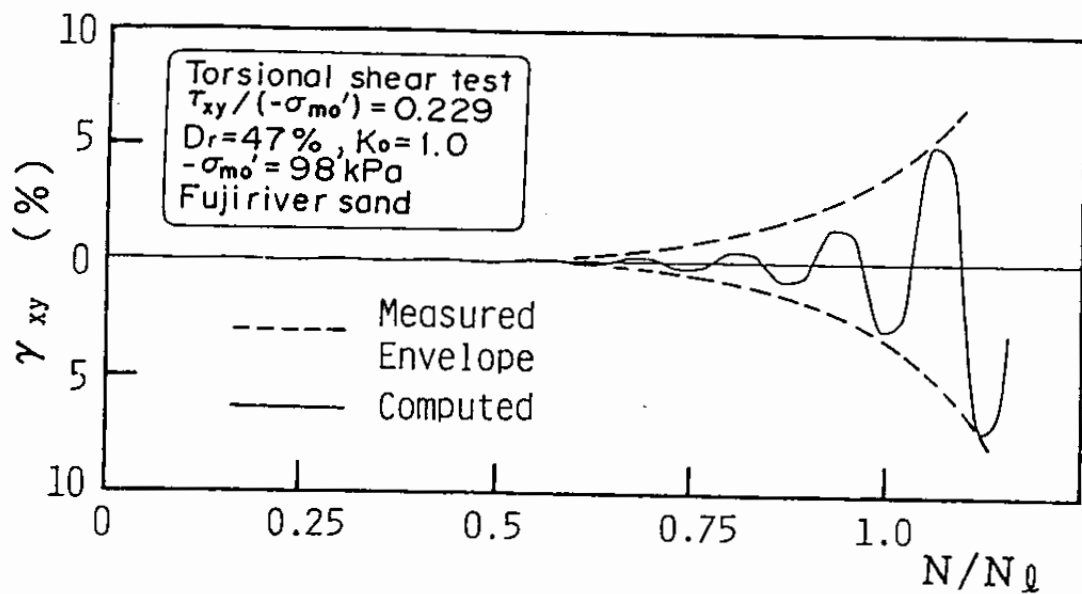


Fig. 3.2 Shear strain amplitude in torsion shear test for loose sand

as indicated in the previous chapter in Fig. 2.5.

- 5) Though the parameter  $p_2$  could also be determined from the pore water pressure generation curve for  $p/(-\sigma_{m0}') > 0.6$ , it is better to determine the parameter  $p_2$  from the envelope of strain amplitude if the primary purpose of the cyclic mobility analysis is to estimate the amount of deformation in soil structures and foundations. The value of  $p_2$  ranges from about 0.6 to 1.5; the greater  $p_2$  is, the faster the shear strain amplitude increases.
- 6) When all the parameters are determined by the steps mentioned above from the laboratory data with a relatively large shear stress ratio, the next step is to examine if these parameters are also appropriate for representing the laboratory data at a relatively small shear stress ratio. If not, then the parameter  $c_1$  is modified in a try and error manner. With increasing  $c_1$ , the higher threshold level is achieved.

### 3.3 Analysis with Initially Isotropic Consolidation Condition

Through the procedures for numerical analysis and parameter identification mentioned earlier, the model performance is examined through the analysis of soil behavior under undrained cyclic loading with the initially isotropic consolidation condition. From the excess pore water pressure generation curve and the shear strain amplitude shown in Figs. 3.1 and 3.2, which correspond to the torsion shear test results shown previously in Figs. 1.1 for Fuji River Sand at relative density of 47 %

reported by Ishihara (1985), the model parameters, shown in the left hand side of Table 3.1, are obtained by the back-fitting procedure mentioned in the previous section. With these parameters, the model gives the computed results shown by solid lines in the same figures. Reasonable adaptability to the soil behavior in the laboratory is indicated by these results.

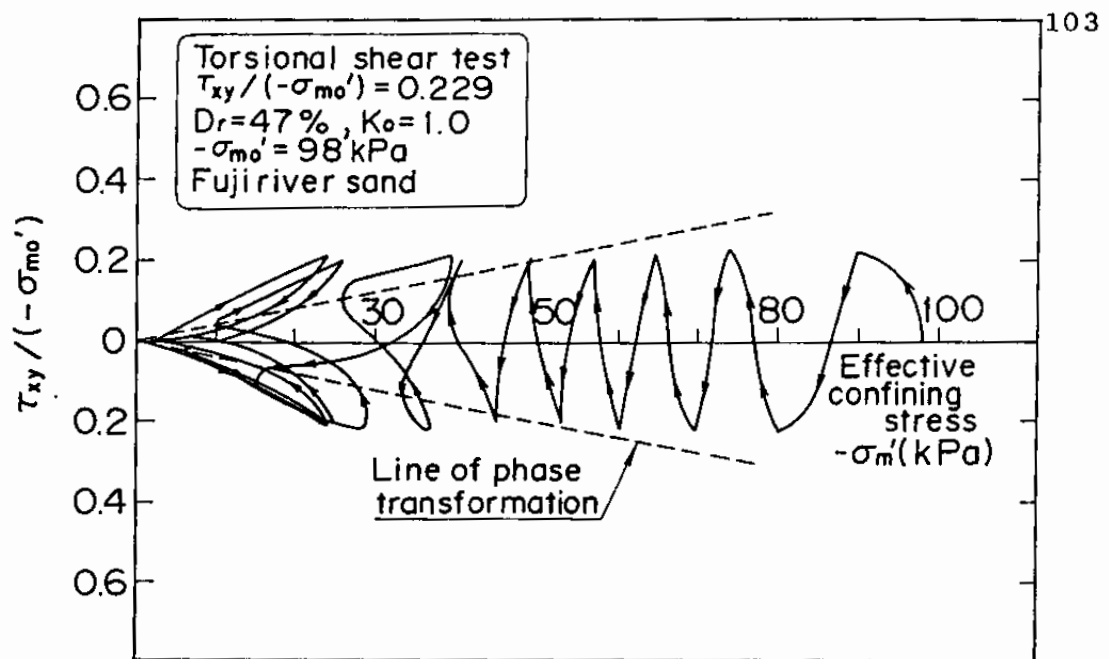
With the soil parameters for the loose sand shown in Table 3.1, the stress paths and the stress strain relations are computed as shown in Figs. 3.3 and 3.4. If a close look is directed to the shape of the computed and measured stress paths shown in Fig. 3.3, such a difference is recognized that the computed stress path does not produce hysteresis loops in the stress space whereas the measured one exhibits hysteresis loops once the stress path goes over the phase transformation line. In this respect, the present model simplifies the physically feasible stress path during the cyclic mobility. Except for this minor difference, the computed and the measured stress paths agree with each other.

Similarly, a close look directed to the stress and strain relations shown in Fig. 3.4 reveals that the initial stiffness of the computed hysteresis curve is more rigid than the measured one. This might easily be corrected by assigning a smaller value for  $G_{ma}$ : in the present computation, the estimate of  $G_{ma}$  was given by adopting a laboratory equation for Toyoura sand (Kokusho, 1980), which was not very applicable in the present case. Overall shapes of the computed and the measured stress strain curves agree with each other. In particular, the simple scheme for numerical robustness works quite well for representing the rapid

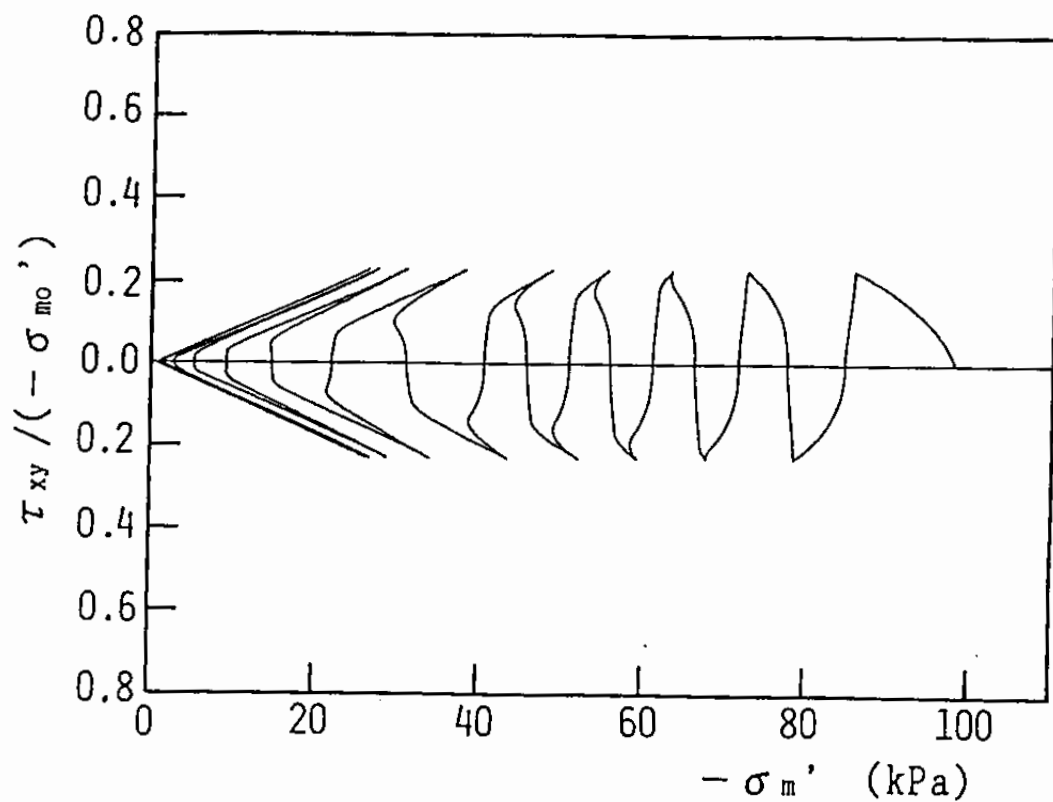
Table 3.1 Model parameters for Fuji River Sand

Parameters	Loose Fuji River Sand	Dense Fuji River Sand
	( $D_r = 47\%$ )	( $D_r = 75\%$ )
$K_a$	270500 kPa	366800 kPa
$G_{ma}$	103700 kPa	140700 kPa
$p_1$	0.45	0.40
$p_2$	1.4	0.72
$w_1$	2.0	2.85
$s_1$	0.0035	0.005
$c_1$	1.0	1.0
$\sin\phi_f'$	0.87	0.91
$\sin\phi_p'$	0.42	0.42
$H_m$	0.3	0.3
$n$	0.45	0.40
$K_f$	$2.0 \times 10^6$ kPa	$2.0 \times 10^6$ kPa

$K_a$  and  $G_{ma}$  are given for  $(-\sigma_{ma}') = 98$  kPa. The computation was done with number of the shear mechanism  $I = 12$  by 50 steps of incremental loadings for 1/4 cycle.



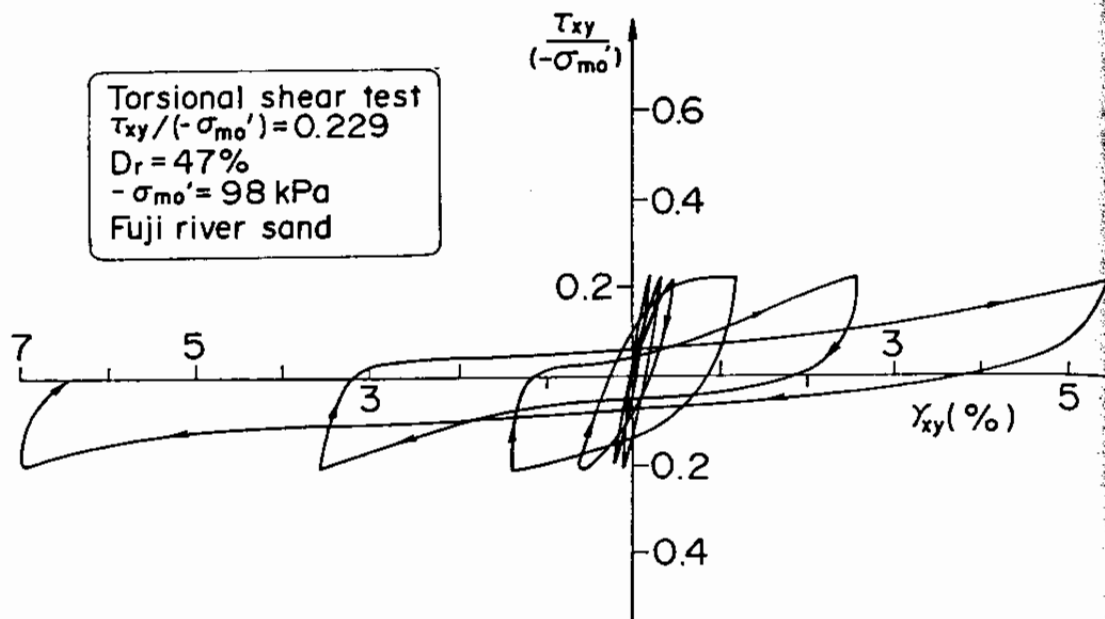
(a) Measured (after Ishihara, 1985)



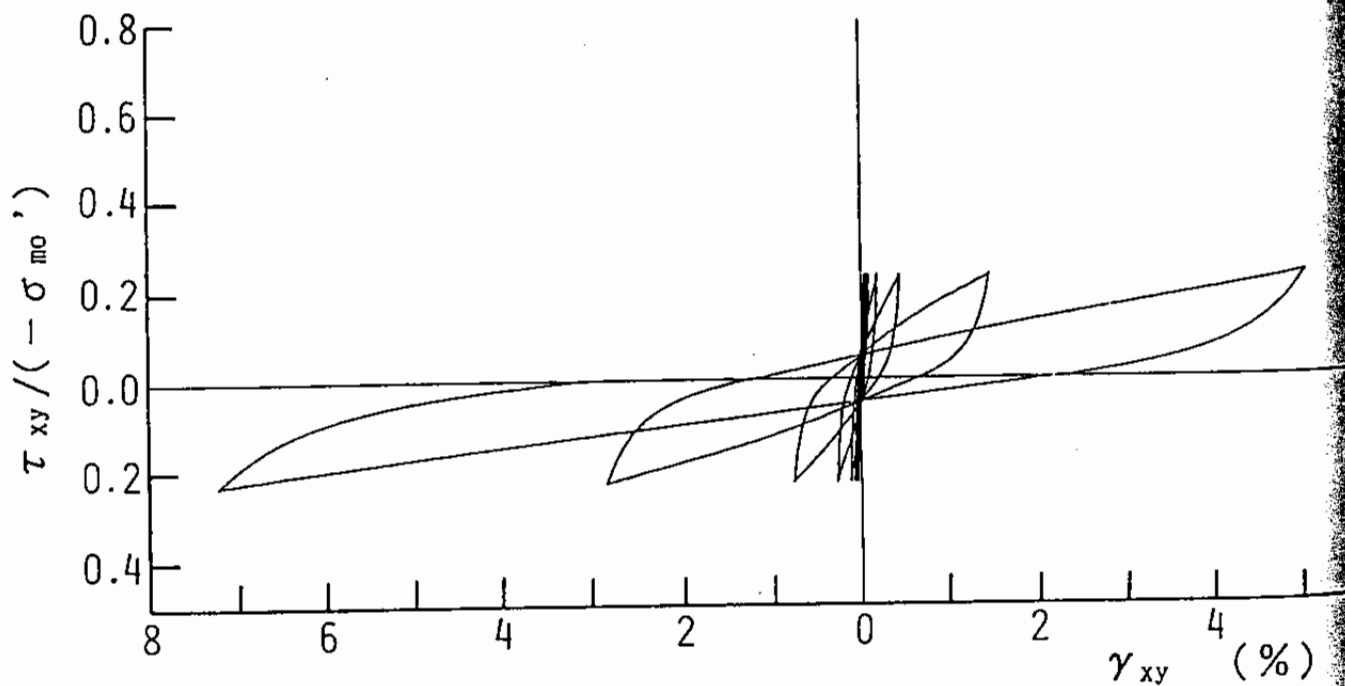
(b) Computed

Fig. 3.3 Stress path for loose sand ( $K_0 = 1.0$ )





(a) Measured (after Ishihara, 1985)



(b) Computed

Fig. 3.4 Stress strain curve for loose sand ( $K_0 = 1.0$ )

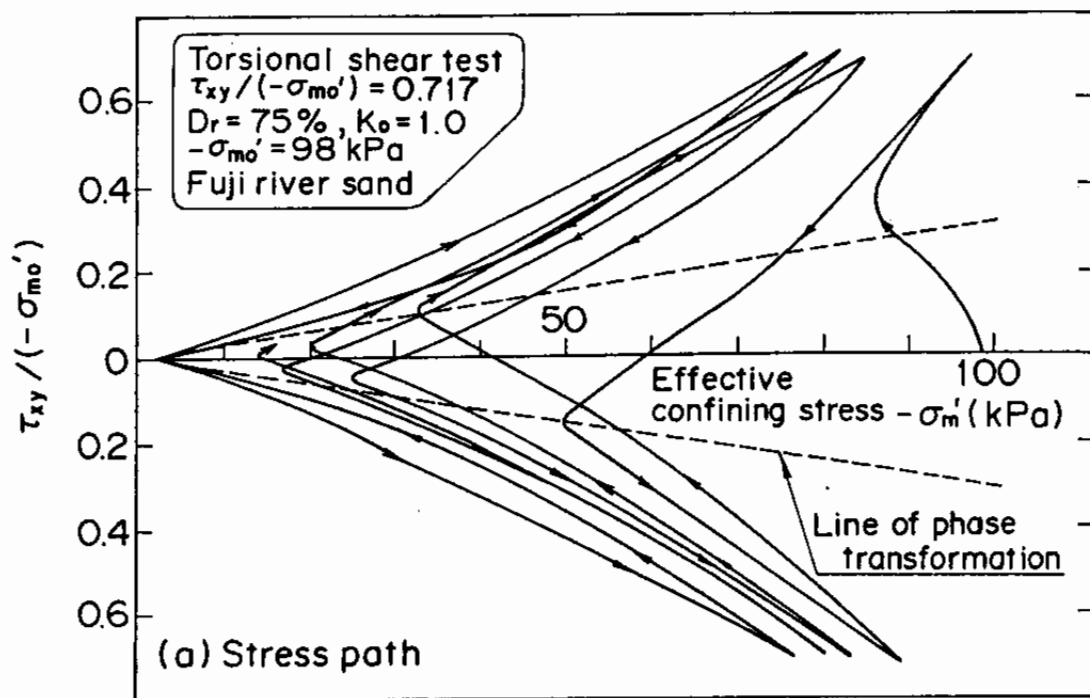
growth of shear strain at least up to the order of several percent.

Similar comparison is also made for dense sand. Parameter identification is done for Fuji River sand of the relative density of 75% shown in Fig. 1.2 in the similar manner. With the soil parameters for the dense sand in Table 3.1, the stress paths and the stress strain relations are computed as shown in Figs. 3.5 and 3.6, indicating again good agreement with the laboratory test results for the dense sand.

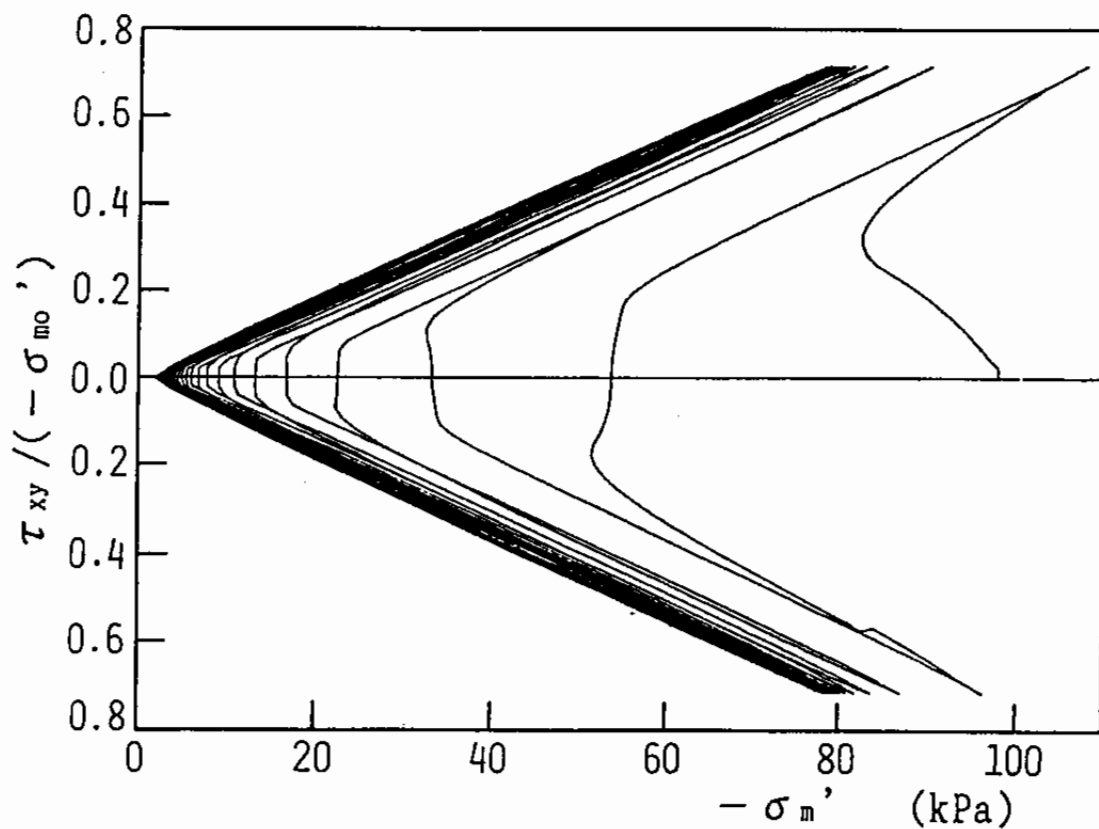
The mechanism mobilized during cyclic loading is quite simple to understand for the initially isotropically consolidated sand. The virtual simple shear mechanisms mobilized during these torsion shear test are only those indicated by the pairs of small circles drawn with solid lines in Fig. 2.1. With each cycle of torsion shear, the circle in Fig. 2.1 begins its growth from the origin toward the positive direction, then shrinks back to the origin, then begins its growth toward the negative direction, and then shrinks back again to the origin. Radius of the circle becomes larger and larger as the cyclic torsion shear goes on.

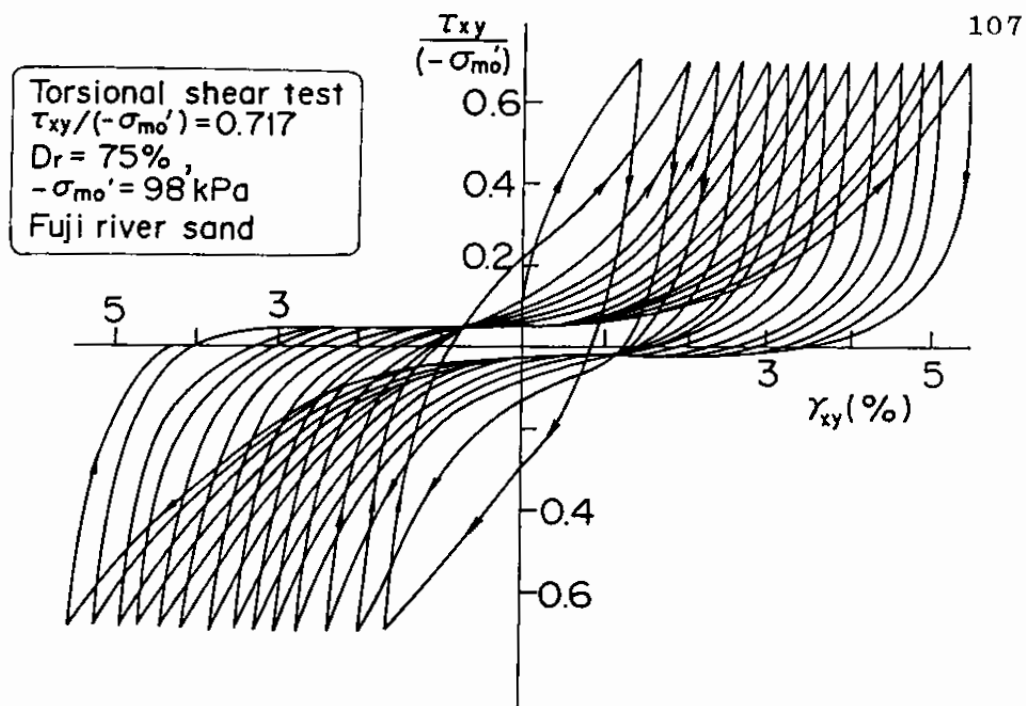
### 3.4 Analysis with Initially Anisotropic Consolidation Condition

With the appropriate applicability of the present model in the isotropic condition seen in the previous section, the next step is naturally to move on to the case with the initially anisotropic consolidation condition. The effect of initial anisotropic consolidation is examined by simulating the undrained torsion shear tests with the earth pressure coefficient at rest

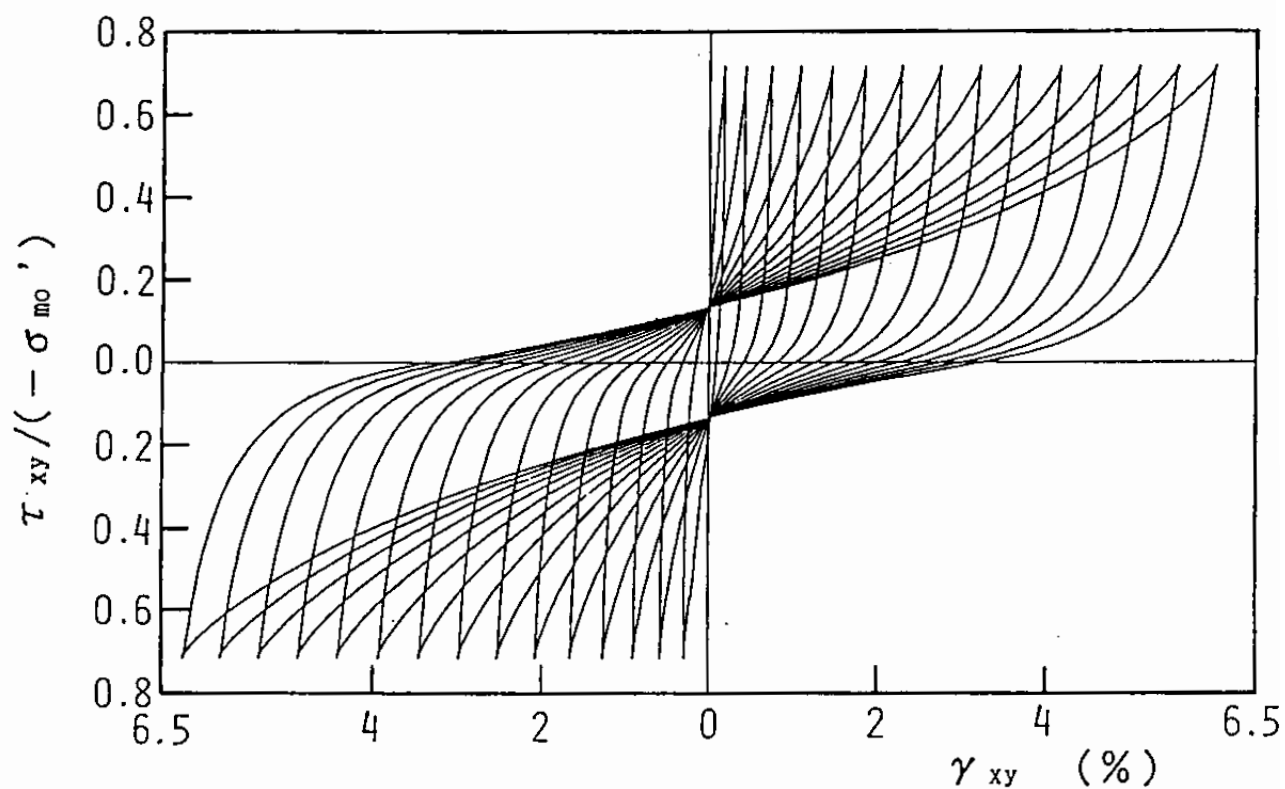


(a) Measured (after Ishihara, 1985)

Fig. 3.5 Stress path for dense sand ( $K_0 = 1.0$ )



(a) Measured (after Ishihara, 1985)



(b) Computed

Fig. 3.6 Stress strain curve for dense sand ( $K_0 = 1.0$ )

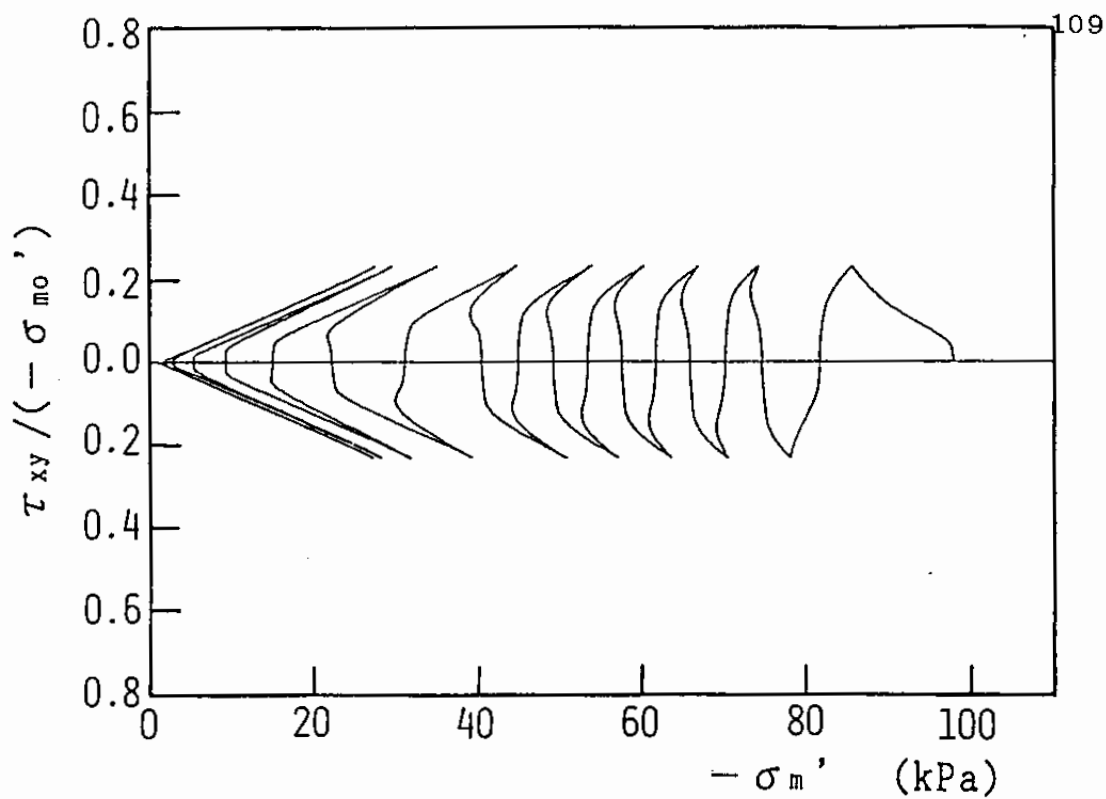
$$K_0 = 0.5.$$

#### 3.4.1 Analysis with Bulging Constrained

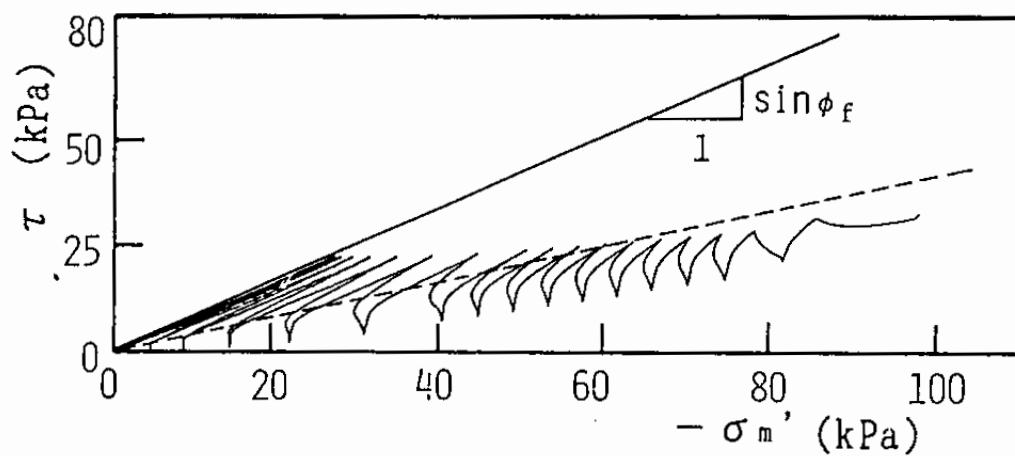
First of all, the soil behavior under the undrained cyclic loading is analyzed with keeping the bulging of soil constrained as in the level ground. The same parameters for the loose sand in Table 3.1 and the same initial confining pressure are used in the computation. The results indicate that the initial deviatoric stress due to  $K_0$  consolidation is gradually released as the cyclic loading continues as shown in Fig. 3.7.

The results also indicate, as seen through the comparison of Fig. 3.7(a) and Fig. 3.8 with Figs. 3.3 and 3.4, that the stress path and the stress strain relation in the initially anisotropically consolidated sand are quite similar to those in the initially isotropically consolidated sand. If the shear stress ratio, i.e. the ratio of the cyclic shear stress over the initial confining pressure, is plotted, as shown in Fig. 3.9, with number of the cyclic loading required to cause shear strain of 5 percent in the double amplitude, the computed result for the isotropically consolidated sand agrees with that for the  $K_0$  consolidated sand. This is consistent with the results identified through the laboratory study (Ishihara, et al, 1977) mentioned in Chapter 1.

The mechanism involved in this type of soil behavior is understood as follows. In the present approach, the effect of the anisotropic consolidation is to induce such a compression shear as those indicated by the upper half of the small circles shown by broken line in Fig. 2.1; i.e. this type of shear mainly



(a) Relation between  $\tau_{xy}/(-\sigma_{m0}')$  and  $(-\sigma_m')$



(b) Relation between  $\tau = (\sigma_1' - \sigma_3')/2$  and  $(-\sigma_m')$

Fig. 3.7 Computed stress path for loose sand (initially  $K_0 = 0.5$  with bulging constrained)

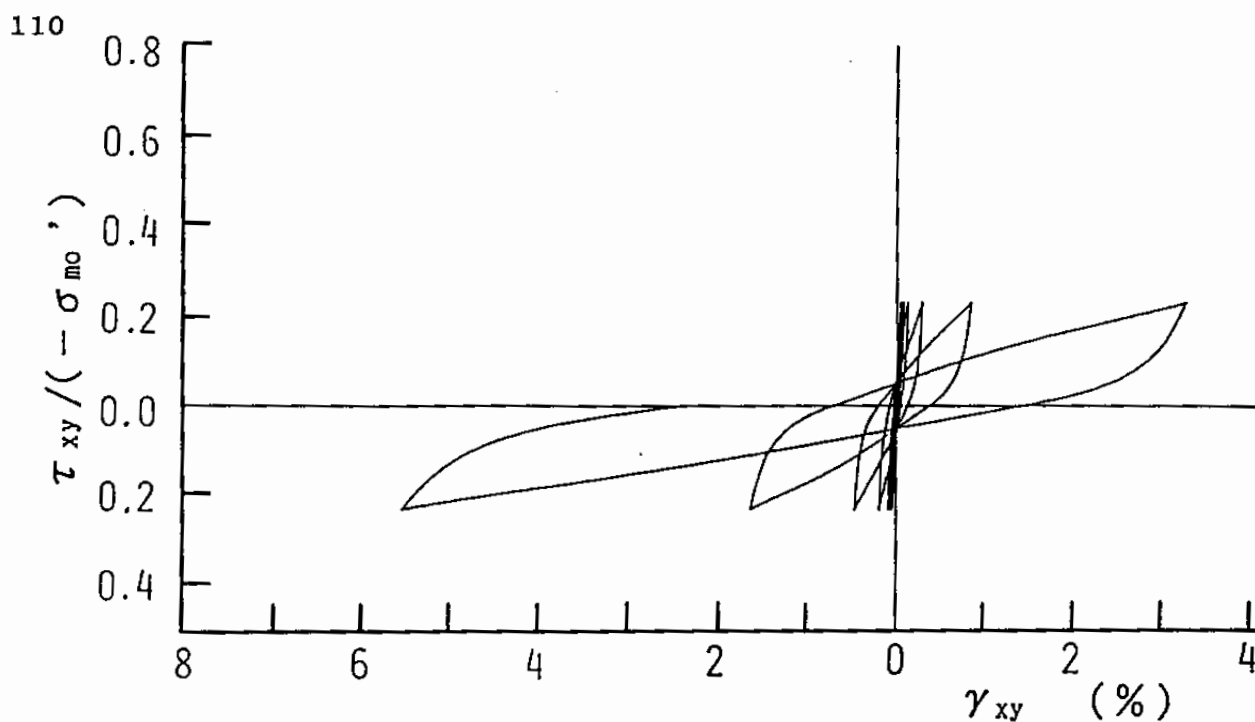


Fig. 3.8 Computed stress strain curve for loose sand (initially  $K_0 = 0.5$  with bulging constrained)

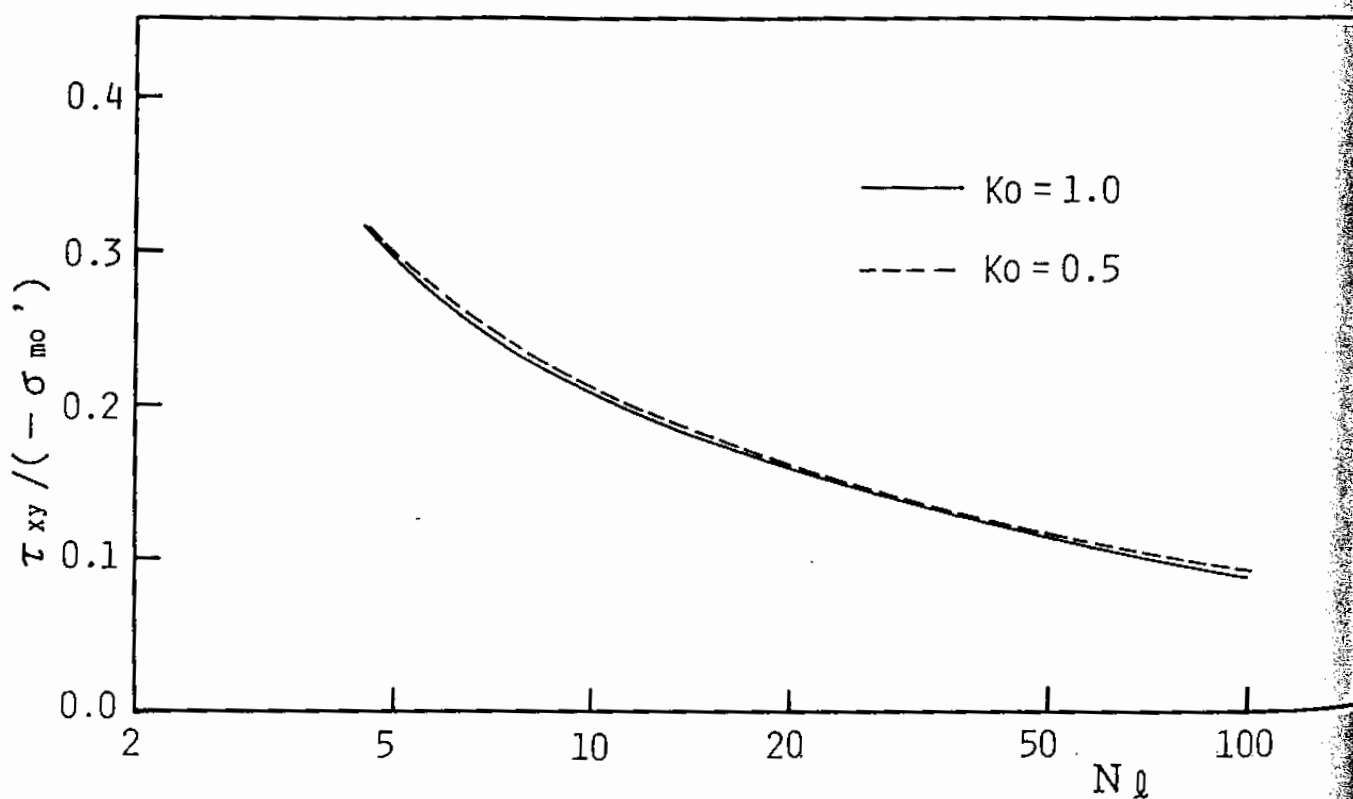


Fig. 3.9 Liquefaction resistances of isotropically ( $K_0 = 1.0$ ) and anisotropically ( $K_0 = 0.5$ ) consolidated soils

affects the virtual simple shear mechanisms oriented to or close to  $\pi/2$  direction relative to x axis. It does not significantly affect the virtual simple shear mechanisms oriented to or close to x axis. The cyclic simple shear induced after the initial anisotropic consolidation involves only of those mechanisms indicated by the solid lines in Fig. 2.1. Thus, the virtual simple shear mechanisms mobilized during the cyclic simple shear are mainly those which were unaffected by the initial anisotropic consolidation. This naturally explains that the behavior of soil under the cyclic simple shear loading is not affected by the initial anisotropic consolidation condition if the initial mean effective stress remains the same.

The commonly adopted practice in the study on the constitutive relation of soils is to interpret the above mentioned behavior of soil by separating the strain increment due to the rotation of principal stress axes from the principal strain increment due to the current principal stress. In contrast, the present approach offers, as seen above, a much more simple and clear perspective upon the mechanism of the behavior of the initially anisotropically consolidated soil.

#### 3.4.2 Analysis with Bulging Unconstrained

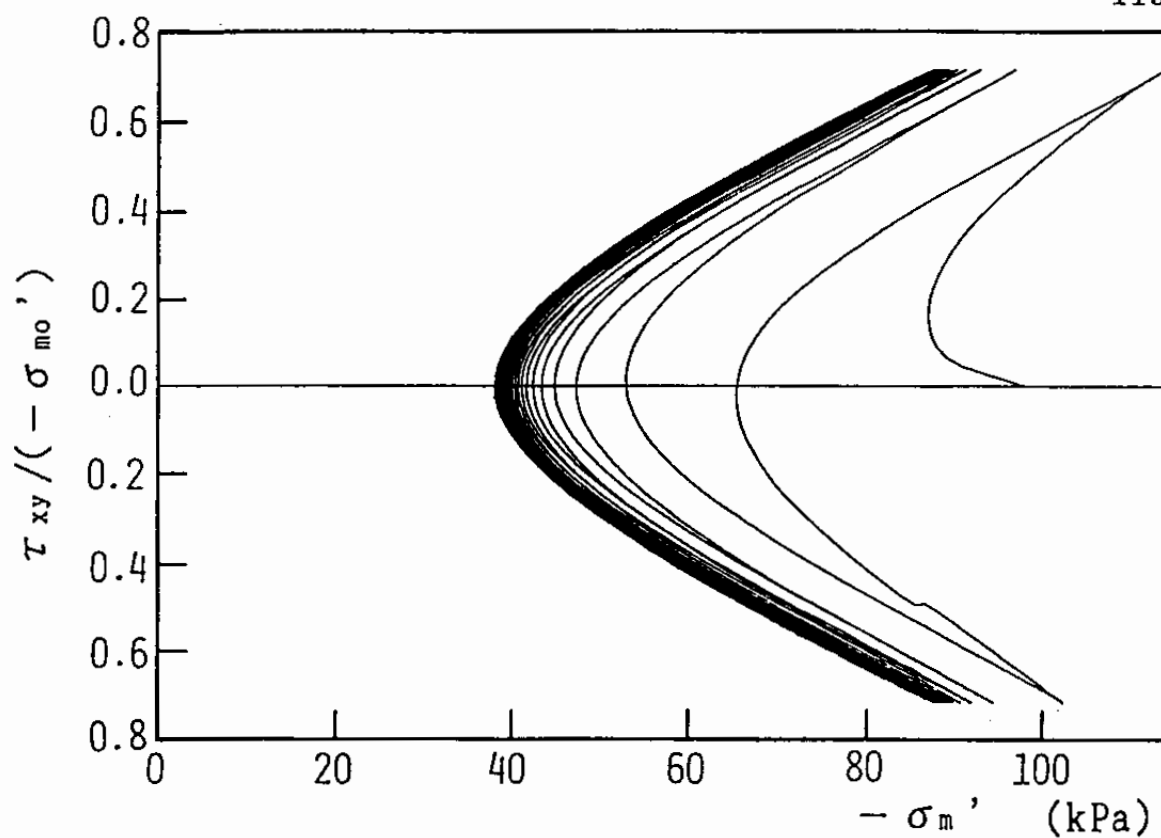
The model performance examined above is closely related to the one dimensional analysis of the cyclic mobility occurring in the level ground in which bulging of soil is constrained. When the two dimensional analysis is conducted for such soil structures as embankments, initial stress due to gravity will act as a driving force for gradual settlement and bulging. In order



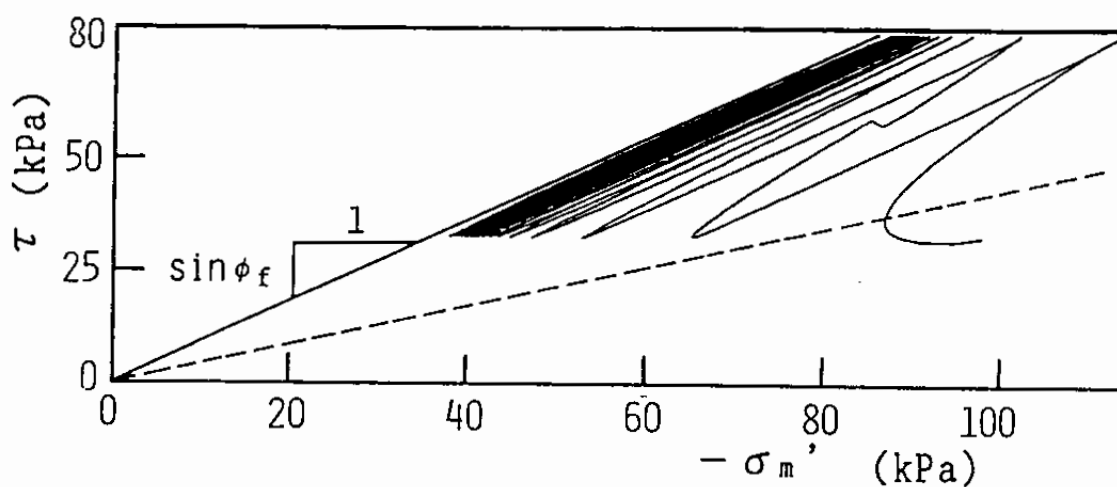
to examine the ability to simulate this type of mechanism, an undrained torsion shear test with initially anisotropically consolidated sand is analyzed with keeping the initial axial stress difference unchanged as the stress boundary condition. The same parameters for the dense sand in Table 3.1 and the same initial confining pressure and the shear stress are used in the computation. By applying such a large amplitude of the shear stress, the numerical robustness of the present approach is more critically examined.

The results, as shown in Figs. 3.10 and 3.11, indicate the limit in decreasing value of  $(-\sigma'_m)$  and the gradual settlement with bulging of soil element, i.e. cumulative increase in the axial strain difference  $\epsilon_x - \epsilon_y$ . These results are consistent with the previous laboratory study (Ishihara and Li, 1972), suggesting reasonable applicability in the two dimensional analysis.

In the present approach, the mechanism involved in this type of analysis is understood as follows. As mentioned in the previous subsection, the effect of the anisotropic consolidation is to induce such a compression shear as indicated by the upper half of the small circles shown by the broken line in Fig. 2.1. The cyclic torsion shear further mobilizes those mechanisms indicated by the solid lines in Fig. 2.1. While the mechanisms indicated by the solid lines repeat the change from the positive to the negative direction and vice versa, the mechanism indicated by the broken line grows toward the positive direction, resulting in the bulging with the settlement of the soil element.

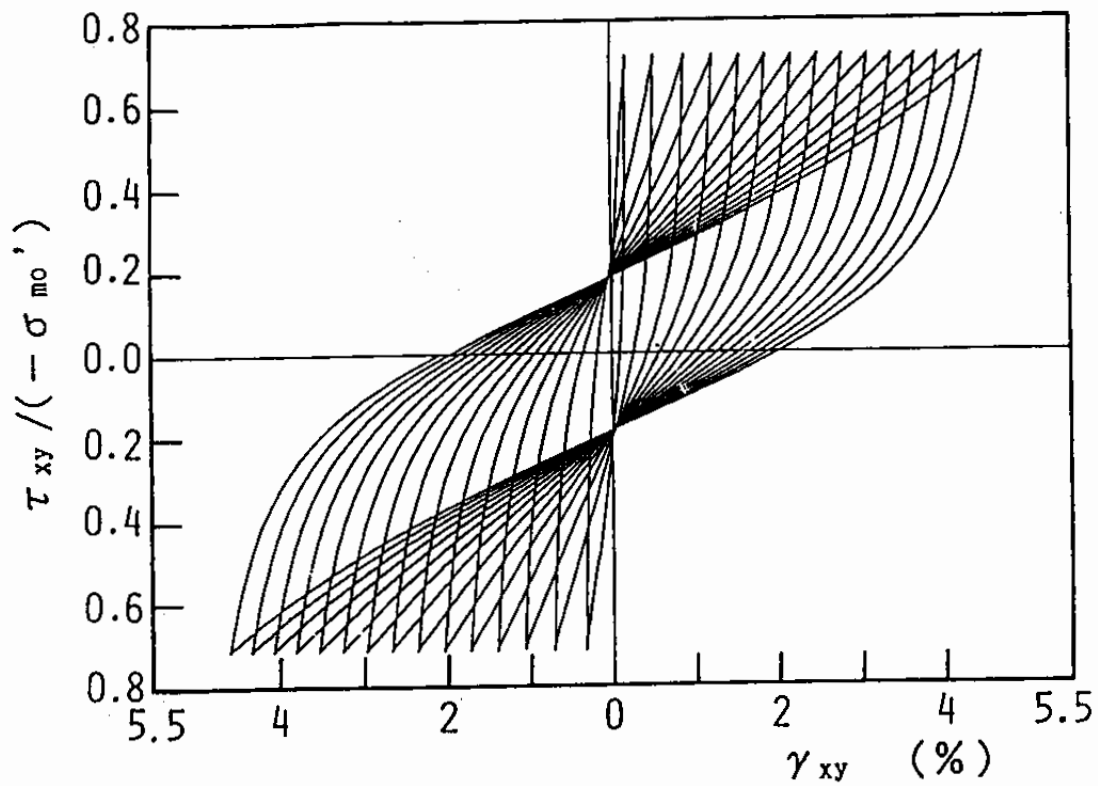


(a) Relation between  $\tau_{xy}/(-\sigma_{m0}')$  and  $(-\sigma_m')$

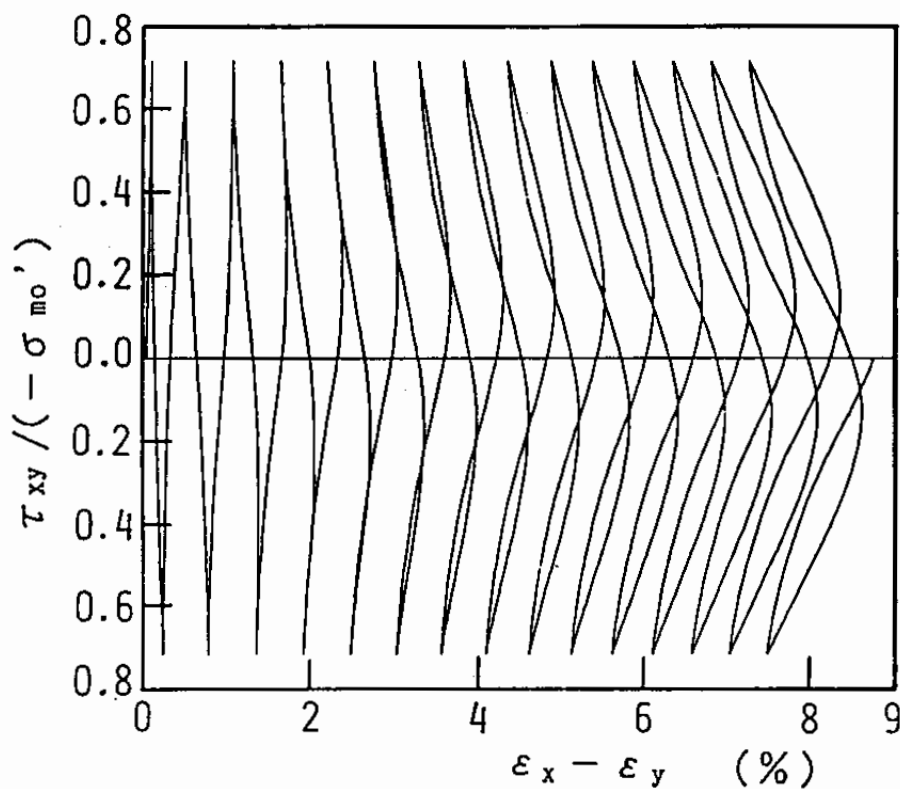


(b) Relation between  $\tau = (\sigma_1' - \sigma_3')/2$  and  $(-\sigma_m')$

Fig. 3.10 Computed stress path for dense sand ( $K_0 = 0.5$  with bulging unconstrained)



(a) Relation between  $\tau_{xy}/(-\sigma_{m0}')$  and  $\gamma_{xy}$



(b) Relation between  $\tau_{xy}/(-\sigma_{m0}')$  and  $(\epsilon_x - \epsilon_y)$

Fig. 3.11 Computed stress strain curve for dense sand ( $K_0 = 0.5$  with bulging unconstrained)

### 3.5 Effect of Initial Mean Effective Stress

Effect of initial mean effective stress on the behavior of soil is one of the most important issues in the physical model testing of soil-structure systems in 1 g gravity field (i.e. a common type of shaking table tests). This aspect of the model performance is examined by computing the stress paths and the stress strain relations under undrained cyclic loading at several initial confining stresses with the same stress ratios. The same parameters for the loose sand shown in Table 3.1 is used for the computation.

The results, as shown in Fig. 3.12, indicate that the stress path is not affected by changing the initial effective mean stress if the shear stress ratio remains the same and the effective mean stress is plotted in the normalized coordinate shown in Fig. 3.12. This is consistent with the previous laboratory findings; i.e. liquefaction resistance defined by excess pore water pressure rise is approximately independent of the initial confining pressure (Lee and Seed, 1967).

The stress and strain relations shown in Fig. 3.13, however, indicate that the strain is affected by the initial mean effective stress. The strain is, as shown in Fig. 3.14, proportional to the square root of the initial mean effective stress. This is consistent with the laboratory results conducted under the drained condition (Pradhan et al, 1989).

These results are a natural consequence of the formulation given in the previous chapter. The stress path is governed by such normalized variables as normalized plastic shear work  $w$  in

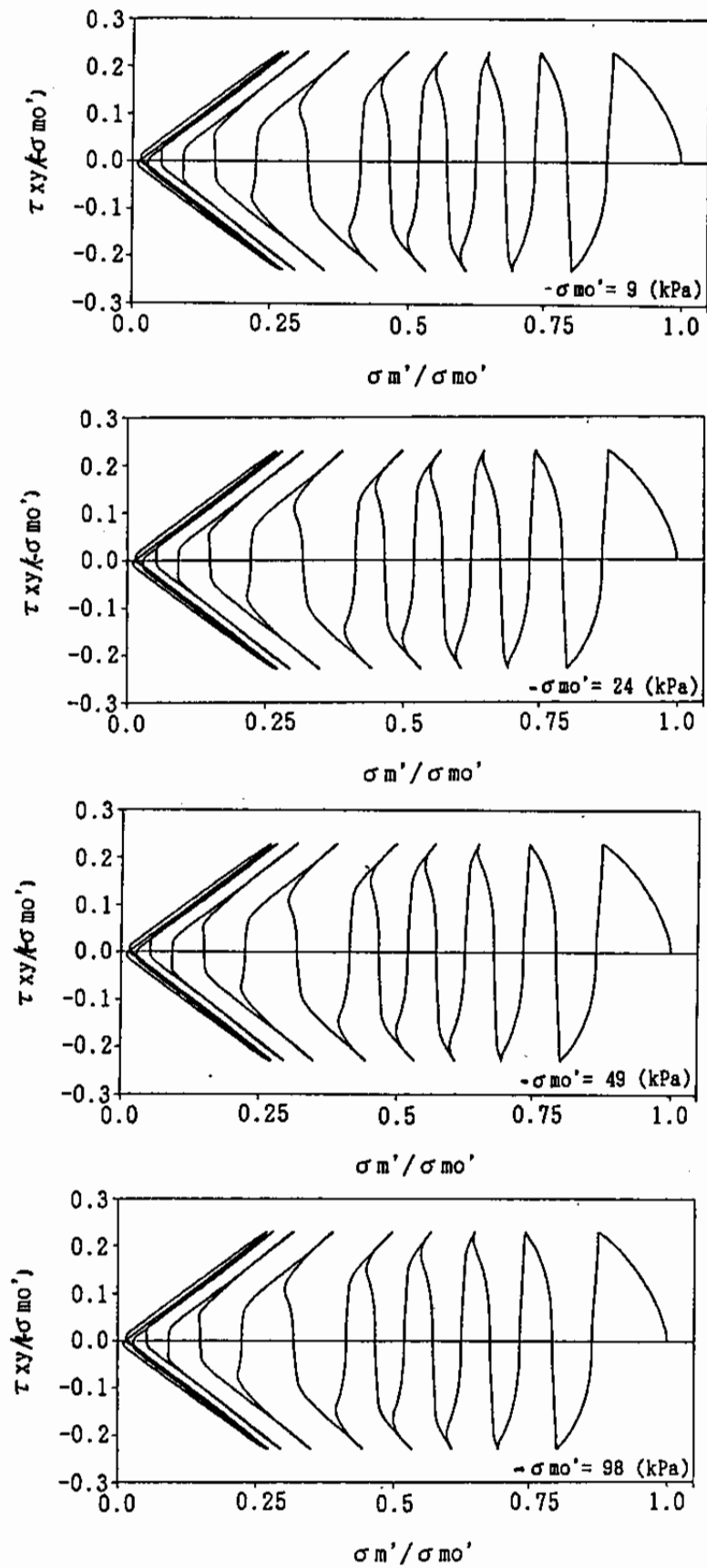


Fig. 3.12 Computed stress paths at initial confining pressures of, from the top to bottom rows, 9, 24, 49 and 98 kPa

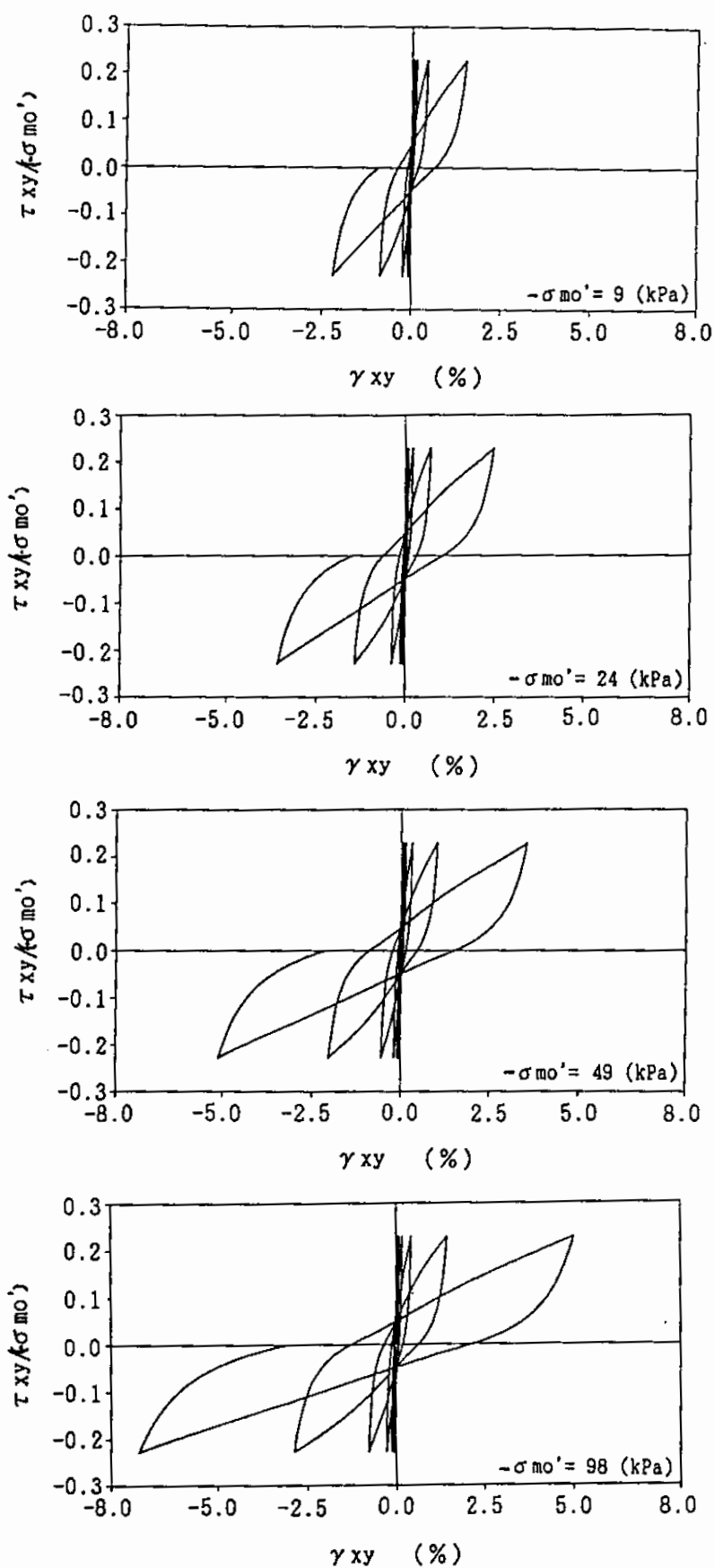


Fig. 3.13 Computed stress strain curves at initial confining pressures of, from the top to bottom rows, 9, 24, 49 and 98 kPa

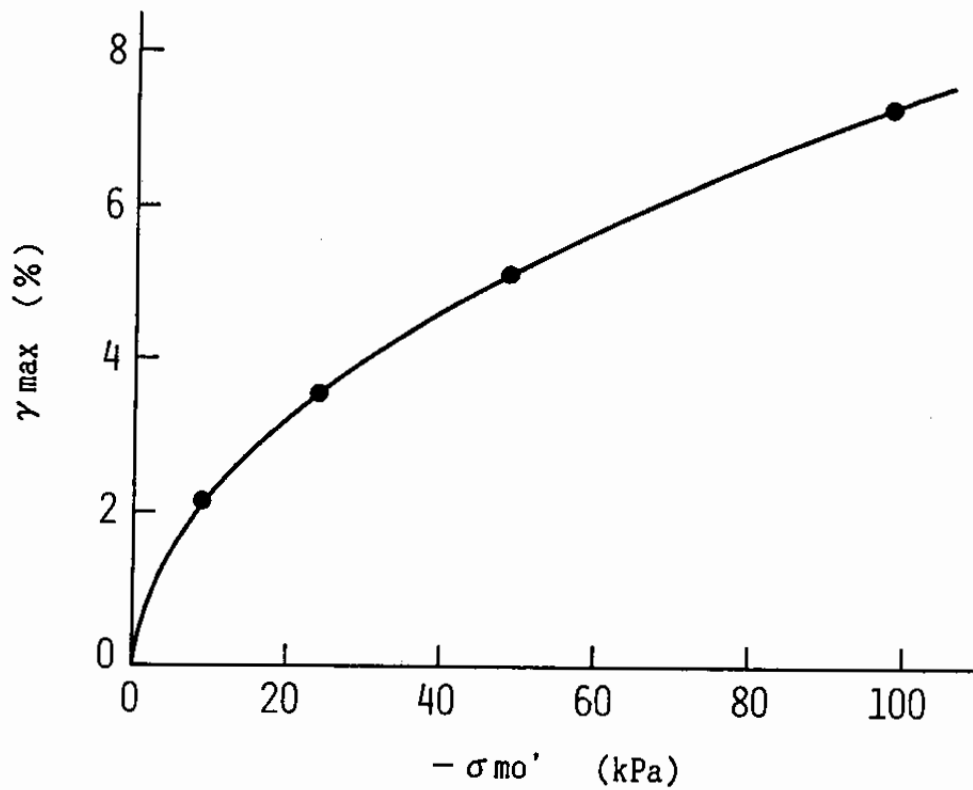


Fig. 3.14 Relation between the maximum shear strain amplitude and the initial confining pressure; the solid line represents a curve proportional to square root of the initial confining pressure

Eq.(2.63) and deviatoric stress ratio  $r$  in Eq.(2.59), both of which are unaffected by the initial mean effective stress. The shear strain, however, is governed by the normalizing factor in Eq.(2.79), which is proportional to the square root of the initial mean effective stress. To be more specific, the normalizing factor in Eq.(2.79) is, as shown in Eq.(2.114), proportional to the reference strain in Eq.(2.66), which is in turn proportional to the square root of the initial confining pressure as understood from Eqs.(2.65) through (2.67).

These properties of soil seen above will affect the overall performance of scaled physical models of soil structures and foundations in 1 g gravity field. Full consideration upon this issue naturally leads to a similitude for physical model testing. A key to this is introducing scaling factors for stress as well as strain. The details are found in a paper by the author (Iai, 1989). An example is also given in a relevant discussion (Iai, 1990).

### 3.6 Applicability to Soil Element Analysis

In the present chapter, the most basic performance of the present model is examined with a single soil element. With the appropriate identification procedure for the model parameters, the present model shows reasonable adaptability to the laboratory data. The rapid as well as gradual increases in the shear strain amplitude greater than several percent in both loose and dense sand are simulated in the numerically robust manner. The effect of initial stress condition, either isotropically or



anisotropically consolidated, is reasonably analyzed in the manner consistent with the laboratory findings. Moreover, the complex mechanism in the simple shear of anisotropically consolidated soil becomes very simple to understand according to the present approach; the key to this is the virtual simple shear mechanisms oriented into arbitrary directions. Effect of the initial effective mean stress is also consistent with the laboratory results. It is concluded that the present model has reasonable applicability in the single element analysis.

#### References

- (1) Iai, S. (1989) : "Similitude for shaking table tests on soil-structure-fluid model in 1g gravitational field," Soils and Foundations, Vol.29, No.1, pp.105-118
- (2) Iai, S. (1990) : A closure on "Similitude for shaking table tests on soil-structure-fluid model in 1g gravitational field," Soils and Foundations, Vol.30, No.2, pp.153-157
- (3) Ishihara, K. and Li, S. (1972) : " Liquefaction of saturated sand in triaxial torsion shear test," Soils and Foundations, Vol.12, No.2, pp.19-39
- (4) Ishihara, K., Iwamoto, S., Yasuda, S. and Takatsu, H. (1977) : "Liquefaction of anisotropically consolidated sand," Proceedings of 9th International Conference on Soil Mechanics and Foundation Engineering, Tokyo, Vol.2, pp.261-264
- (5) Ishihara, K. (1985) : "Stability of natural deposits during earthquakes," Proceedings of 11th International Conference

on Soil Mechanics and Foundation Engineering, San Francisco, Vol.1, pp.327-376

- (6) Kokusho, T. (1980) : "Cyclic triaxial test of dynamic soil properties for wide strain range," Soils and Foundations, Vol.20, No.2, pp.45-60
- (7) Lee, K.L. and Seed, H.B. (1967) : "Cyclic stress conditions causing liquefaction of sand," Journal of Soil Mechanics and Foundation Division, ASCE, Vol.92, No.SM1, pp.47-70
- (8) Pradhan, T.B.S., Tatsuoka, F. and Sato Y. (1989) : "Experimental stress-dilatancy relations of sand subjected to cyclic loading," Soils and Foundations, Vol.29, No.1 pp.45-64
- (9) Zienkiewicz, O.C. and Bettess, P. (1982) : "Soils and other saturated media under transient, dynamic conditions; general formulation and the validity of various simplifying assumptions," in Pande, G.N. and Zienkiewicz, O.C. (eds.), Soil Mechanics - Transient and Cyclic Loads, pp.1-16

## CHAPTER 4

### ONE DIMENSIONAL ANALYSIS OF LEVEL GROUND

Behavior of level ground shaken by strong earthquake motions is an issue of a wide engineering concern especially when the ground consists of saturated cohesionless soil. It often involves high excess pore pressure rise and presents a potential threat to stability of soil structures and foundations. The cyclic mobility defined in the earlier chapter is one of the most relevant mechanisms to this phenomenon.

Analysis of the level ground is of one dimensional nature and hence is of the most fundamental application of the cyclic mobility model. The level ground is, as mentioned in the previous chapter, initially at the anisotropic consolidation condition and then is shaken in the simple shear mode. The mechanism involves rotation of principal stress axes as mentioned earlier. How the present cyclic mobility model will perform in this type of analysis is yet to be known through the analysis. In this chapter, applicability of the present cyclic mobility model is examined by conducting shaking table tests of level model ground consisting of loosely deposited saturated sand.

#### 4.1 Shaking Table Tests

##### 4.1.1 Outline of Model Tests

The level model ground in the present study has dimensions of about 2 meters in diameter and height, contained in a stack of 64 aluminum rings. Three series of shaking table tests are

reported in the present study; two of them are shaken with a sinusoidal input motion, the rest with an earthquake input motion.

The tests were originally conducted as a part of the study on performance of gravel drains which were installed in a sand deposit as a remedial measure against liquefaction (Iai, 1988). Out of the nine series of model tests conducted with and without a gravel drain, three model tests without a gravel drain, conducted as a reference representing performance of pure sand deposit, are selected for the present study.

In the present study, the two series with a sinusoidal input motion will be called R-300 and R-600 series, the rest with an earthquake input motion will be called R-800 series, as were originally called in the previous study on the gravel drain.

#### 4.1.2 Shaking Table and Container

##### (1) Shaking Table

The shaking table used in the model testing is of electromagnetic type. This type of shaking tables is known to achieve the best accuracy in reproducing input motions. Degree-of-freedom of motion of the shaking table is one in the horizontal direction. Dimensions of the table are four meters in length by 3.5 meters in width. More specifics on the shaking table are shown in Table 4.1.

##### (2) Stack of 64 Aluminum Rings

Upon the shaking table, a container is set up for conducting

Table 4.1 Specifications on the shaking table

Items	Specifications
Freedom of shaking	One horizontal direction
Maximum amplitude of displacement	18 tonf G
Maximum total load (including dead load)	40 tonf
Dead load	15 tonf
Dimensions of the table	4 m (in the direction of vibration)×3.5m
Maximum amplitude of displacement	10cm
Maximum amplitude of velocity	25cm/s
Maximum amplitude of acceleration when the maximum load is shaken	0.45G
Shaking motion	Arbitrary motions controlled by input data
Effective frequency range	from 1 to 100 Hz

the model testing of loosely deposited saturated sand. The container, as shown in Fig. 4.1, is made of a stack of 64 aluminum rings; each ring has the inside diameter of 190 cm, the outside diameter of 194 cm and the thickness of 3 cm. The total height of the stack amounts to 207 cm. In order to reduce the friction between the rings, roller bearings of 0.245 cm in diameter are inserted at eight locations along the circumference of the rings. On the top of the container, a load of 2.5 tf in weight is placed for preventing rocking motion of the container during shaking. Ball bearings of 3.8 cm in diameter are inserted between the load and the top edge of the container in order to reduce the friction between them.

In addition to the stack of rings, an inner cell is used because the model ground is saturated with water. A rubber membrane of 0.13 cm in thickness is used as the inner cell.

After carefully setting up the rings and the rubber membrane, the exact inside diameter, including the thickness of the rubber membrane, is measured by filling up the container with water. The repeated measurements result in the average value of 189.6 cm as the inside diameter of the container.

#### 4.1.3 Instrumentation

##### (1) Measured items

Response of the level model ground is monitored by recording excess pore water pressures, displacements and accelerations. In addition, density of the level model ground is determined by measuring the total weight and the volume of the sand poured into

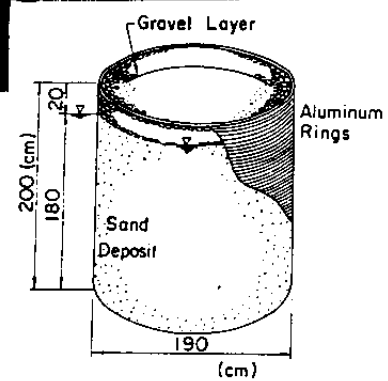


Fig. 4.1 A stack of 64 aluminum rings on the shaking table

the container. Cone penetration resistance and shear wave velocity are also measured for determining the initial condition of the model sand deposit.

## (2) Arrangement of the instruments

The instruments such as pore water pressure gauges and accelerometers are, as shown in Fig. 4.2, deployed in an array configuration. The original reason for adopting the array configuration was for measuring spacial variation of the pore water pressure within the model ground when the gravel drain is installed in the middle of the model ground. When the gravel drain is not installed as are in the present cases, the array configuration does enhance reliability in the measurement.

## (3) Instruments

The following instruments are used in the present study.

### a) Pore water pressure gauges

The pore water pressure gauges used in the present study are of strain gauge type. They are calibrated by changing the level of the pore water pressure gauges within water, which is filled in a water pool of about 1.2 m in depth. The outputs of the pore water pressure gauges during the calibration are examined for such specifics as linearity and hysteresis. The results confirm that noises and errors contained in the outputs are less than 1 % in the pressure ranges to be measured in the present study. Stability of these instruments are confirmed by conducting the calibration before and after the shaking table tests.

Specific weight of the pore water pressure gauges is so



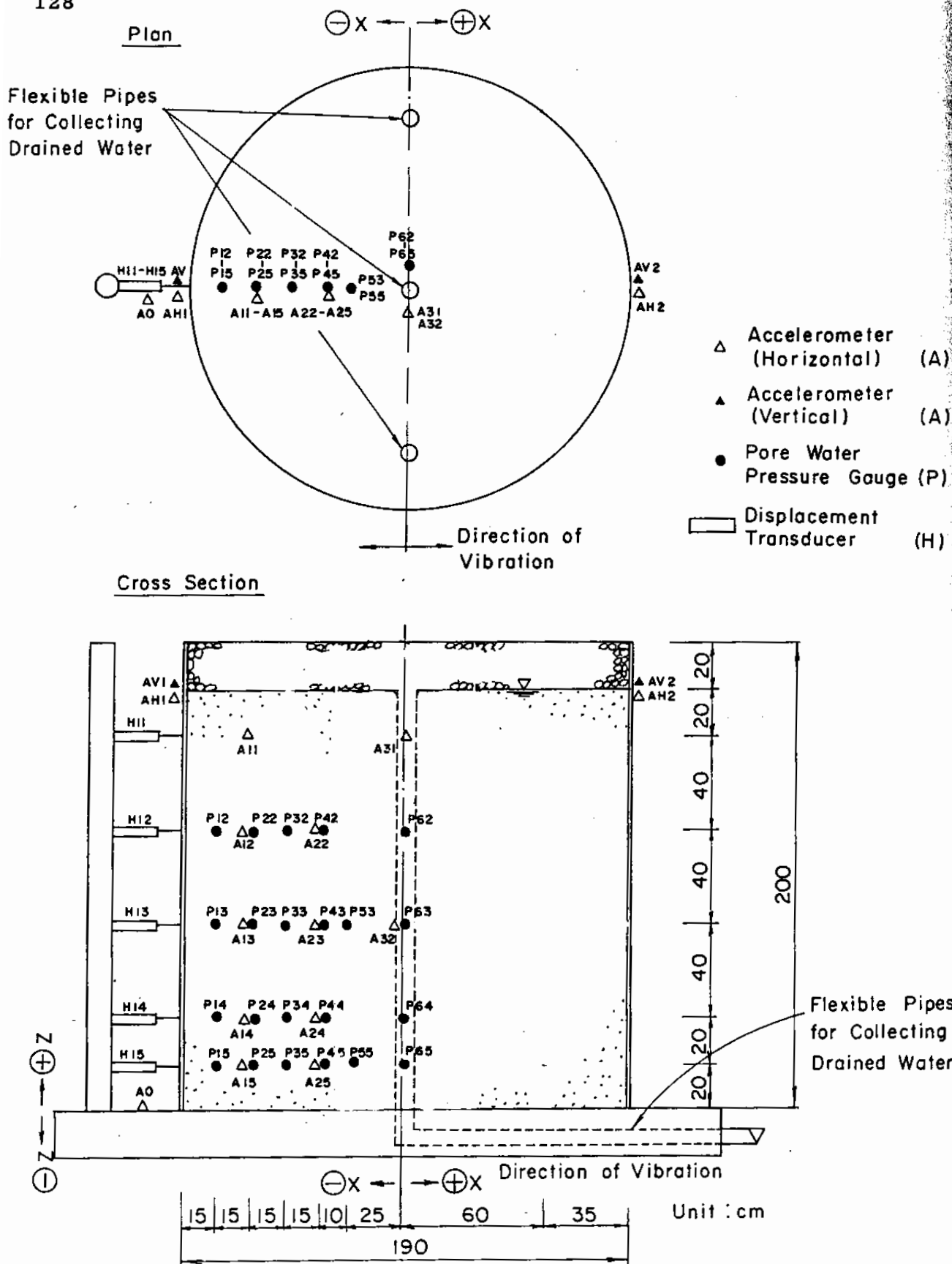


Fig. 4.2 Typical locations of the instruments

adjusted as to be the same as that of the saturated sands by using attachments made of styrofoam as shown in Fig. 4.3 (a). In addition, locations of the pore water pressure gauges are fixed by using fishing lines. As shown in Fig. 4.3 (b), the fishing lines are suspended from the cross beams placed at the top of the container. Bottom ends of the fishing lines are fixed at the base of the container. Tensions given to the fishing lines are adjusted with miniature turnbuckles in order to mitigate the undesirable effects on dynamic response of the model ground.

After fixing the pore water pressure gauges with the fishing lines, the model ground is made by pouring sand into water; the details in the pouring procedure will be described in the later subsection. As the sand poured in, the water is gradually leveled up and, when the level of the water becomes high enough, small air bubbles are removed within the water from the pore water pressure gauges in order to assure the accuracy in the pore water pressure measurement.

#### b) Displacement transducers

The displacement transducers used in the present study are of inductance type, minimizing undesirable reaction force possibly to be applied from the transducers to the model ground. Main bodies of these transducers are attached to a rigid steel pole which is rigidly fixed to the shaking table as shown in Fig. 4.2. The other ends of the transducers are fixed to the aluminum rings of the soil container and thus the transducers measure displacements of model ground at five levels.

#### c) Accelerometers

Two types of accelerometers are used in the present study.

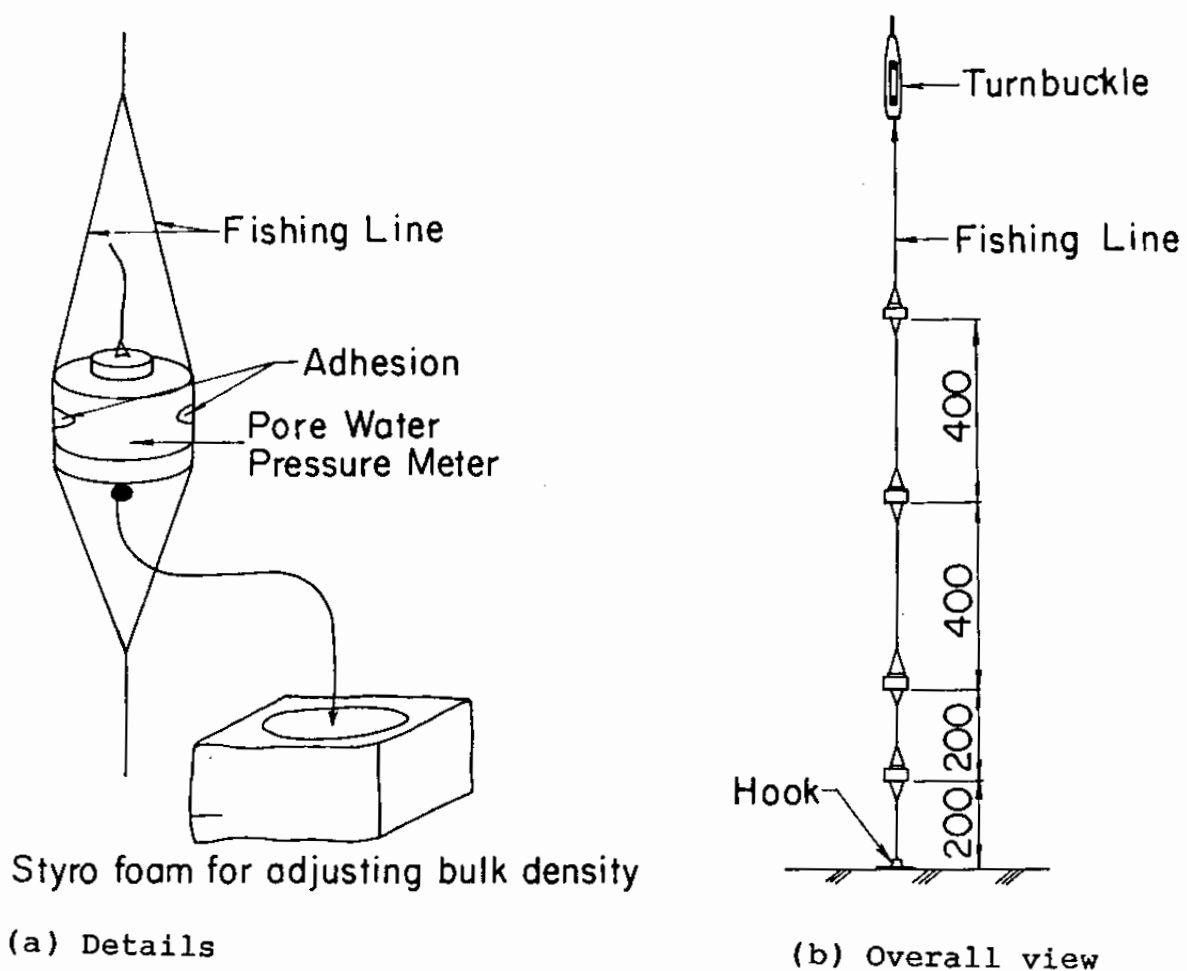


Fig. 4.3 Attachment for pore water pressure gauges

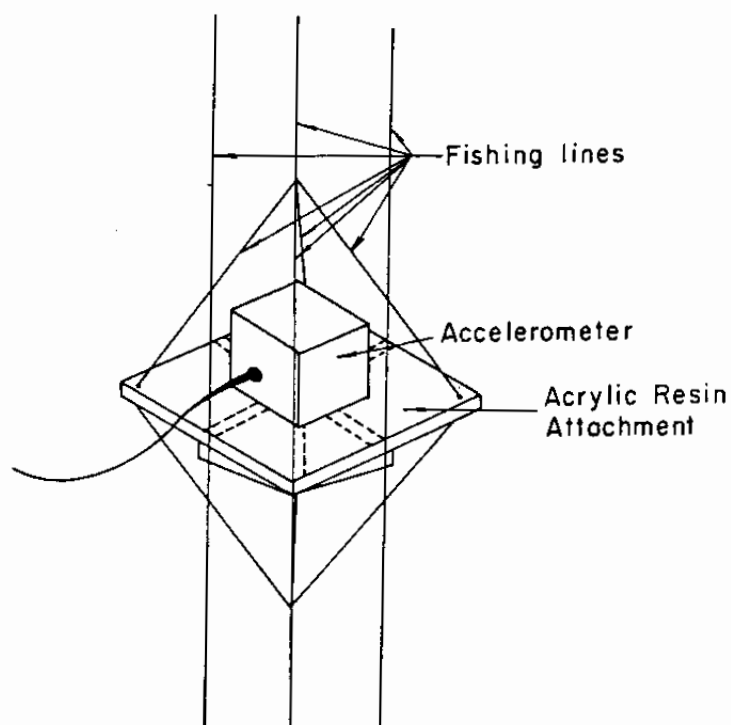


Fig. 4.4 Attachment for accelerometers

One has the bulk density being approximately the same as that of the saturated sand. The other has larger bulk density but has such an attachment as shown in Fig. 4.4 for ensuring better fit with the sand deposit. The fishing lines are used for fixing positions of the accelerometers as in the same manner as for the pore water pressure gauges. At the final stage for fixing the accelerometers in the sand deposit, fine adjustments are made for leveling the accelerometers by monitoring the output of each instrument. All the upper parts of the fishing lines suspended from the crossbeams are cut, when the model ground is completed, in order to minimize undesirable effect of the fishing lines on the accelerometers.

#### d) Other instruments

In addition to the instruments mentioned above, a loadcell is used for measuring weights of the sand for computing density of the model ground. The loadcell is calibrated six times during the model testing by using iron weights. The result of the calibration reveals fluctuation of 0.8 %, which amounts to 3.5 % errors in estimating the relative densities of the sand deposit in the present study.

#### e) Specification of the instruments

More specifics in the above-mentioned instruments are summarized in Table 4.2.

### 4.1.4 Properties of Sand

The sand used for the shaking table tests was taken at Gaiko district of the Akita Port in Japan. Exact location for the soil

Table 4.2 Specifications of the instruments

Kind of Instrument	Mechanism of Sensor	Capacity	Dimensions (mm)	Weight (gf)	Frequency range of uniform sensitivity (Hz)	Locations of the instruments
Pore water pressure meter	Strain gauge type	0.5kgf/cm <sup>2</sup>	$\phi$ 40, t = 30	170	0—3000	P 12-15, P 22-25, P 30, P 32-35, P 42-45, P 53, P 62-65
Loadcell	Strain gauge type	1000kgf	$\phi$ 68, t = 143	2700	—	L 1 for measuring the weights of sands and gravels
Accelerometer	Strain gauge type	$\pm 2$ G	56×61×27	200	0—90	A0, A11-15
		$\pm 2$ G	30×27×22	60	0—56	A V1-2, A H0-2, A 22-25, A 31-32
Displacement transducer	Inductance type	$\pm 200$ mm	830×75×70	2600	—	H11
		$\pm 50$ mm	330×65×60	900	—	H12-13
		$\pm 10$ mm	330×65×60	900	—	H14-15
Cone penetrometer	Portable single tube type, Capacity: 100 kgf Cone: angle=30°; projected area=3.23 cm <sup>2</sup> ; reversally tapered					

sampling is shown by x-mark in Fig. 4.5. The area around this location was reclaimed with sand which was dredged from the nearby sea bottom. The area liquefied during the 1983 Nihonkai-Chubu Earthquake of magnitude 7.7 (Tsuchida et al, 1985).

The sand has fines content ( i.e. percentage of soil particles finer than 0.074 mm by weight) of less than 5 %. Such a small amount of fine particles is believed to have little influence upon the liquefaction resistance of the sand. In the present study, the fine particles are completely washed out for mitigating the tendency for poured sand to form thin layers of fines due to segregation during pouring process. In this way uniformity in the model sand deposit is ensured in the present study.

The grain size accumulation curves are shown in Fig. 4.6 for the sand of which fine particles have been washed out. Physical properties and permeability of the sand are shown in Table 4.3 and Fig. 4.7. The maximum and the minimum density of the sand, shown in Table 4.3, are obtained by adopting the testing procedure indicated by the Japanese Society of Soil Mechanics and Foundation Engineering (1979).

In order to evaluate the mechanical properties of the sand used in the model testing, triaxial tests are conducted under the drained condition at the low confining pressures of 30 and 49 kPa. The results are shown in Fig. 4.8.

In addition, undrained cyclic loading tests are conducted with a triaxial testing apparatus under the initial confining pressures of 98 kPa. Unfortunately the sand used for the undrained cyclic loading test is not exactly the same as that

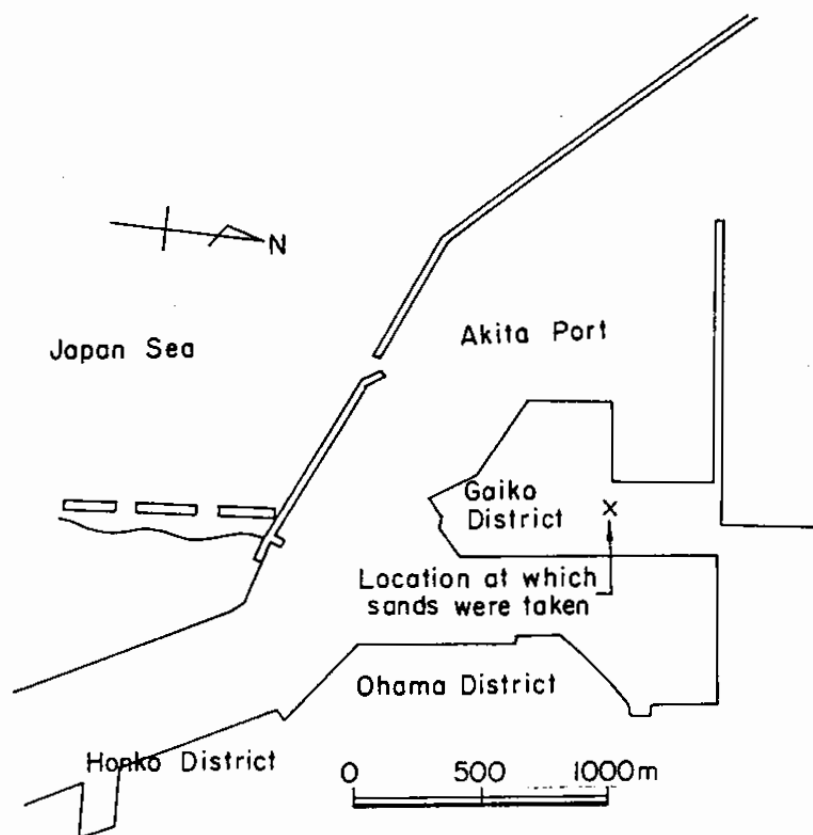


Fig. 4.5 Plan of Akita port and location of sand sampling

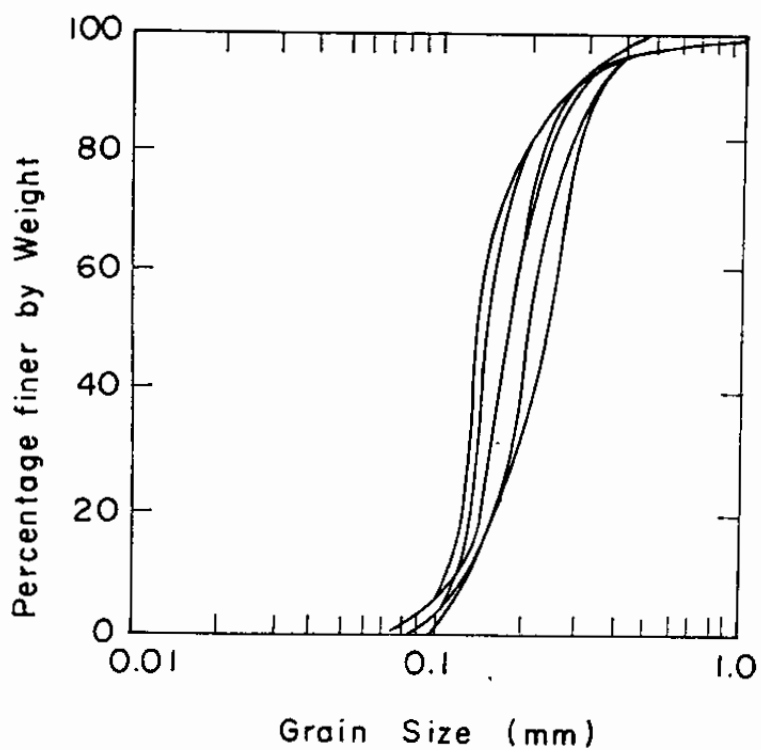


Fig. 4.6 Grain size accumulation curves of Gaiko sand

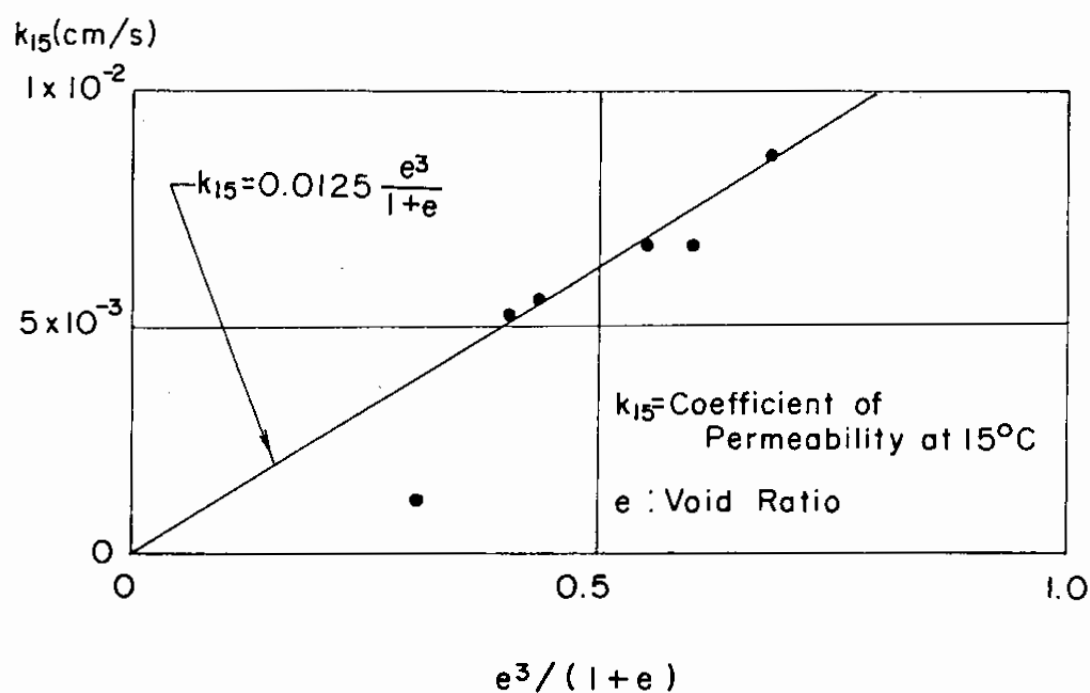


Fig. 4.7 Coefficient of permeability of Gaiko sand

Table 4.3 Physical properties of Gaiko sand

Date of Test	Oct. 18, 1984	Nov. 13, 1984	Nov. 13, 1984	Nov. 15, 1984	Nov. 15, 1984	Jan. 9, 1985	Jan. 29, 1985	Average	Standard Deviation
Specific Gravity $G_s$	2.665	2.662	2.667	2.672	2.676	2.662	2.663	2.667	0.005
Grading {	0.4	0.4	0.4	0.3	0.4	0.1	0.3	0.33	0.10
	99.3	99.2	99.1	98.7	99.0	99.2	99.3	99.1	0.2
	0.3	0.4	0.5	1.0	0.6	0.7	0.4	0.56	0.2
$D_{60}$ (mm)	0.14	0.18	0.23	0.18	0.21	0.15	0.18	0.181	0.03
$D_{10}$ (mm)	0.11	0.12	0.14	0.12	0.14	0.12	0.13	0.126	0.01
Coefficient of Uniformity $U_c$	1.3	1.5	1.6	1.5	1.5	1.3	1.4	1.44	0.10
$e_{\max}$	1.346	1.355	1.349	1.342	1.361	1.375	1.341	1.353	0.011
$e_{\min}$	0.879	0.866	0.856	0.849	0.870	0.886	0.851	0.865	0.013



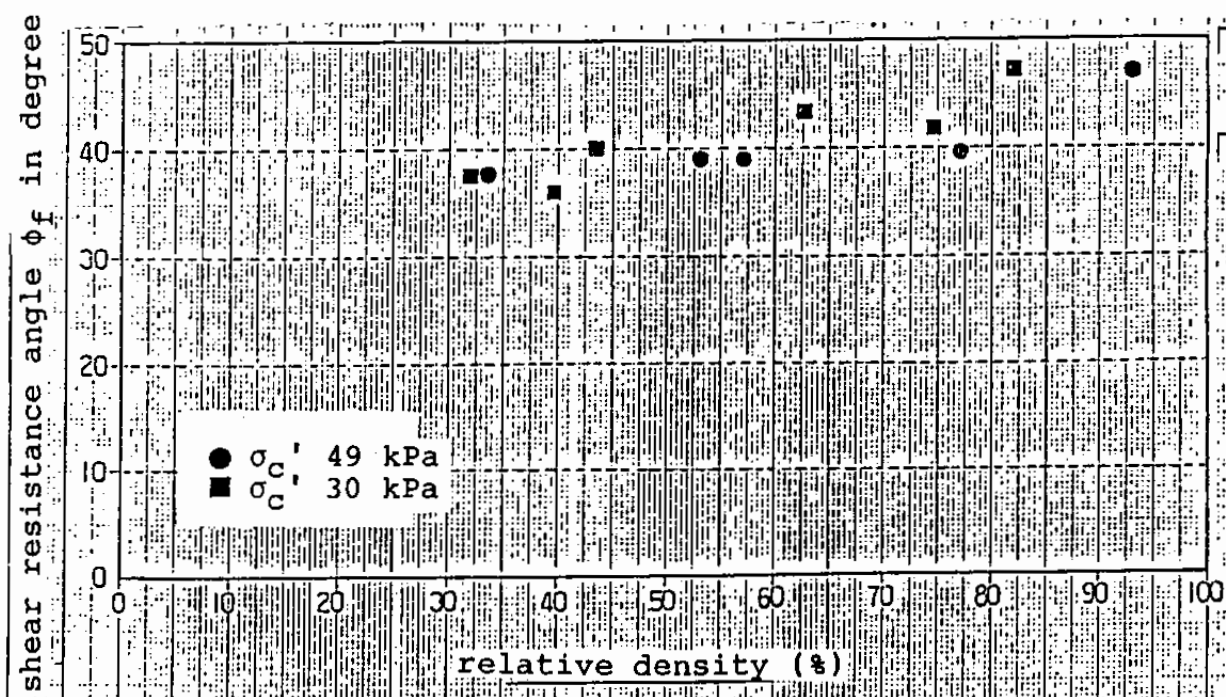


Fig. 4.8 Shear resistance angles of Gaiko sand

used in the shaking table tests or in the drained triaxial tests; the original sand taken from Gaiko district is used for the undrained cyclic loading test. The amount of the fines contained in the original sand is, as mentioned earlier, less than 5 % and hence the author believes that this much of fines will not cause a significant influence upon the properties of sand under cyclic loading. The maximum and the minimum void ratios of the sand used for the undrained cyclic loading test are 1.300 and 0.798, which are slightly different from those of the sand used for the shaking table tests and the drained triaxial tests shown in Table 4.3. In the present study, relative densities of the sand specimens for the undrained cyclic loading test are calculated with the maximum and the minimum void ratios obtained for the sand used for the shaking table tests and the drained triaxial tests.

The results of the undrained triaxial cyclic loading tests are shown in Figs. 4.9 and 4.10. The initial confining pressure is 98 kPa. The coefficients of volume compressibility are also obtained by measuring the amount of the pore water drained after the undrained cyclic loading. The results are presented in Fig. 4.11.

#### 4.1.5 Model Preparation

The level model ground is prepared, as illustrated in Fig. 4.12, through the following procedure.

##### (1) Pouring water

First of all, the instruments are fixed with the fishing

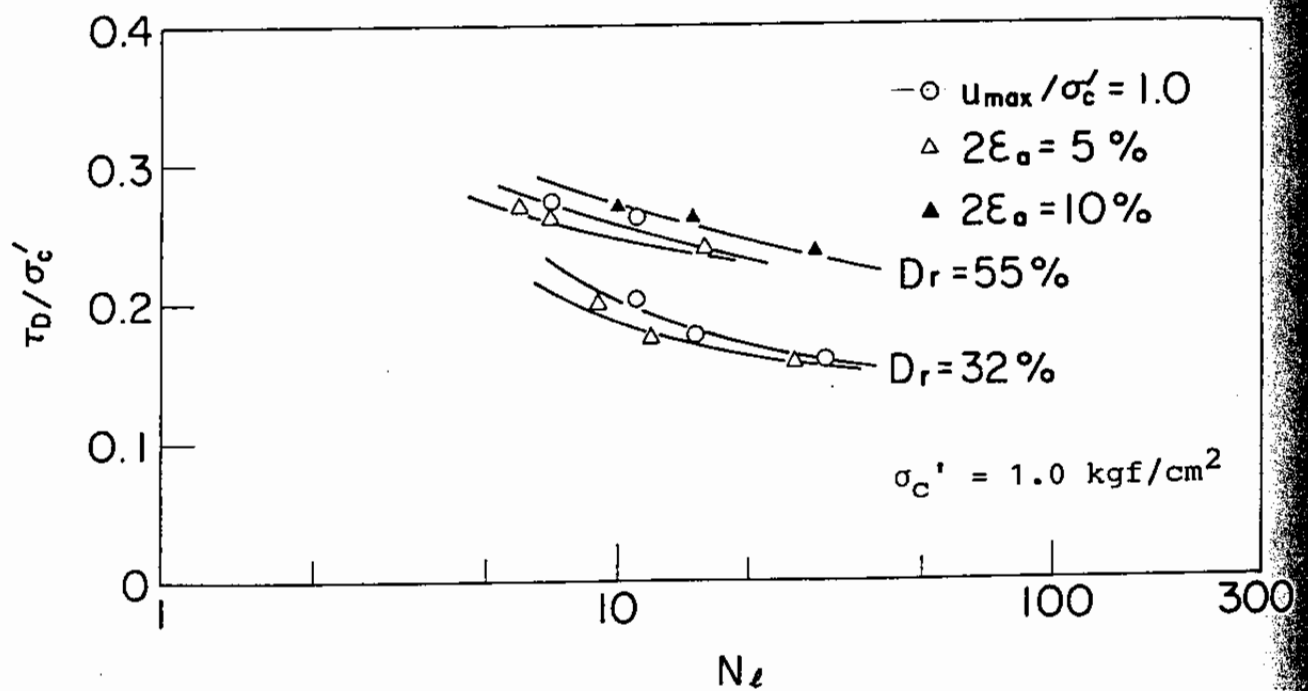


Fig. 4.9 Liquefaction resistance curves of Gaiko sand

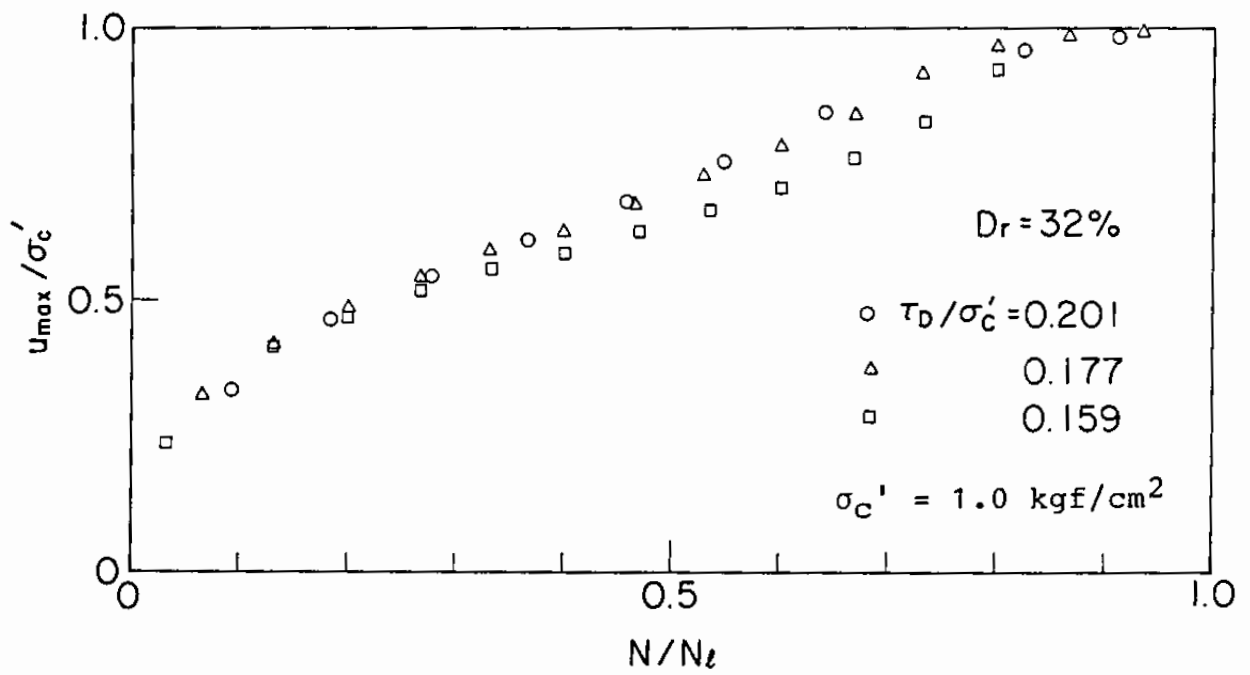
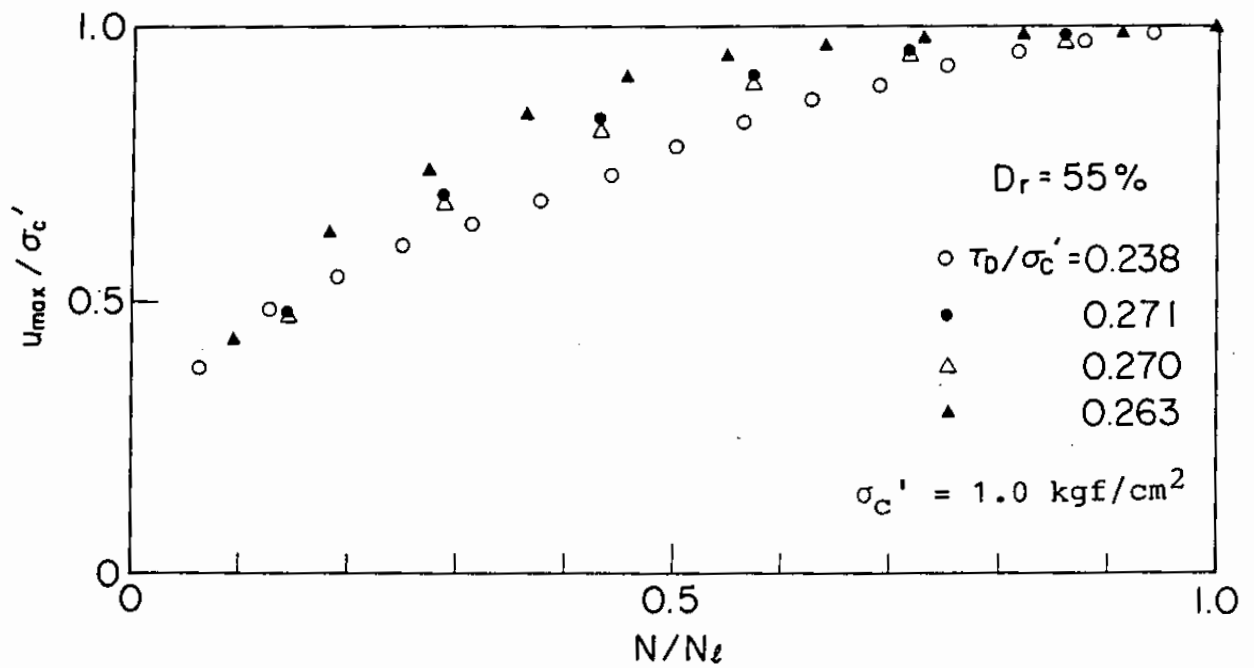
(a)  $D_r = 32 \%$ (b)  $D_r = 55 \%$ 

Fig. 4.10 Pore water pressure generation curves of Gaiko sand

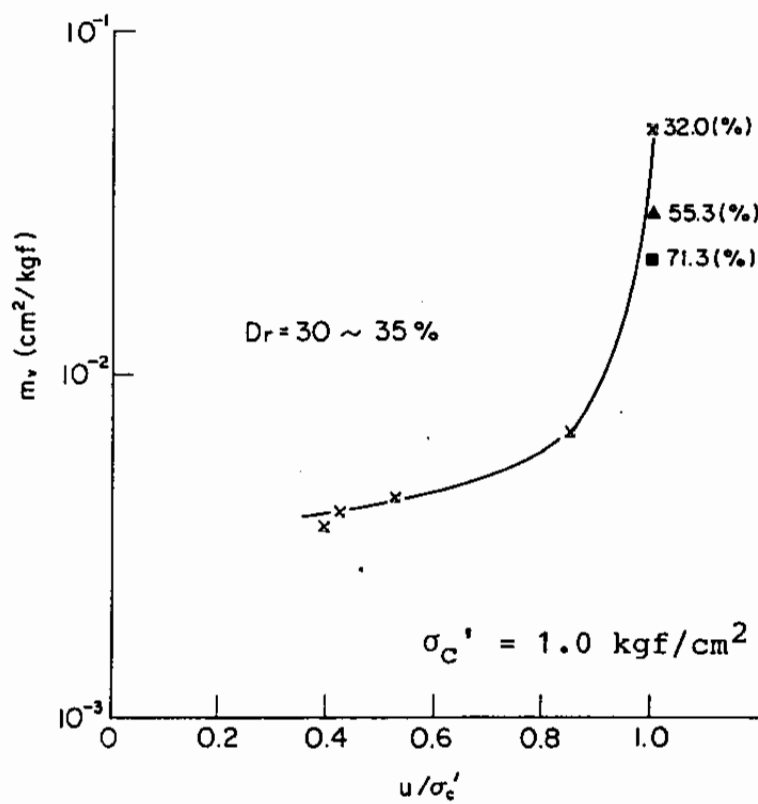
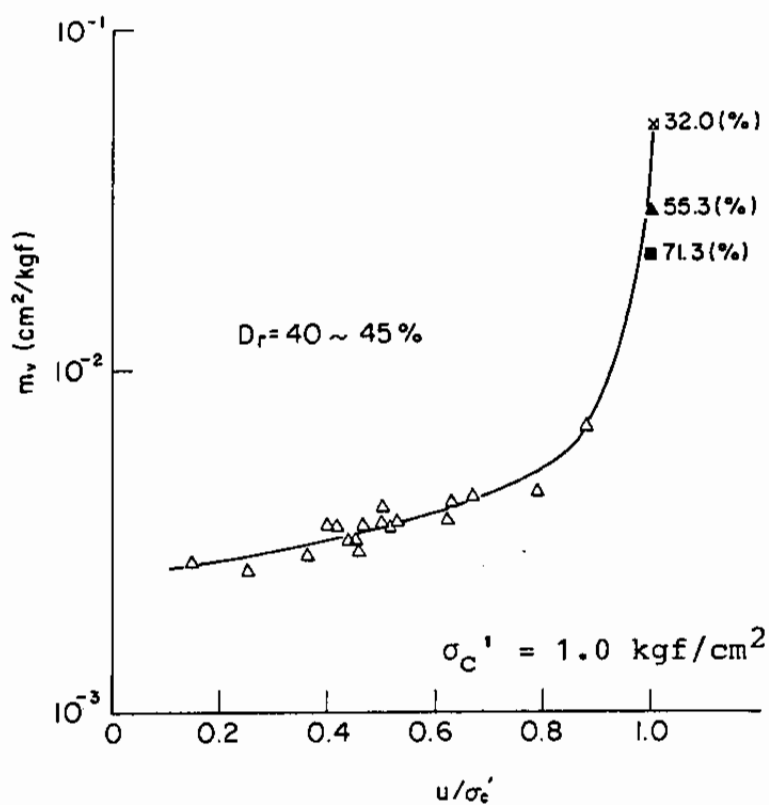
(a)  $D_r = 30 - 35 \%$ (b)  $D_r = 40 - 45 \%$ 

Fig. 4.11 Coefficient of compressibility of Gaiko sand

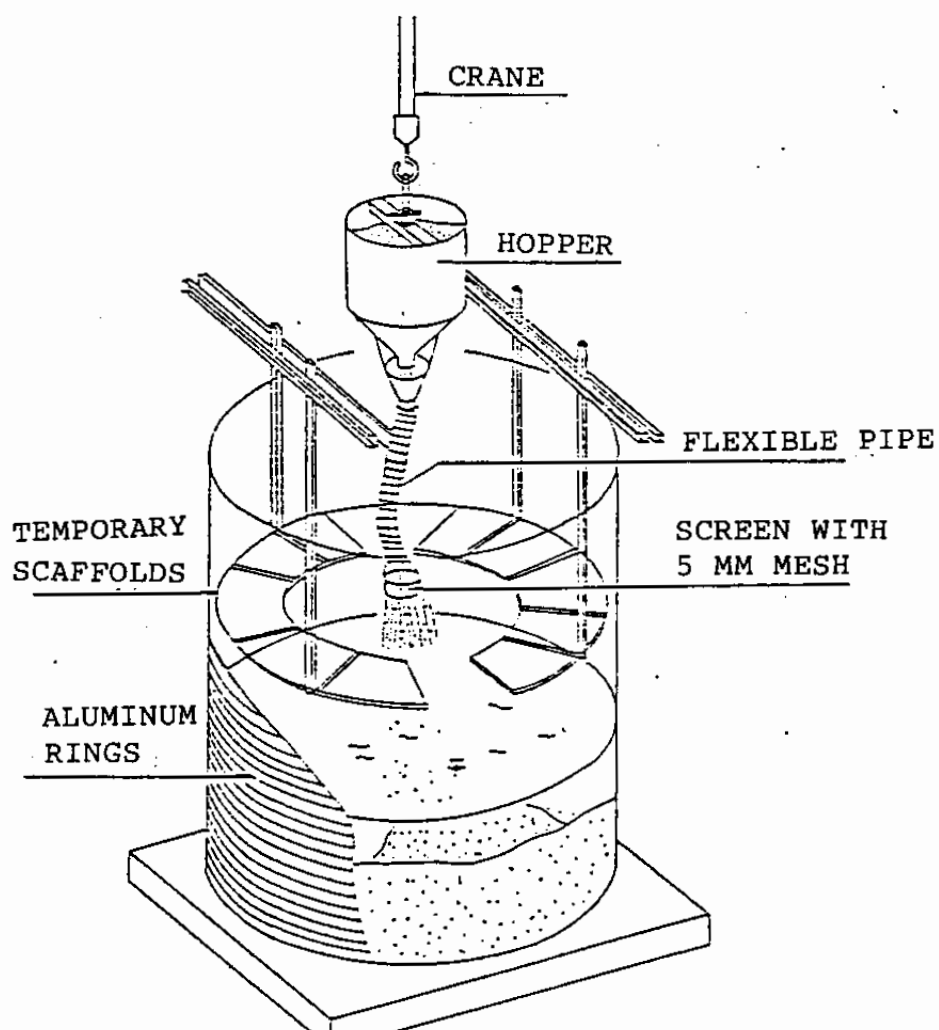


Fig. 4.12 Procedure for model preparation

lines as mentioned earlier. Secondly, temporary scaffolds are suspended from the steel framework constructed around the soil container in order to provide engineers the footholds for preparing the model ground with minimum disturbance to the soil deposit. Water is then poured into the container up to the level of 30 cm. Small air bubbles are removed, as mentioned earlier, from the front surfaces of the pore water pressure gauges when the level of water becomes high enough to work on.

### (2) Pouring sands

Sand is then poured into the water for forming the model ground. The sand has been oven dried before pouring and stored in the hoppers of  $0.5 \text{ m}^3$  in capacity. The weight of the dry sand is measured with a loadcell before pouring. An engineer on the temporary scaffold then carefully pours the sand into water with a hose attached to the hopper. At the other end of the hose, a screen with 5 mm mesh is attached to the nozzle for reducing the speed of pouring sand particles. The level of the screen is kept at the level of about 20 cm above the water level. While the sand is poured into water, the level of the sand deposit is continually monitored by another engineer for ensuring the level of the sand deposit being at least 5 cm below the water level. The sand deposit is thus leveled up to about 20 cm. Then, the temporary scaffold is leveled up to 20 cm ready for the next stage of pouring.

### (3) Forming gravel layer

After the above-mentioned process of pouring water and sand

is repeated nine times, the surface of the sand deposit is carefully leveled at the height of 180 cm. Exact level of the model ground is measured at the grid points shown in Fig. 4.13 for computing density of the model ground. Cone penetration tests are also conducted for examining uniformity in the density of the sand deposit.

Gravel layer is then formed in the thickness of 20 cm by carefully placing crushed stones on the top of the sand deposit. Grain size accumulation curves of the crushed stones are shown in Fig. 4.14. The water level is kept at the top of the sand deposit.

Finally, as partly mentioned earlier, a weight of 2.5 tf is placed at the top edge of the stack of aluminum rings for preventing rocking motion of the model ground. The load is applied only to the stack of rings.

#### 4.1.6 Initial Densities and Other Properties of Models

The model grounds made by the aforementioned procedure have initial properties summarized in Table 4.4. Shear moduli at small strain level, shown in this table, are obtained before the shaking test with two methods; one using shear wave velocity measured through impulse response tests of the model, the other using a resonant frequency of the model. The impulse response test is conducted by lightly hitting the edge of the shaking table with a wooden hammer. The resonant test is conducted with sinusoidal input motions of about 5 Gals in amplitude for the duration of 10 cycles at each frequency. A typical record of the impulse test and a typical result of the resonant test are shown



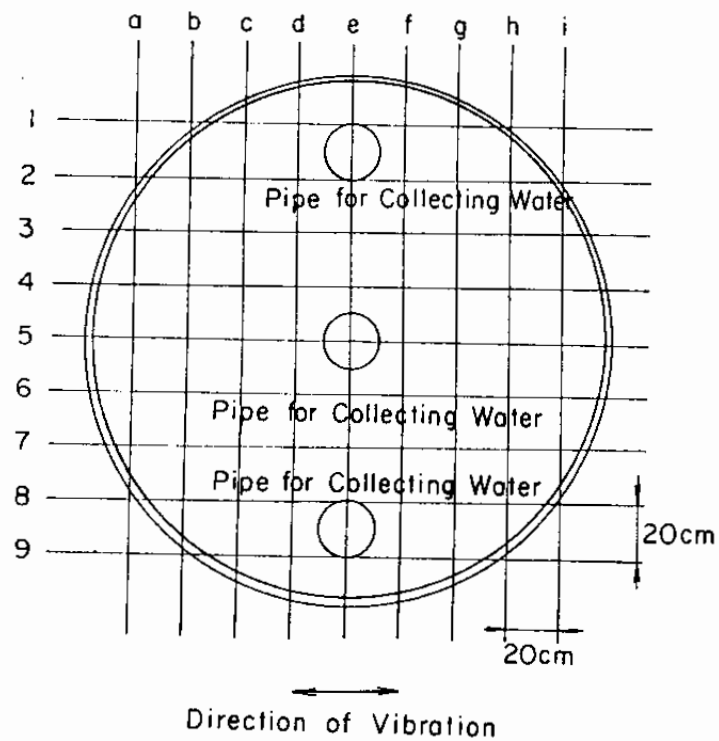


Fig. 4.13 Grid points for measuring level of model ground

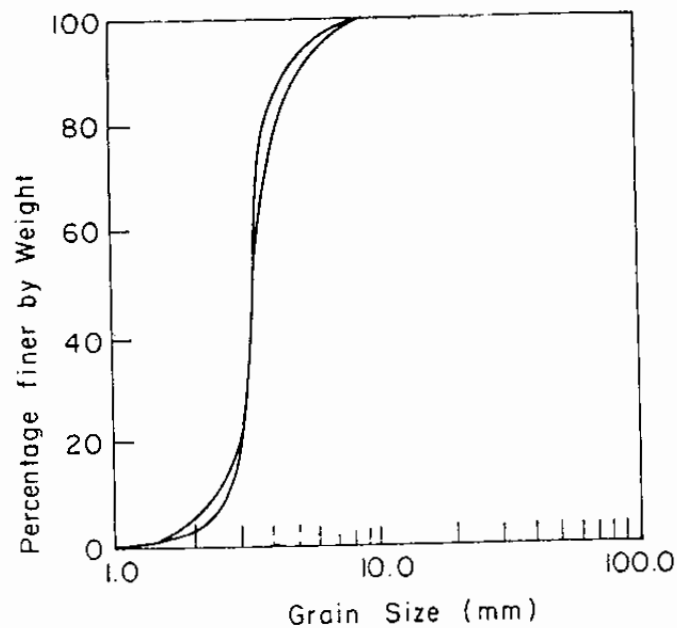


Fig. 4.14 Grain size accumulation curves of crushed stone

Table 4.4 Initial properties of the model ground

Series No.	H1 (cm)	H2 (cm)	$\gamma_{sat}$ (gf/cm <sup>3</sup> )	$\gamma_d$ (gf/cm <sup>3</sup> )	$e$	$D_r$ (%)	$k_{15}$ (cm/sec)	$T$ (°C)	$k_T$ (cm/sec)	$\gamma_{d0}$ (gf/cm <sup>3</sup> )	$G_0$ (kgf/cm <sup>2</sup> )
R-300	201.2	181.0	1.757	1.211	1.201	31	$9.8 \times 10^{-3}$	14	$9.6 \times 10^{-3}$	1.501	126/84
R-600	200.6	184.1	1.753	1.205	1.212	29	$10.1 \times 10^{-3}$	13	$9.5 \times 10^{-3}$	1.425	108/93
R-800	203.2	182.9	1.747	1.196	1.228	25	$10.4 \times 10^{-3}$	9	$8.8 \times 10^{-3}$	1.377	116/91

H1, H2: heights of top of the gravel layer and surface of the sand deposit

$\gamma_{sat}$ ,  $\gamma_d$ : saturated and dry unit weights of sand deposit

$e$ : void ratio of sand deposit

$D_r$ : relative density of sand deposit

$k_{15}$ ,  $k_T$ : coefficients of permeability of sand deposit at 15°C and at T°C

$T$ : temperature of water in centigrade

$\gamma_{d0}$ : dry unit weight of gravel layer

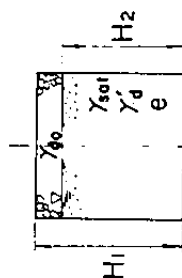
$G_0$ : shear modulus at small strain level

(value obtained by impulse test/value obtained by resonant test)

$$D_r = \frac{e_{max} - e}{e_{max} - e_{min}} = \frac{1.346 + e}{1.346 - 0.879}$$

Sand  $G_s = 2.665$ ,

$$k_{15} = 0.0125 \frac{e^2}{1+e}$$



in Fig. 4.15 and 4.16.

The properties of the model ground after the entire series of shaking tests are determined through the similar tests as shown in Table 4.5.

The cone penetration tests, as shown in Fig. 4.17, indicate that initial densities of the model ground are practically uniform along the depth. The densities after the shaking, however, do not seem to be uniform along the depth.

#### 4.1.7 Input Motion

Input motions used for the present study are, as mentioned earlier, of sinusoidal and earthquake wave forms. The sinusoidal input motion is of 2 Hz and of 20 cycles. The earthquake motion is a reproduction from the strong acceleration record at Akita Port during 1983 Nihonkai-Chubu Earthquake of magnitude 7.7 recorded at about 100 km from the epicenter. The wave form of the input motion used in R-800 series is shown in Fig. 4.18.

As mentioned earlier, each series of tests consists of several stages of tests shaken with the input motions of various amplitudes. Each stage are designated with a sequential number such as R-301, R-302, etc. The entire set of these tests are summarized in Table 4.6 with the case numbers and the maximum accelerations of the input motions together with representative values of the maximum excess pore water pressures generated in the sand deposit. Out of these cases, five cases, i.e. R-302, R-303, R-602, R-603 and R-802, are selected for the present study because they are considered to be shaken at the virgin conditions, i.e. shaken at the conditions without major pre-

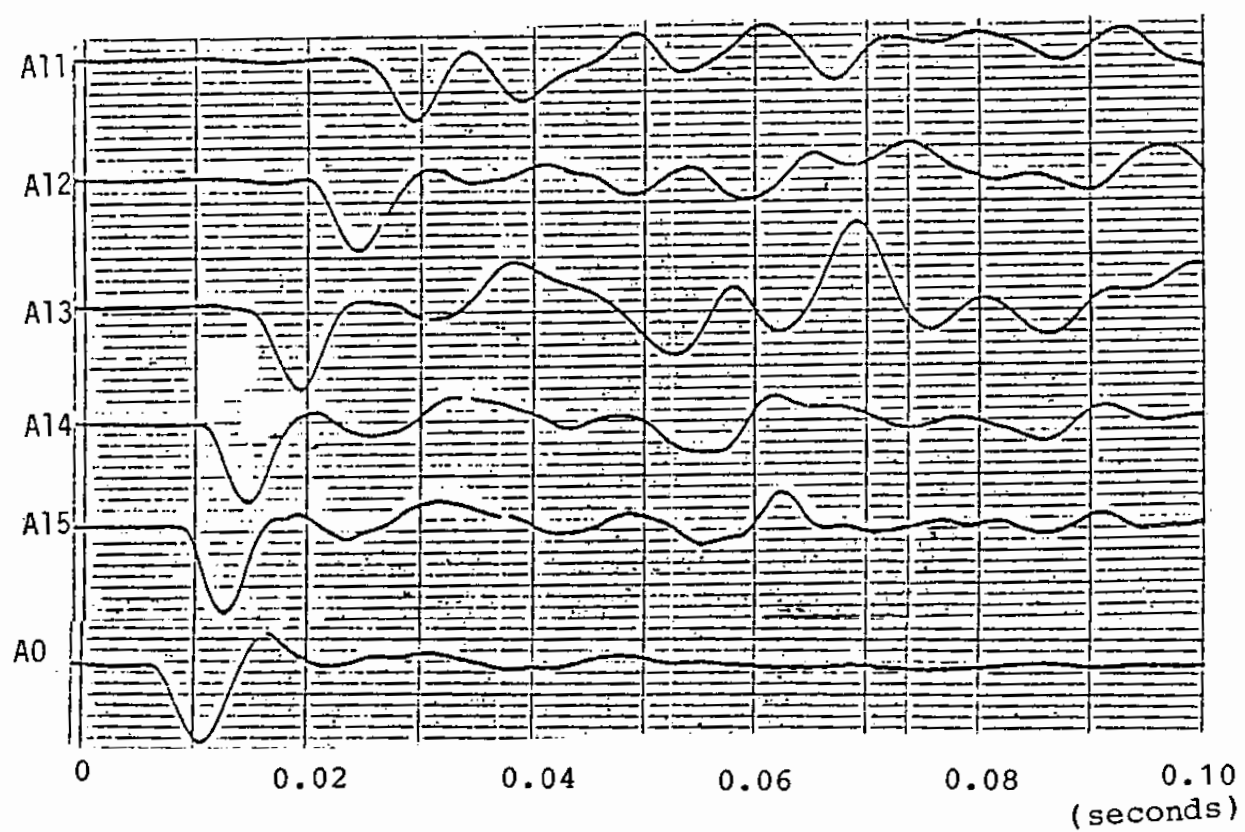


Fig. 4.15 A record in the impulse test

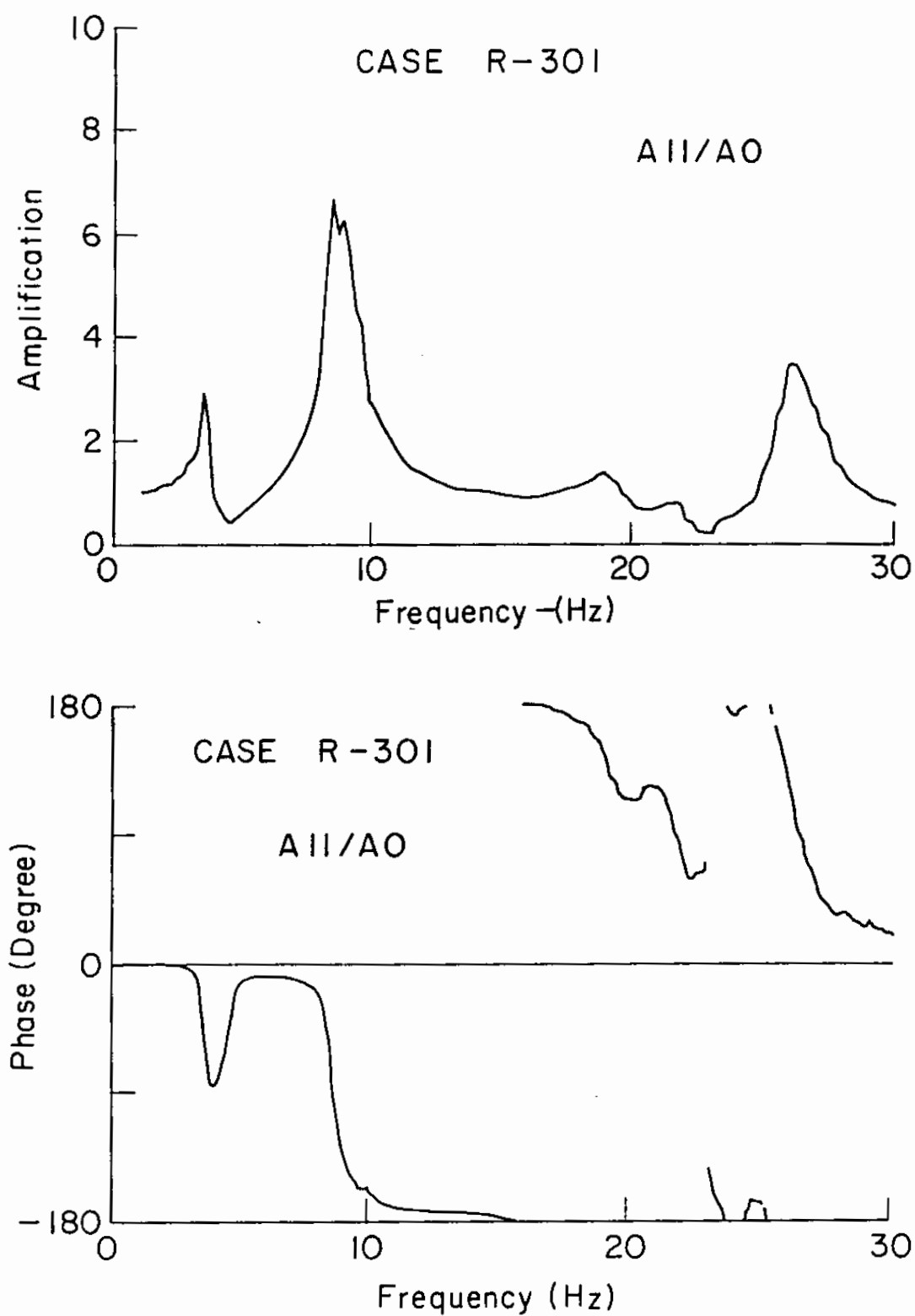


Fig. 4.16 Result of a resonant test

Table 4.5 Properties of the model ground after the shaking test

Series No.	$Dr$ (%)	$\gamma_{sat}$ (gf/cm <sup>3</sup> )	$e$	$G_0$ (kgf/cm <sup>2</sup> )
R-300	48	1.779	1.124	110/69
R-600	41	1.772	1.155	121/73
R-800	50	1.789	1.112	151/90

$Dr$  : relative density

$\gamma_{sat}$  : saturated unit weight of sand deposit

$e$  : void ratio of sand deposit

$G_0$  : shear modulus at small strain level

(value obtained by impulse test/value obtained by resonant test)

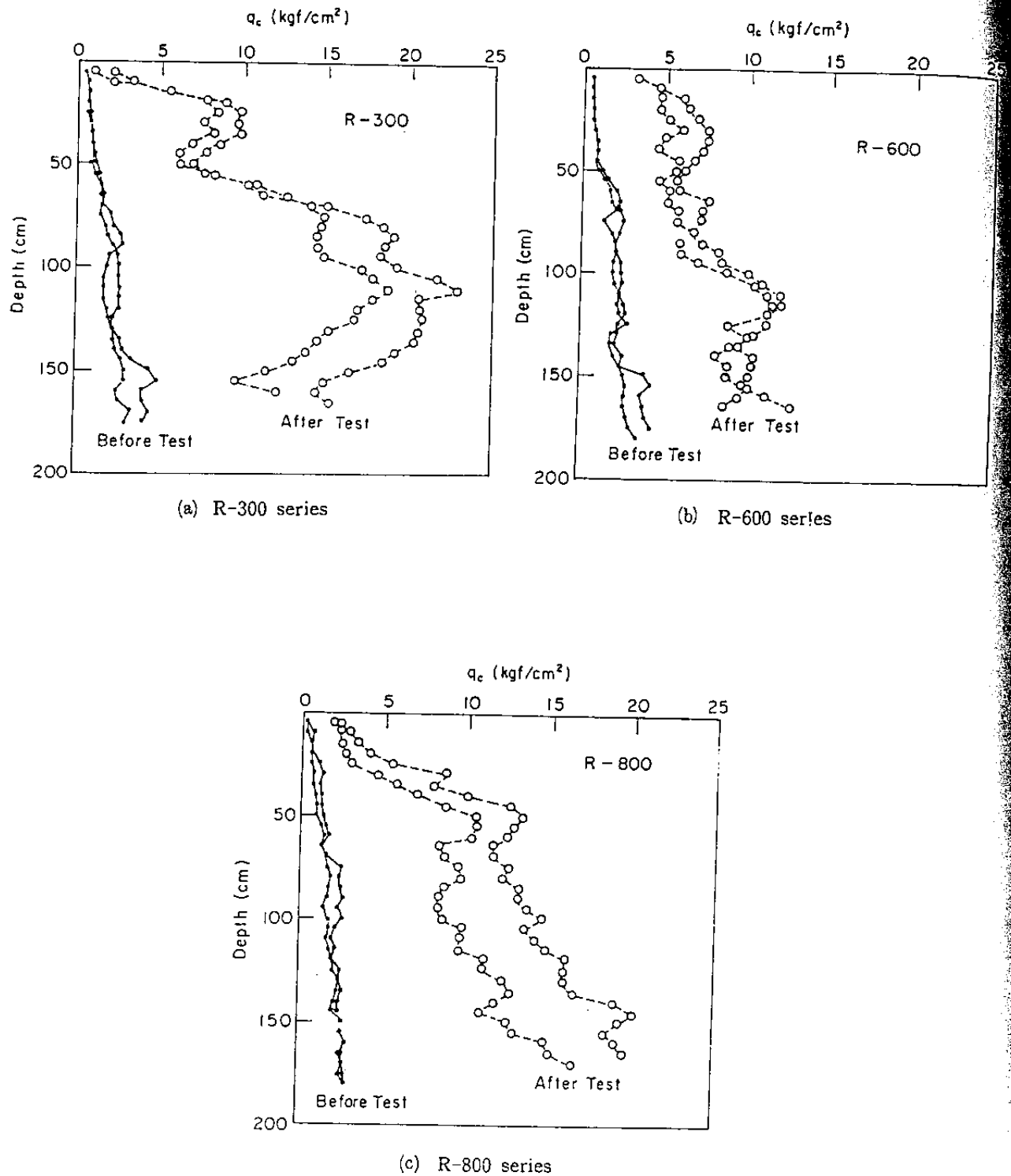


Fig. 4.17 Cone penetration resistances before and after shaking

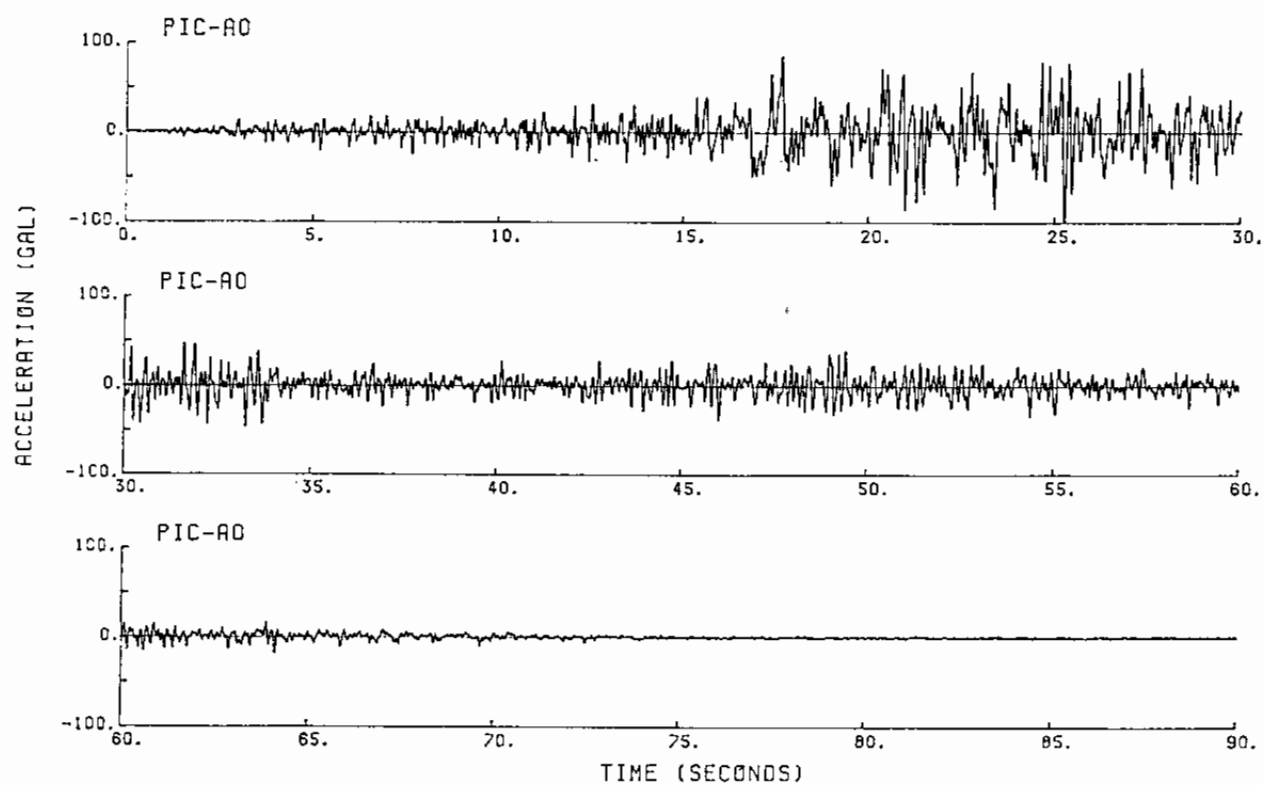


Fig. 4.18 Input earthquake motion used for R-800 series



Table 4.6 Levels of the input acceleration and result of maximum excess pore water pressure ratio

(a) R-300 series

Date: Nov. 19, 1984  
Temperature: 14°C in air

Case No.	$\alpha_{\max}$ (Gal)	$u_{\max}/\sigma_{v0}'$	$Dr$ (%)
R-301	5.5*	0.01	31.0
302	50	0.63	
303	81	1.01	
304	48	0.98	
(305)	—	—	
306	6.2*	0.15	
307	34	0.14	
308	49	0.15	
309	74	0.96	
310	68.5	0.92	
311	6.7*	0.02	
312	33.5	0.08	
313	47	0.14	
314	76	0.89	
315	107	0.81	
316	5.4*	—	65.7

 $\alpha_{\max}$ : Max. Acceleration of Input Motion $u_{\max}/\sigma_{v0}'$ : Max. Excess Pore Water

Pressure Ratio at P 23

 $Dr$ : Relative Density

\*: Resonant Test

(b) R-600 series

Date: Dec. 17, 1984  
Temperature: 13°C in water  
13.5°C in air

Case No.	$\alpha_{\max}$ (Gal)	$u_{\max}/\sigma_{v0}'$	$Dr$ (%)
R-601	3.4*	0.01	28.7
602	30.0	0.16	(29.0)
603	84.0	1.01	(39.6)
604	61.0	1.03	(47.6)
605	9.1*	0.03	—
606	59.5	0.99	(52.8)
607	59.5	0.97	(56.7)
608	13.1*	0.02	58.2

 $\alpha_{\max}$ : Max. Acceleration of Input Motion $u_{\max}/\sigma_{v0}'$ : Max. Excess Pore Water

Pressure Ratio at P 13

 $Dr$ : Relative Density, ( ) is obtained by settlement gauges

\*: Resonant Test

(c) R-800 series

Date: Jan. 12, 1985  
Temperature: 9°C in water  
10°C in air

Case No.	$\alpha_{\max}$ (Gal)	$u_{\max}/\sigma_{v0}'$	$Dr$ (%)
R-801	7.0*	0.01	25.3
802	104.5	0.90	(29.1)
803	157.6	0.98	(34.6)
804	226.4	1.02	(40.8)
805	8.5*	0.02	—
806	95.9	0.55	(42.0)
807	150.7	0.55	(43.6)
808	192.5	0.57	(45.3)
809	13.4*	0	46.3

 $\alpha_{\max}$ : Max. Acceleration of Input Motion $u_{\max}/\sigma_{v0}'$ : Max. Excess Pore Water

Pressure Ratio at P 13

 $Dr$ : Relative Density, ( ) is obtained by settlement gauges

\*: Resonant Test

stress history.

## 4.2 Results of the Model Tests

### 4.2.1 Results for Sinusoidal Input Motion

#### (1) Excess pore water pressure

When the model ground is shaken by the sinusoidal input motion of 2 Hz for the duration of 10 seconds, excess pore water pressures gradually increase as shown in Figs. 4.19 through 4.22. Levels of the input motions at the shaking table are 30, 50, 81 and 84 Gals in the cases R-602, R-302, R-303 and R-603, respectively, and the results for sinusoidal input motions are shown in this order. The alphabet and number appearing at the beginning part of each time history, e.g. "PIC-P12", corresponds to that given to each instrument shown in Fig. 4.2. In Figs. 4.19 through 4.22, excess pore water pressures are normalized by the initial vertical effective stresses at each location of the instrument. Layout of the time histories shown in those figures approximately corresponds to that of the instruments if the lower half of the figures could be moved to the right side of the upper half.

The maximum pore water pressure ratios attained in these tests are about 0.2 and 0.6 in the cases R-602 and R-302, respectively. The ratios reach 1.0 at about 3 seconds in the case R-303 and at about one second earlier than this in the case R-603. Initial relative densities of the model grounds are about 29 % in all of the cases and hence the difference in the levels

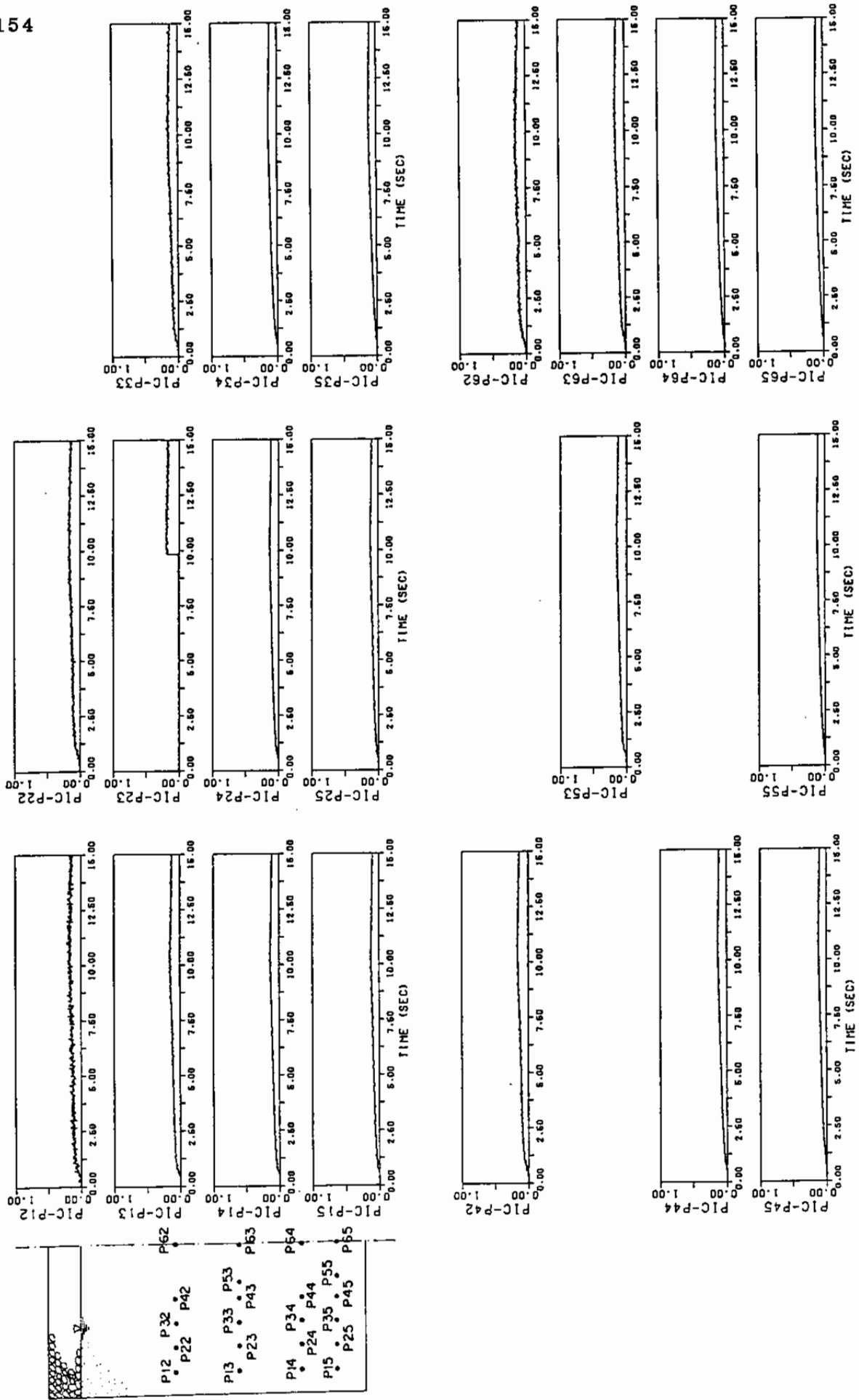


Fig. 4.19 Measured excess pore water pressure ratios in Case R- 602; 30 Gals

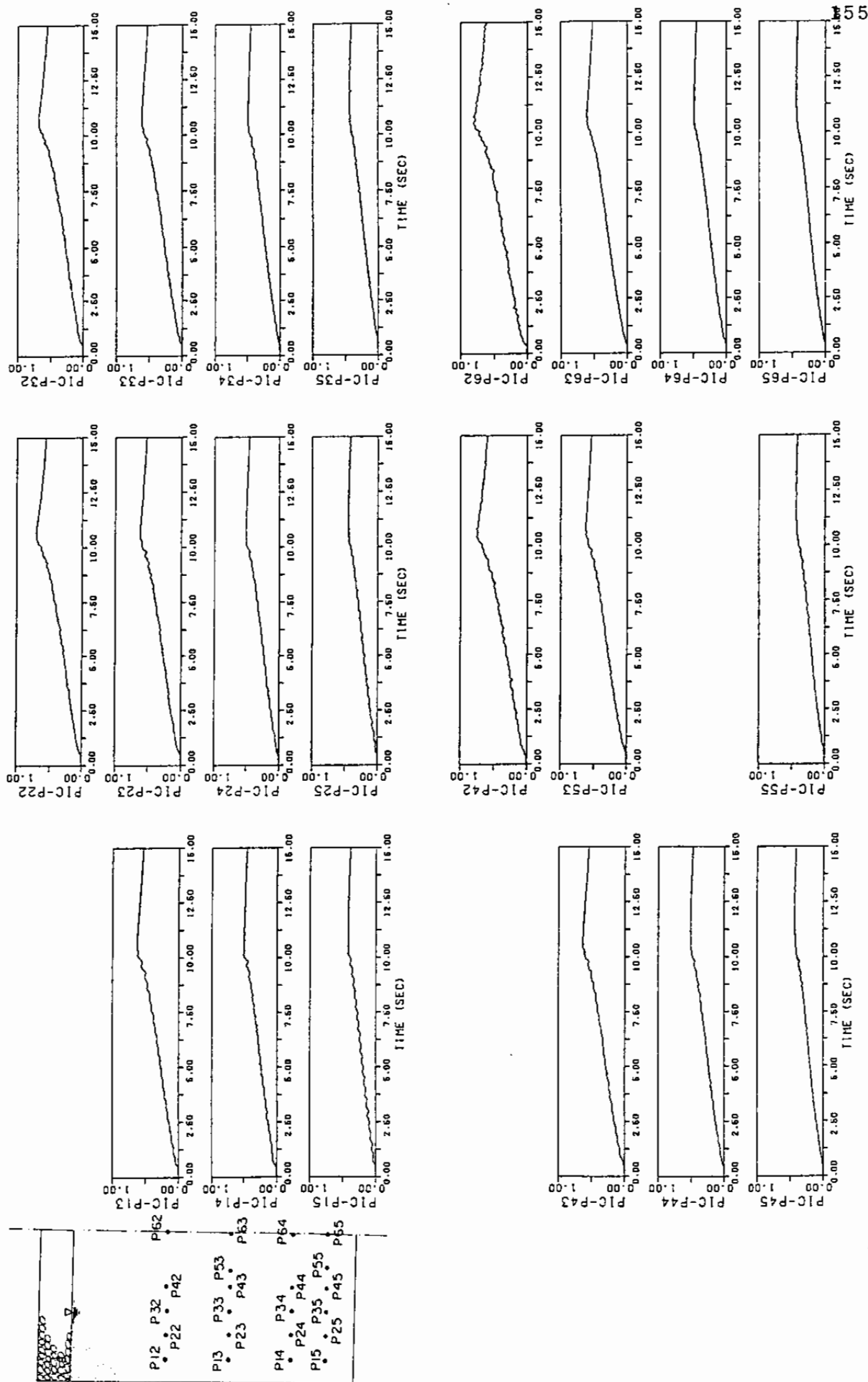


Fig. 4.20 Measured excess pore water pressure ratios in Case R-302; 50 Gals

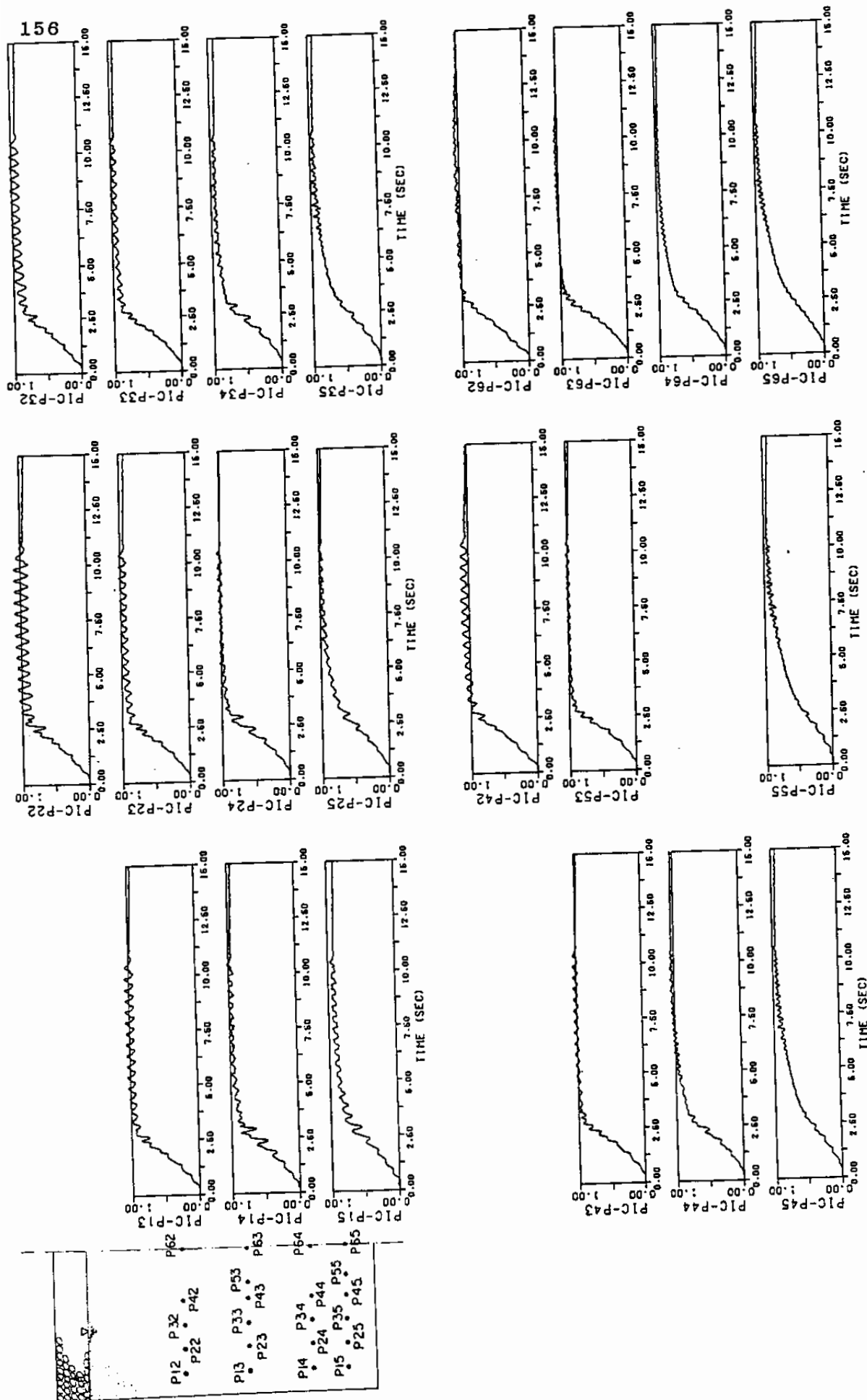


Fig. 4.21 Measured excess pore water pressure ratios in Case R-303; 81 Gals

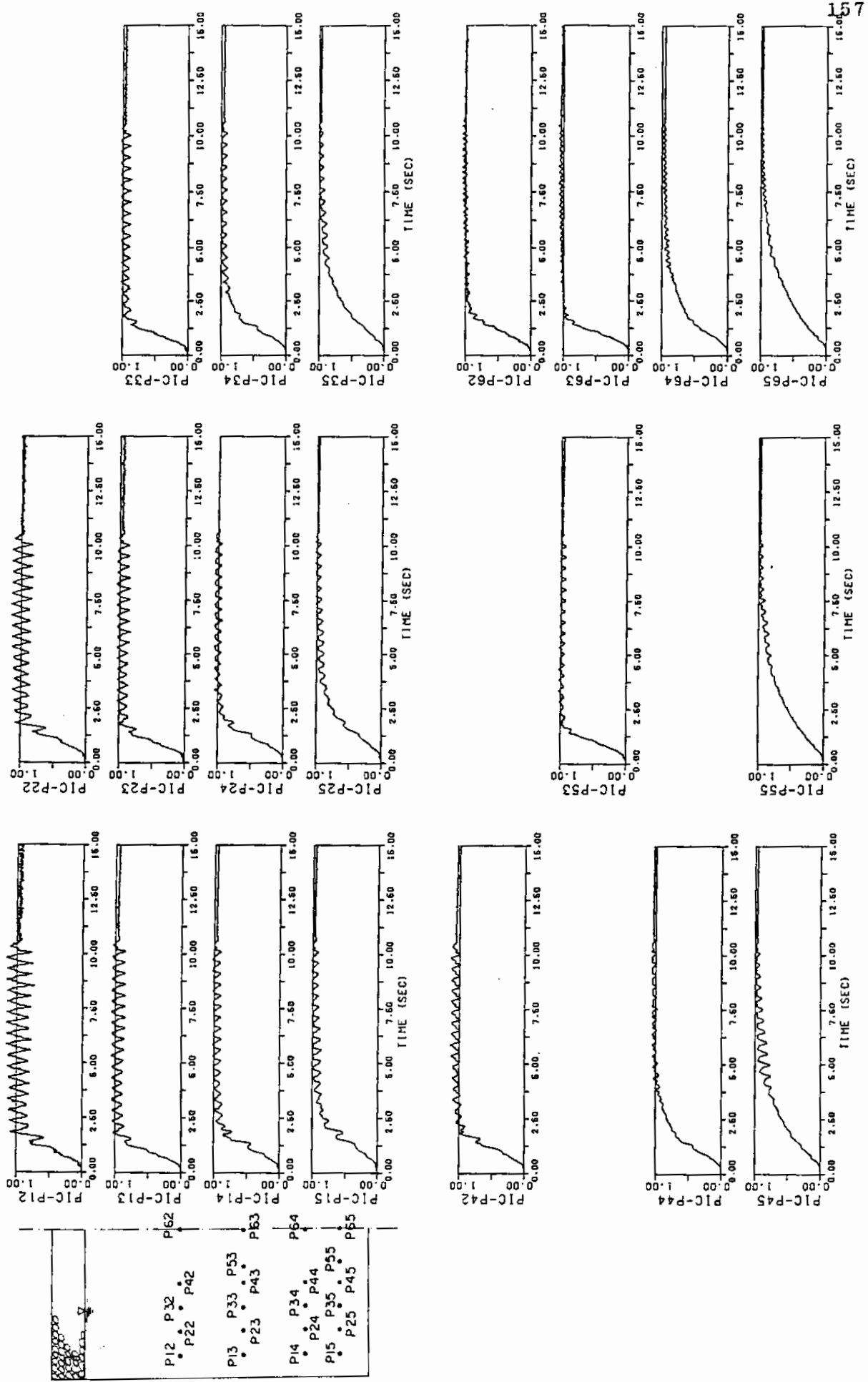


Fig. 4.22 Measured excess pore water pressure ratios in Case R- 603; 84 Gals

of the shaking might be a main cause for the varying degree of excess pore water pressure generation.

Some possibility was anticipated of an arching effect due to the friction between the rubber membrane and the model ground and hence of non-uniformity in the excess pore water pressures measured at the same depth in the model ground. The results shown in Figs. 4.19 through 4.22, however, assure that uniformity is indeed achieved throughout the model ground in the excess pore water pressures measured at the same depth.

When the shaking stops at 10 seconds, the excess pore water pressures begin to decrease. Obviously effect of dissipation of excess pore water pressures is involved not only after the shaking but also during the shaking. The rate of decrease in excess pore water pressures is, as shown in those figures, slower than the rate of increase during the 10 seconds of shaking, indicating that the dissipation during the shaking in these tests has a minor effect relative to that of the excess pore water pressure generation. In consequence, the increasing part of excess pore water pressures in these tests is basically approximated with the mechanism of undrained behavior of saturated sand.

## (2) Accelerations and displacements

A dynamic response of the model ground corresponding to those excess pore water pressures results in the accelerations and displacements shown in Figs. 4.23 through 4.26. The alphabet and number for each time history, e.g. PIC-A15, corresponds to that of each instrument shown in Fig. 4.2. In particular, the

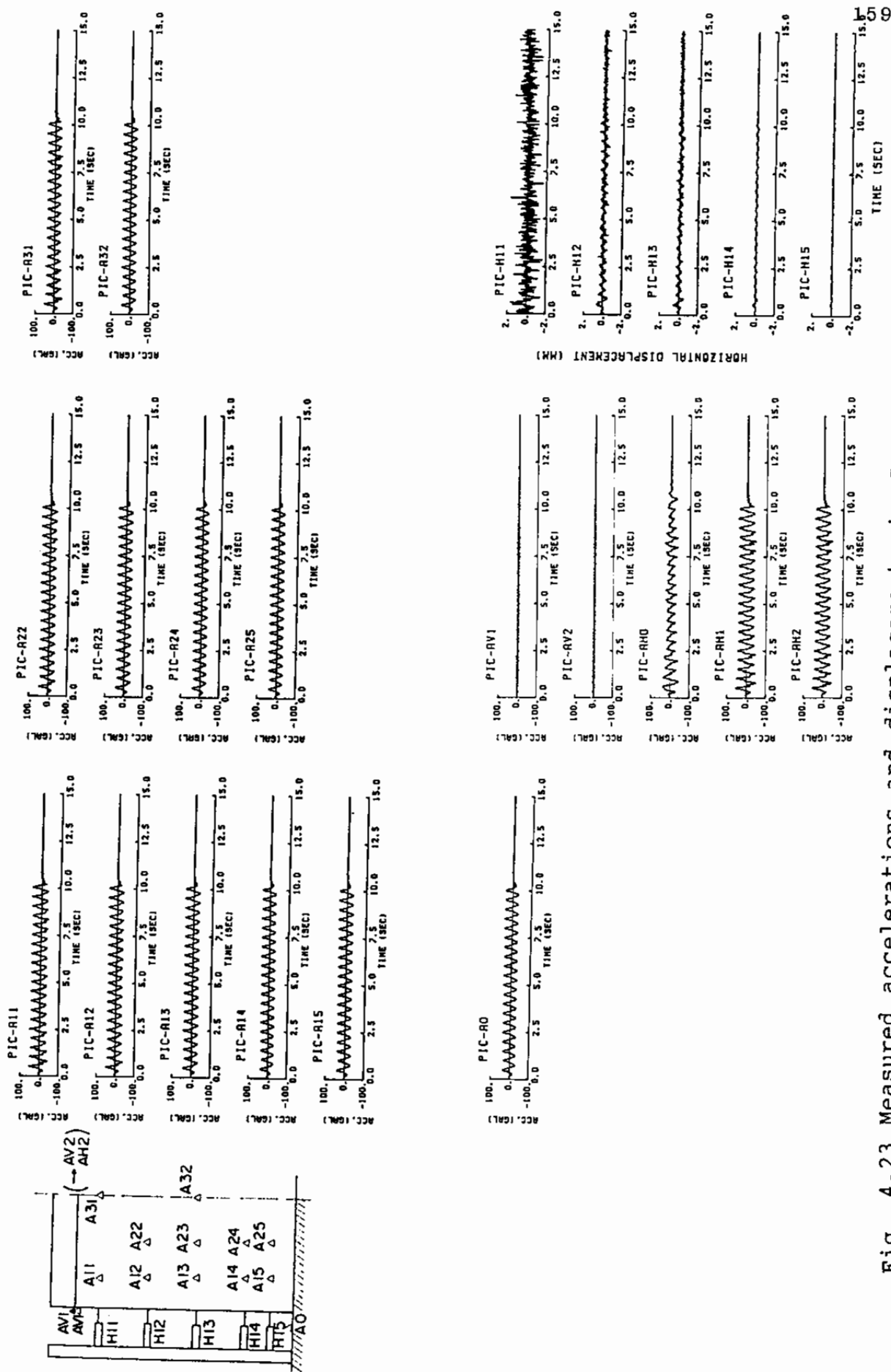


Fig. 4.23 Measured accelerations and displacements in Case R-602; 30 Gals



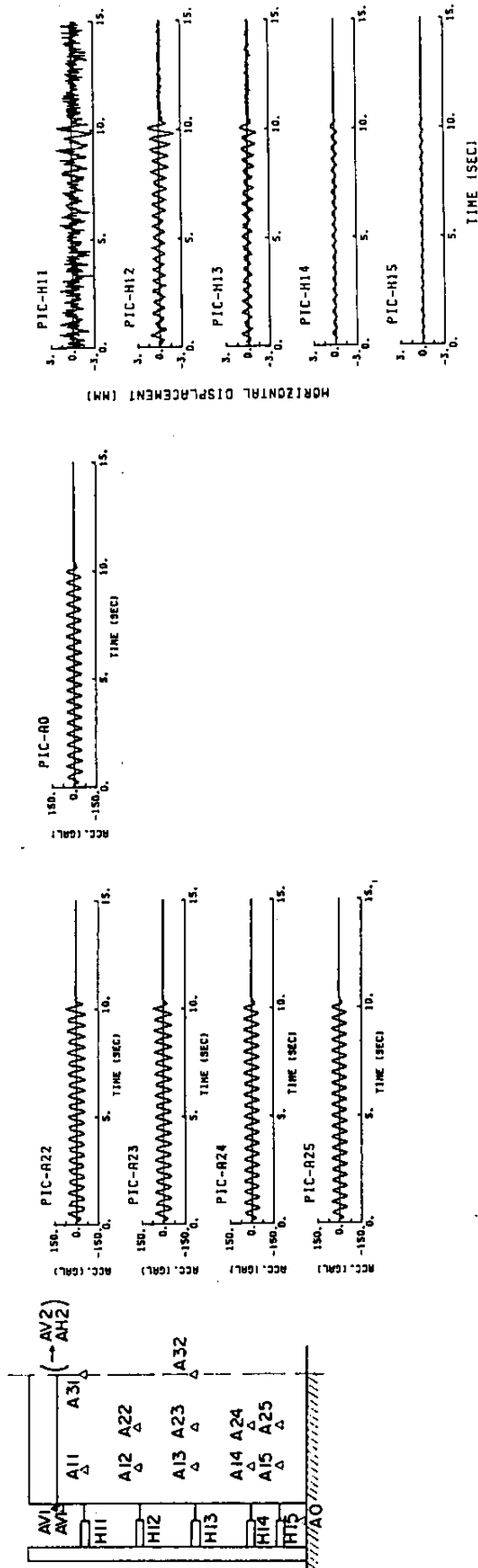


Fig. 4.24 Measured accelerations and displacements in Case R-302; 50 Gals

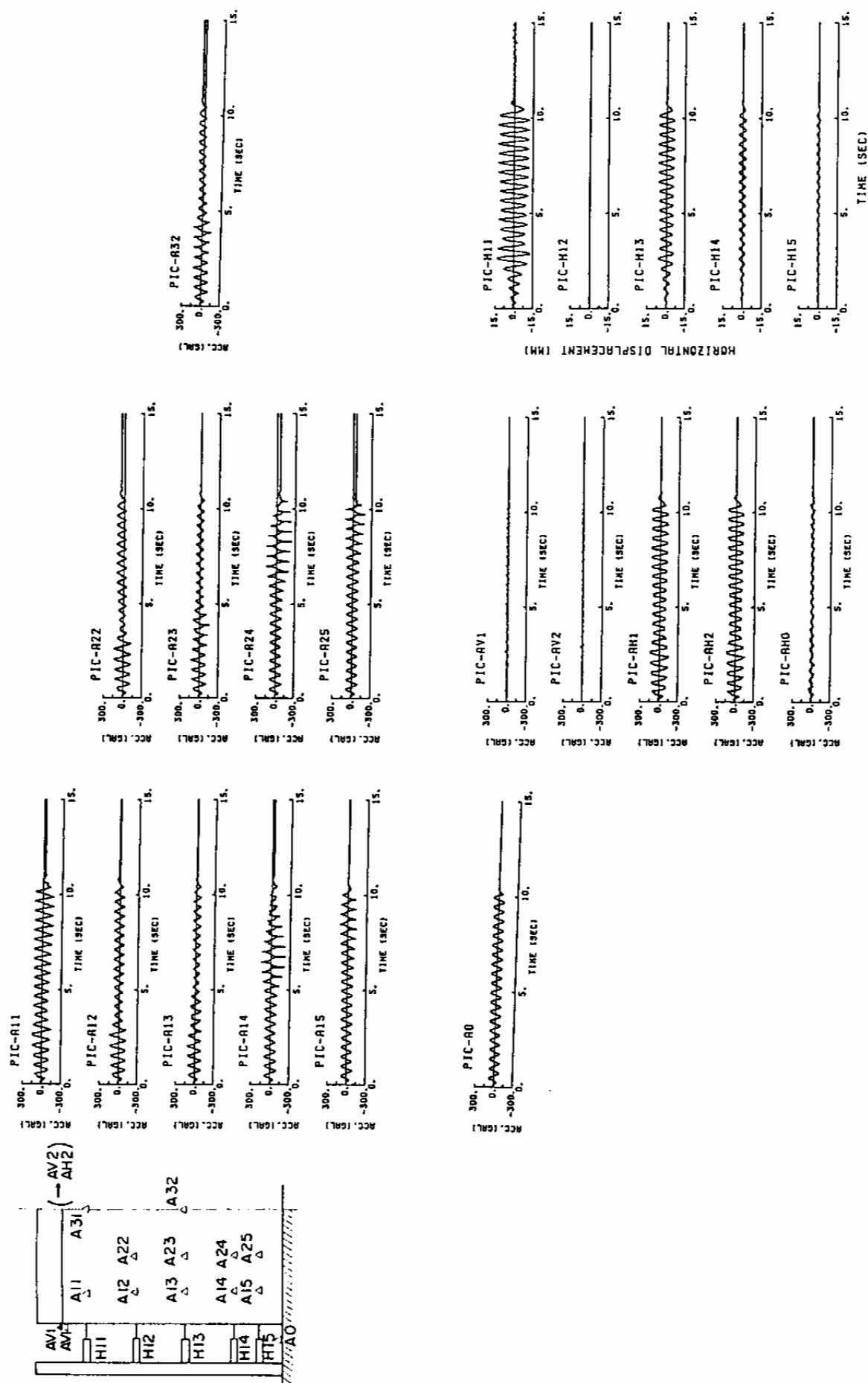


Fig. 4.25 Measured accelerations and displacements in Case R-303; 81 Gals

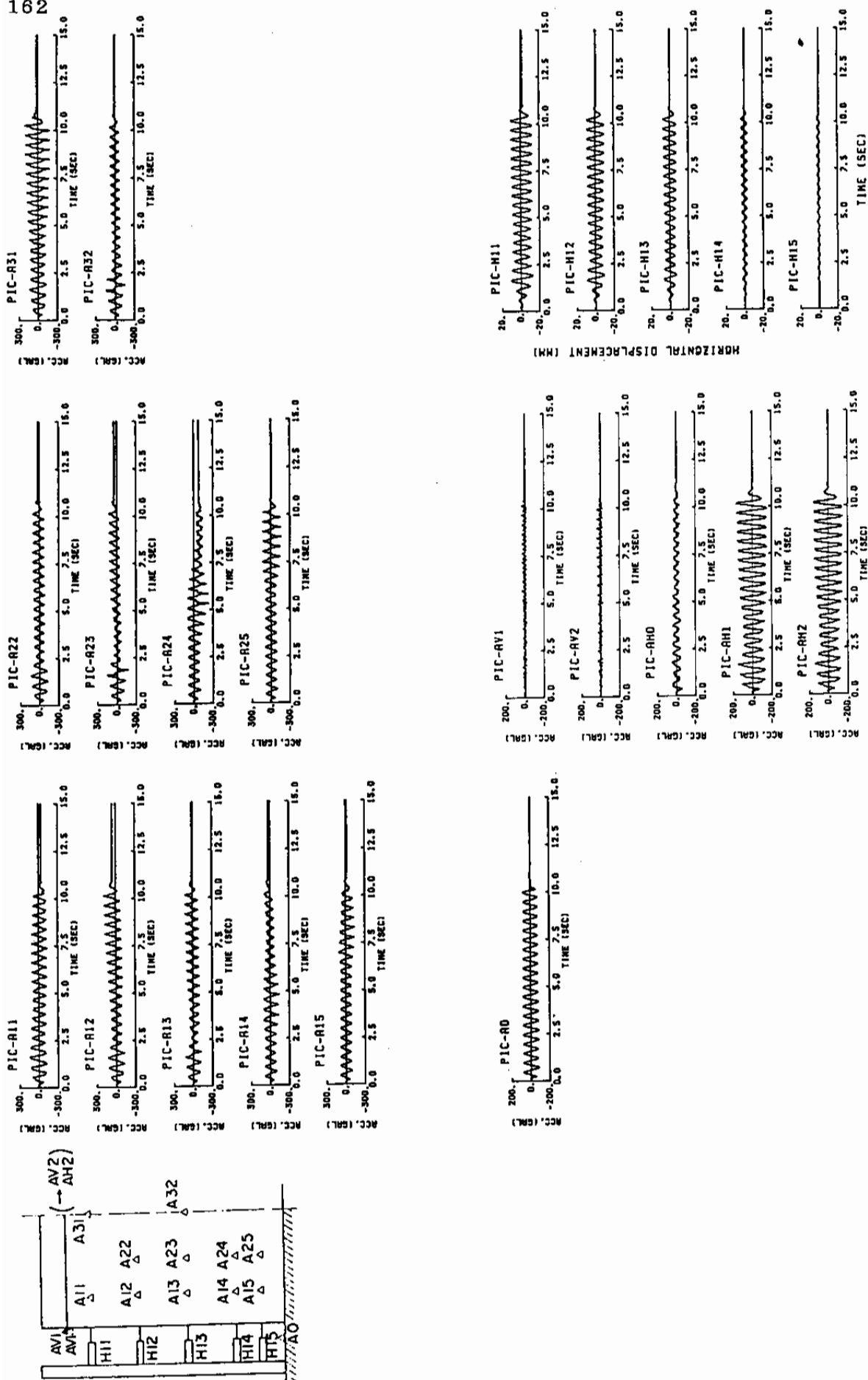


Fig. 4.26 Measured accelerations and displacements in Case R-603; 84 Gals

time history of  $A_0$ , shown in the lower left corner, is the acceleration of the shaking table. The time history of  $A_{H0}$ , shown at the third row in the center column of the lower half of the figures, is the horizontal acceleration of the load put on the top edge of the container for suppressing the rocking motion of the model ground, the time histories of  $AV_1$  and  $AV_2$ , shown above that of  $A_{H0}$ , are the vertical acceleration of the top edge of the container for detecting rocking motion. Those of  $A_{H0}$ ,  $AV_1$  and  $AV_2$ , in an ideal case, should show a null sequence (i.e. zero acceleration). In Figs. 4.23 through 4.26, those of  $AV_1$  and  $AV_2$  show that rocking motion is indeed suppressed but that of  $A_{H0}$  shows some amount of friction force is transmitted through the ball bearings between the load and the top edge of the container.

In order to see the relation among excess pore water pressure, acceleration and displacement, typical time histories are reproduced in Figs. 4.27 through 30 with the distribution of the maximum excess pore water pressure ratios in Fig. 4.31. These figures indicate that, when the excess pore water pressures reach about half of the initial vertical effective stress, the amplitudes of displacements significantly increase. Some changes are also recognized in the acceleration but they are not very remarkable partly because the aforementioned adverse effect exists due to the friction force transmitted from the load put on the top edge of the container.

#### 4.2.2 Response for Earthquake Input Motion

##### (1) Excess pore water pressure

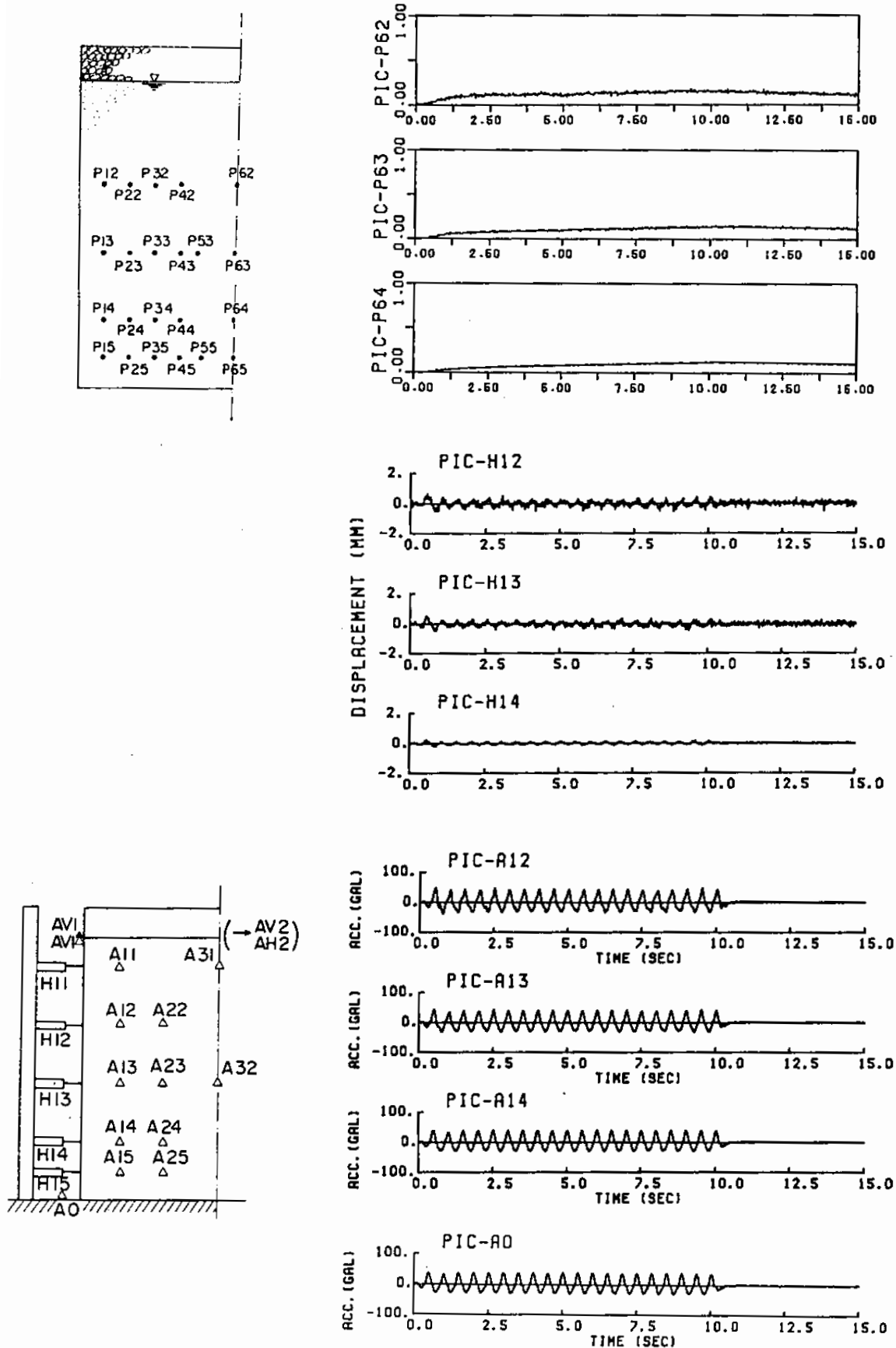


Fig. 4.27 Summary results in Case R-602

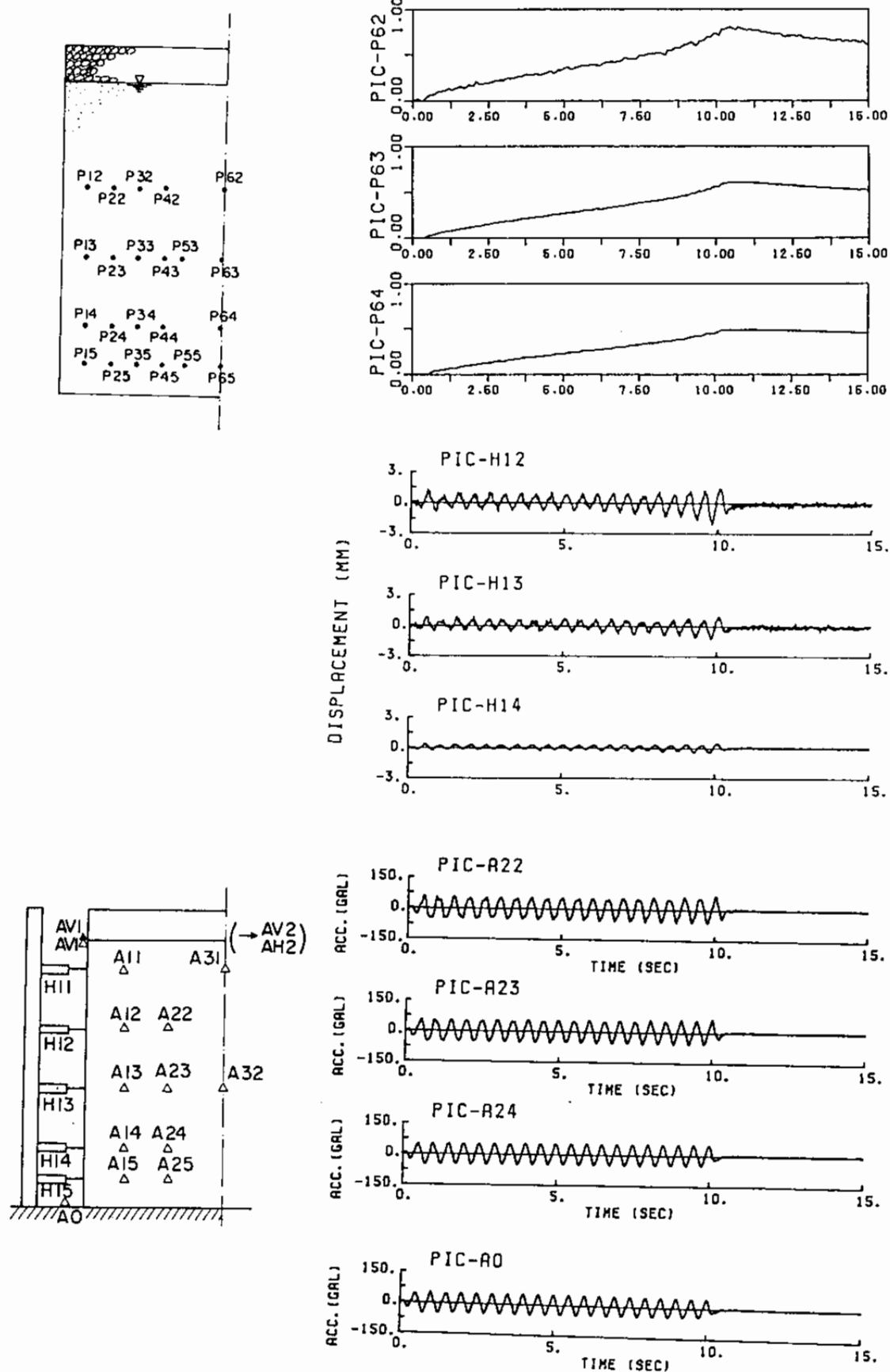


Fig. 4.28 Summary results in Case R-302

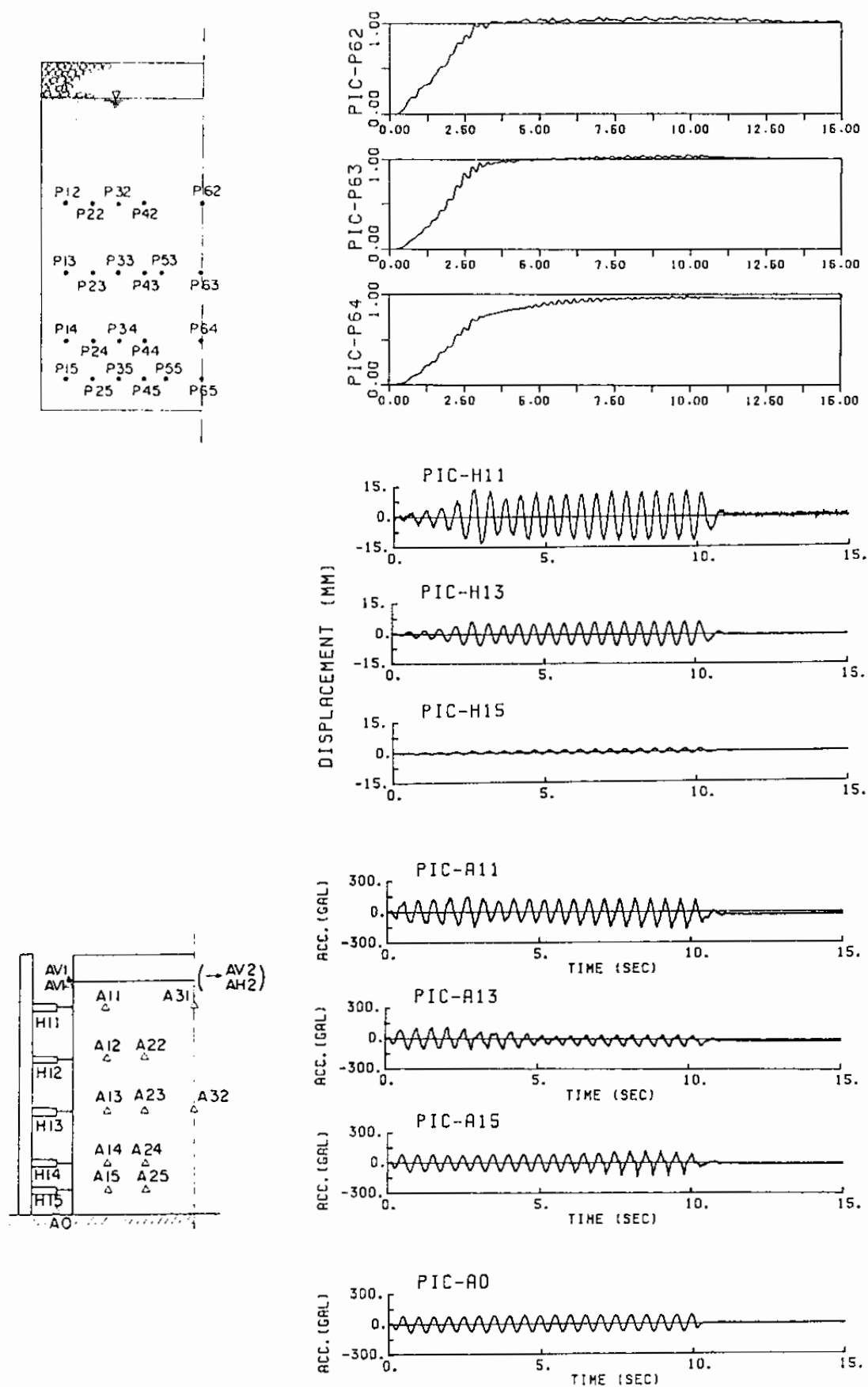


Fig. 4.29 Summary results in Case R-303

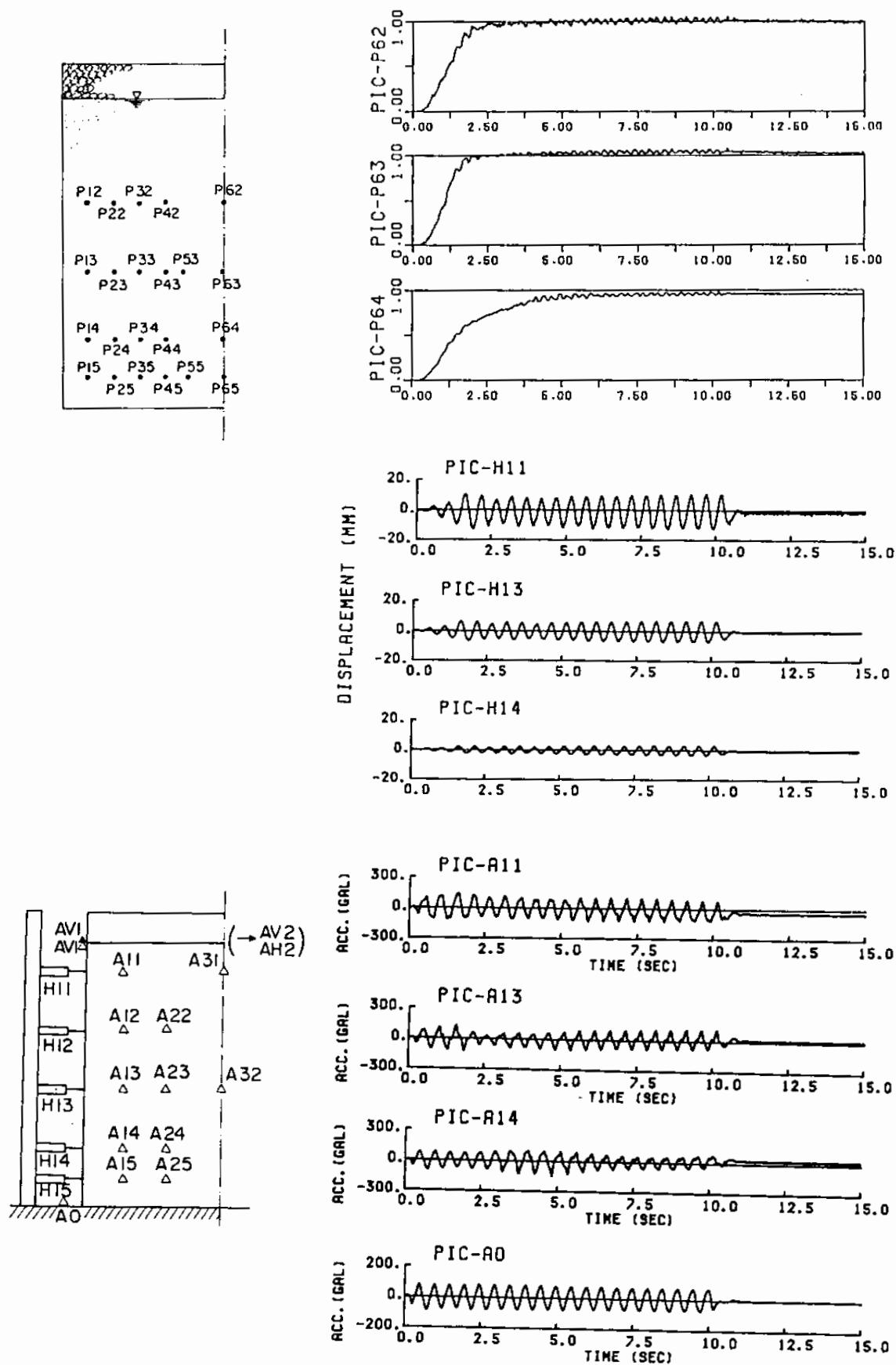


Fig. 4.30 Summary results in Case R-603



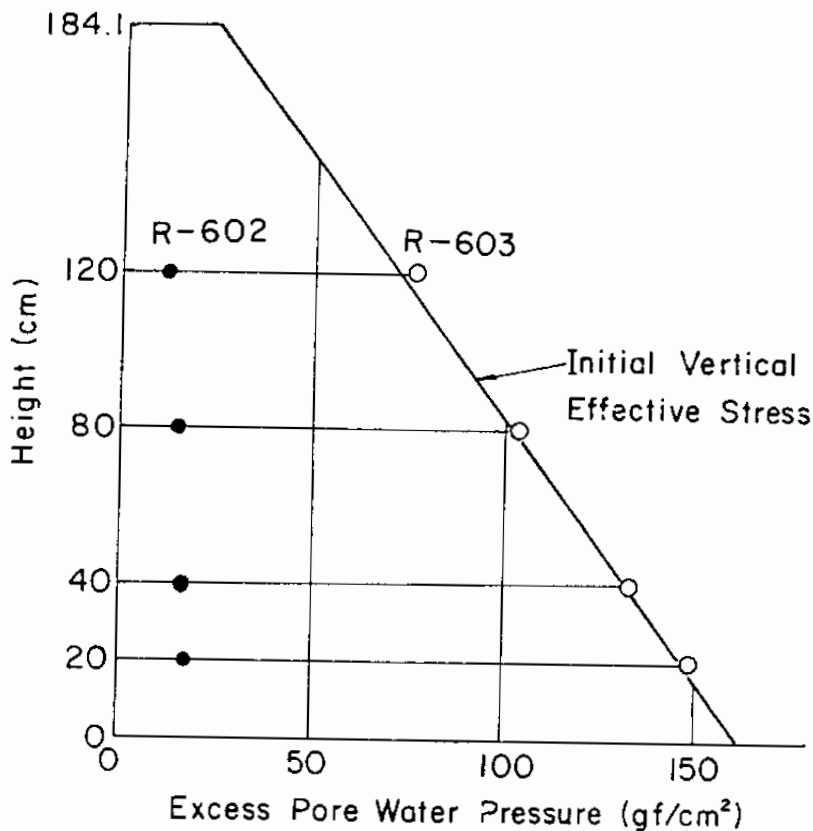
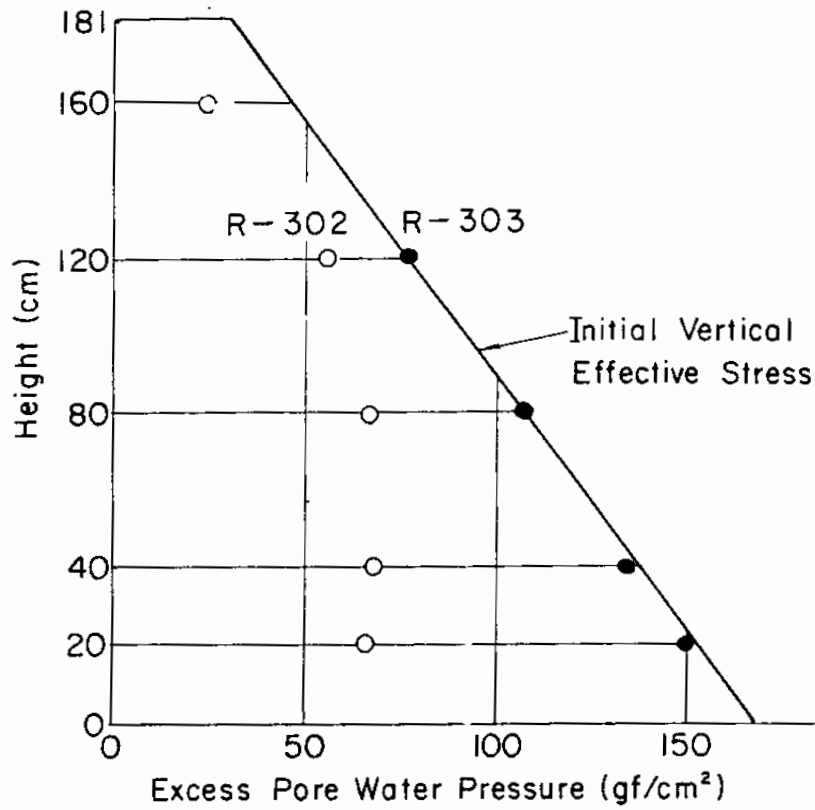


Fig. 4.31 Distribution of maximum excess pore water pressures in Case R-602, R-302, R-303 and R-603

Earthquake excitation is composed of various kinds of half cycles of waves; some are large, some are small, some are long, some are short, some contains high frequency components, some contains only low frequency components. If, for example, a strong pulse-like excitation is applied, excess pore water pressure will be increased virtually under the undrained condition. If a smaller excitations are repeated after this, excess pore water pressure will still be generated but effect of dissipation might be possibly stronger, resulting in the decrease in the excess pore water pressure even during the shaking.

This type of behavior of the model ground is recognized when the model ground is shaken by the earthquake input motion shown in Fig. 4.18 for the duration of 90 seconds. Excess pore water pressures gradually increase up to about 30 seconds as shown in Fig. 4.32 and after that they gradually decrease though the shaking continues in the smaller amplitude. The maximum acceleration of the input motion is 105 Gals measured at the shaking table.

If a closer look is directed to the time histories, instantaneous high rates of increase in excess pore water pressures are recognized at about 18 and 22 seconds. The maximum excess pore water pressure ratios attained in the test are about 1.0. Uniformity is confirmed in the excess pore water pressures measured at the same depth in the model ground. The rate of increase in the excess pore water pressures is much faster than that of decrease, indicating that increasing part of the excess pore water pressure in this test is basically approximated with the mechanism of undrained behavior of saturated sand.

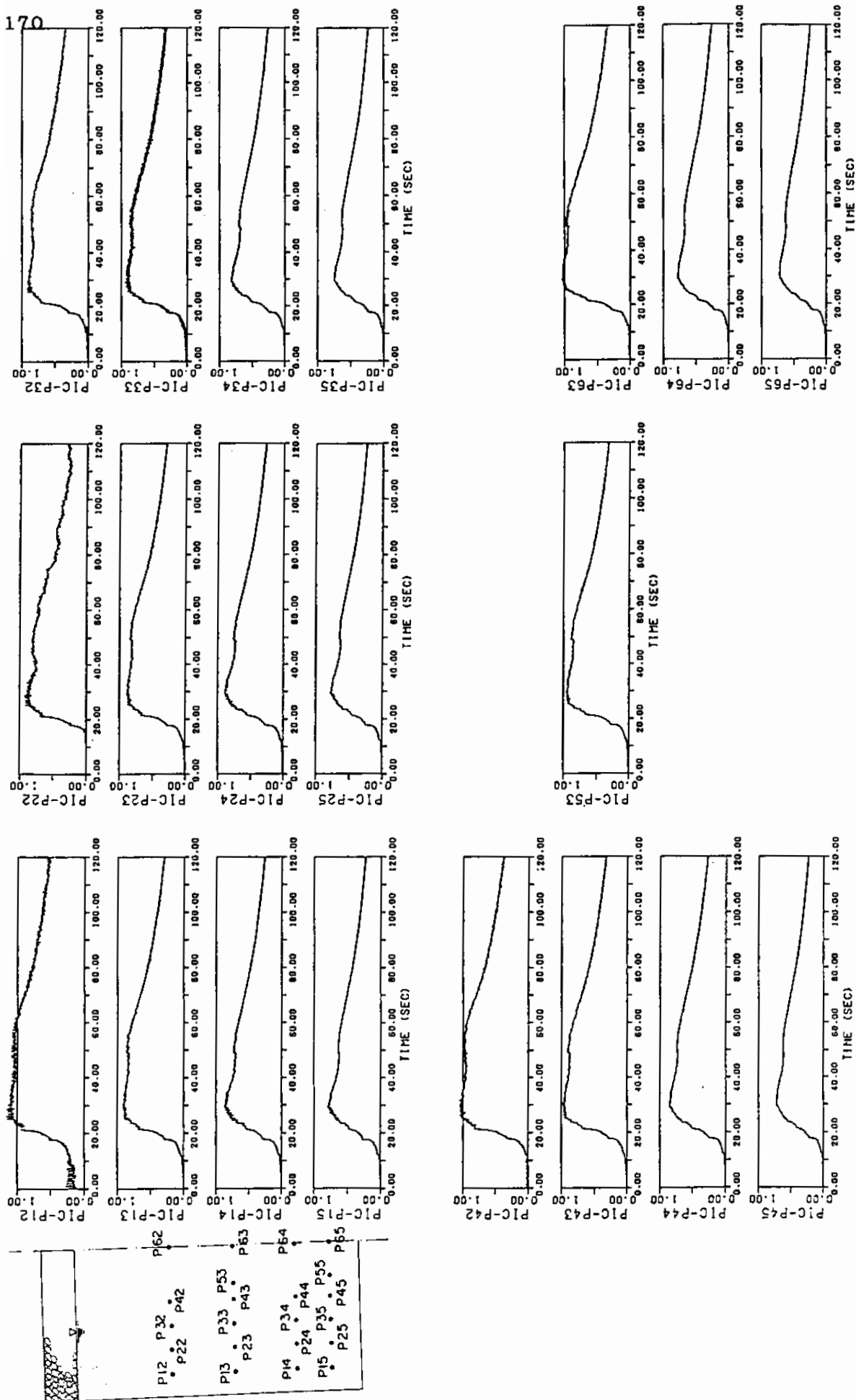


Fig. 4.32 Measure excess pore water pressure ratios in Case R-802; 105 Gals

## (2) Accelerations and displacements

A dynamic response of the model ground corresponding to those excess pore water pressures results in the accelerations and displacements shown in Figs. 4.33 and 4.34.

In order to see the relation among excess pore water pressure, acceleration and displacement, typical time histories are reproduced in Fig. 4.35 with the distribution of the maximum excess pore water pressure along depth in Fig. 4.36.

## 4.3 Soil Parameter Identification

As mentioned in Chapters 2 and 3, the proposed model needs 10 soil parameters to be specified in the analysis. Three parameters relate to the shear behavior of sand, the rest relate to the volumetric and dilatancy behavior.

### 4.3.1 Parameters for Shear Behavior

Parameters for shear behavior to be specified for the present model are elastic shear modulus  $G_{ma}$  at an effective confining pressure of  $\sigma_{ma}'$ , shear resistance angle  $\phi_f'$  and the limiting value of hysteretic damping factor  $H_m$  (i.e. the hysteretic damping factor at large shear strain amplitude.)

The elastic shear modulus  $G_{ma}$  in the present analysis is determined from the shear wave velocity measured through the impulse test. The effective confining pressure of  $\sigma_{ma}'$  is calculated at the middle level of the model ground by assuming  $K_0 = 0.5$ . The shear resistance angle  $\phi_f'$  is read off from Fig. 4.8 at the relative density of 29 %. Finally, the limiting value

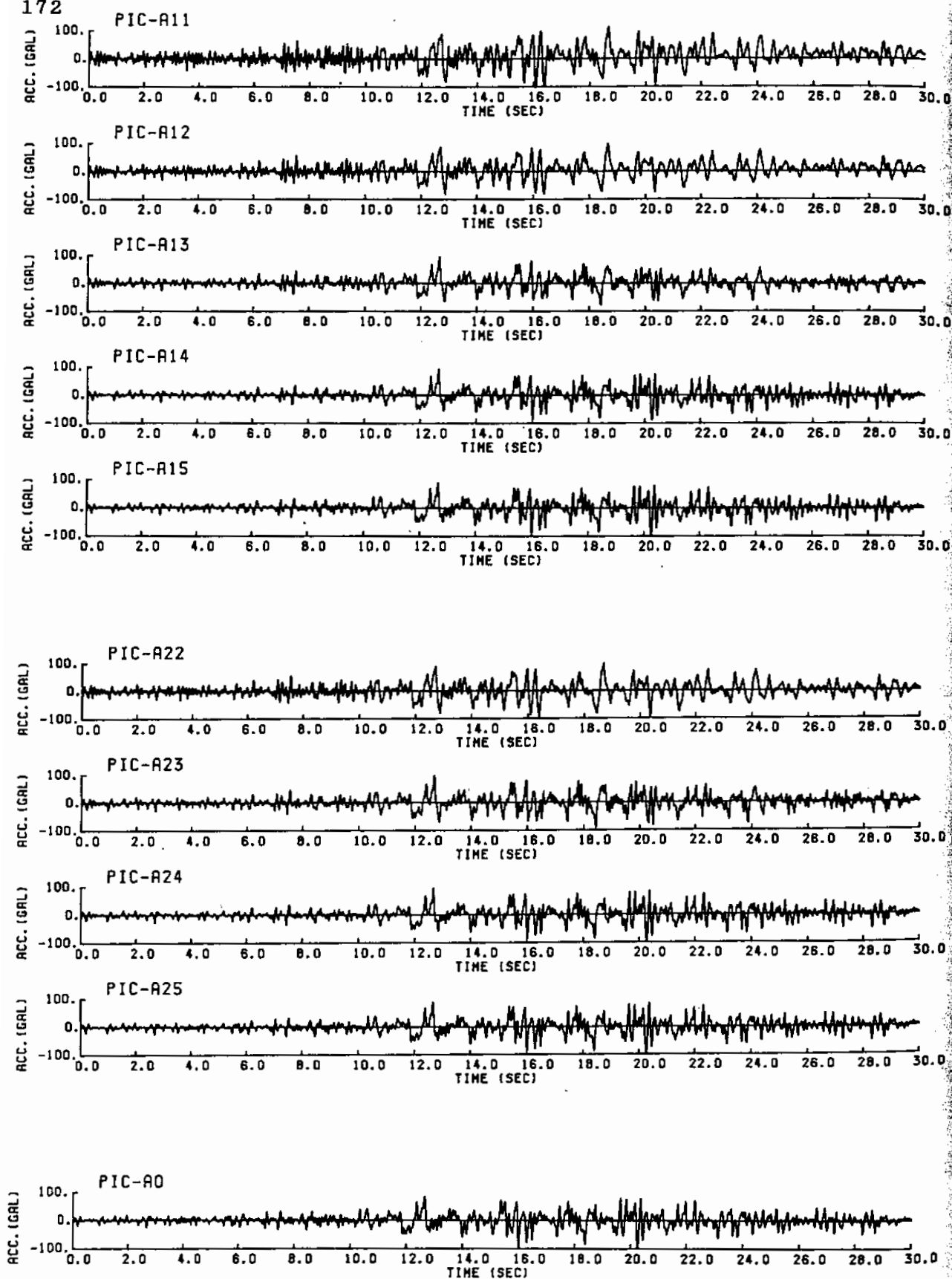


Fig. 4.33 Measured accelerations in Case R-802; 105 Gals

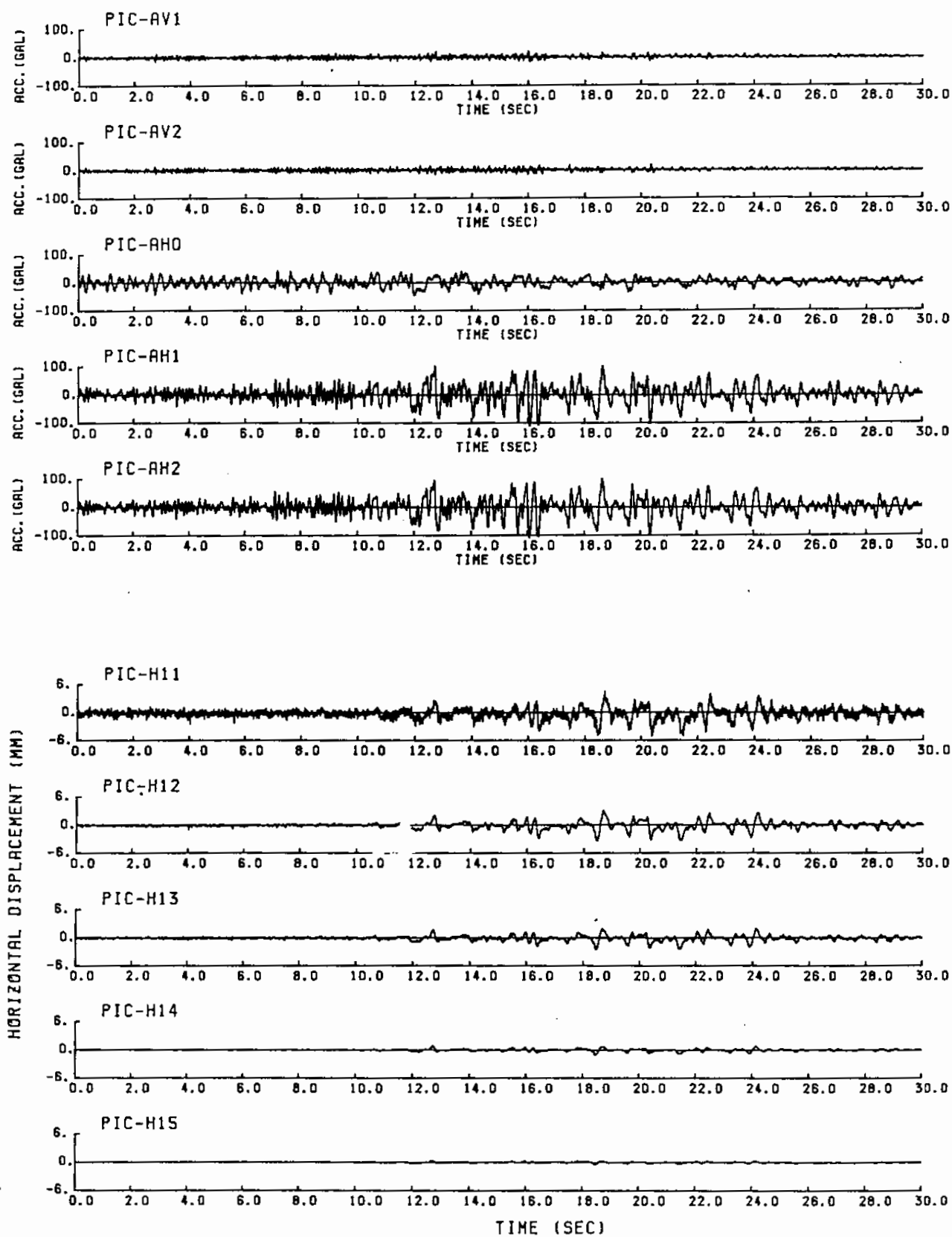


Fig. 4.34 Measured accelerations and displacements in Case R-802; 105 Gals

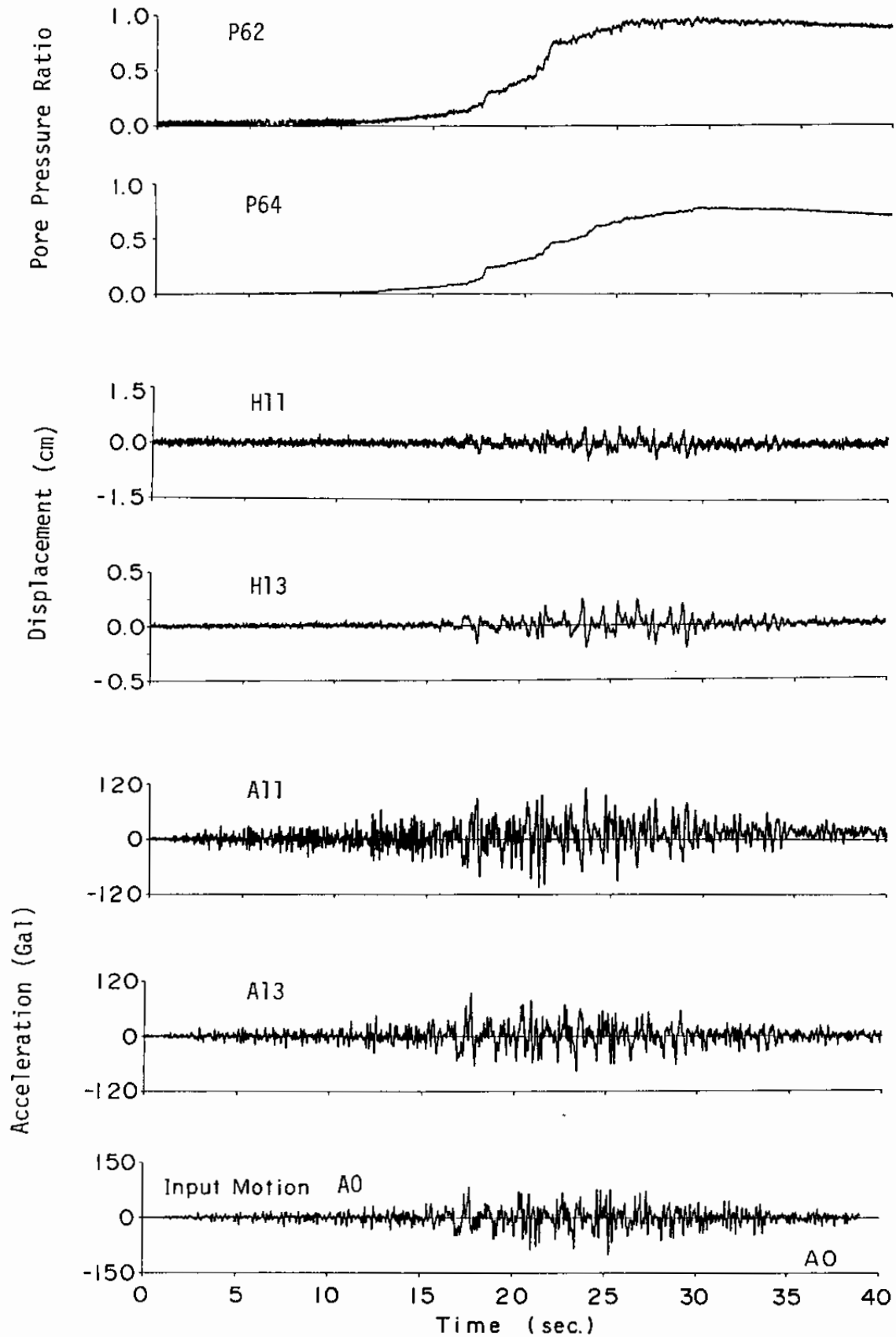


Fig. 4.35 Summary results in Case R-802

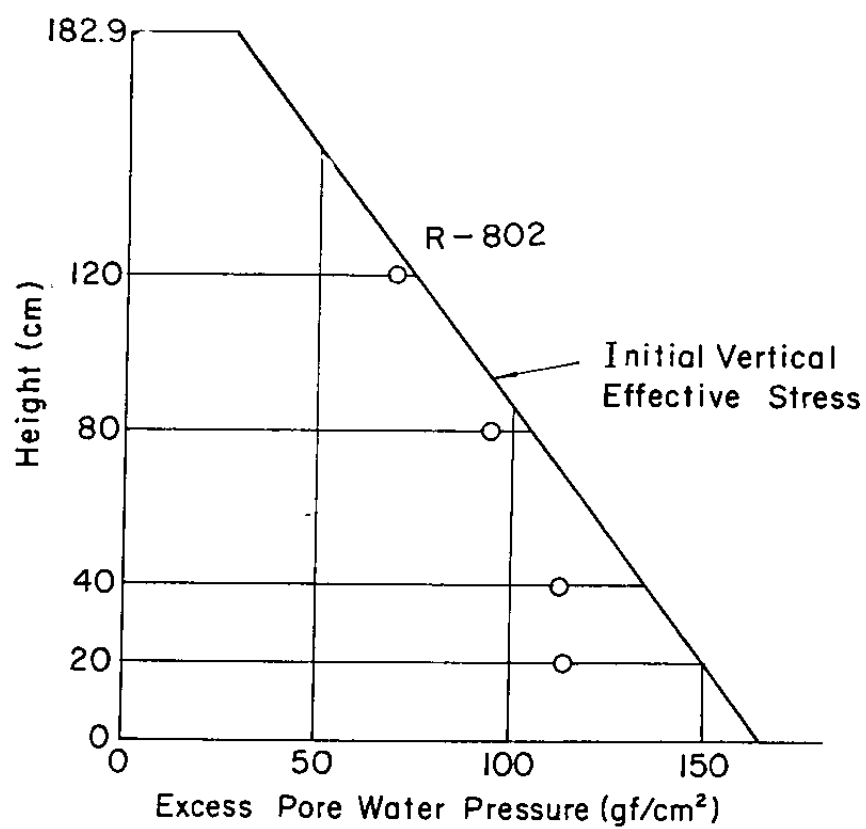


Fig. 4.36 Distribution of maximum excess pore water pressure in Case R-802



of hysteretic damping factor  $H_m$  is determined as 30 % by referring to the previous studies on the dynamic properties of sand shown in Fig. 1.5.

#### 4.3.2 Parameters for Volume Change

The parameters to be specified for volume change are the rebound modulus of soil skeleton  $K_a$  at the effective confining pressure of  $\sigma_{ma}'$ , phase transformation angle  $\phi_p'$  and the rest of five parameters  $p_1$ ,  $p_2$ ,  $w_1$ ,  $S_1$  and  $c_1$  defining dilatancy of cumulative volume decrease.

The rebound modulus of soil skeleton  $K_a$  is determined by assuming that Poisson's ratio is 0.3. This choice of Poisson's ratio brings the coefficient of earth pressure at rest about 0.5 when the initial static analysis is conducted with 1 g gravity. Unfortunately no laboratory data is found for suggesting the value of phase transformation angle of Gaiko sand. By referring to the phase angle of Kawagishi-cho Sand (Ishihara et al, 1989), phase transformation angle  $\phi_p'$  is assumed to be the round off value of 30 degrees.

The rest of five parameters  $p_1$ ,  $p_2$ ,  $w_1$ ,  $S_1$  and  $c_1$  are determined by the procedure mentioned in the Section 3.2 based on the laboratory data shown in Figs. 4.9 through 4.10. It is assumed that the undrained triaxial stress condition, with the initial isotropic consolidation condition, produces the soil behavior similar to that at the undrained plane strain condition. This assumption might be appeared rather crude at first sight but it can be justified as follows.

The present model is, as mentioned earlier, formulated for

simulating two dimensional behavior of soil as an approximation. If the present model is extended for three dimensional behavior of soil, additional virtual simple shear mechanisms will be necessary so that the virtual simple shear mechanisms are directed at arbitrary directions in the three dimensional space. With the extended model, there will be additional contribution from the additional virtual simple shear under either the triaxial or the plane strain conditions. Their contributions obviously will depend on the test conditions. There is, however, a common virtual simple shear mechanism of which contribution is predominant during these tests; i.e. the virtual simple shear mechanism oriented along the direction of cyclic shear loading. Consequently, though there is a difference between the soil behaviors during the two types of tests, the difference is considered minor.

The parameters thus determined are shown in Table 4.7. The computed liquefaction resistance curve and the excess pore water pressure rise are shown in Figs. 4.37 and 4.38. As shown in Fig. 4.38, the present model, with the aforementioned parameters for shear, does not give a good fit to the measured excess pore water pressure rise. If a better fit is attempted to the measured excess pore water pressure rise, then the shear strain amplitude becomes too large and a fit to the liquefaction resistance curve becomes worse. Thus, the parameters are determined as they are. The typical effective stress path and the stress strain curve computed by the present model are also shown in Fig. 4.39.

Table 4.7 Soil parameters for Gaiko sand

---

G <sub>ma</sub>	= 11400 kPa
K <sub>a</sub> (bulk modulus of soil skeleton)	= 24700 kPa
$\sigma'_{ma}$ (effective confining pressure	
for G <sub>ma</sub> and K <sub>a</sub> )	= 6.0 kPa
$\phi_f$ (effective friction angle)	= 37 degree
$\phi_p$ (phase transformation angle)	= 30 degree
S <sub>1</sub>	= 0.005
w <sub>1</sub>	= 5.95
p <sub>1</sub>	= 0.5
p <sub>2</sub>	= 0.9
c <sub>1</sub>	= 1.8

---

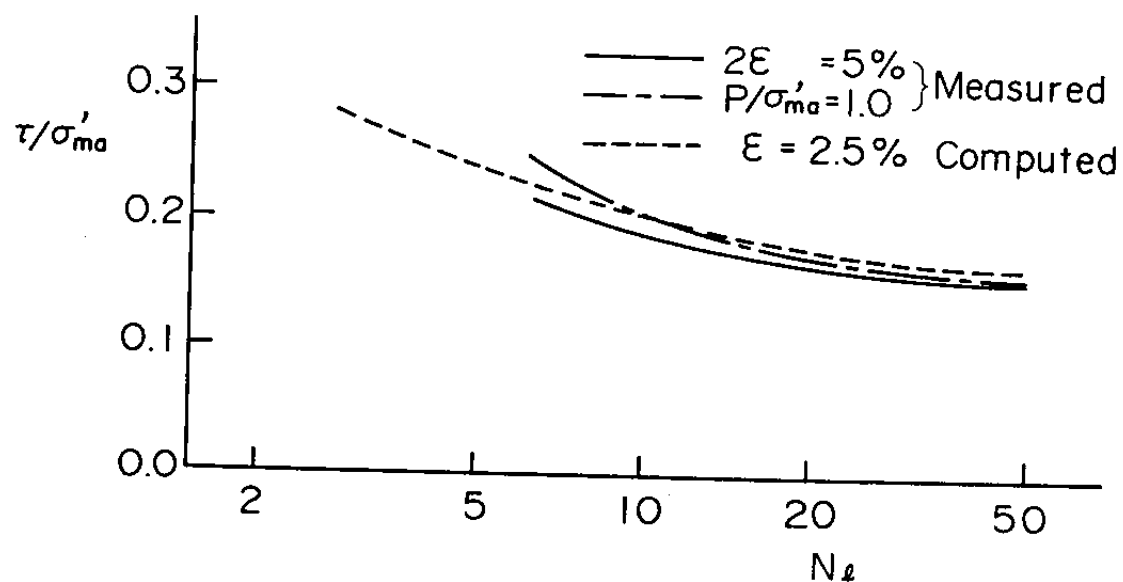


Fig. 4.37 Computed and measured liquefaction resistance curves

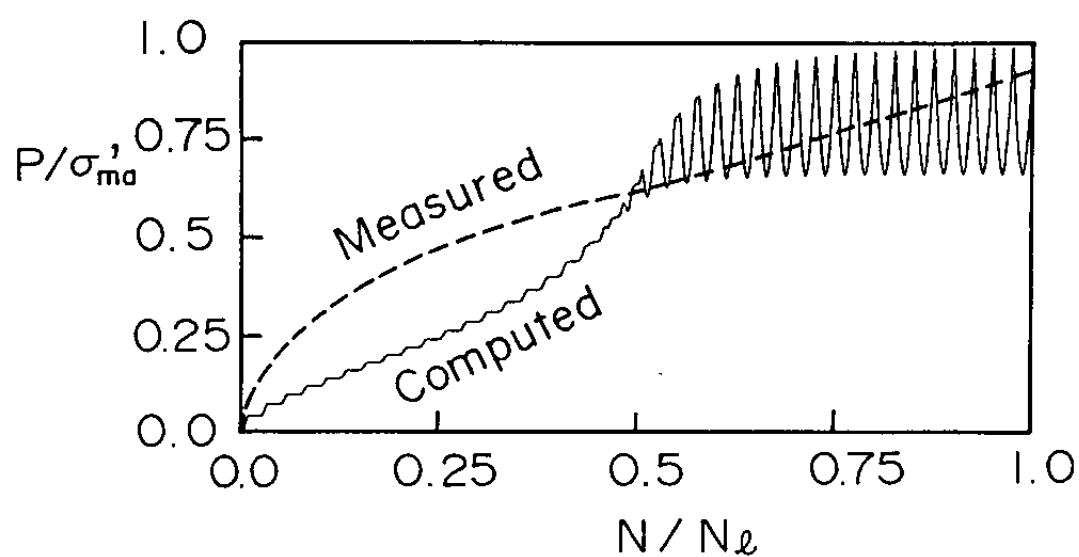


Fig. 4.38 Computed and measured pore water pressure rise

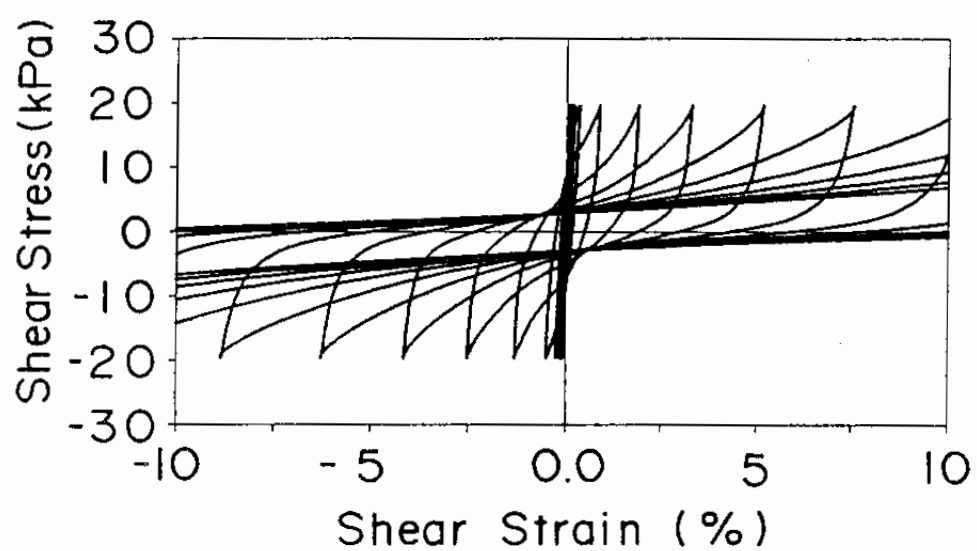
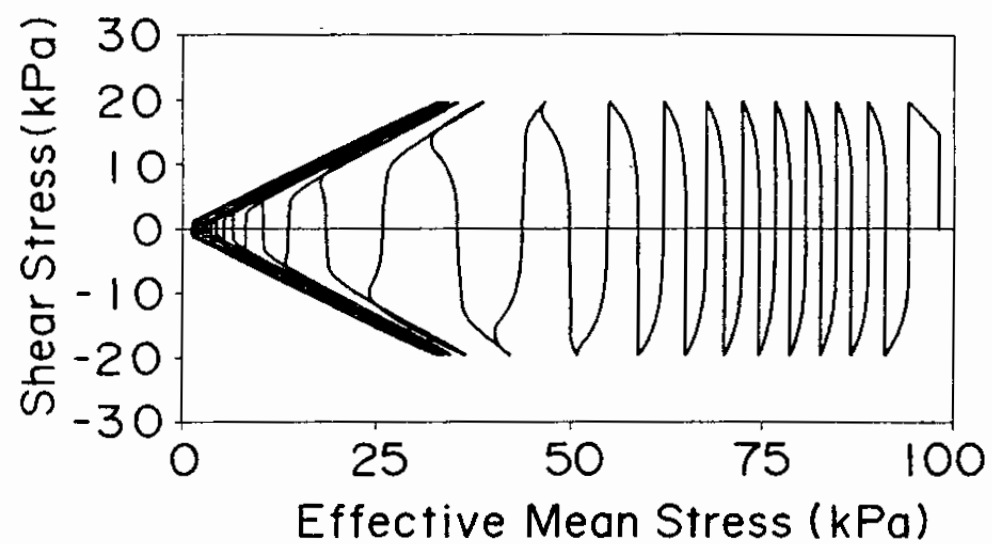


Fig. 4.39 Computed undrained cyclic behavior of Gaiko sand

## 4.4 Analysis of Level Model Ground

### 4.4.1 Response to Sinusoidal Input Motion

The response of the model sand deposit is computed by representing the continuous soil deposit with 20 soil layers of finite elements as shown in Fig. 4.40. For ensuring stability in the numerical analysis, small amount of Rayleigh damping is used with  $\alpha = 0$  and  $\beta = 0.0001$ . Rayleigh damping is gradually reduced in accordance with the progress of cyclic mobility. Time integration is done by Wilson's  $\theta$ -method with  $\theta = 1.4$  and time interval of  $\Delta t = 0.01$  seconds. For simplicity, the response is computed with the undrained condition.

#### (1) Excess Pore Water Pressure

When the level model ground is shaken in the case R-602 with the maximum acceleration of 30 Gals, the excess pore water pressures are computed as shown in Fig. 4.41. In this figure, pressures are normalized with the initial effective vertical stress at each depth. There is such a tendency that the computed excess pore water pressures show a sudden increase at the first half cycle of loading whereas there is none in the measured ones. The overall trend, however, is such that the computed and the measured excess pore water pressures are in accord with each other.

When the model ground is shaken in the case R-302 with the maximum acceleration of 50 Gals, the excess pore water pressures are computed as shown in Fig. 4.42. At the middle depth of the level ground, the computed and the measured excess pore water

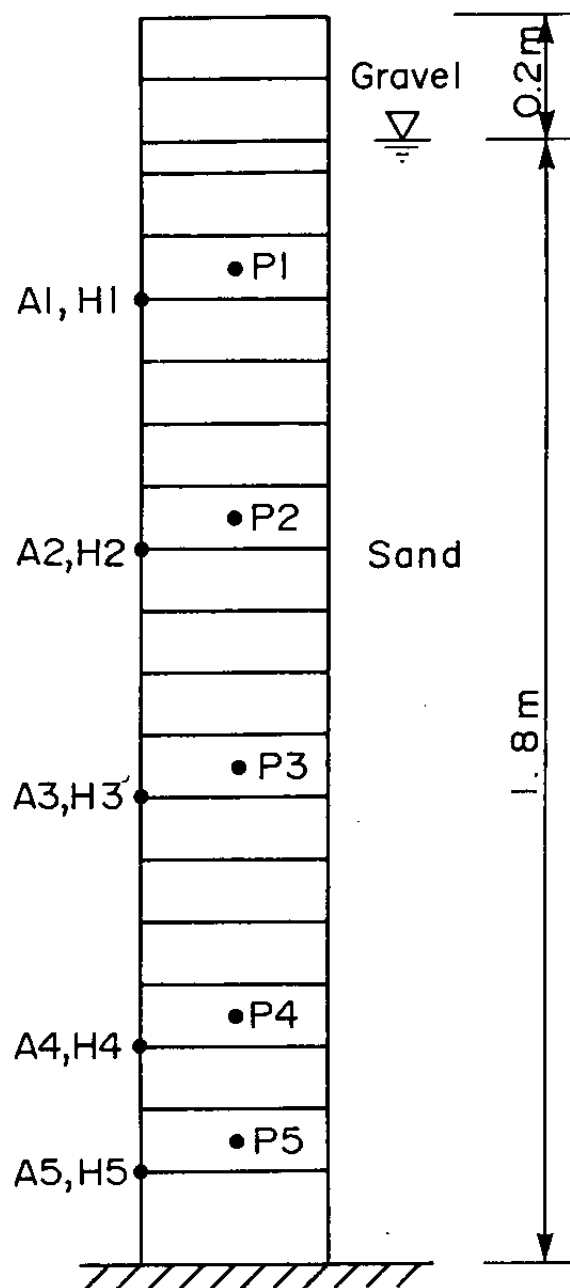


Fig. 4.40 Finite element mesh for the present analysis

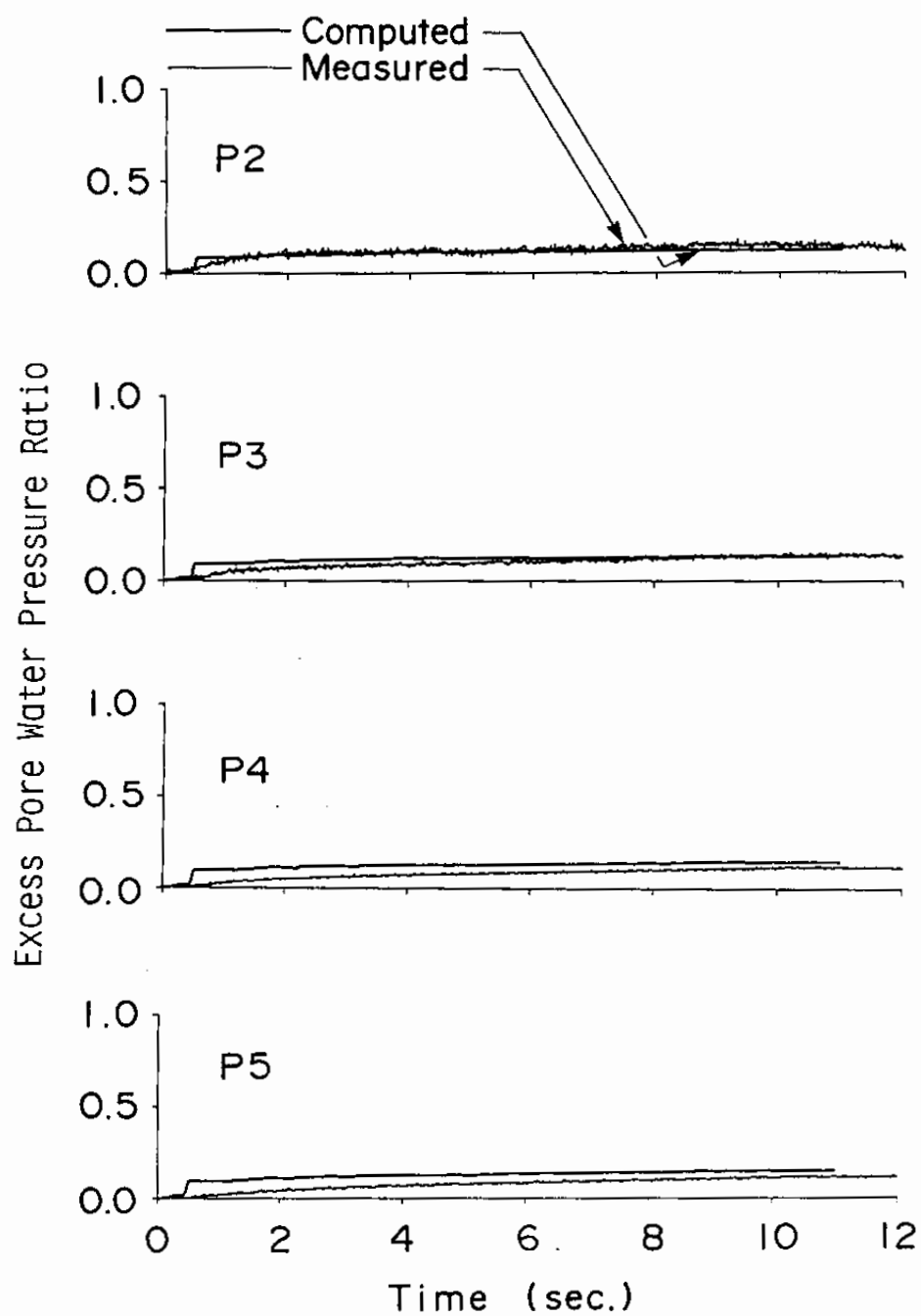


Fig. 4.41 Computed and measured excess pore water pressure ratios in Case R-602



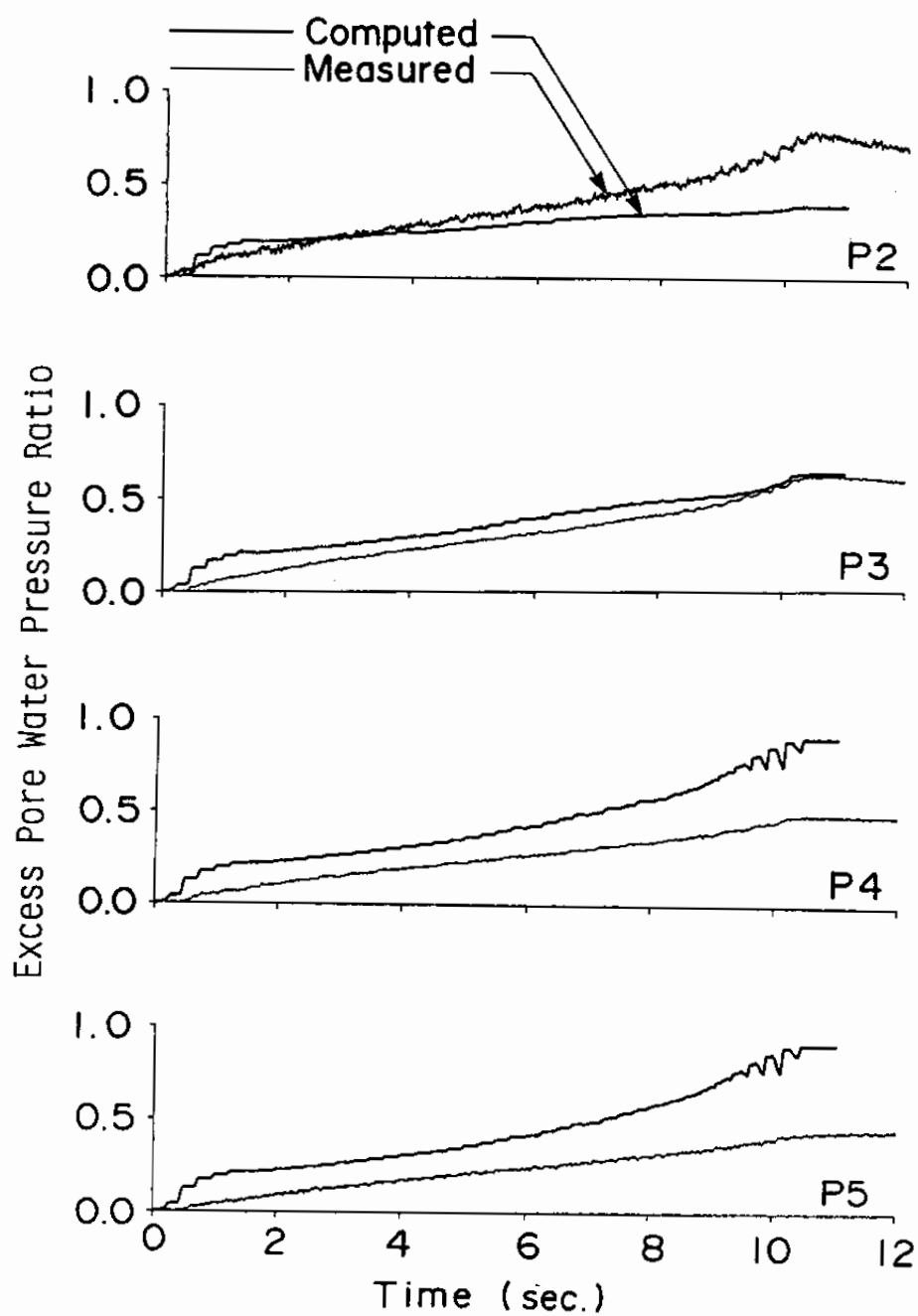


Fig. 4.42 Computed and measured excess pore water pressure ratios in Case R-302

pressures are in accord with each other. There is such a trend, however, that upper part of the sand deposit shows larger pressure than the computed value whereas the lower part shows smaller pressure. The author suspects this might be due to the effect of redistribution of excess pore water pressures within the sand deposit.

When the model ground is shaken in the cases R-303 and R-603 with the maximum acceleration of 81 and 84 Gals, the excess pore water pressures are computed as shown in Figs. 4.43 and 4.44. There is such a tendency that the computed excess pore water pressures rise slightly faster than the measured ones. The computed value, however, simulates overall trend in the excess pore water pressure rise.

The present analysis is done under the undrained condition whereas the actual model sand deposit are shaken under the partially drained condition. If those effect are taken into account, closer agreement will be obtained between the computed and the measured excess pore water pressures. In consequence, the present model is capable of simulating the excess pore water pressures in the level ground.

## (2) Horizontal Displacement

When the excess pore water pressure is small, in the case R-602, computed horizontal displacements relative to the base of the soil container are generally smaller than the measured ones as shown in Fig. 4.45. The author suspects that this may be due to the adverse effect of the friction force transmitted from the load at the top edge of the container.

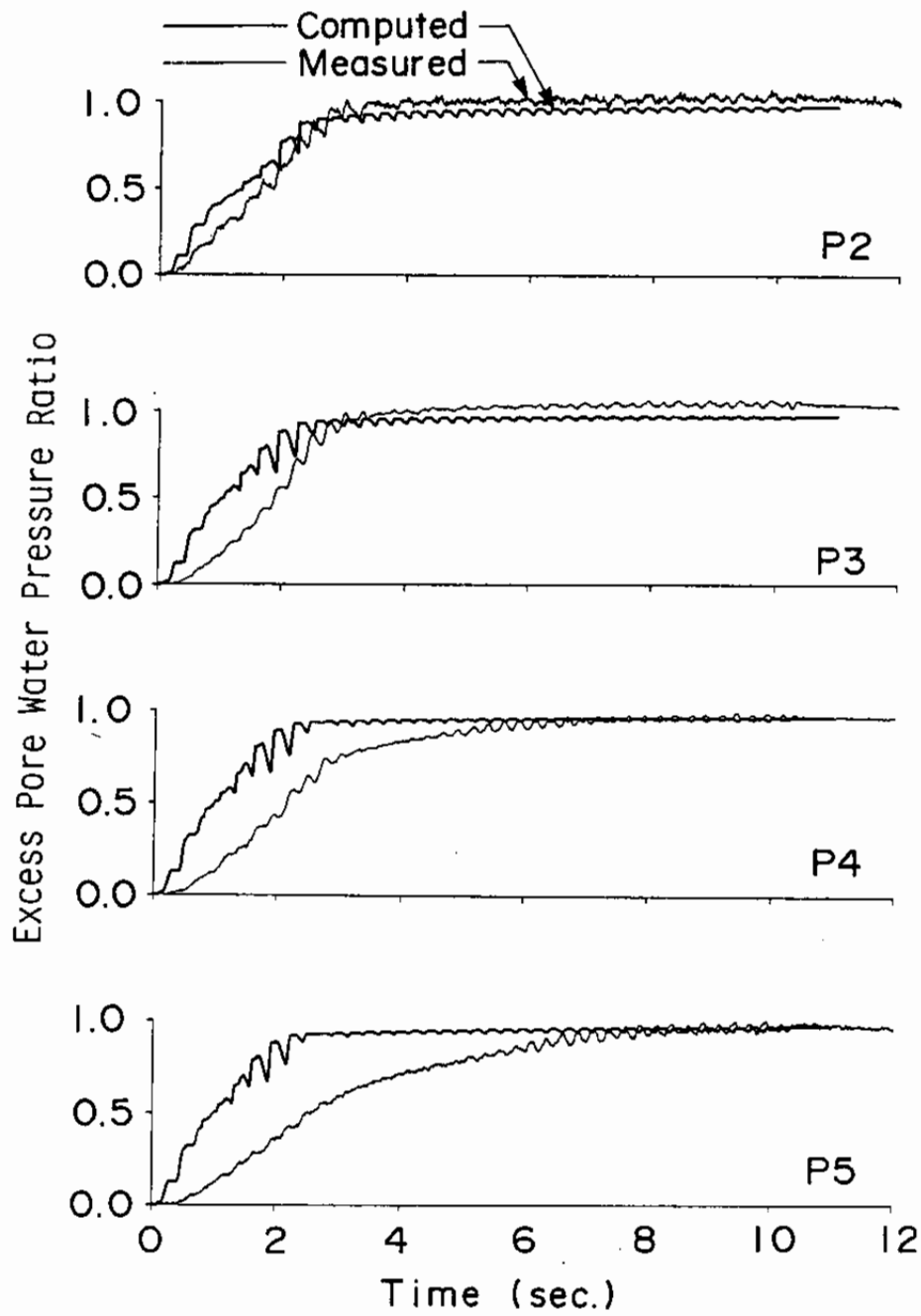


Fig. 4.43 Computed and measured excess pore water pressure ratios in Case R-303

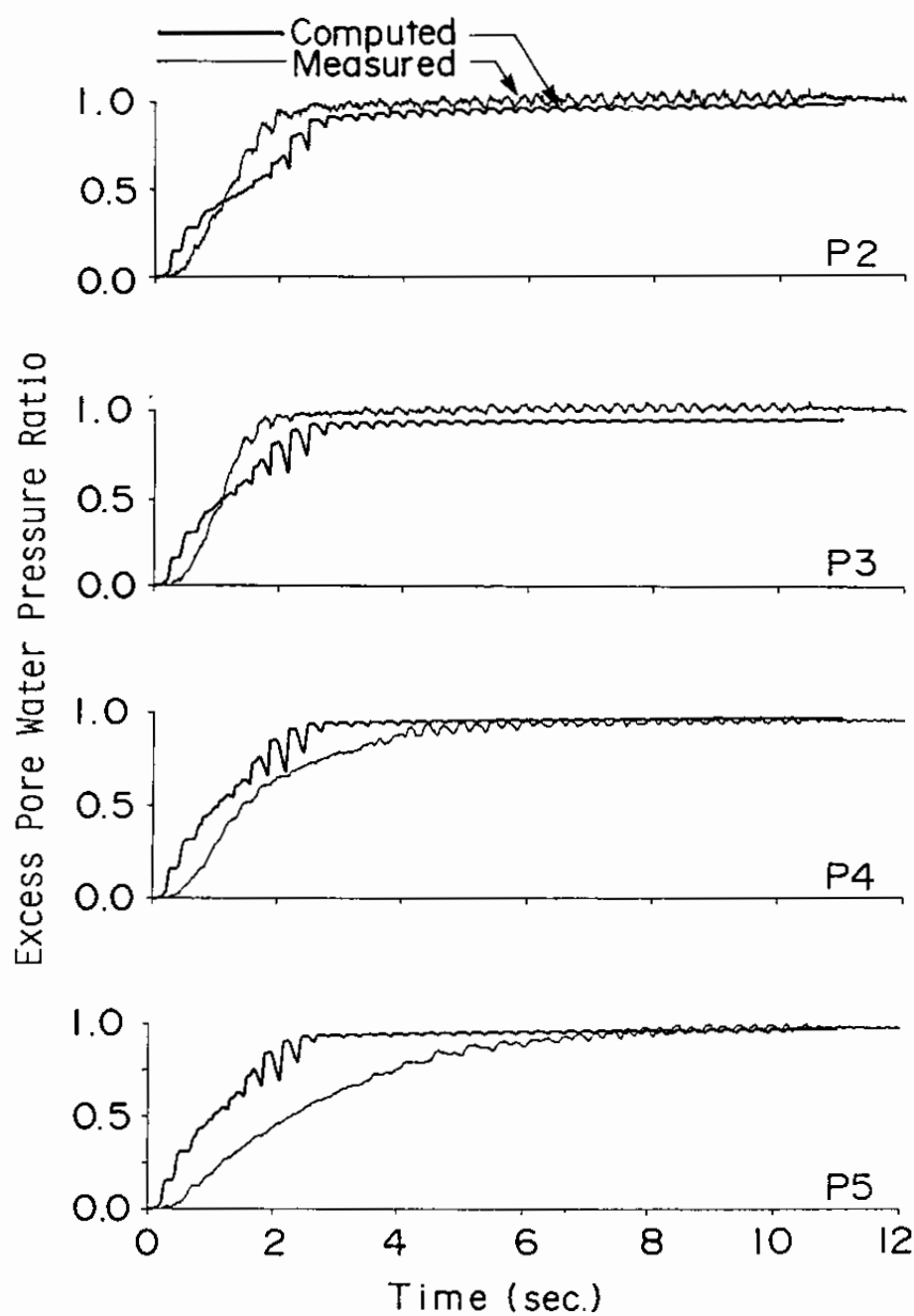


Fig. 4.44 Computed and measured excess pore water pressure ratios in Case R-603

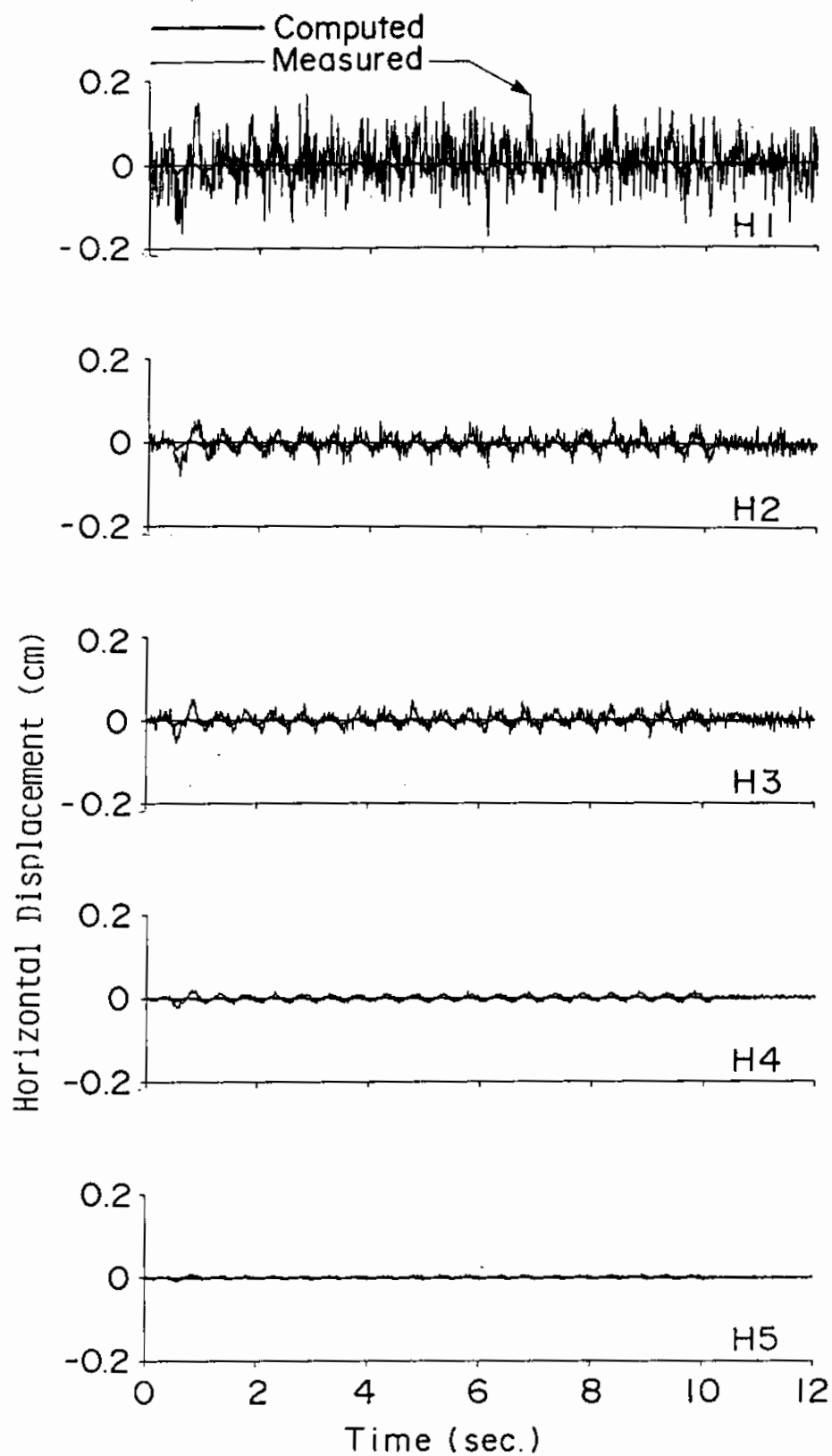


Fig. 4.45 Computed and measured displacements in Case R-602

The similar trend is recognized in the case R-302 as shown in Fig. 4.46. There is a sudden increase in the computed displacements at about 10 seconds, at which the computed excess pore water pressure at the lower level of the sand deposit reaches about 90 percent of the initial effective vertical stress. Much more gradual increase is recognized in the measured displacement. These inconsistencies are attributed to the difference in the computed and the measured excess pore water pressures as seen earlier in Fig. 4.42.

When the excess pore water pressure reaches the initial vertical effective stress as in cases R-303 and R-603, computed displacement are in accord with the measured ones as shown in Figs. 4.47 and 4.48 except for the upper two levels, in which measured displacement is larger than the computed one. The adverse effect of the load might be one of the causes for this.

### (3) Acceleration

When the excess pore water pressure is small as in case R-602 and R-302, computed response accelerations are in accord with the measured ones as shown in Figs. 4.49 and 4.50. A closer look into the details of the wave forms reveals that the analysis tends to amplify the high frequency components of small amplitude at higher levels of the sand deposit whereas the shaking tests tend to dampen them out. The author suspects again that the friction force transmitted through the load of 2.5 tf at the top of the container might be one of the causes for the inconsistency.

When the excess pore water pressure reaches the initial

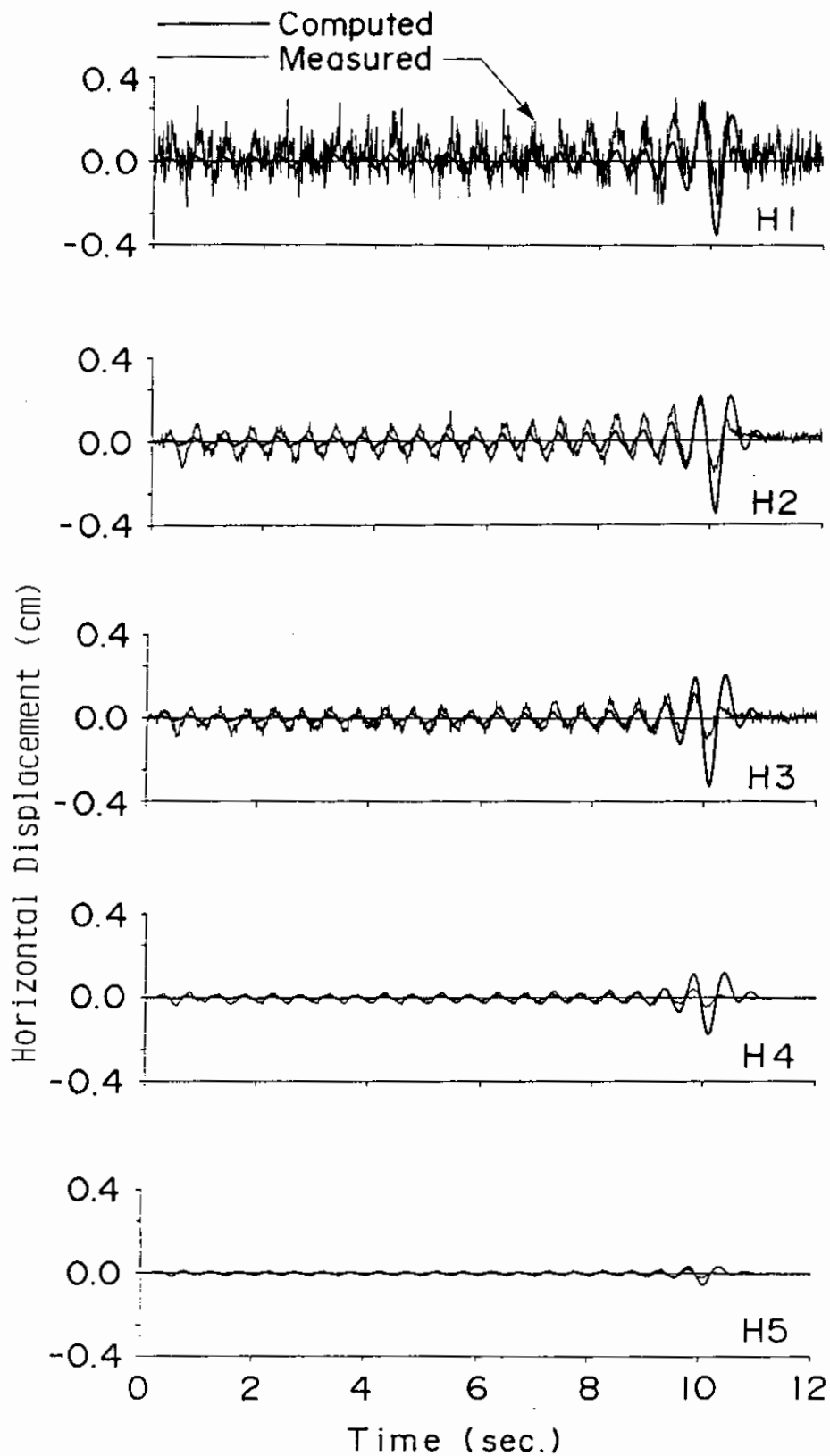


Fig. 4.46 Computed and measured displacements in Case R-302

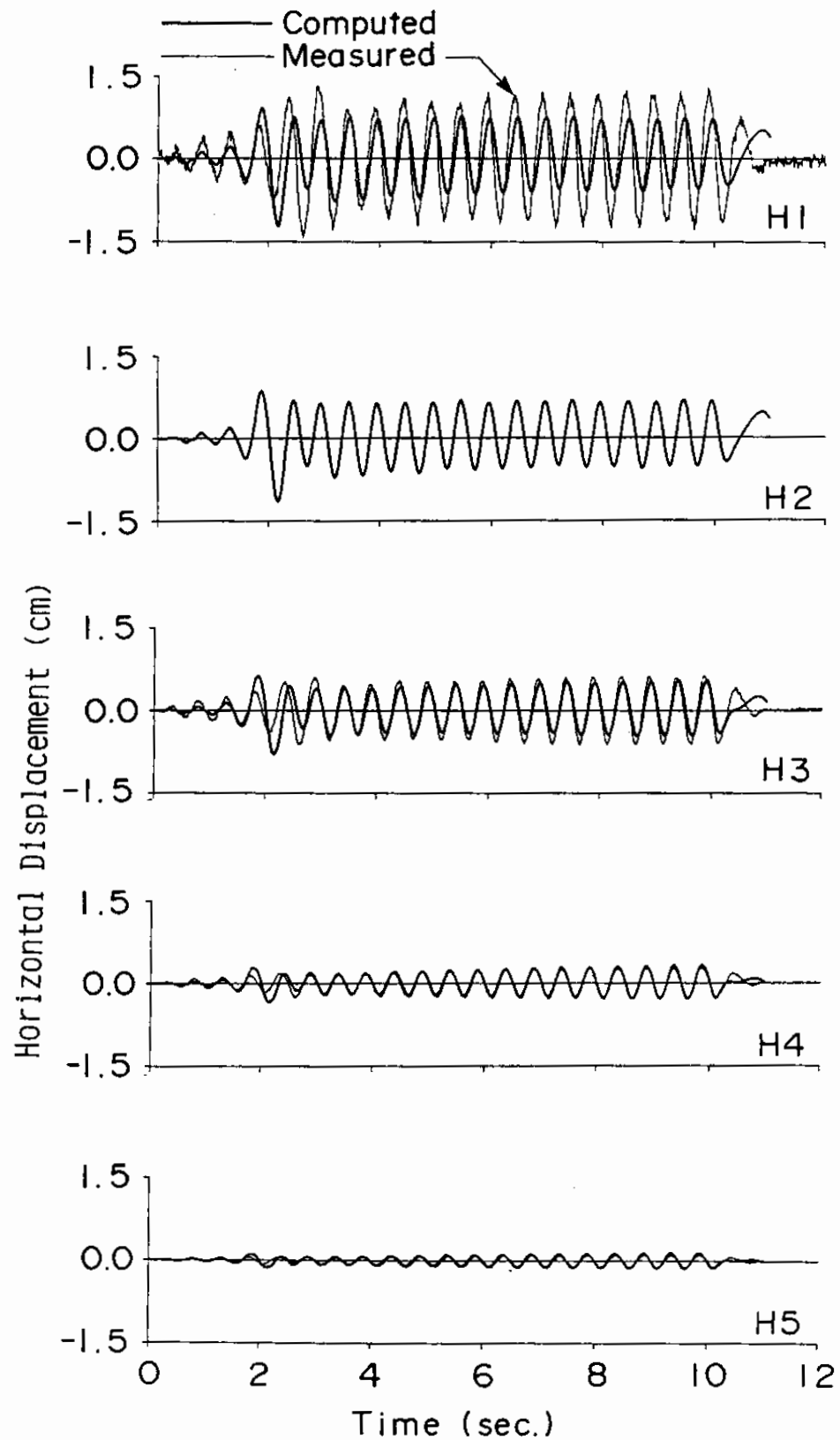


Fig. 4.47 Computed and measured displacements in Case R-303



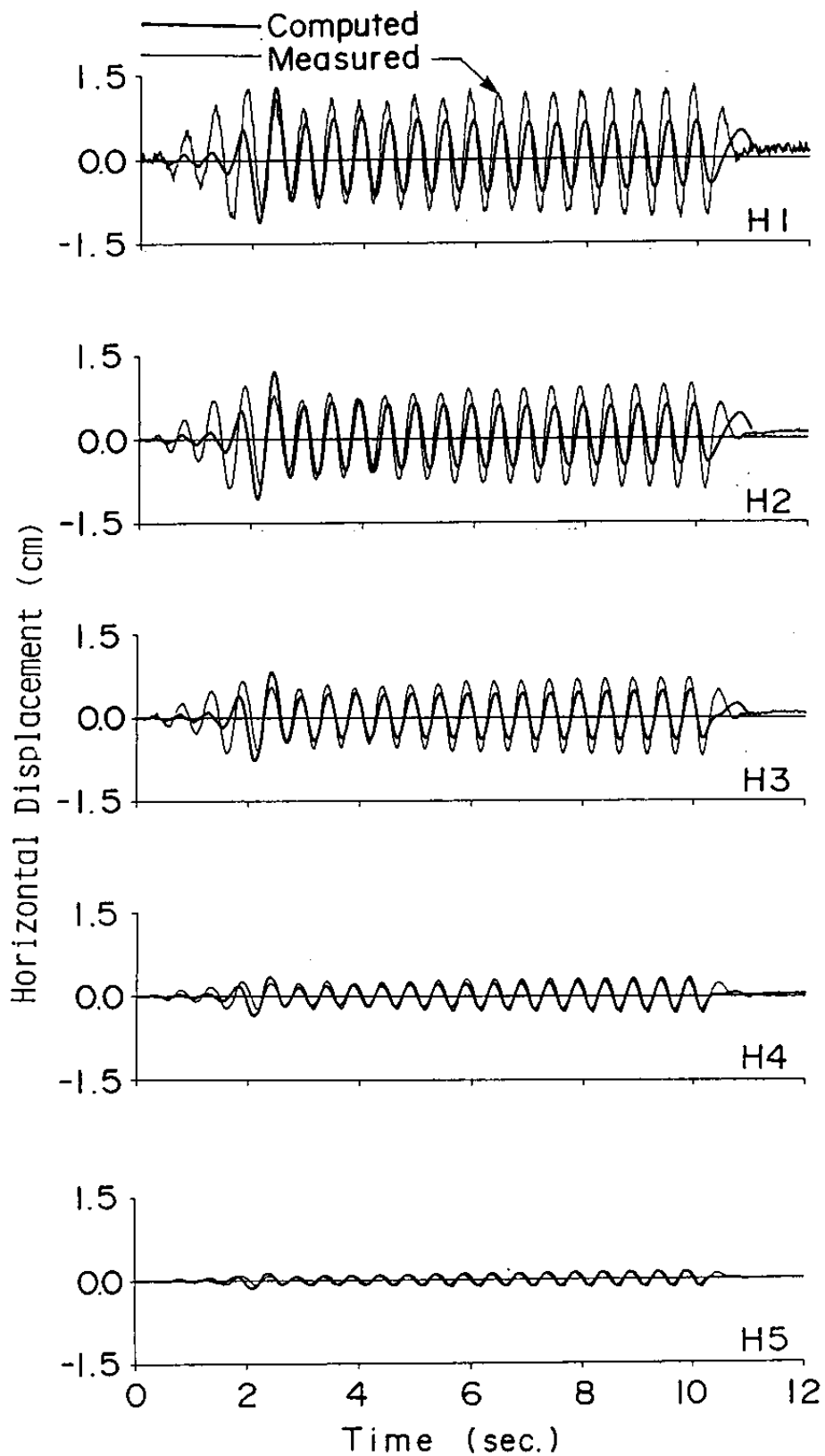


Fig. 4.48 Computed and measured displacements in Case R-603

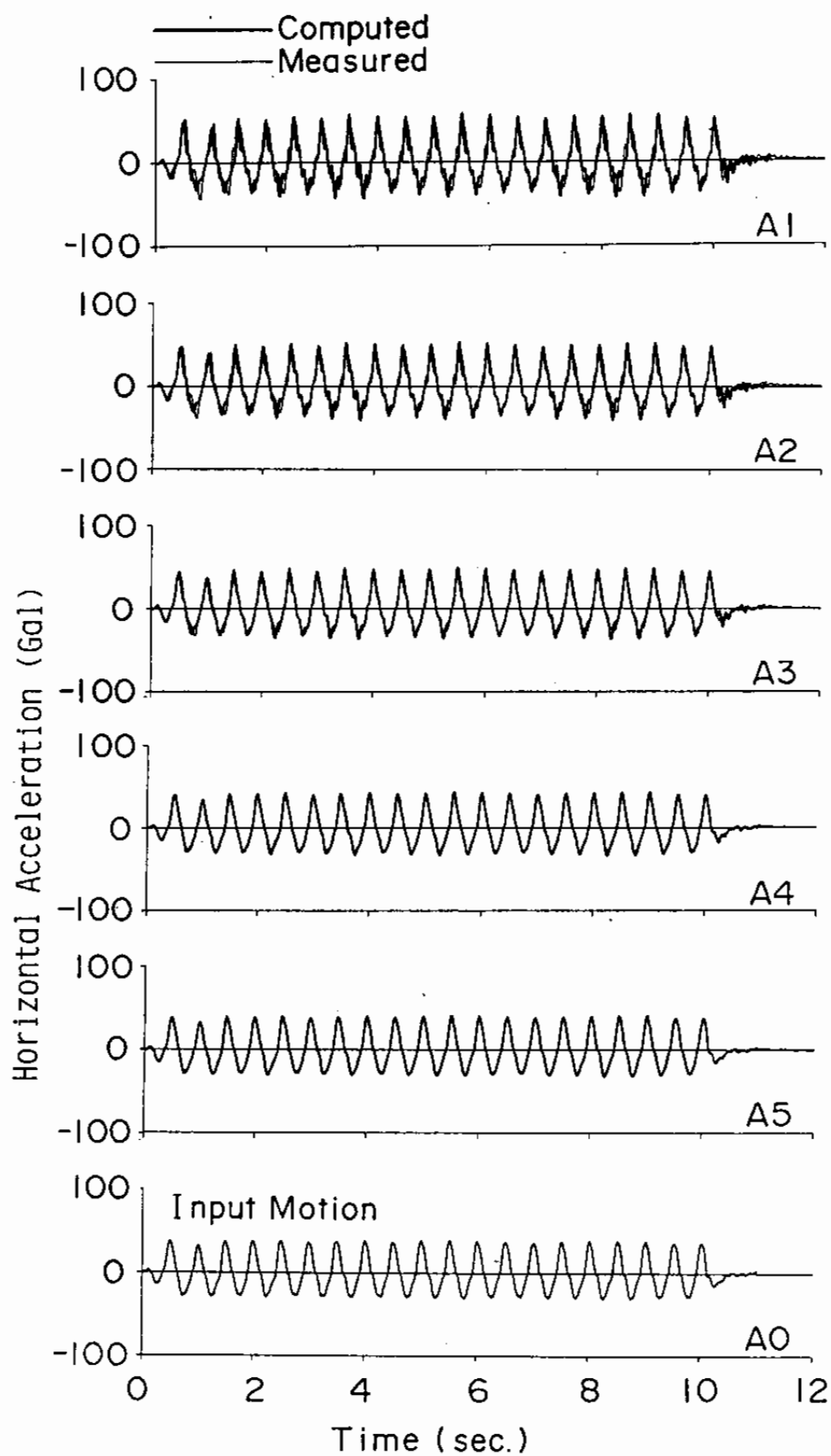


Fig. 4.49 Computed and measured accelerations in Case R-602

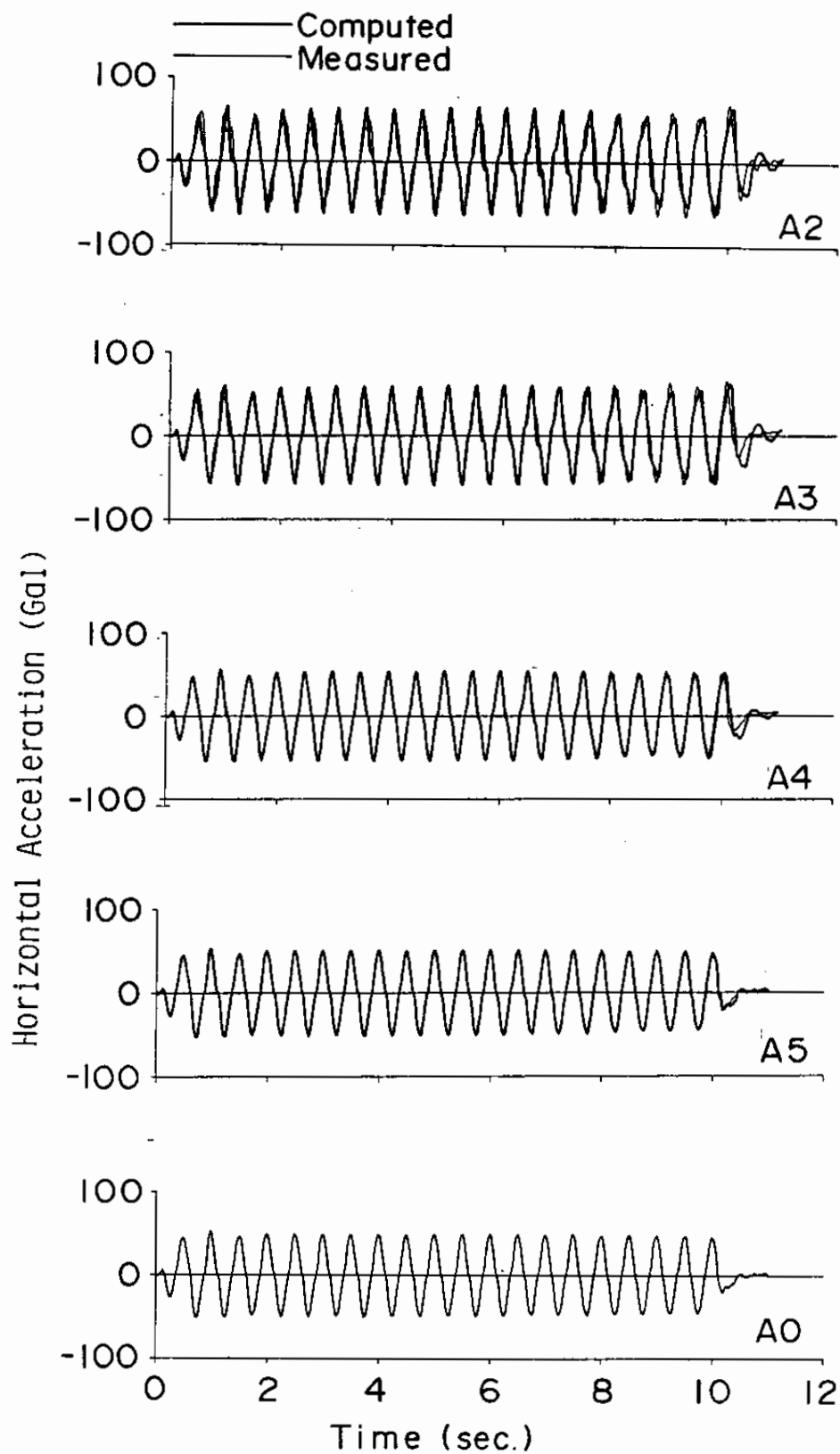


Fig. 4.50 Computed and measured accelerations in Case R-302

vertical effective stress as in cases R-303 and R-603, computed response accelerations are not very much in accord with the measured ones as shown in Figs. 4.51 and 4.52. The analysis shows small amplitudes in the acceleration response after about 2.5 seconds whereas the experiment shows a temporary decrease in the amplitude when the excess pore water pressure reaches the initial effective vertical stress but then shows increase in the amplitude with a spiky wave form. Though such a spiky wave form is generally believed to be due to the effect of instantaneous recovery of the effective confining stress, no instantaneous decrease in the measured excess pore water pressures is seen in Figs. 4.43 and 4.44.

If a consistency is sought between the computed and the measured results, such a common trend can be observed that just after liquefaction the amplitude decreases in the computed and the measured accelerations. In overall conclusion, however, the results can not be said consistent with each other as to the wave form of the acceleration. The author suspects again the friction force is the main cause for the inconsistency.

#### 4.4.2 Response to Earthquake Input Motion

##### (1) Excess Pore Water Pressure

Similarly to the response analysis to the sinusoidal input motions, the response of model sand deposit is computed with the earthquake input motion shown in Fig. 4.18. The computed excess

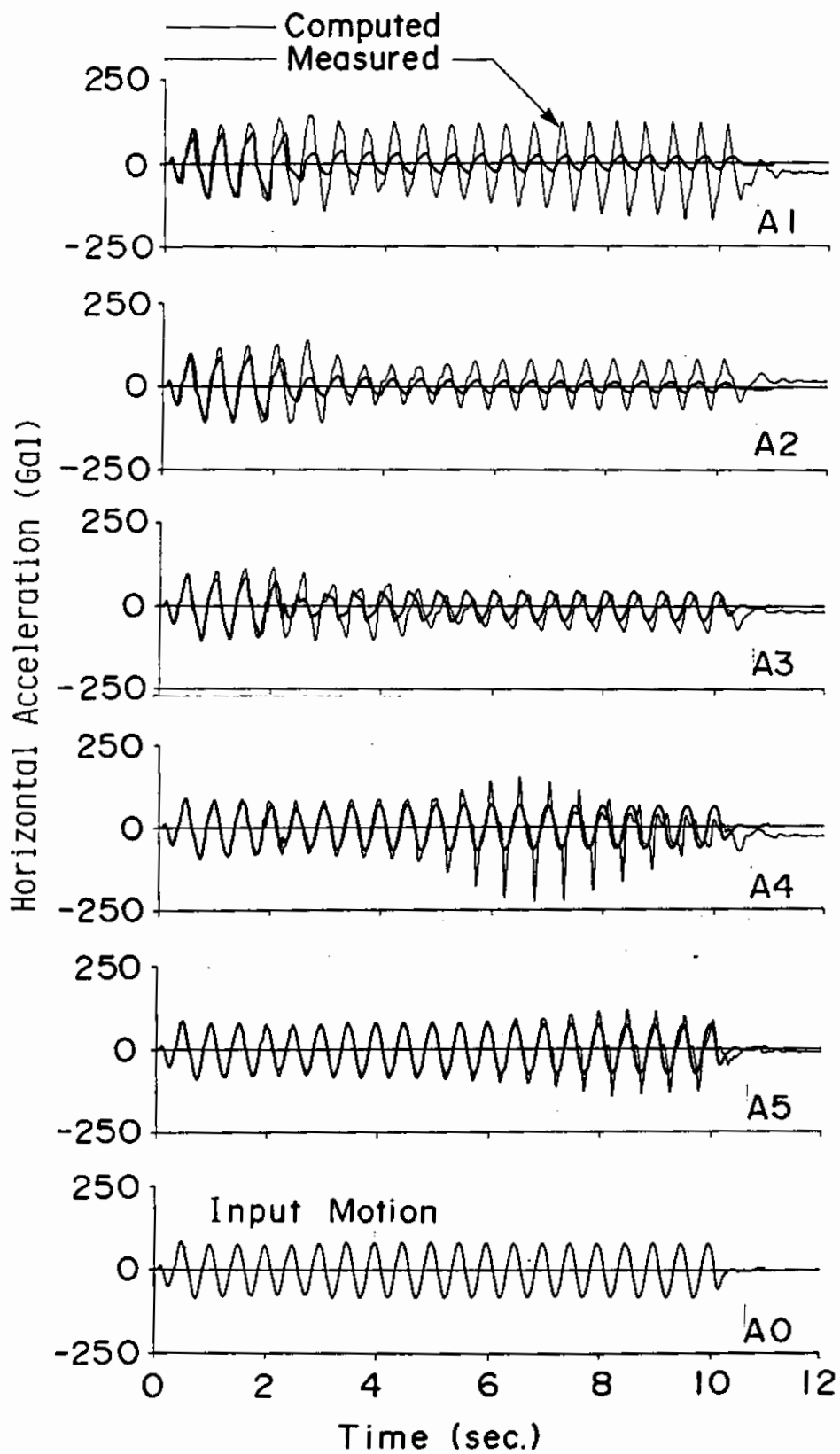


Fig. 4.51 Computed and measured accelerations in Case R-303

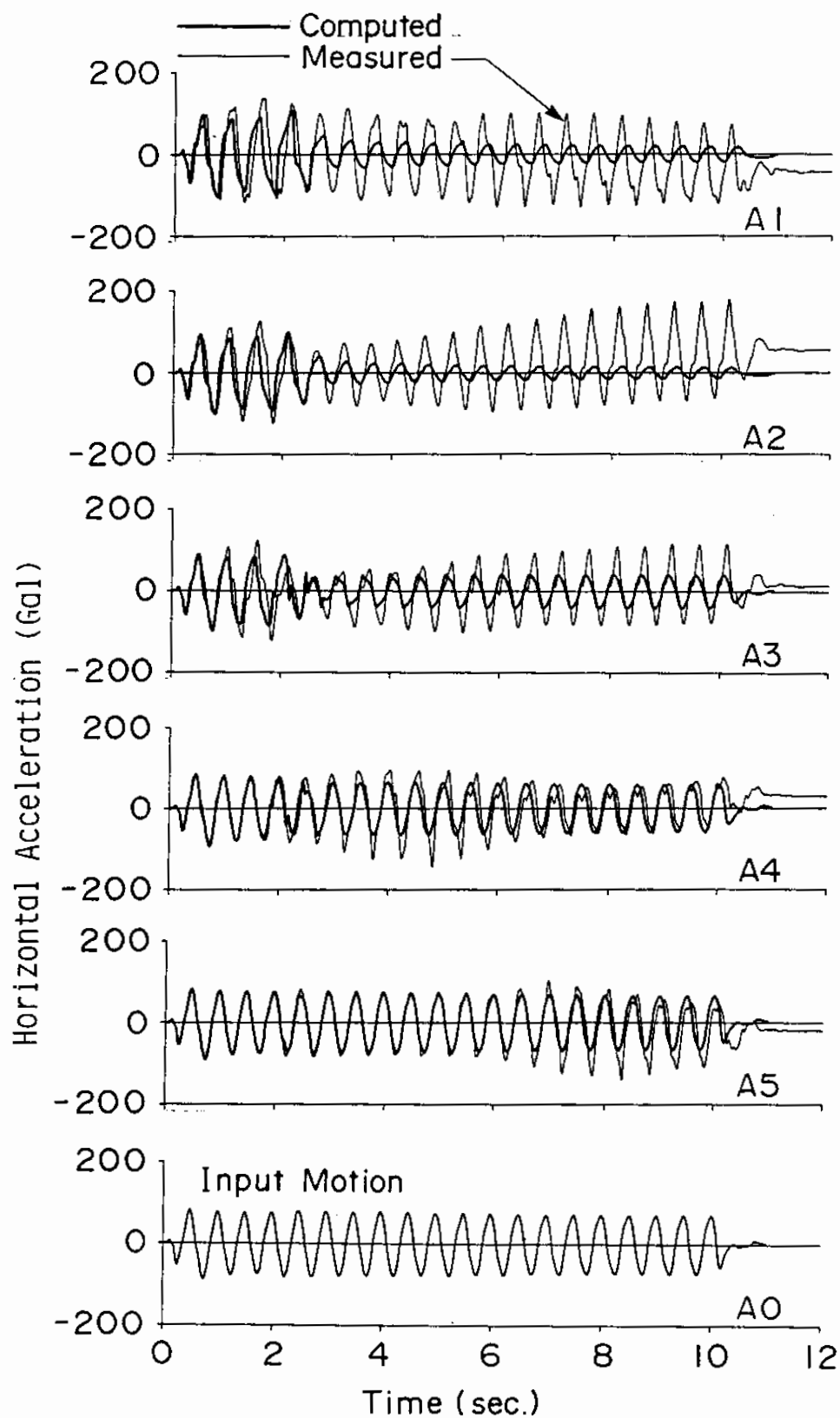


Fig. 4.52 Computed and measured accelerations in Case R-603

pore water pressures, as shown in Fig. 4.53, begin their rises from the beginning of the shaking whereas the measured excess pore water pressures do not begin their rises until about 15 seconds of the shaking. Should the effect of the drainage is taken into account in the analysis, these inconsistencies could be remedied to some degree.

The computed maximum excess pore water pressures are smaller than the measured ones at the middle level of the sand deposit whereas the computed ones are greater in the upper level of sand deposit. This trend is totally in contrast to the case R-302 shown in Fig. 4.42. The reason for this might be due to difference in the vibration modes of the sand deposit in accordance with the type of input motion.

## (2) Displacement

The computed displacements relative to the base of the container are, as shown in Fig. 4.54, larger than the measured ones at the upper level of the sand deposit whereas they are smaller at the lower level of the sand deposit. This tendency is consistent with that seen in the excess pore water pressures. In consequence, should the computed excess pore water pressures be more consistent with the measured ones, the computed displacement should also be more consistent with the measured ones.

At the upper level of the sand deposit, residual displacements are recognized in the computed displacements whereas there is none in the measured ones. The author suspects the rubber membrane used as an inner cell might be the cause for this.

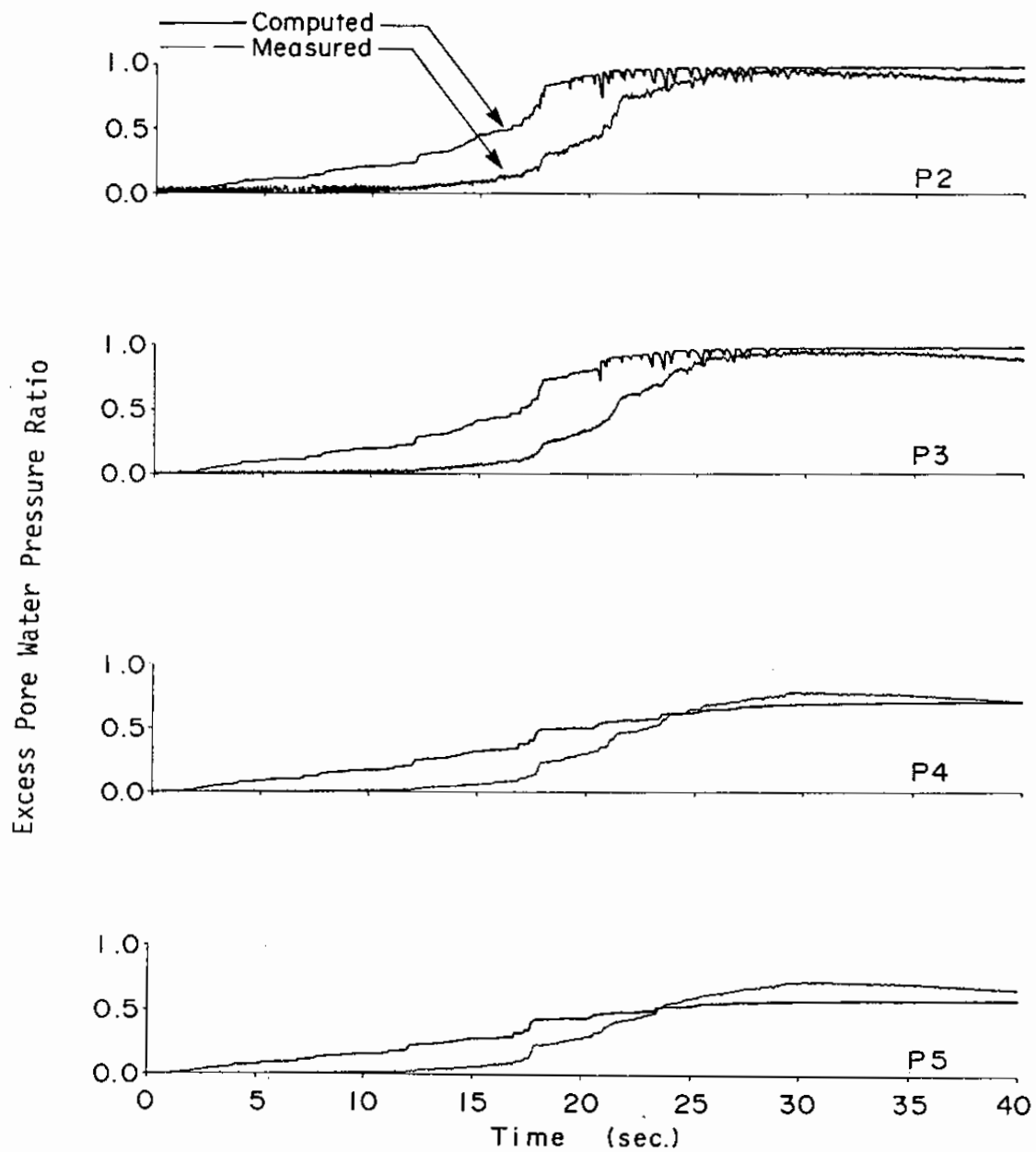


Fig. 4.53 Computed and measured excess pore water pressure ratios in Case R-802



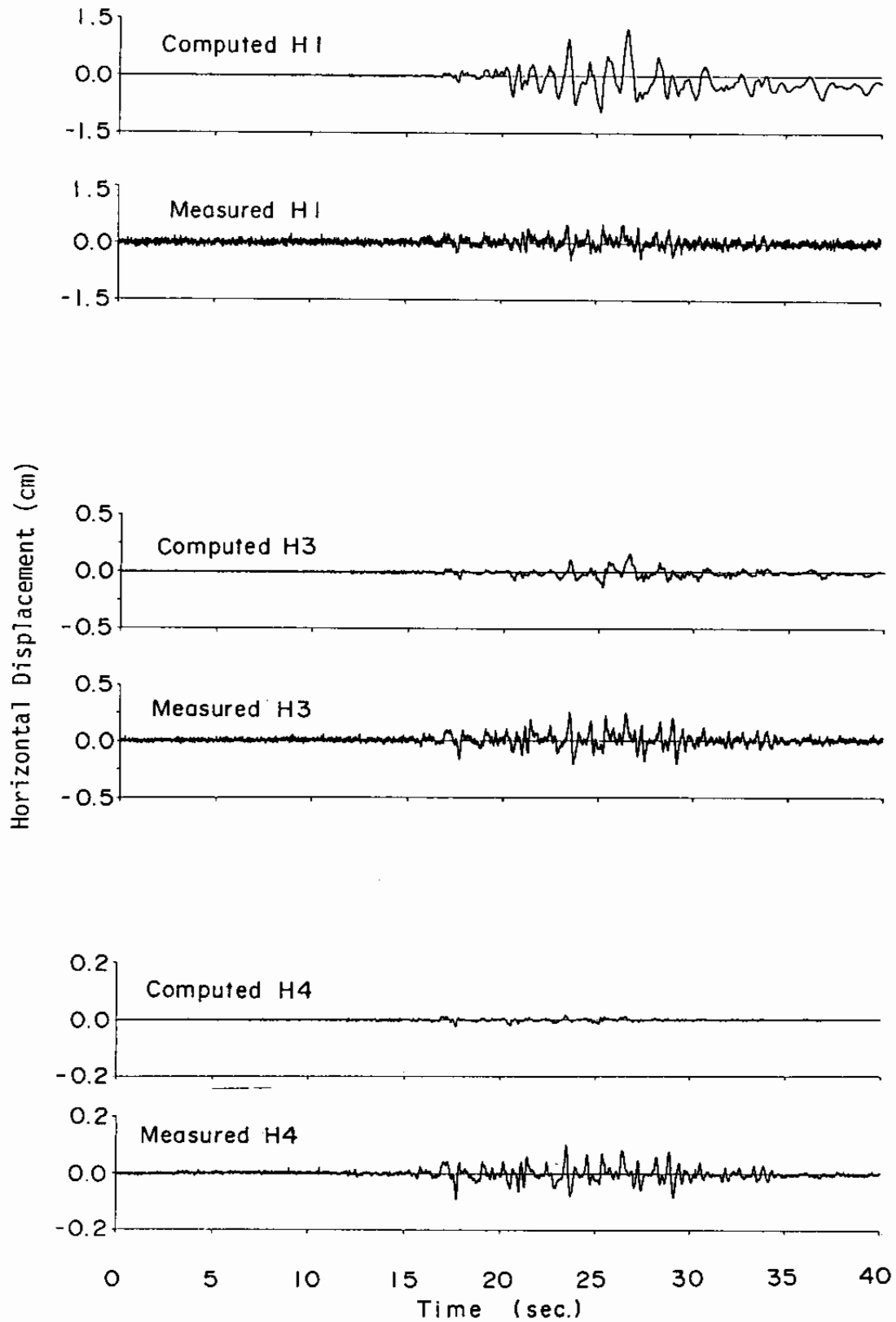


Fig. 4.54 Computed and measured displacements in Case R-802

### (3) Acceleration

The computed response accelerations, as shown in Fig. 4.55, are in accord with the measured ones at the lower level of the sand deposit whereas the difference becomes significant at the upper level. This tendency is consistent with that seen in the excess pore water pressures. In consequence, should the computed excess pore water pressures be more consistent with the measured ones, the computed accelerations should also be more consistent with the measured ones.

### 4.5 Applicability to Level Ground Analysis

In this chapter, one dimensional analysis is conducted on the behavior of level model ground. Though some inconsistency is recognized between the computed and the measured excess pore water pressures, the inconsistency is of minor degree and considered to be overcome by taking into account the effects of the partial drainage within the sand deposit and the adverse effect of the friction force in the container. Inconsistency is also recognized between the computed and the measured displacements and accelerations but this is also considered to be overcome in the similar manner.

Thus, some degree of difficulty is recognized in representing the behavior of level ground in the present study but it is considered to be overcome by taking into account the additional factors relevant to those shaking table tests conducted in this study. It is concluded that the present approach has fundamental applicability in the analysis of level

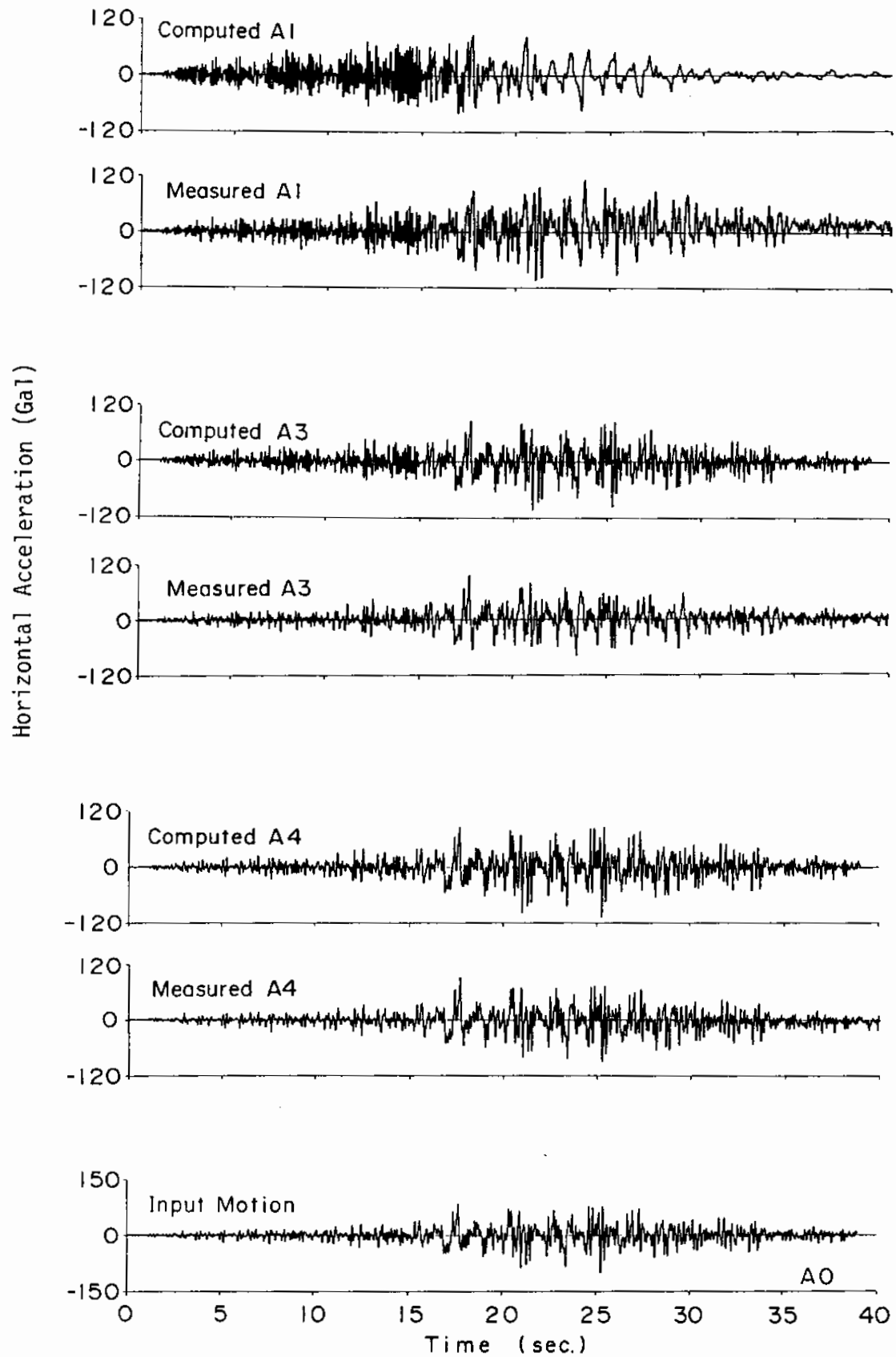


Fig. 4.55 Computed and measured accelerations in Case R-802

ground.

#### References

- (1) Iai, S. (1988) : "Large scale model tests and analyses of gravel drains," Report of the Port and Harbour Research Institute, Vol.27, No.3, pp.25-160
- (2) Ishihara, K. et al (1989) : "Effective stress analysis of level ground and soil structures," Research Committee Report, Proceedings of the Symposium on Seismic Performance of Level Ground and Soil Structures, Japanese Society of Soil Mechanics and Foundation Engineering, pp.50-136 (in Japanese)
- (3) Japanese Society for Soil Mechanics and Foundation Engineering (1979) : Methods for Testing Soils, pp.25-188 (in Japanese)
- (4) Tsuchida, H., Noda, S., Inatomi, T., Uwabe, T., Iai, S., Ohneda, H. and Toyama, S.: "Damage to port structures by the 1983 Nihonkai-Chubu Earthquake," Technical Note of the Port and Harbour Research Institute, No.511, March 1985, 447p. (in Japanese)

## CHAPTER 5

## TWO DIMENSIONAL ANALYSIS OF SHEET PILE QUAY WALLS

In the previous chapter, applicability of the present model is studied through one dimensional analysis of level ground. The next step is naturally to move on to two dimensional analysis.

The fundamental mechanism in producing deformation of soils and foundations, when soils and foundations are subject to cyclic mobility, is existence of initial stress and its release in accordance with deformation. The deformation of soil causes redistribution of stress. Redistributed stress, in turn, causes further deformation. How the initial stress is released due to the redistribution of stress depends on material properties, geometrical configuration and boundary conditions given to a specific issue in hand.

The simplest case of two dimensional analysis was seen in Chapter 3 with a single element of soil, which was initially at  $K_0$  condition and gradually exhibited settlement and bulging under cyclic loading. A more realistic case study is conducted in this chapter on the performance of sheet pile quay walls during 1983 Nihonkai-Chubu Earthquake of magnitude 7.7. Effective stress analysis of quay walls is one of the most difficult types of analysis because soils in front of and behind a sheet pile are initially in nearly passive and active failure states, which pose a potential difficulty in the numerical analysis. In the effective stress analysis with the conventional type of models, a small fraction of error contained in the stress causes, in the vicinity of the failure line, a very large error in the strain,

as mentioned in the earlier chapters, sometimes resulting in divergence in the iteration solution process.

Thus, the analysis of sheet pile quay walls in the present chapter offers an opportunity for conducting one of the most critical examinations into the applicability of the present model in the two dimensional analysis.

## 5.1 Earthquake and Damage

### 5.1.1 1983 Nihonkai-Chubu Earthquake

On May 26, 1983, Nihonkai-Chubu Earthquake of magnitude 7.7 hit northern part of Japan. The fault of the earthquake is located in the Japan Sea (i.e. 'Nihonkai' in Japanese), as shown in Fig. 5.1, dipping with the angle of about 30 degrees toward the east direction. With the shallow focal depth of 14 km, the earthquake caused Tsunami, killing about 100 people. The specific earthquake data are summarized in Table 5.1.

The maximum accelerations recorded at the Akita Port, which is located about 100 km from the epicenter, are 190, 205 and 41 Gals in north-south, east-west and vertical directions. The recording was done with a SMAC-B2 accelerograph installed at the location shown in the lower right corner of Fig. 5.1(c). The ground below the accelerograph, as shown in Fig. 5.2, consists of loosely deposited coarse and fine sands of about six meters in thickness, below which lies the base of tertiary origin for the entire area of the Akita Port. Contour lines of the base in the Akita Port area are shown in Fig. 5.3, indicating the accelerograph is located at the shallowest part of the base of

Table 5.1 Earthquake data of 1983 Nihonkai-Chubu Earthquake

Date and Time	12:00 May 26, 1983
Location of Hypocenter	
Latitude	40.35 N
Longitude	139.08 E
Depth	14 km
Magnitude	7.7

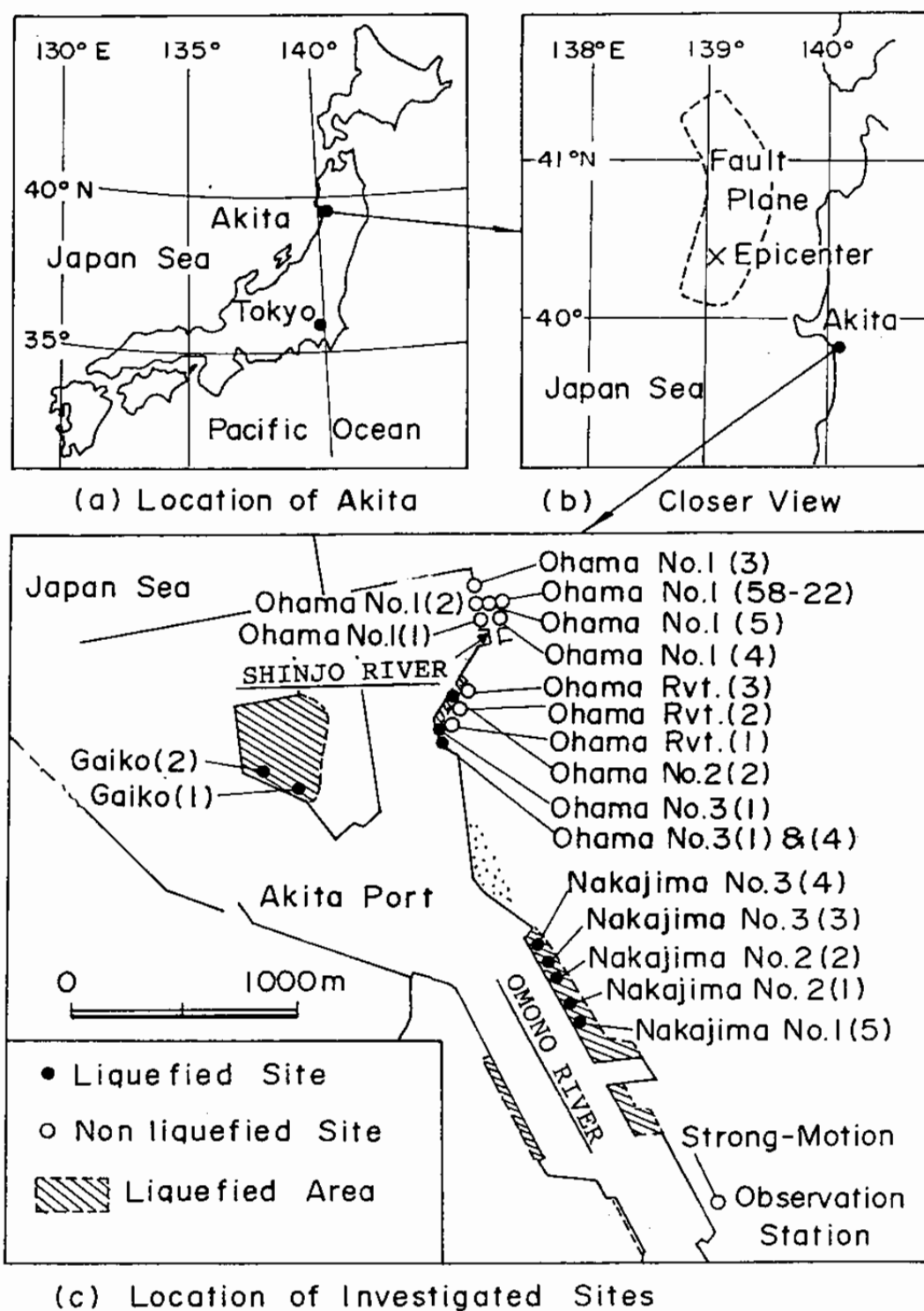


Fig. 5.1 Fault of 1983 Nihonkai-Chubu Earthquake and soil liquefaction at Akita Port



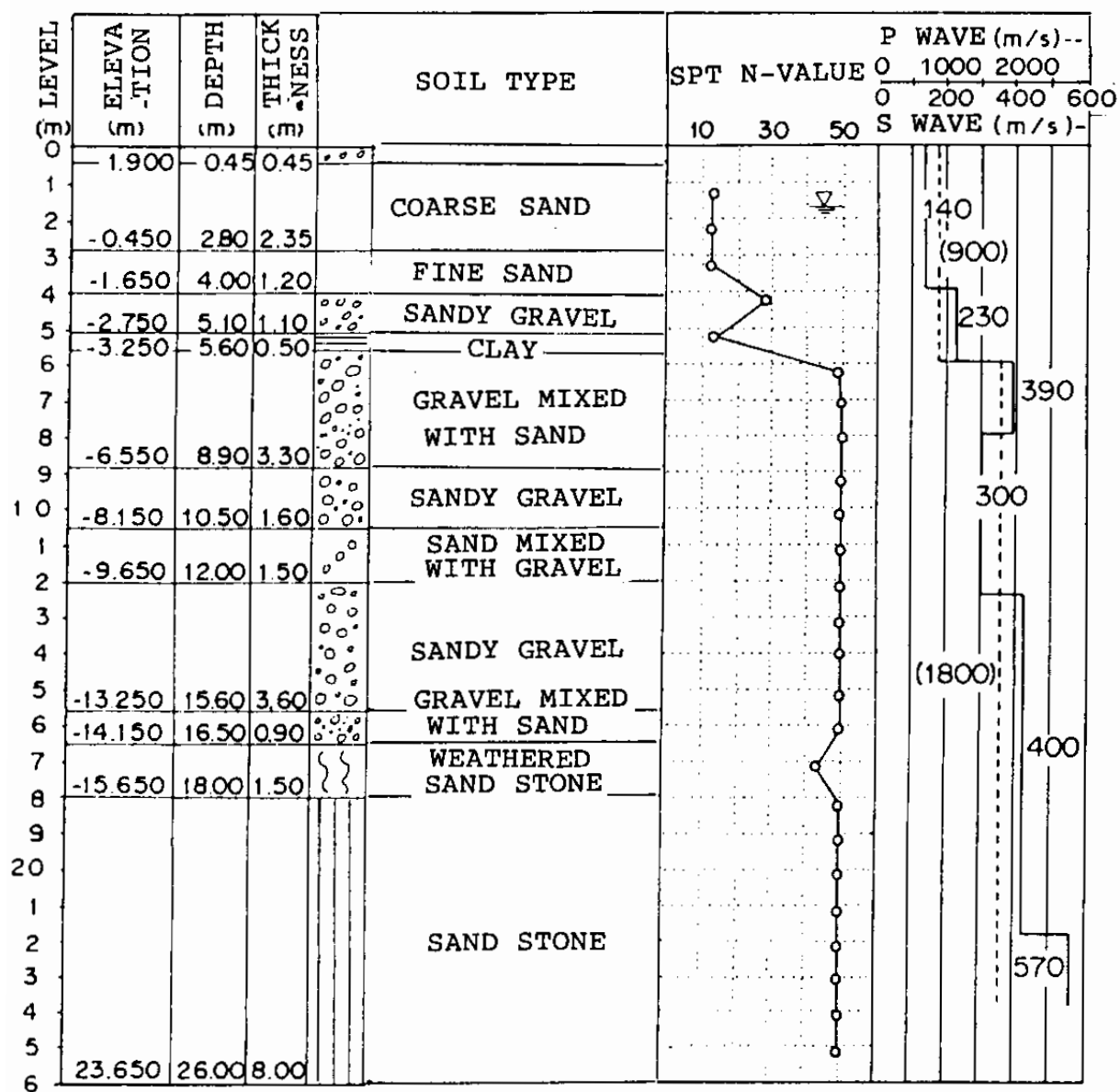


Fig. 5.2 Ground condition at the strong-motion observation site at Akita Port

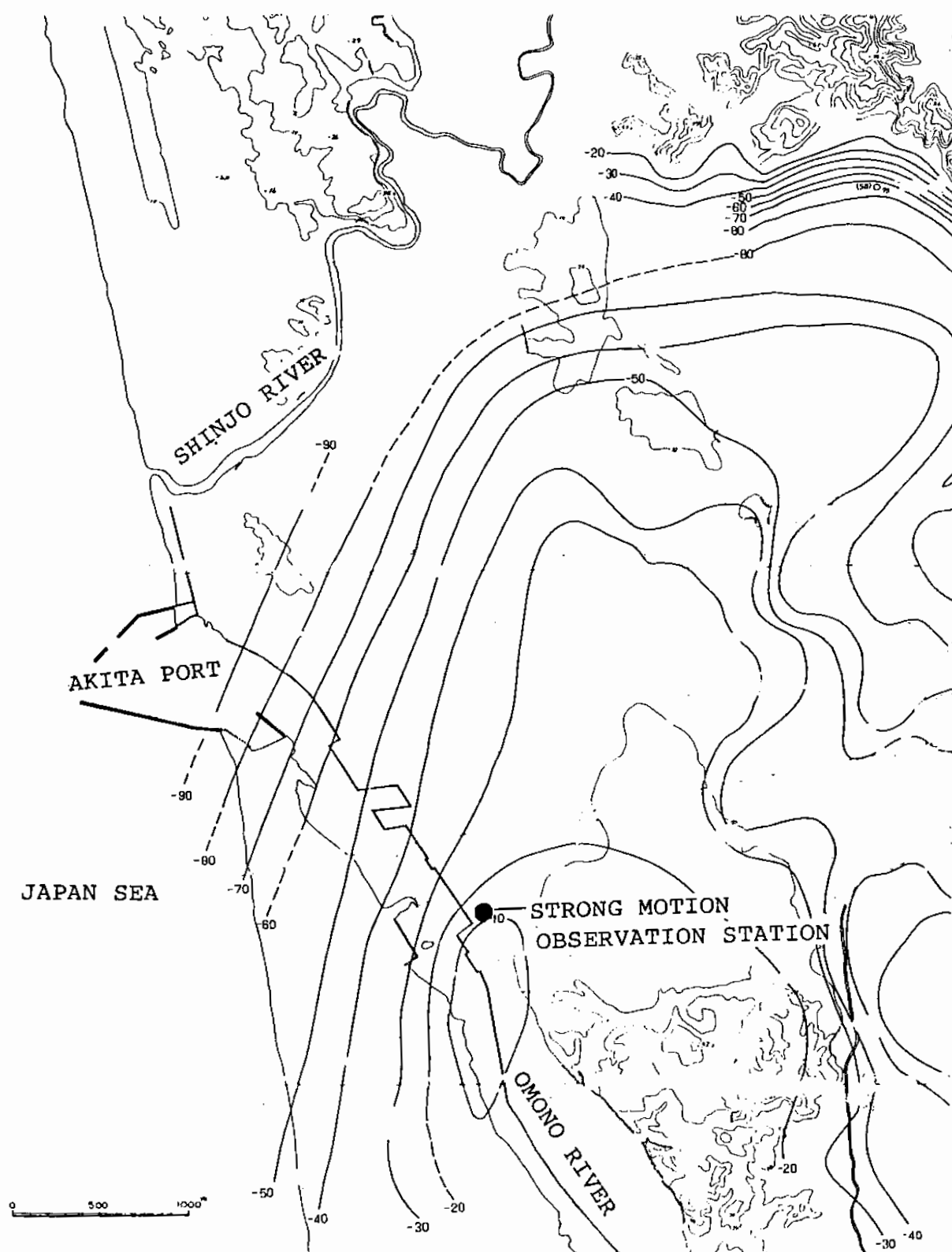


Fig. 5.3 Counter lines of the base of tertiary origin in the Akita Port area; negative figures at the contour lines indicate depth in meters (after Kano, 1965)

tertiary origin in the area. The deposit did not liquefy during the earthquake and thereby the earthquake motion recovered from the accelerograph was not affected by the soil liquefaction occurring in the other part of the area in the Akita Port. The recorded time histories of the earthquake motion are digitized and corrected for the instrument response through the procedure developed by the author and his colleagues (Iai et al, 1978) and are shown in Fig. 5.4 (Kurata et al, 1983).

#### 5.1.2 Damage at Akita Port

##### (1) Akita Port

The Akita Port, shown in Fig. 5.1, is situated at the estuaries of the Omono and Shinjo Rivers. The estuary of the Shinjo River, originally located as shown in Fig. 5.3 together with the former coastal line of the Akita Port, was relocated as shown in Fig. 5.1 when the Ohama No.1 and No.2 Wharves were constructed.

The port facilities consist of quay walls constructed along the Omono River with a backfilling method. The port suffered damage due to liquefaction of backfill sand during the earthquake. The liquefaction occurred at the locations shown in Fig. 5.1(c).

Among the liquefied sites in the Akita Port, as seen in the same figure, there exist several sites which did not liquefy during the earthquake. They consist of quaternary deposits of medium to dense sand.

In this study, two sites, out of the liquefied and the non-

S-1567 AKITA-S

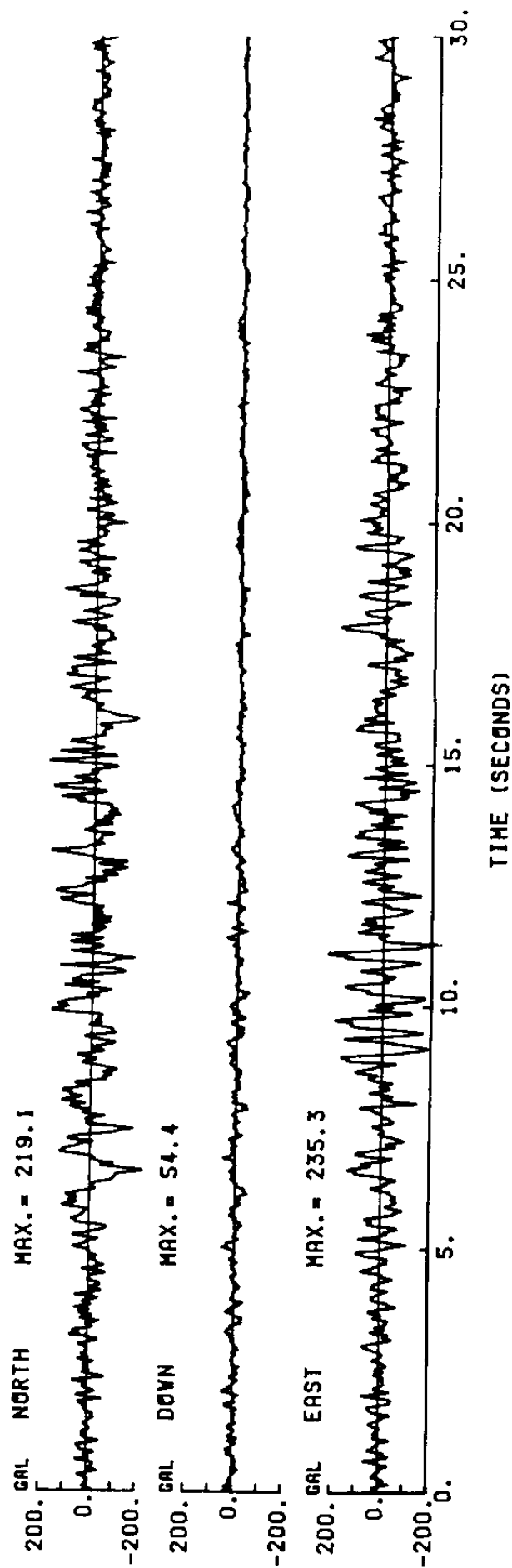


Fig. 5.4 Acceleration record at Akita Port

liquefied sites, are selected for the analysis; one is the site at the Ohama No.2 Wharf at which liquefaction occurred, the other is the one at the Ohama No.1 Wharf at which liquefaction did not occur. These wharves, as shown in Fig. 5.1(c), are located side by side at the estuary of the Shinjo River.

## (2) Damaged quay wall

The quay wall at the Ohama No.2 Wharf had such a cross section as shown in Fig. 5.5 at the time of the earthquake. The earthquake caused liquefaction of back fill sand, as mentioned earlier, and resulted in deformation in the sheet pile as shown in the same figure with broken lines. An eyewitness, who had narrowly escaped from the truck on the Ohama No.2 Wharf shown in Fig. 5.6, identifies that the quay wall deformed with the motion of the earthquake (Tsuchida et al, 1985). The deformed sheet piles, taken out from the quay wall after the earthquake, are shown in Fig. 5.7.

Displacement at the top of the sheet pile, plotted along the face line of the quay wall, is shown in Fig. 5.8. As shown in the same figure, the displacement is obviously constrained by the corner structures at both ends of the Ohama No.2 Wharf. In the present analysis, the deformation at the middle part, indicated by SECTION A in Fig. 5.8, is considered as the representative two dimensional deformation of the quay wall at the Ohama No.2 Wharf and this part of deformation is analyzed in the present study. The horizontal displacement at the top of the sheet pile ranges from about 1.2 to 1.8 meters. The settlement at the middle part of the apron is about 1.4 meters, being almost the same as the





Fig. 5.7 Deformed sheet pile taken out from the quay wall

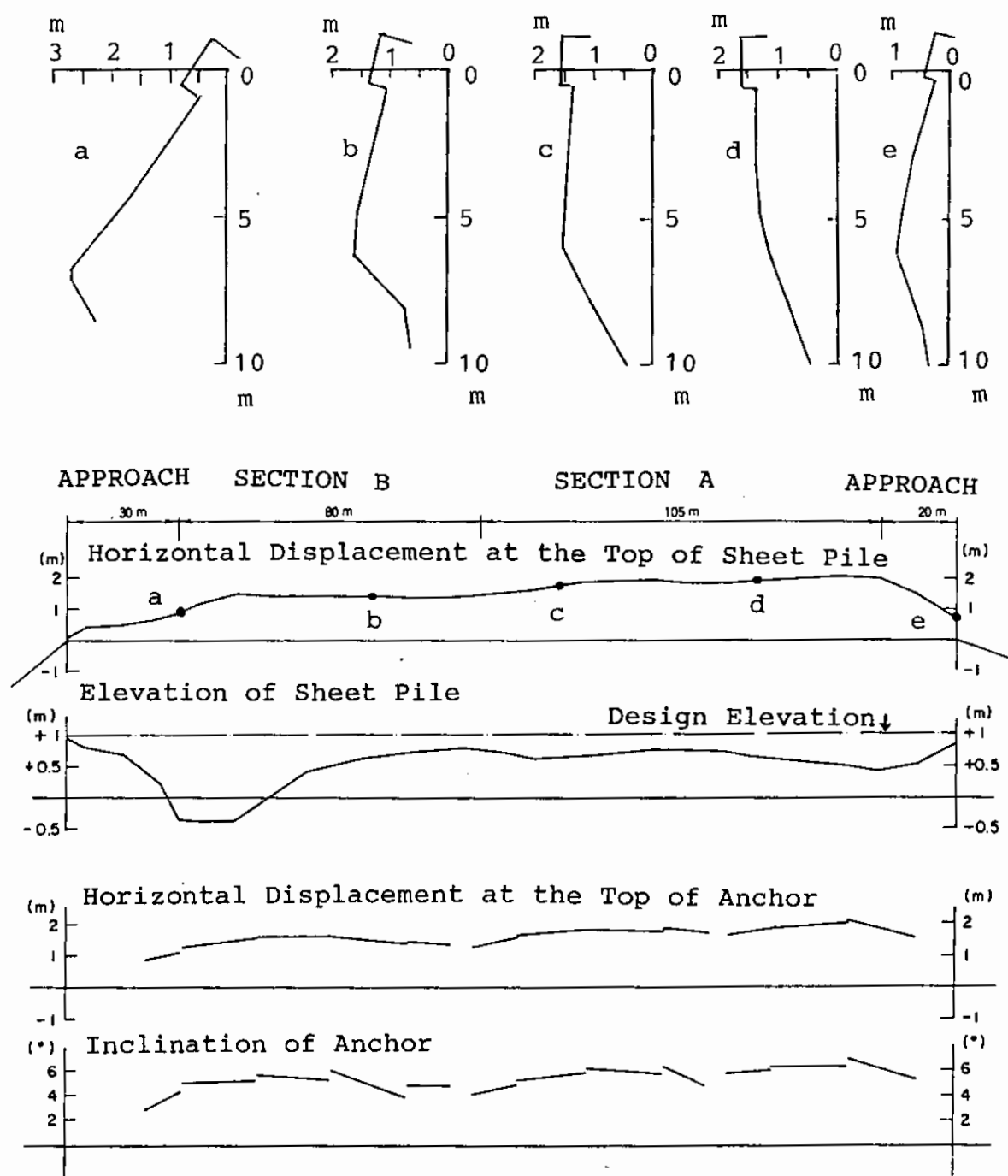


Fig. 5.8 Displacements at the top of the sheet pile and at the anchor and inclination of the anchor



horizontal displacement of the sheet pile.

The displacement at the top of the sheet pile is evidently associated with the displacement of the anchor piles as shown in Fig. 5.8; the anchor was pulled by the sheet pile toward sea, accordingly inclined due to the reduced resistance in the liquefied backfilling sand.

The Ohama No.2 Wharf consists of such soil layers as shown in Fig. 5.9 with the grain size accumulation curves of soils shown in Figs. 5.10 and 5.11. In particular, the average grain size  $D_{50}$  of the soils distributes along the depth as shown in Fig. 5.12. The upper layer of medium sand, which was used as the filling material, is originally a part of a deposit from the Shinjo River and dredged from the sea bottom for backfilling whereas the lower layer of fine sand is a deposit from the Omono River.

In-situ impulse testing with a down hole method is conducted at the Ohama No.3 Wharf which is adjacent to the Ohama No.2. The results, shown in Fig. 5.13, promise a very good estimate on the in-situ initial shear modulus of the ground.

### (3) Quay wall without damage

The quay wall at the Ohama No.1 Wharf has the cross section similar to that at the Ohama No.2 Wharf as shown in Fig. 5.14. In particular, the type of the sheet pile and the water depth of the quay wall at the Ohama No.1 Wharf are exactly the same as those at the Ohama No.2 Wharf. The ground consists of quaternary deposits, shown in Fig. 5.15, without any back filling. Evidently the SPT N-values at the upper layer of medium sand at the Ohama



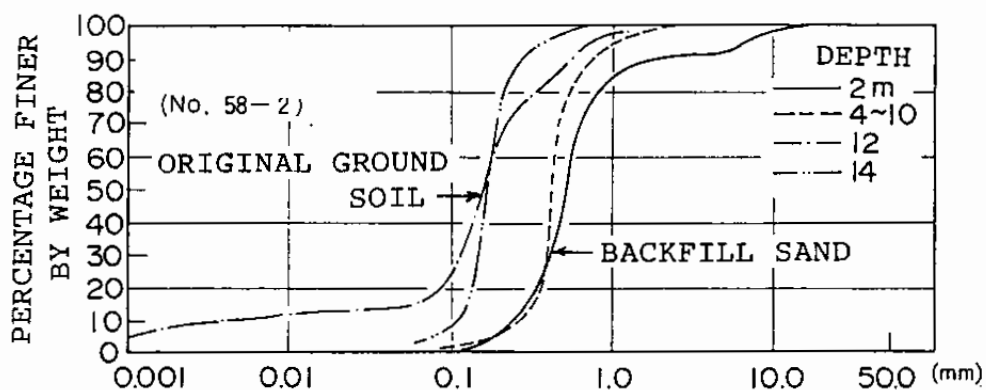


Fig. 5.10 Grain size accumulation curves of soils at Ohama No.2 Wharf; soils from upper part of the ground

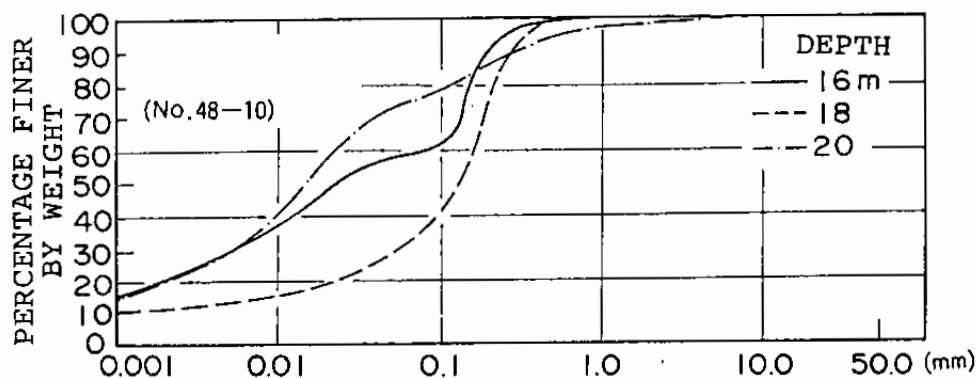


Fig. 5.11 Grain size accumulation curves of soils at Ohama No.2 Wharf; soils from lower part of the ground

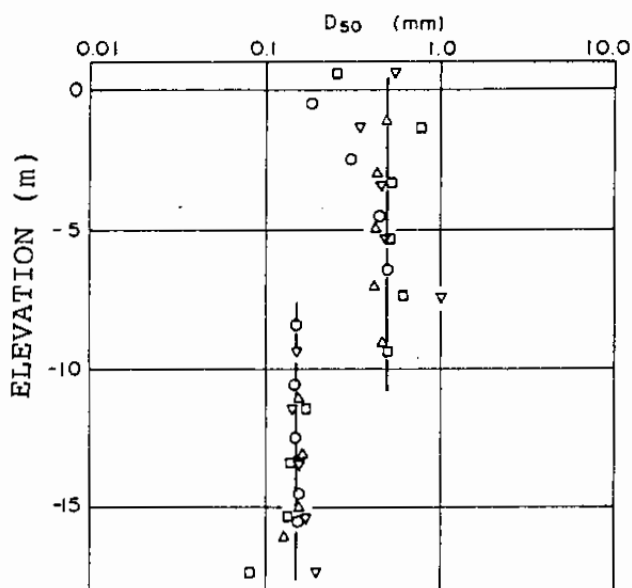


Fig. 5.12 Distribution of  $D_{50}$  ( i.e. mean grain size) at Ohama No.2 Wharf

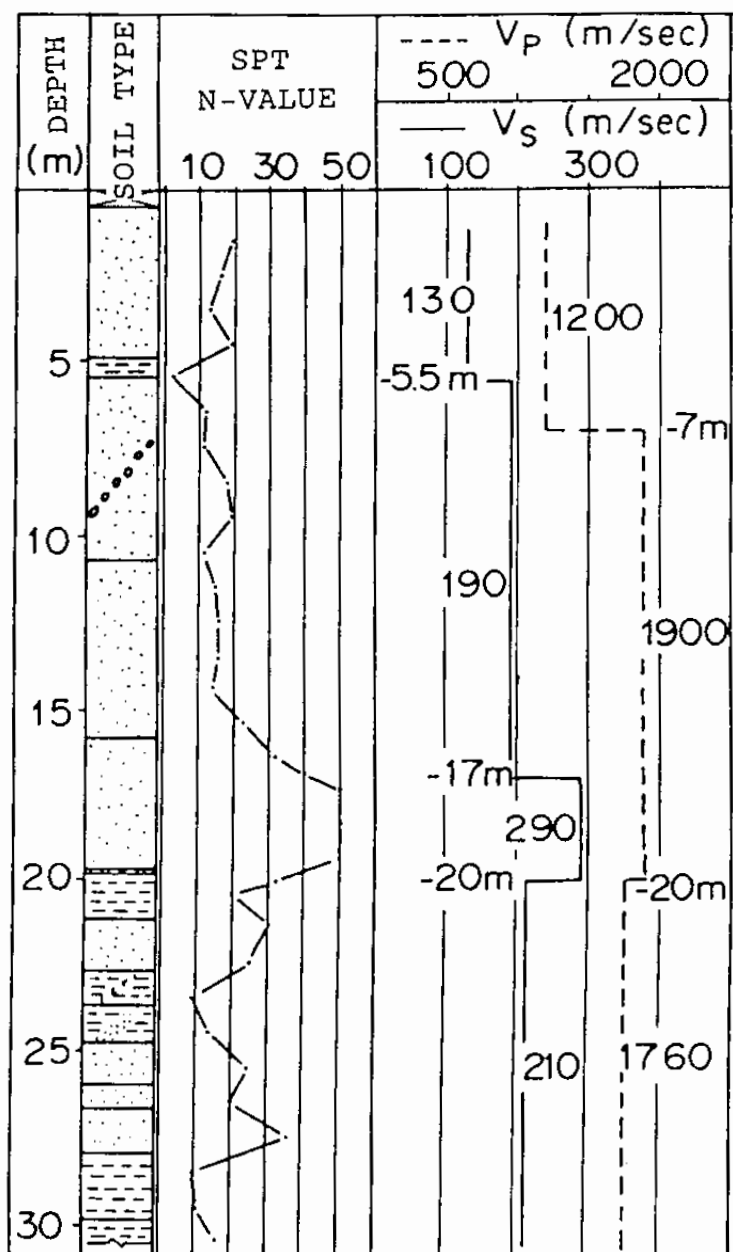


Fig. 5.13 Impulse test results and ground condition at Ohama No.3 Wharf, adjacent to Ohama No.2 Wharf

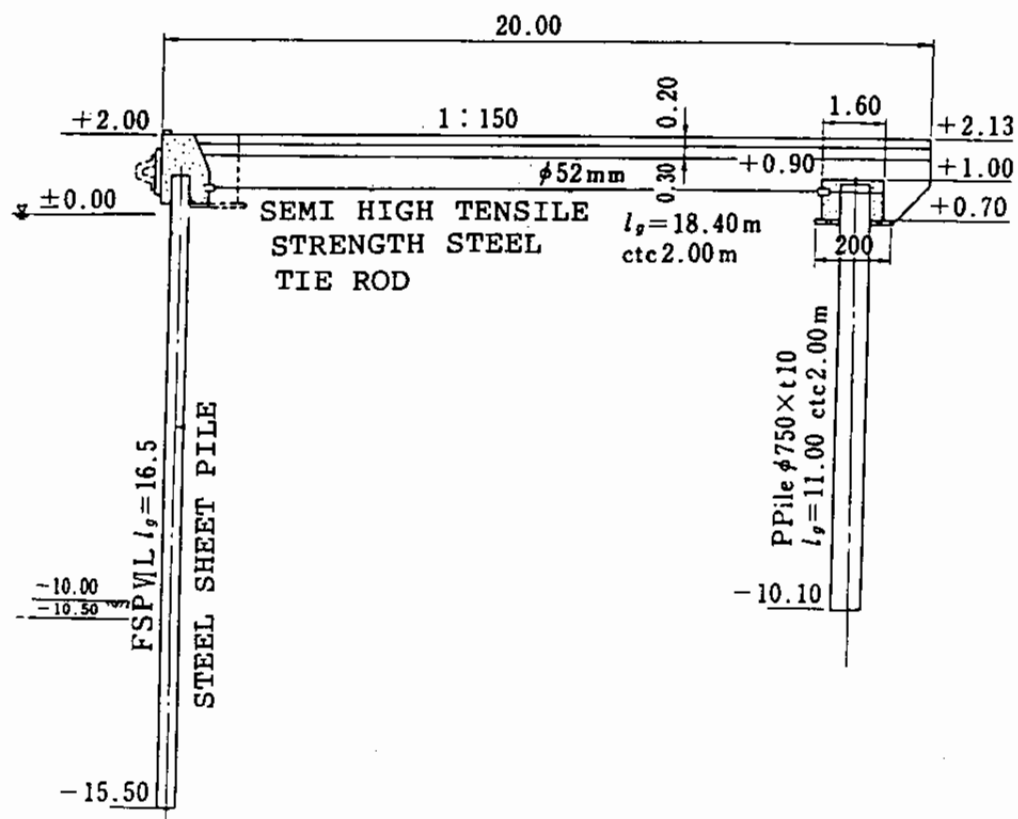


Fig. 5.14 Cross section of quay wall at Ohama No.1 Wharf

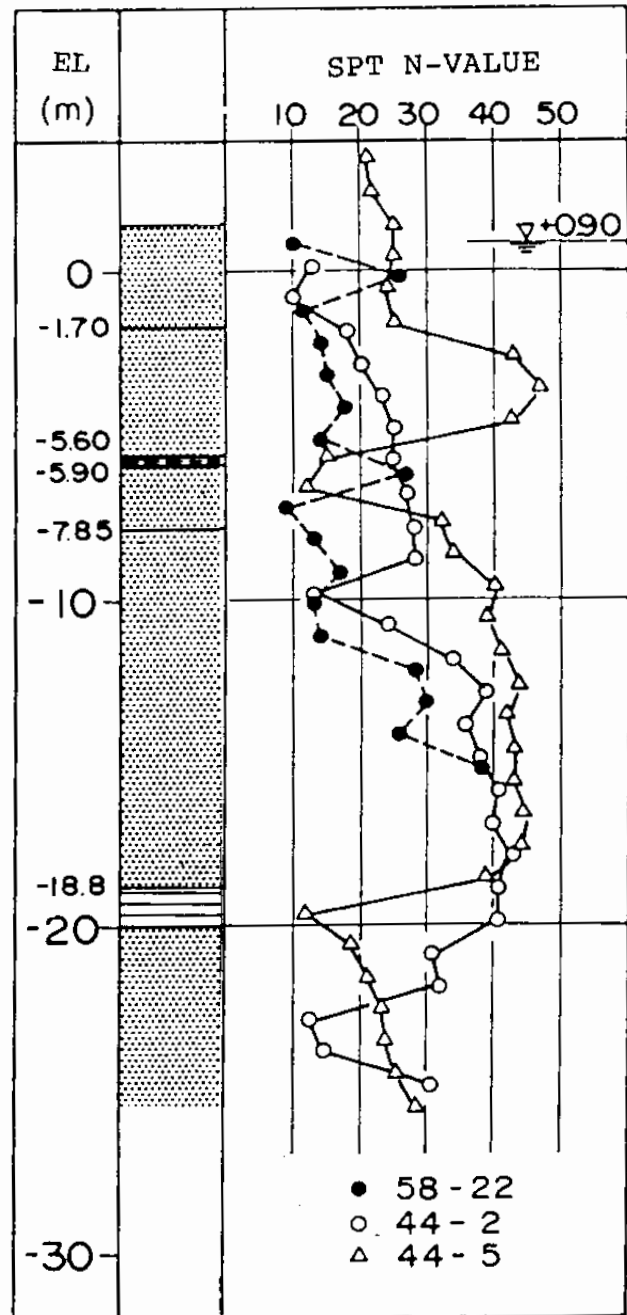


Fig. 5.15 Ground conditions at Ohama No.1 Wharf

No.1 Wharf is higher than those at the Ohama No.2 Wharf. The grain size accumulation curves and the average grain size distribution are shown in Figs. 5.16 through 5.18. The soil profile at Ohama No.1 Wharf is thus quite similar to that the Ohama No.2 Wharf except for the SPT N-values of the ground.

#### (4) Undrained cyclic properties of backfilling sand

The backfilling sands at the Ohama No.2 Wharf are taken from the Akita Port and undrained cyclic triaxial tests are conducted on the reconstituted samples. The results are shown in Fig. 5.19.

The sand at the upper part of the Ohama No.1 Wharf has the same grain size accumulation curves as that of the backfilling sand at the Ohama No.2 Wharf. Both of the sands are considered being the same sand originally deposited from the Shinjo River and hence the test results in Fig. 5.19 also apply to the sands at upper part of the Ohama No.1.

The fine sand which constitutes the lower layers of both of the wharves has the same grain size accumulation curves as that of Gaiko sand shown in Chapter 3. Both of the sands are considered being the same deposit from the Omono River and hence the test results shown in Chapter 3 are considered as representative of the properties of the lower fine sand layers.

When the soil parameters are determined for the analysis, the in-situ liquefaction resistance should be estimated from the SPT N-values. The field correlations between the SPT N-values and the shear stress ratio are obtained by several researchers. The recent studies conducted by Tokimatsu and Yoshimi (1983), Seed et al. (1985) and the author and his colleagues (Iai et al, 1989)

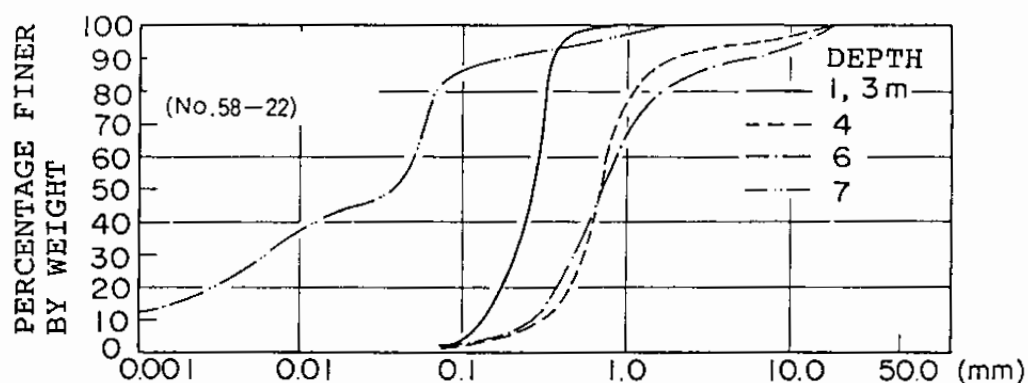


Fig. 5.16 Grain size accumulation curves of soils at Ohama No.1 Wharf; soils from upper part of the ground

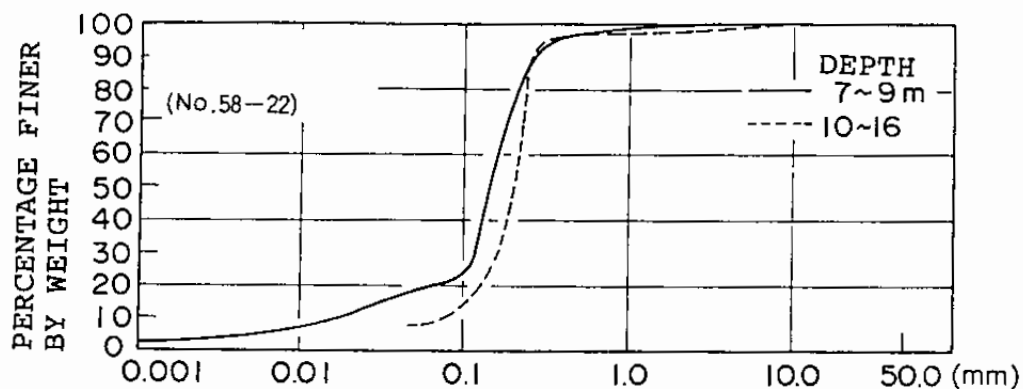


Fig. 5.17 Grain size accumulation curves of soils at Ohama No.1 Wharf; soils from lower part of the ground

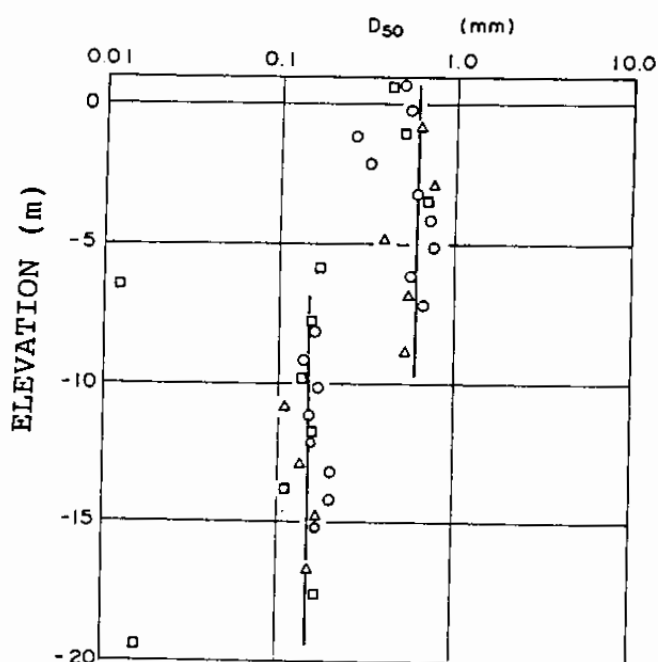


Fig. 5.18 Distribution of  $D_{50}$  (i.e. mean grain size) at Ohama No.1 Wharf



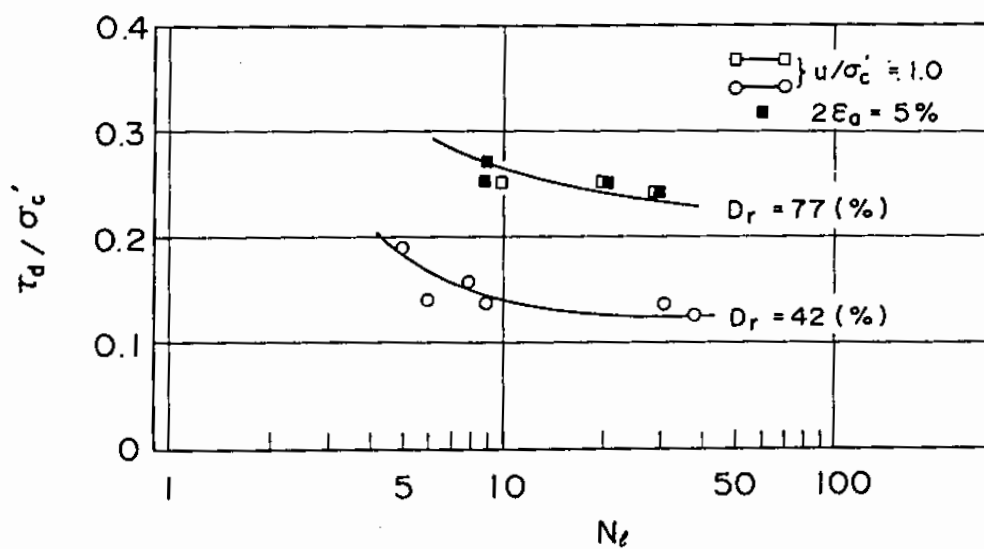


Fig. 5.19 Liquefaction resistance curves of backfill sand at Ohama No.2 Wharf

agree quite well among themselves as shown in Fig. 5.20. The in-situ liquefaction resistance is hence estimated from the SPT N-value through the correlation shown in this figure when the estimated relative density is higher than about 60 % rather than to use the laboratory results of the reconstituted samples.

## 5.2 Modeling of Soils, Structures and Sea

### 5.2.1 Modeling of Soils at Akita Port

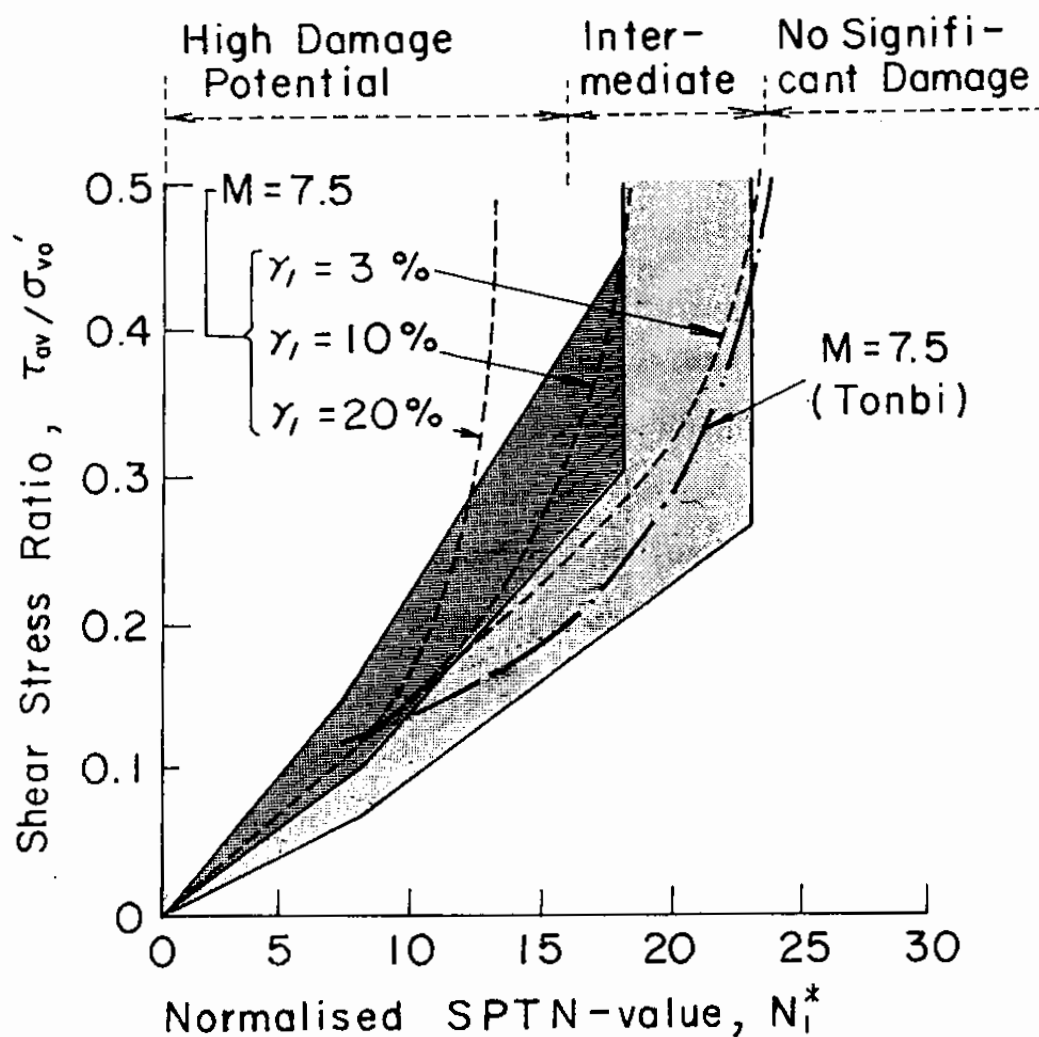
The backfill sand and the foundation of the quay wall at the Ohama No.2 Wharf are, in the analysis, idealized into four kinds of soil layers as shown in Fig. 5.21. The soil layers are further idealized into the finite elements as shown in Fig. 5.22. The quay wall at the Ohama No.1 Wharf is idealized in the similar manner as shown in Fig. 5.23. In this figure, the layer designated as Layer 2' is the one with higher SPT N-value than Layer 2 at the Ohama No.2 Wharf. Layer 4 at the Ohama No.1 Wharf is the same as Layer 4 at the Ohama No.2 Wharf.

The parameters of the soils in the present cyclic mobility model are determined from the results of the in-situ impulse testing with the down-hole method mentioned earlier and the laboratory data obtained under undrained cyclic loading shown in the previous section. The details for determining the soil parameters will be described below.

The elastic shear modulus  $G_{ma}$  is determined from the shear wave velocity obtained through the in-situ impulse testing with the down hole method conducted at the Ohama No.3 Wharf located in the vicinity of the Ohama No.2 Wharf. The effective confining

— · — · — Tokimatsu and Yoshimi  
(1983)

----- Seed et al (1985)\*\*



\* Corrected for the effective vertical stress of  $1 \text{ kgf/cm}^2$  ( $98 \text{ kN/m}^2$ )

\*\* Average Japanese SPT energy ratio (73%) is used for comparison

Fig. 5.20 Correlation between the SPT N-value and liquefaction resistance; a boundary between the darker and lighter hatches is the correlation by the author et al (1989)

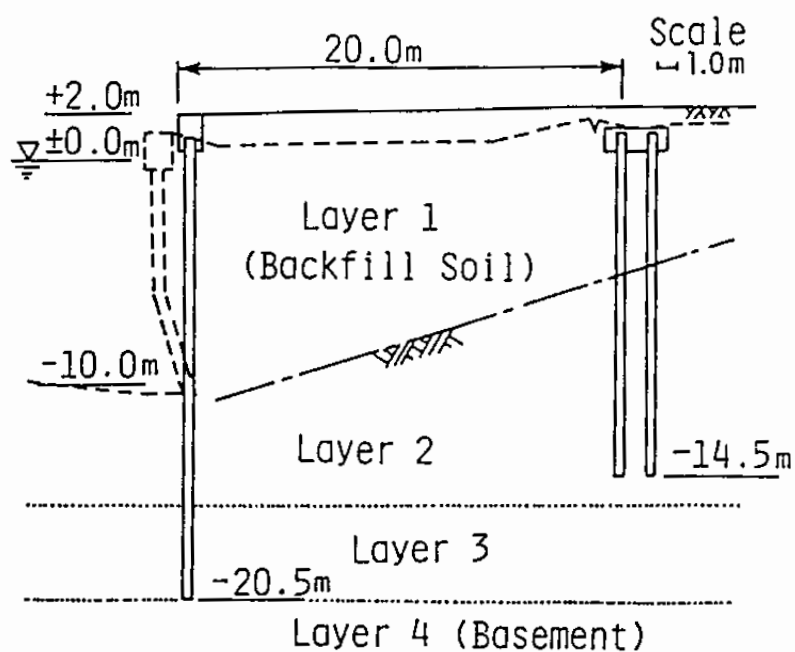


Fig. 5.21 Idealized soil layers in Ohama No.2 Wharf

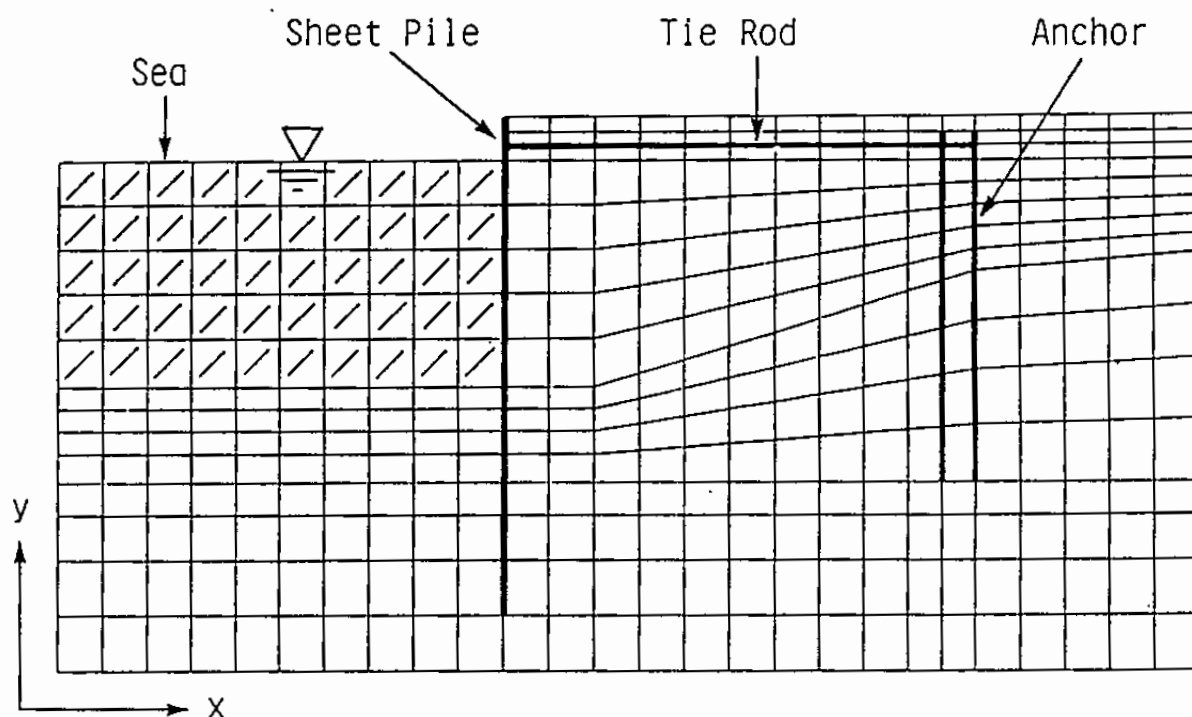


Fig. 5.22 Finite element mesh of a quay wall at Ohama No.2 Wharf

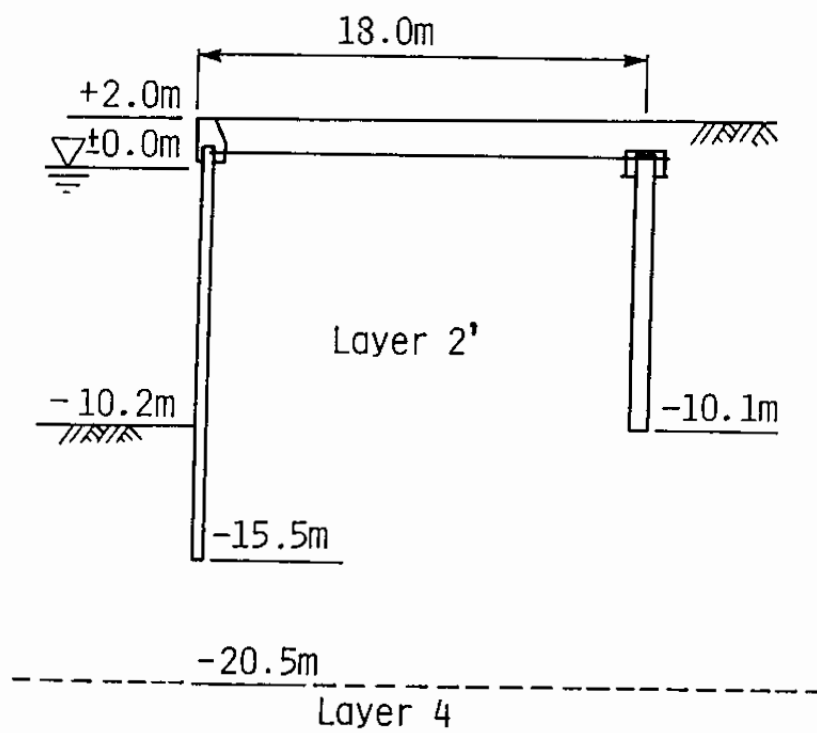


Fig. 5.23 Idealized soil layers in Ohama No.1 Wharf

pressure of  $\sigma_{ma}'$  for each soil layer is calculated by assuming  $K_0 = 0.5$ . The shear resistance angle  $\phi_f'$  is determined from the laboratory test data. Finally, the limiting value of hysteretic damping factor  $H_m$  is determined as 30 % by referring to the results of the previous studies on dynamic properties of sand shown in Fig. 1.5.

The rebound modulus of soil skeleton  $K_a$  is determined by assuming that Poisson's ratio is 0.3 as was done in the previous chapter. Phase transformation angle  $\phi_p'$  is assumed to be 30 degrees. The rest of five parameters  $p_1$ ,  $p_2$ ,  $w_1$ ,  $S_1$  and  $c_1$  are determined by the procedure mentioned in the section 3.2 based on the laboratory data shown in Fig. 5.19 with the estimation procedure from the SPT N-values mentioned earlier.

The soil parameters determined in this manner are summarized in Table 5.2. With these parameters, the present model closely simulates the liquefaction resistances of the soils at the Akita Port as shown in Figs. 5.24. An example is given in Fig. 5.25 of the stress path and the stress strain relation of the backfill sand.

Among the four soil layers idealized for the analysis, there exists a layer of clayey soil. The modeling of the clayey soil need a slight modification in the present model. The modification is in fact a simplification. The author postulates in the present analysis that the clayey soil did not significantly change the effective mean stress during the earthquake shaking and, as an approximation, kept the initial effective mean stress being constant throughout the shaking. This is obviously a crude approximation. As a compensation, the effective angle of shear

Table 5.2 Soil parameters used for quay wall analysis

	LAYER 1	LAYER 2	LAYER 2'	LAYER 3	LAYER 4
G <sub>ma</sub> (kPa)	33800	72200	72200	74970	168200
K <sub>a</sub> (kPa)	89930	192100	192100	199470	447530
- $\sigma_{ma}'$ (kPa)	50	110	69	140	157
$\phi_f$ (degree)	37	41	43	39	44
$\phi_p$ (degree)	30	30	30	--	30
S <sub>1</sub>	0.005	0.005	0.005	--	0.005
w <sub>1</sub>	0.5	8.5	14.0	--	3.8
p <sub>1</sub>	0.4	0.5	0.5	--	0.5
p <sub>2</sub>	0.42	0.8	1.0	--	0.84
c <sub>1</sub>	1.5	3.3	4.6	--	2.4

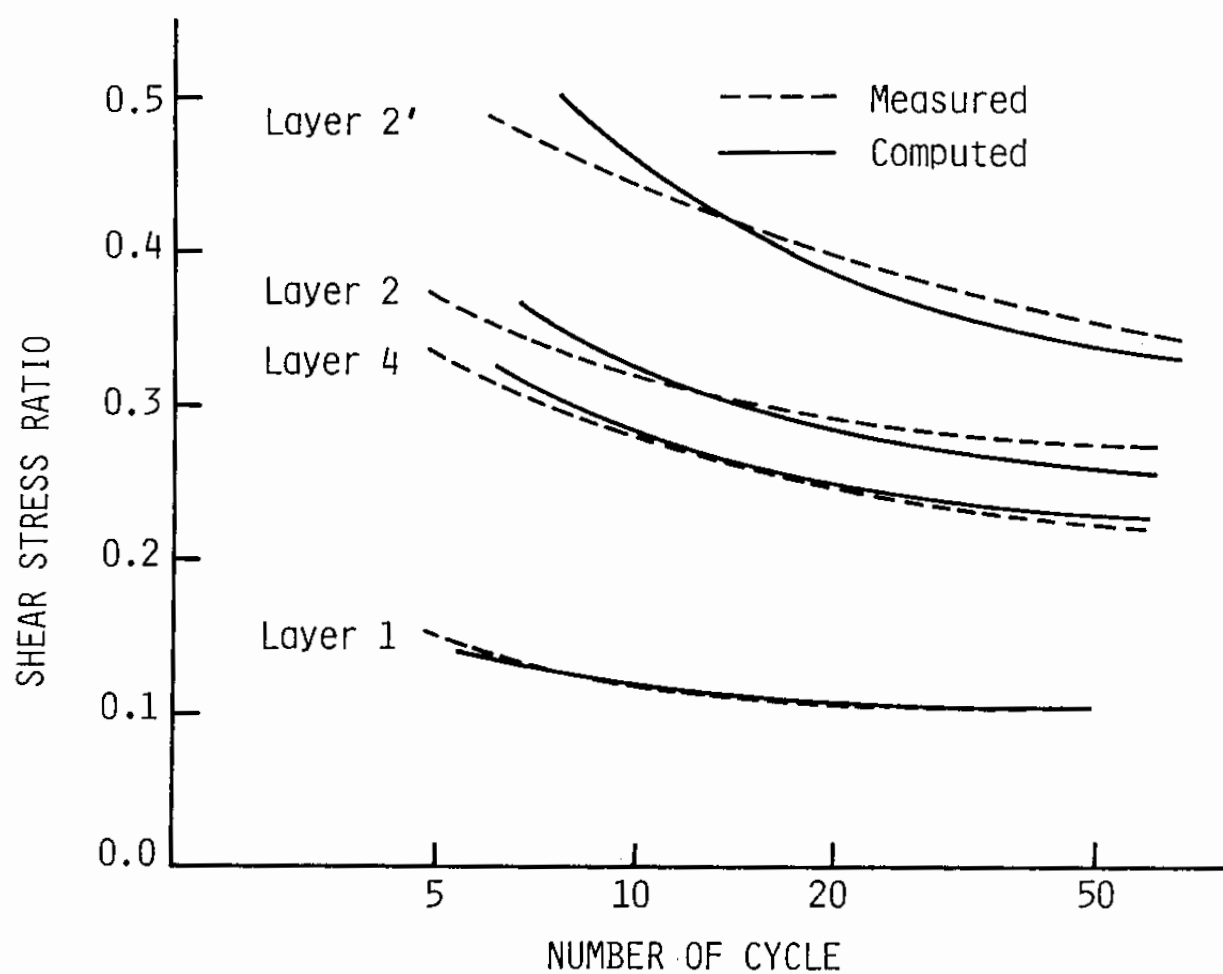


Fig. 5.24 Measured (or estimated from SPT N-value) and computed liquefaction resistance curves for soil layers at the Ohama No.1 and No.2 Wharves



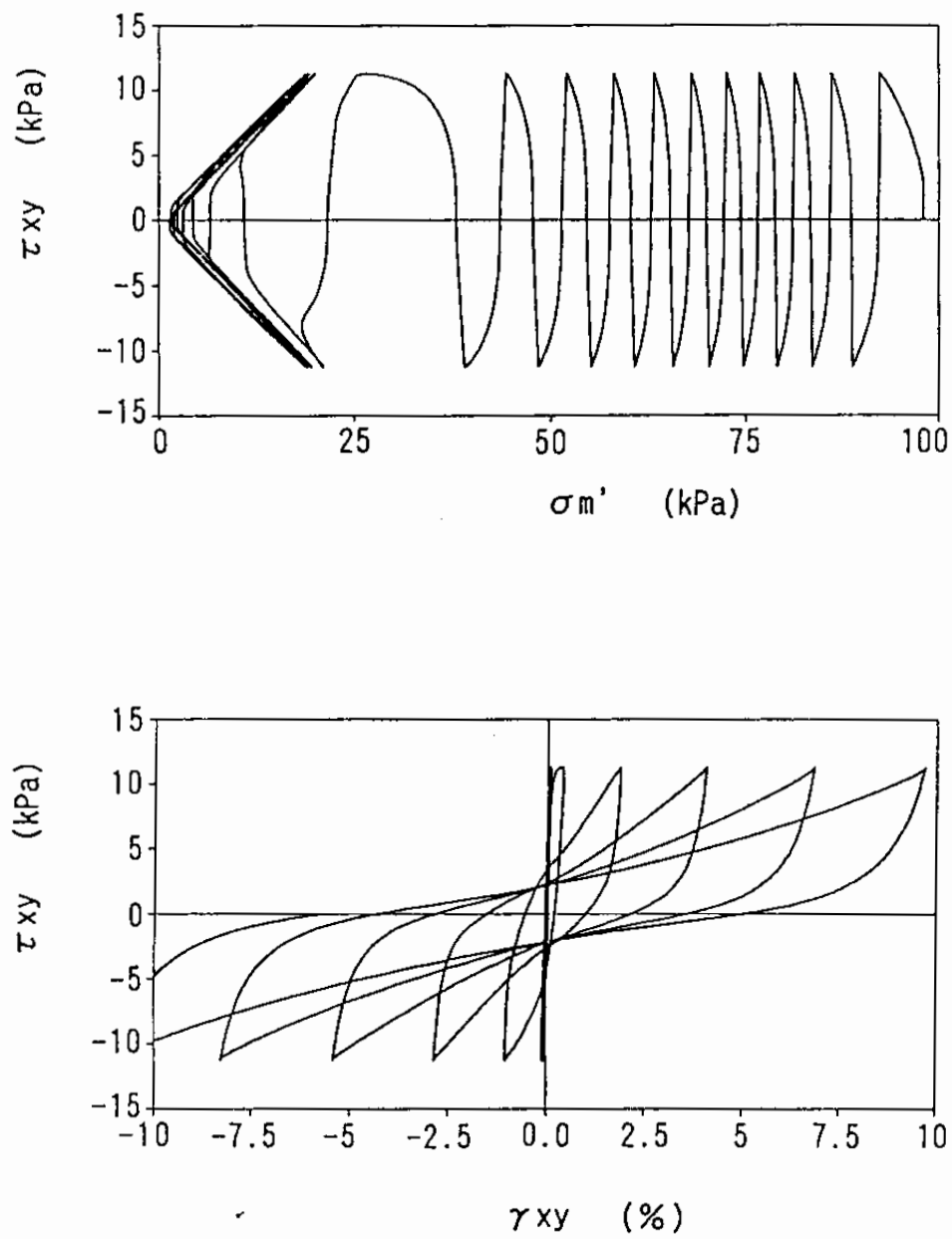


Fig. 5.25 Computed results for soil in Layer 1 in undrained cyclic loading test

resistance of clay is so adjusted as to give the appropriate undrained shear strength measured in the laboratory through the unconfined undrained compression shear testing.

### 5.2.2 Modeling of Sheet Pile, Anchor and Soil-Structure Interface

The quay walls at the Ohama No.1 and No.2 wharves have the same type of sheet piles as mentioned earlier. The sheet pile is of FSP-VI<sub>L</sub> type, having the constants, per unit breadth of the beam, the second moment of area of  $8.6 \times 10^{-4} \text{ m}^4$ , cross sectional area of  $0.0306 \text{ m}^2$ , and density of  $7.5 \text{ t/m}^3$ . In the analysis, the sheet pile is simulated with a linear beam element. It is well known that the displacement field in the commonly used beam element (e.g. Zienkiewicz, 1977) is incompatible with that of the soil element and this causes an undesirable effect on the computed results. In the present study a beam element is used of which displacement field is exactly compatible with that of soil element (Hinton and Owen, 1977).

No friction is assumed to be acting between the soil and the sheet pile. This is done in the analysis by imposing such a condition that the displacements of the nodal points of the soil element and the beam element be the same with each other in the horizontal direction but can take independent values in the vertical direction.

The tie rod is simulated by a linear beam element of which mass is assumed to be zero and is connected with the sheet pile and the anchor piles by hinges. No interaction is taken into account between the soil and the tie rod. This is done in the analysis by simply specifying the geometry of the beam element

without any connection with the soil elements.

The anchor pile is idealized also by the linear beam elements. Two rows of the anchor piles, at the Ohama No.2 Wharf, are idealized by the linear beam elements, of which top ends are rigidly fixed with each other. No friction is assumed to be acting between the soil and the anchor piles. The numerical implementation of this is done in the similar way as mentioned earlier.

### 5.2.3 Modeling of Sea Water

The sea water is modeled as incompressible fluid and is formulated as an added mass matrix (Zienkiewicz, 1977). The equilibrium of the fluid at the solid-fluid interface, as shown in Fig. 5.26, is such that the inertia of the fluid caused by the acceleration of the solid should be in balance with the gradient of pore water pressure. In its explicit form, the equilibrium equation at the interface is written by

$$\frac{\partial p}{\partial n} = -\rho \frac{\partial^2}{\partial t^2} (U_n) \quad (5.1)$$

in which  $U_n$  is the normal component of the displacement. With the differential equation governing the pressure distribution during small amplitude motions, the water is idealized into a mass matrix. For details, see the aforementioned reference.

## 5.3 Initial and Boundary Conditions and Input Motion

### 5.3.1 Static Analysis with Gravity

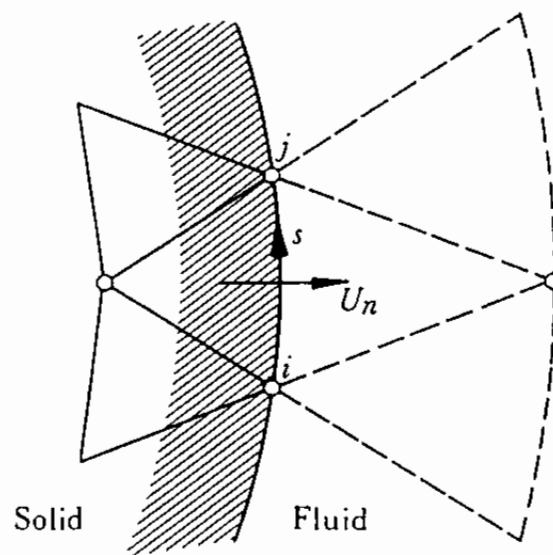


Fig. 5.26 A solid-fluid interface (after Zienkiewicz, 1977)

Before conducting the analysis on the behavior of the quay walls during the earthquake, static analysis is conducted with gravity for idealizing the initial stress acting before the earthquake. The same constitutive model is used as in the dynamic analysis with the drained condition.

Obviously an ideal static analysis can be done by closely simulating the steps taken for construction of structures; i.e. by simulating the backfilling process or the excavation process and, if any, the pre-stress histories on the ground due to the previous small earthquakes. These steps, if taken, are obviously so complicated that the static analysis itself can become a major research subject. In the present analysis, such a complication is avoided because the main target is the analysis of the cyclic mobility. The author assumes that a simple one step loading of gravity will give a reasonable approximation of the initial stress condition for the dynamic analysis to be conducted afterwards.

The results of the static analysis due to gravity are shown in Figs. 5.27 and 5.28. The initial earth pressures in front of and behind the sheet pile are of active and passive earth pressures as naturally expected. The corresponding bending moment reveals zero point at around the sea bed level, being consistent with the previous experimental studies by Arai and Yokoi (1965).

### 5.3.2 Boundary Conditions

During the dynamic analysis, the dynamic waves should be appropriately permitted to transmit from the field of the analysis, shown in Fig. 5.22, to the outside field because the

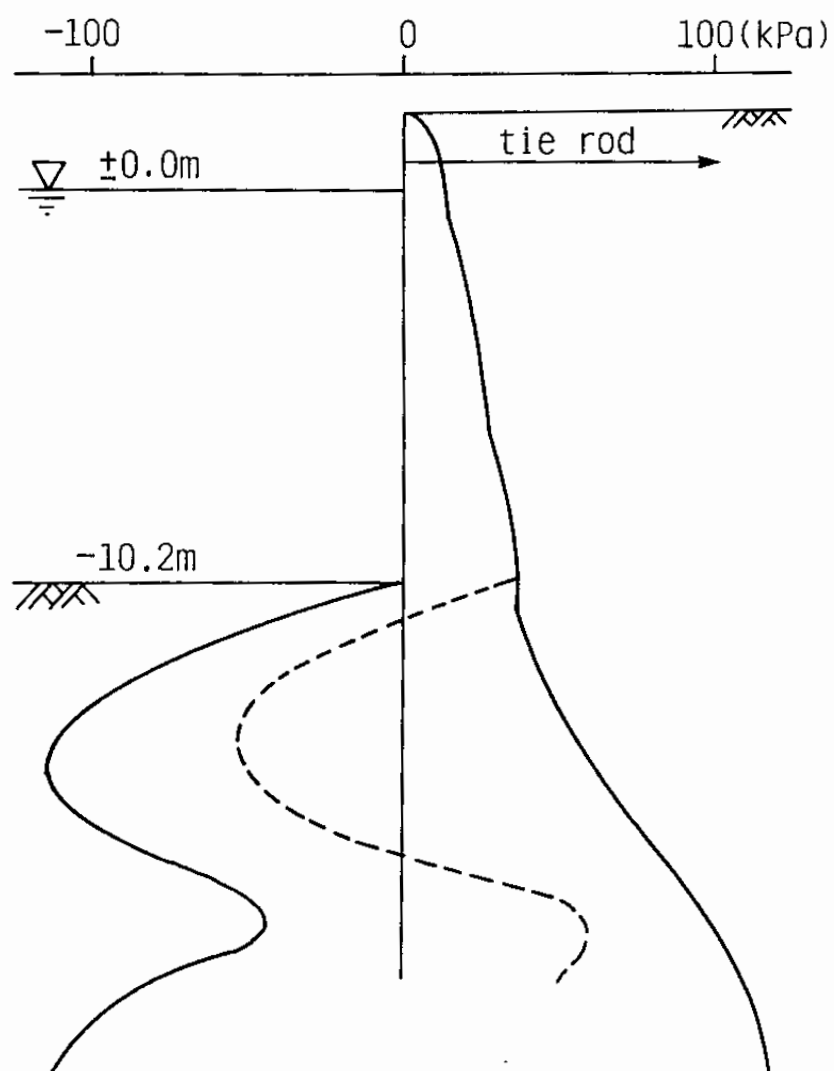


Fig. 5.27 Initial earth pressure due to gravity

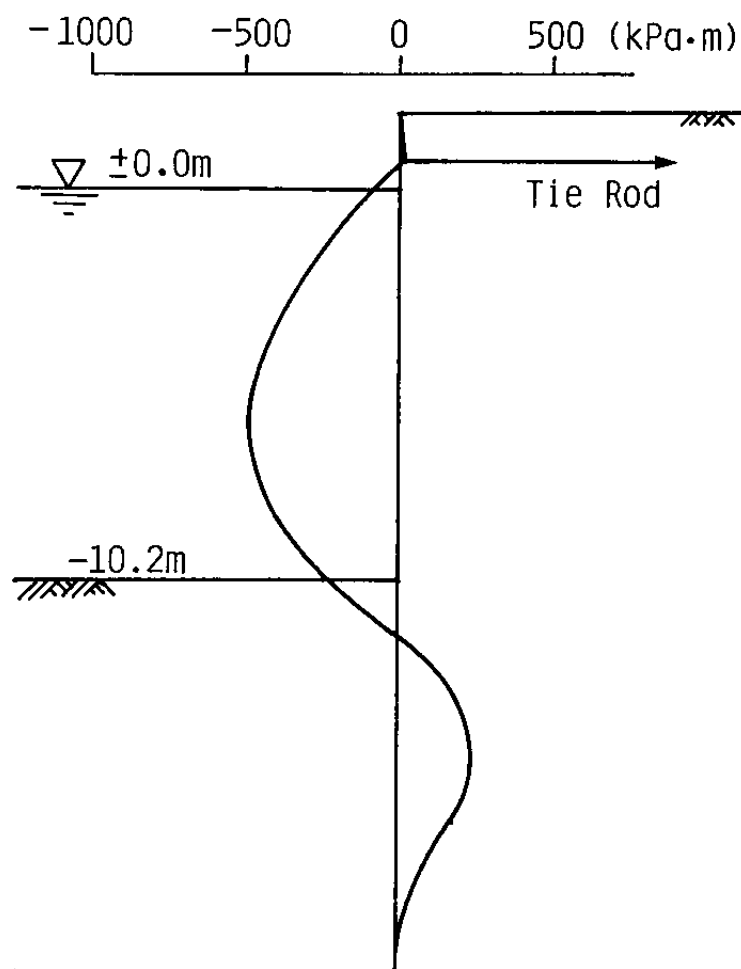


Fig. 5.28 Initial bending moment due to gravity

boundaries of the field fixed for the analysis do not exist in reality. In order to take into account this fact in an approximate manner, the side and the bottom boundaries in Fig. 5.22 are simulated by the viscous dampers.

The dynamic analysis should also appropriately take into account the effect of the earthquake waves transmitted from the outside field. In the present analysis, the incident wave transmitted vertically to the bottom boundary is given through the viscous damper at the bottom boundary. The free field motions, i.e. the one dimensional responses at outside fields consisting of level grounds at the far fields in the side boundaries, are also computed in the similar manner and given through the viscous dampers at both sides of the boundaries.

The results of the free field response analyses at the land part of the Ohama No.2 Wharf are shown in Figs. 5.29 and 5.30. In this analysis, even when the excess pore water pressure almost reaches the initial vertical effective stress, the acceleration at the ground surface does not decrease to a very small value. This might be due to sporadically occurring decreases in excess pore water pressures, shown the middle row in Fig. 5.30, due to the cyclic mobility associated with long period motion of about 2 seconds.

### 5.3.3 Input Motion and Time Integration

With the initial and boundary conditions stated above, the dynamic analysis is conducted on the behaviors of the steel sheet pile quay walls at the Akita Port. As an input motion, the earthquake motion recorded at the Akita Port, shown in Fig. 5.4,



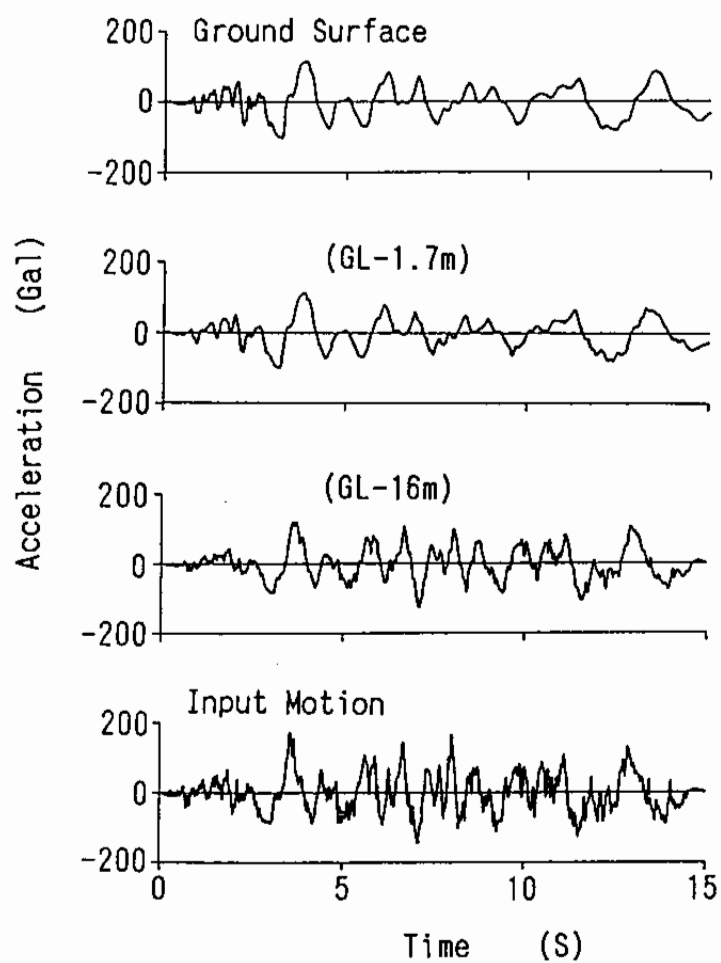


Fig. 5.29 Response accelerations in the free field

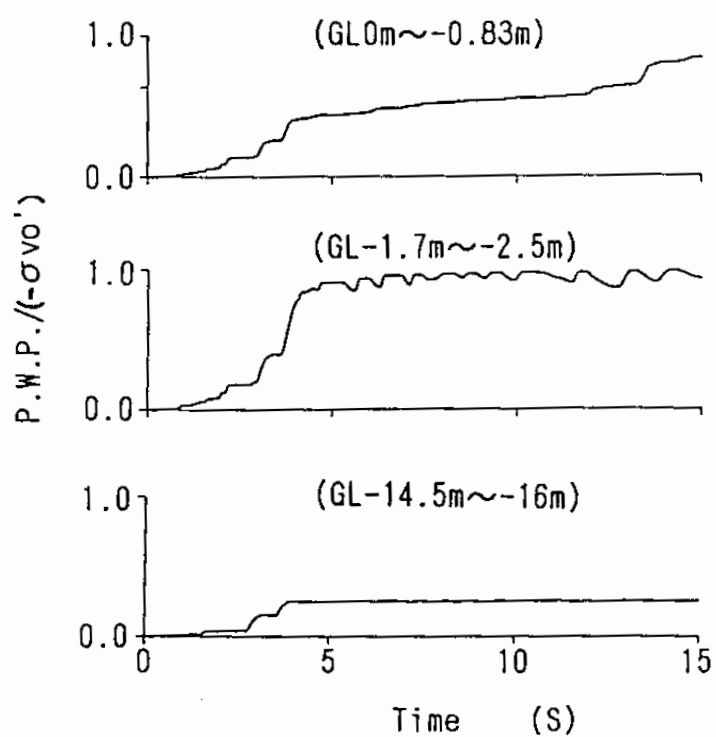


Fig. 5.30 Excess pore water pressures in the free field

is at first deconvoluted by equivalent linear method for obtaining the incident wave, and transformed into the normal directions to the face lines of the quay walls as shown in Fig. 5.31. The input motions thus obtained are shown in Fig. 5.32.

The dynamic analysis of the quay walls is conducted under the undrained condition (Zienkiewicz et al, 1982). The numerical integration is done by Wilson- $\theta$  method ( $\theta = 1.4$ ) at the time step of 0.01 seconds. Rayleigh damping ( $\alpha = 0$  and  $\beta = 0.005$ ) which is proportionally decreasing with the degree of cyclic mobility is used for ensuring the stability of the numerical solution process.

#### 5.4 Analysis of a Damaged Quay Wall

##### 5.4.1 Earthquake Response and Deformation

The numerical simulation of the quay wall, after 14 seconds of shaking, results in the deformation shown in Fig. 5.33 at the Ohama No.2 Wharf; deformations towards sea are mainly recognized at the soil wedges in front of and behind the sheet pile.

Instantaneous directions of the response accelerations, shown in Figs. 5.34, indicate rotational motions, possibly Rayleigh waves, are generated in the vicinity of the ground surface due to the interaction between the sheet pile and the backfilling sand.

The maximum acceleration at the top of the quay wall is about 190 Gals as shown in Fig. 5.35. In this figure and the figures to follow, the alphabets indicate the locations shown in Fig. 5.33. As the shaking continues, the horizontal displacements

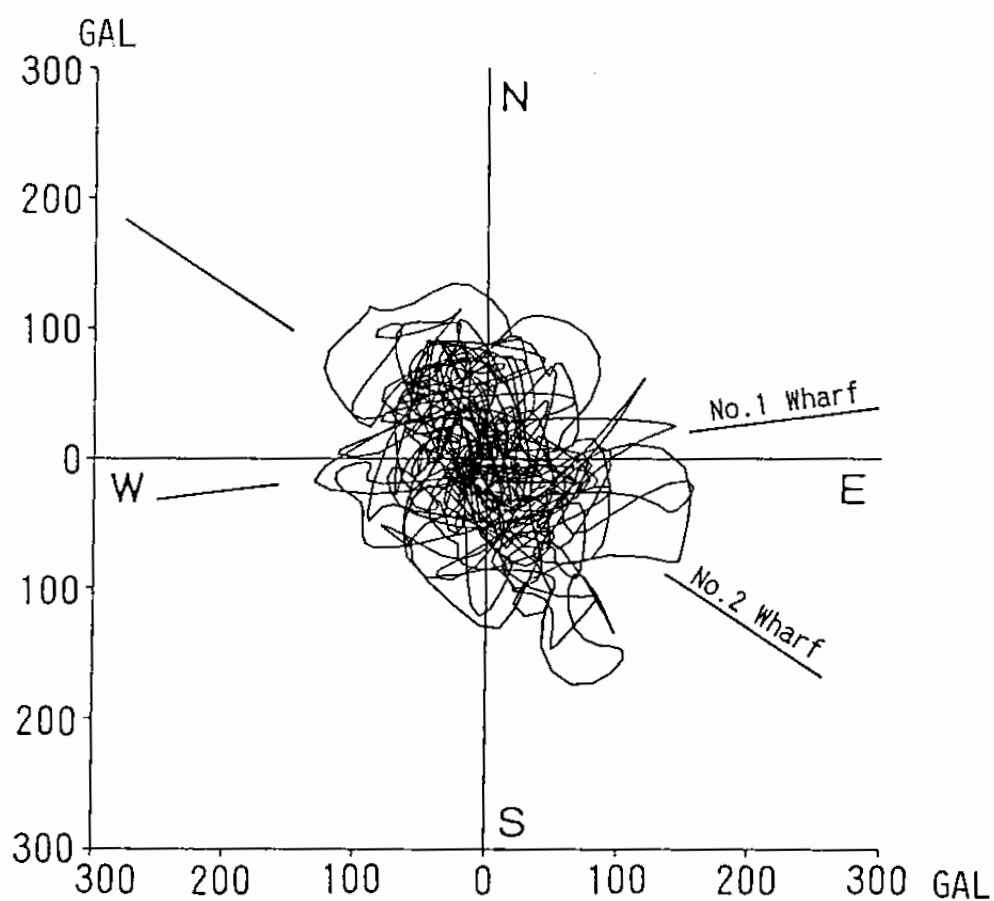


Fig. 5.31 Acceleration loci of incident wave to Akita Port and normal directions to face lines of quay walls at Ohama No.1 and No.2 Wharves

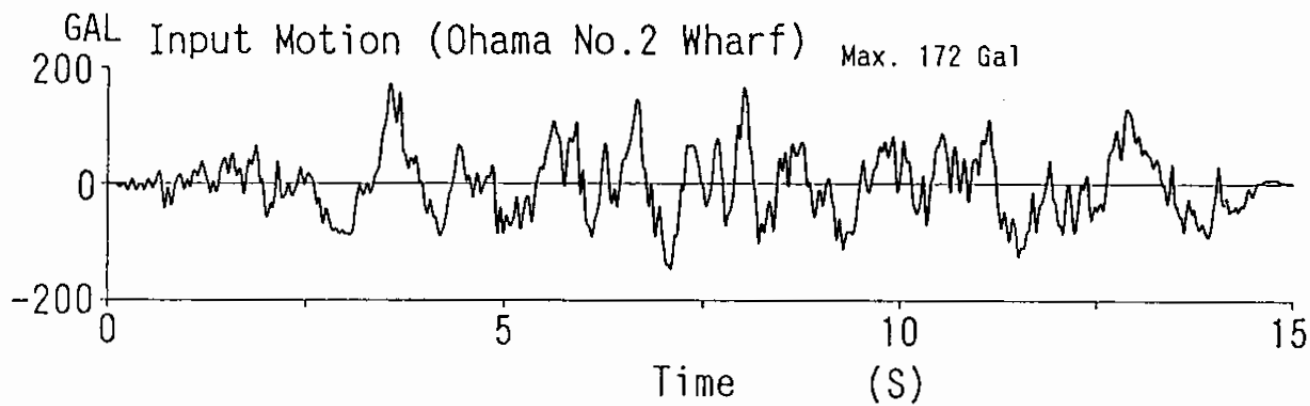
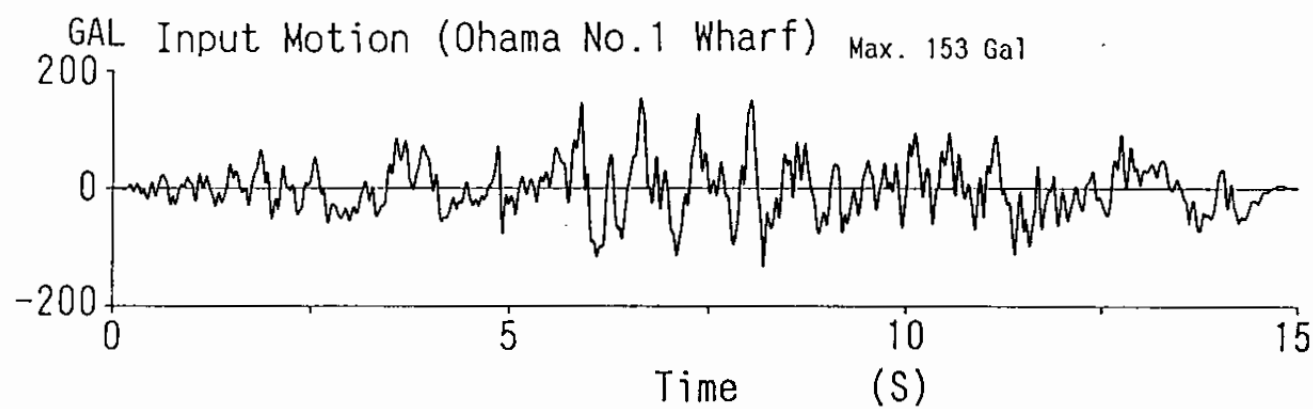


Fig. 5.32 Input earthquake motions; incident waves to Ohama No.1 and No.2 Wharves plotted with twice the amplitude

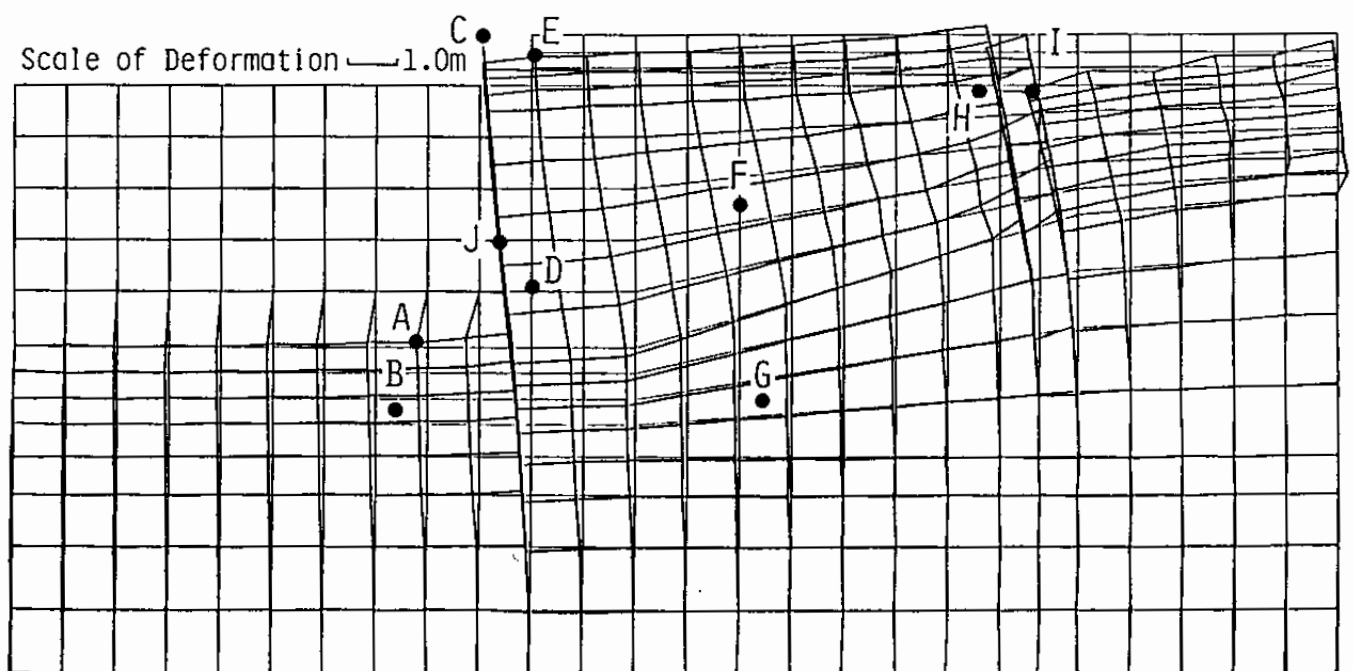


Fig. 5.33 Computed deformation of quay wall at Ohama No.2 Wharf  
at the end of 14 second shaking

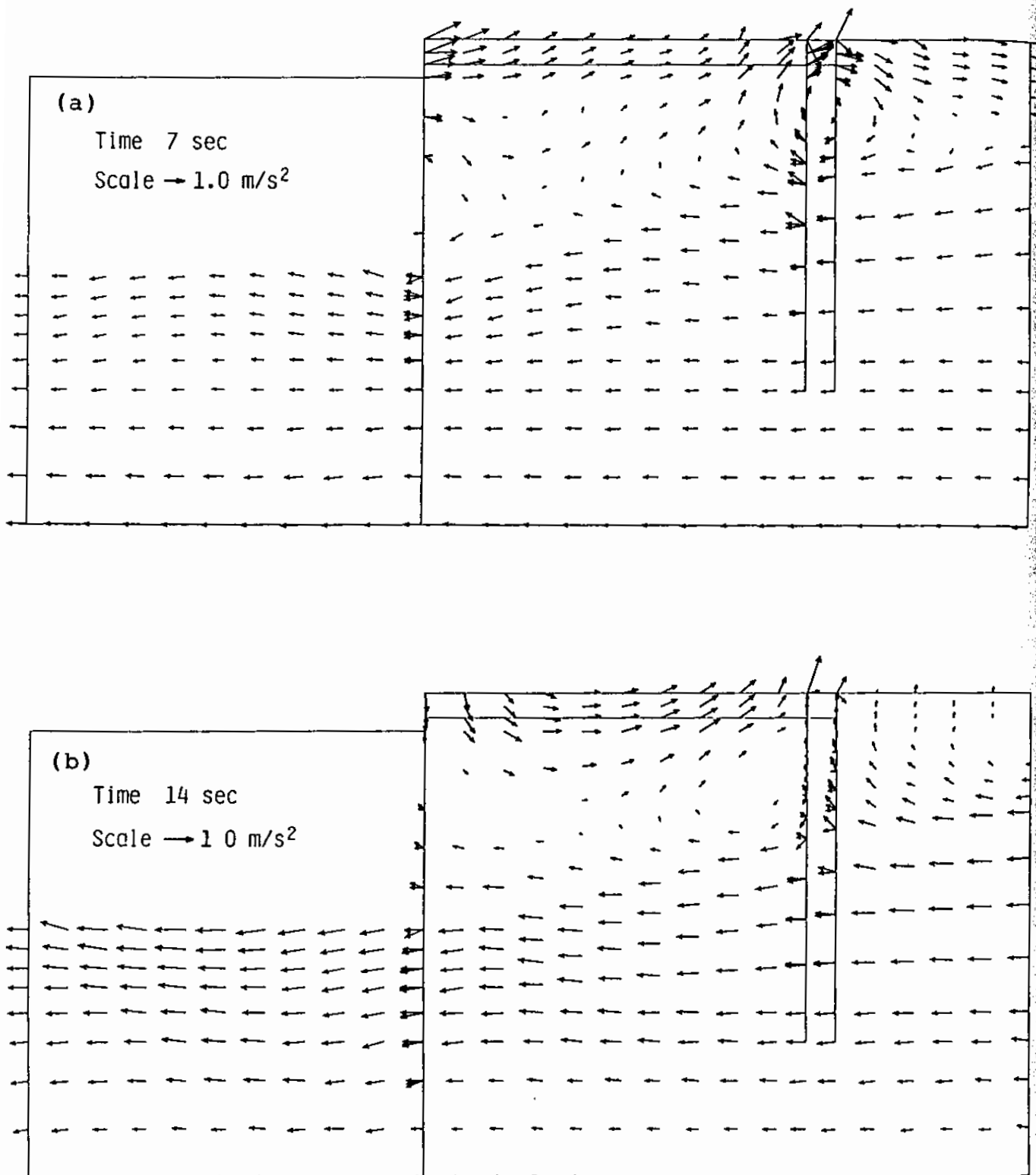


Fig. 5.34 Computed distribution of accelerations at Ohama No.2 Wharf; (a) at 7 seconds and (b) at 14 seconds

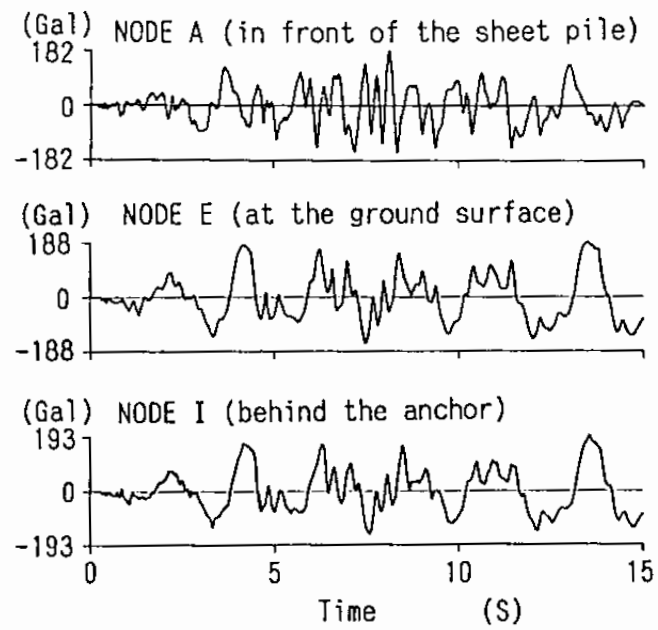


Fig. 5.35 Horizontal response acceleration at Ohama No.2 Wharf

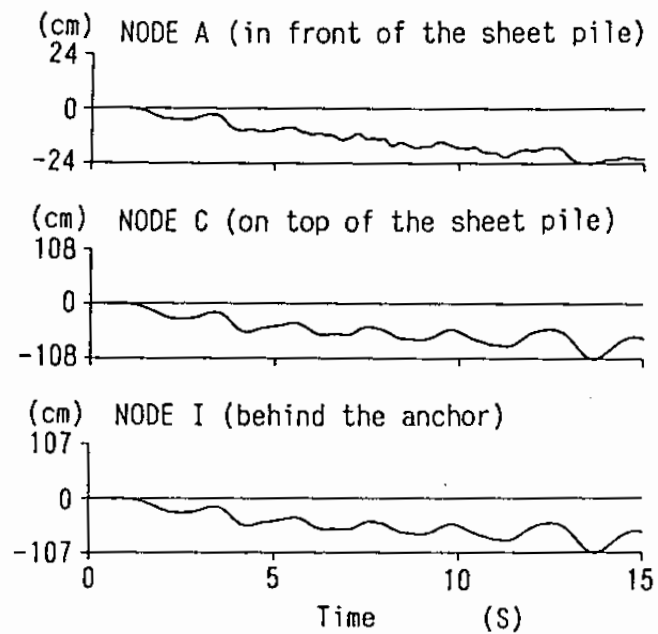


Fig. 5.36 Horizontal response displacement at Ohama No.2 Wharf



gradually increase towards sea as shown in Fig. 5.36. The backfill soil behind the sheet pile gradually settles as shown in the lower two rows in Fig. 5.37 whereas the sea bed in front of the sheet pile gradually swells as shown in the same figure.

The horizontal displacement at the sheet pile is computed as about 1.0 meter at the end of the shaking whereas the observed displacement ranges, as mentioned earlier, from about 1.1 to 1.8 meters, indicating the computed displacement is close to the range of the observed values.

The settlement behind the sheet pile is computed as about 0.6 meters at the end of the shaking whereas the observed settlement, as mentioned earlier, is about 1.4 meters. Should the effect of yielding of the sheet pile and drainage of pore water be included in the analysis, the computed settlement would be greater. In this context, the computed settlement is not contradictory to the observed settlement.

#### 5.4.2 Earth Pressure and Bending Moment

The earth pressures, i.e. the normal total stresses (= the normal effective stresses + the excess pore water pressures), acting on the sheet pile after 15 seconds of shaking, shown in Fig. 5.38, become greater than those before the shaking. The earth pressures behind the sheet pile at 15 seconds of shaking become about the same as that of  $K_0 = 1.0$  condition. Though the effect of the inertia acting exactly at 15 seconds is ambiguous, the computed value of the earth pressure is, in an approximate sense, consistent with the results of the previous laboratory study on the earth pressures acting on the fixed wall due to

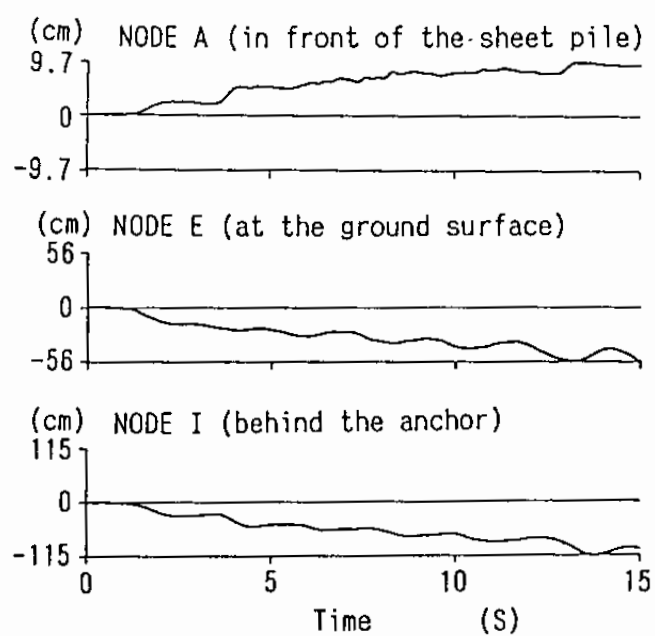


Fig. 5.37 Vertical response displacement at Ohama No.2 Wharf

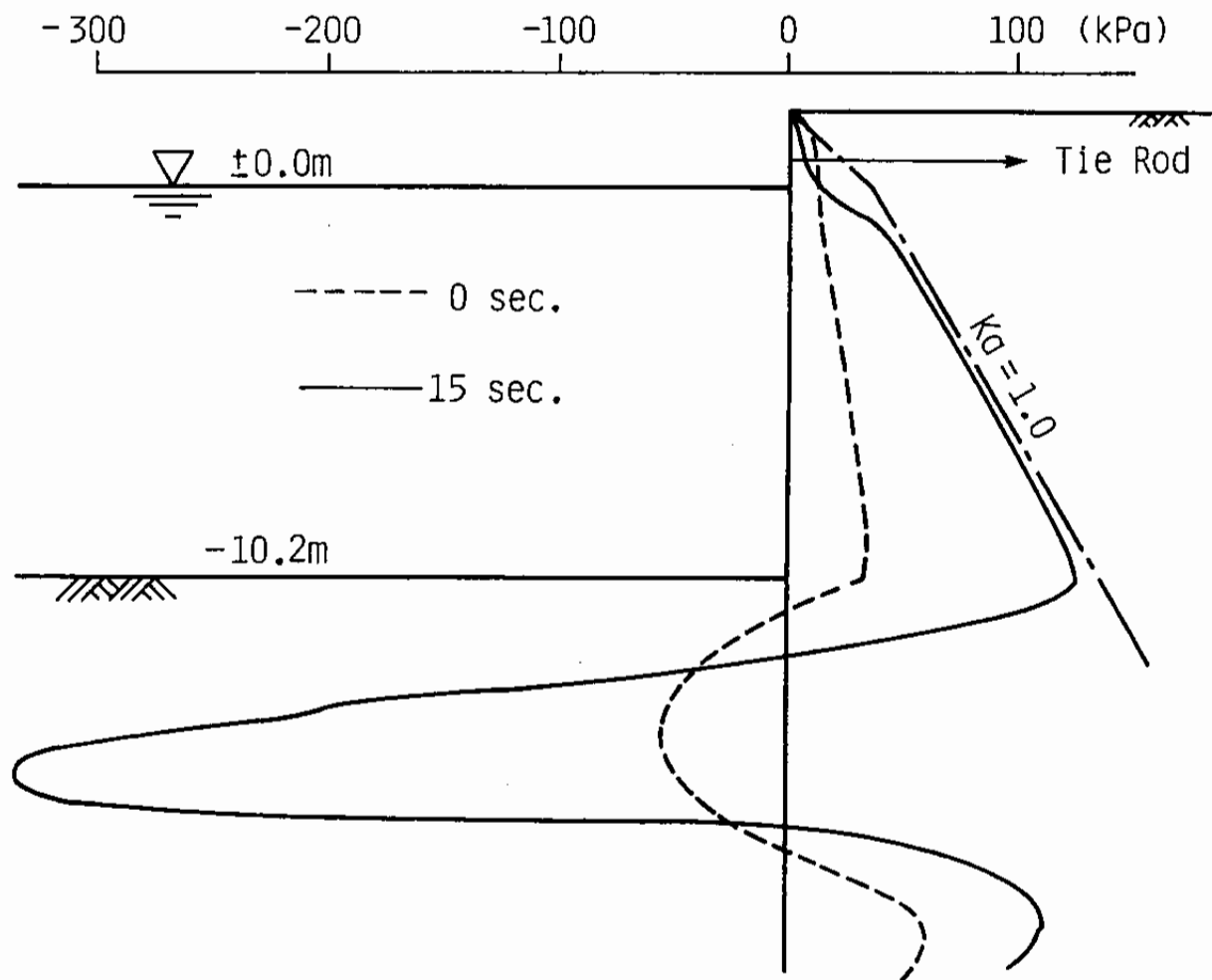


Fig. 5.38 Normal stresses on sheet pile before and after the earthquake at Ohama No.2 Wharf

liquefied soil (Tsuchida, 1968).

In accordance with those changes in the normal total stresses, the bending moment of the sheet pile rapidly becomes larger as shown in Fig. 5.39. In particular, the bending moment at the level of 6 meters below the water level gradually increases as shown in Fig. 5.40.

The maximum stress due to bending is computed as 470000 kPa as shown in Fig. 5.39 whereas the yield strength of the steel sheet pile is 300000 kPa, which is far less than the earthquake induced bending stress computed in the analysis. This indicates that the observed phenomenon, i.e. the failure of the sheet pile, is well explained by the analysis because, as mentioned earlier, the sheet pile is idealized in the analysis with the linear beam element, which are assumed never to fail.

The analysis also indicates some possibility of yielding at about 14 meters below the water level. This might be caused by the strong resistance of the firm ground below the sea bed. There was one sheet pile which was able to be dragged out from the ground instead of being cut at the sea bottom level. The sheet pile shows a crack at a level of 12.2 meters below the water level. Thus, the analysis is not contradictory to the evidence.

Excess pore water pressures in the soils in front of and behind the sheet pile are computed as shown in Fig. 5.41. The excess pore water pressure rapidly increases behind the sheet pile at the initiation of the shaking. The excess pore water pressure in front of the sheet pile, however, fluctuates around the value of zero possibly because of the high liquefaction resistance of the soil.

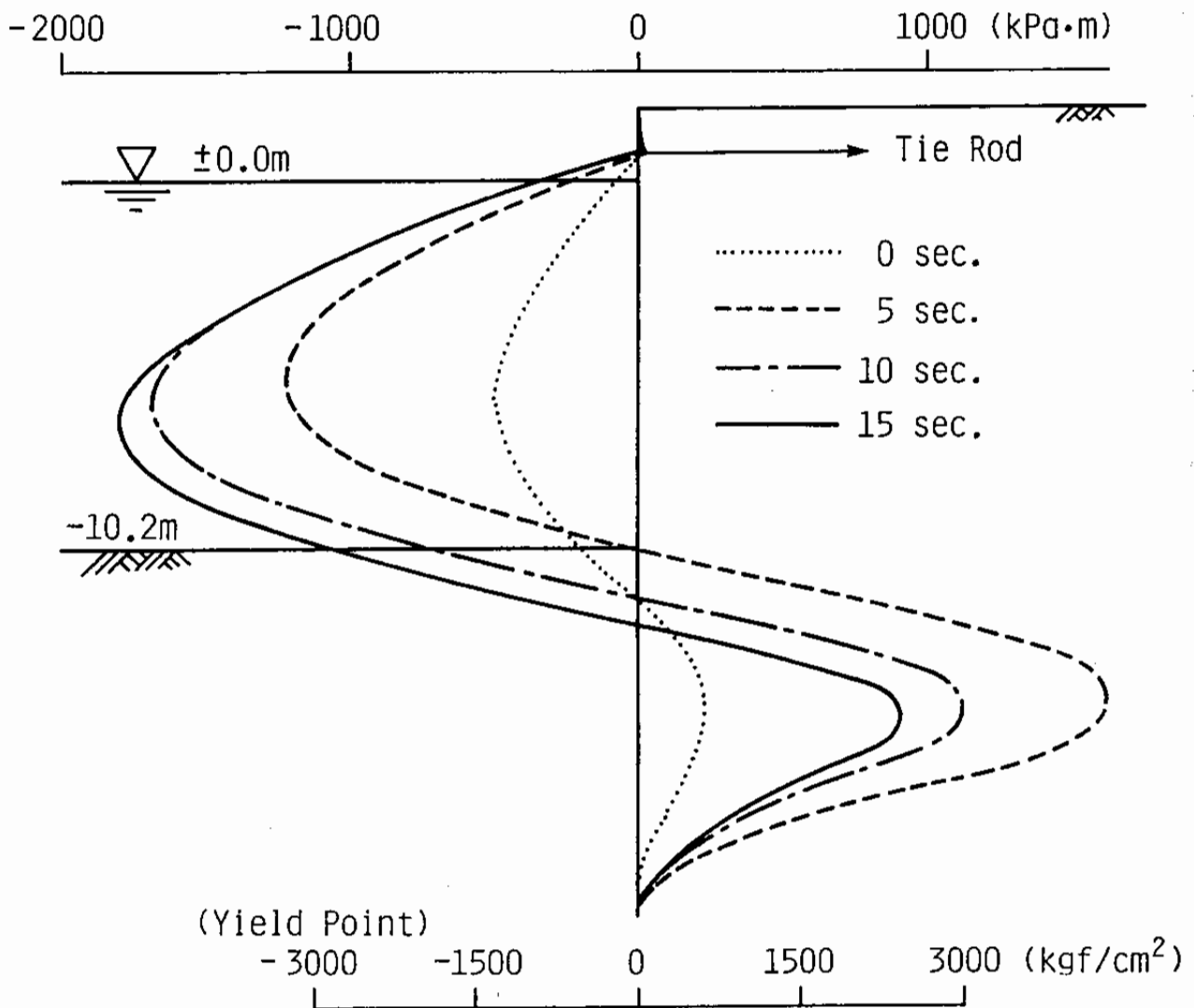


Fig. 5.39 Bending moment (shown in upper scale) and bending stress (shown in lower scale) before and after the earthquake at Ohama No.2 Wharf

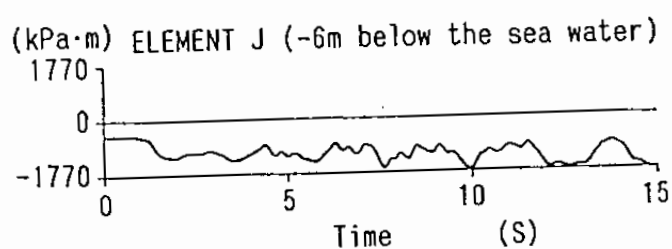


Fig. 5.40 Time history of bending moment at the elevation of  
- 6 m at Ohama No.2 Wharf

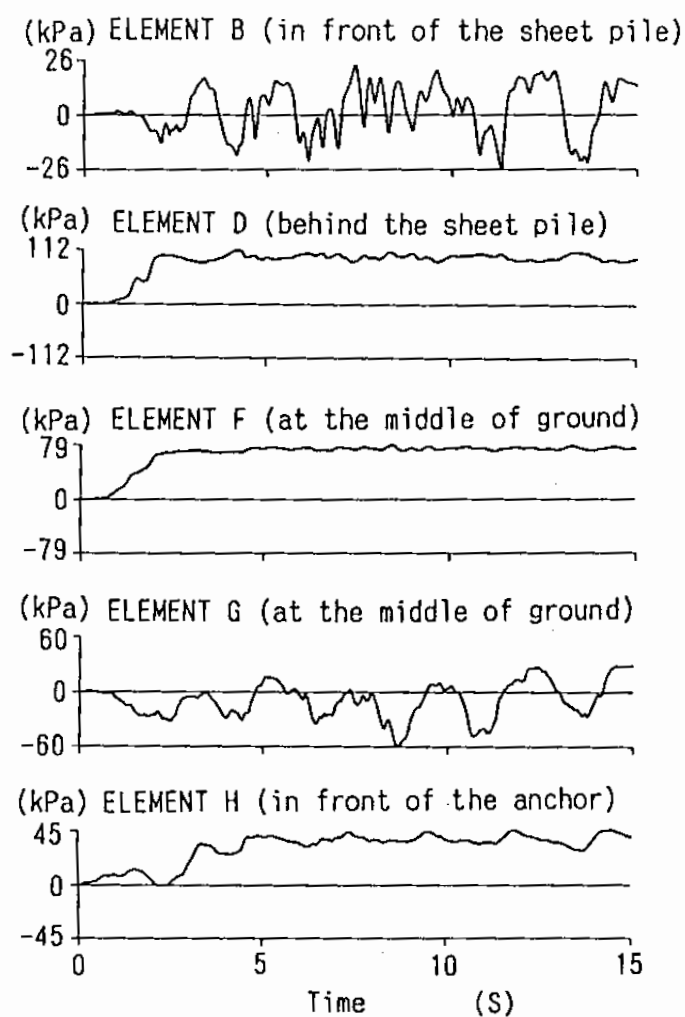


Fig. 5.41 Excess pore water pressures at Ohama No.2 Wharf

#### 5.4.3 Comparison between Observed and Computed Results

Though the observed data during the earthquake are far from satisfactory, the results of the analysis presented so far are consistent with many of the observed phenomena relevant to the deformation of the sheet pile quay wall at the Ohama No.2 Wharf. It is concluded that the approach taken in the present analysis is capable of representing the essential features of the observed damage to the sheet pile quay wall during the earthquake.

#### 5.5 Mechanism of Deformation

Though stress and strain in the soil of the quay wall at the Ohama No.2 Wharf were not measurable during the earthquake, it may still be worth to look at the computed results of the stress paths and stress-strain relations in order to understand how the deformation is induced during the earthquake. The results will tell us whether the mechanism of the deformation represented by the present model is consistent with the natural understanding of the mechanism of deformation such as stated in the beginning of the present chapter; i.e. existence of initial stress and its release in accordance with the cyclic mobility.

In order to look into this aspect of the analysis, four soil elements are selected in this study; soil elements in front of and behind the sheet pile (i.e. the elements B and D in Fig. 5.31), soil elements between the sheet pile and the anchor (i.e. the elements F and G) and a soil element in front of the anchor (i.e. the element H).

In the present analysis, the x-y coordinates are taken as

shown in Fig. 5.22 and the stress components are defined as shown in Fig. 5.42. Definitions for strain components are similarly given. In particular, compression stress and strain are defined negative as mentioned in the earlier chapter.

The following five relations regarding stress and strain are shown for each element;

- (1) the effective stress path; i.e. the relation between the effective mean stress :  $-\sigma_m' = -(\sigma_x' + \sigma_y')$  and the deviatoric stress  $\tau = \sqrt{\tau_{xy}^2 + [(\sigma_x' - \sigma_y')/2]^2}$ ,
- (2) the stress strain relation in compression shear mode shown in Fig. 5.42(b); i.e. a relation between axial stress difference  $(\sigma_y' - \sigma_x')$  and axial strain difference  $(\epsilon_y - \epsilon_x)$  with such a mode shown in the same figure defined positive,
- (3) the stress strain relation in simple shear mode shown in Fig. 5.42(c); i.e. a relation between shear stress  $\tau_{xy}$  and shear strain  $\gamma_{xy}$ ,
- (4) the relation relevant to direction and rotation of principal stress axis; i.e. the relation between axial stress difference  $(\sigma_y' - \sigma_x')$  and shear stress  $\tau_{xy}$
- (5) the relation relevant to direction and rotation of principal strain axis; i.e. the relation between axial strain difference  $(\epsilon_y - \epsilon_x)$  and shear strain  $\gamma_{xy}$ .

#### 5.5.1 Stress and Strain in front of Sheet Pile

In front of the quay wall at the soil element B in Fig. 5.33, the deviatoric stress  $\tau = \sqrt{\tau_{xy}^2 + [(\sigma_x' - \sigma_y')/2]^2}$  increases, as shown in Fig. 5.43(a), just after the start of shaking and the effective confining pressure  $(-\sigma_m')$  increases due to the



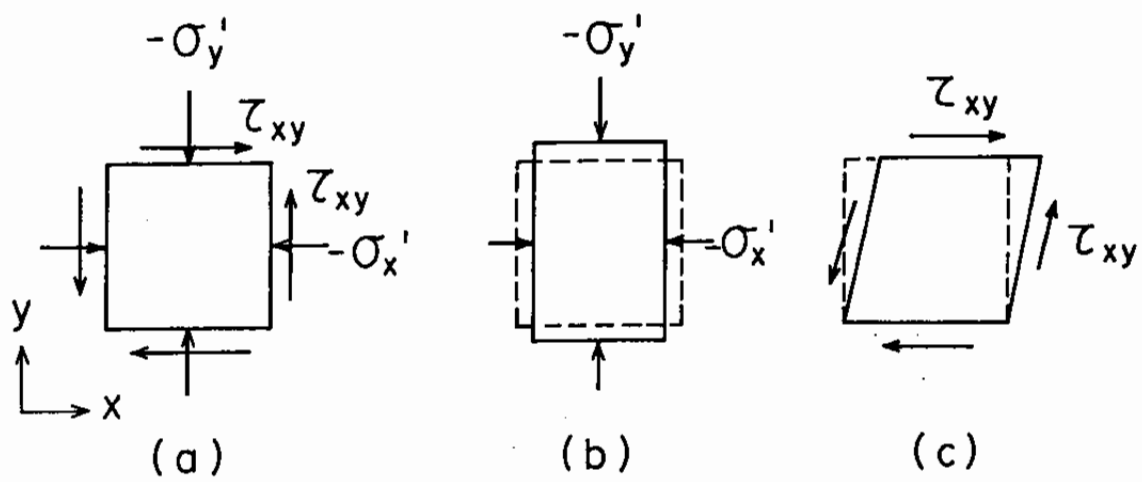


Fig. 5.42 Schematic figure of stresses and shear mechanisms

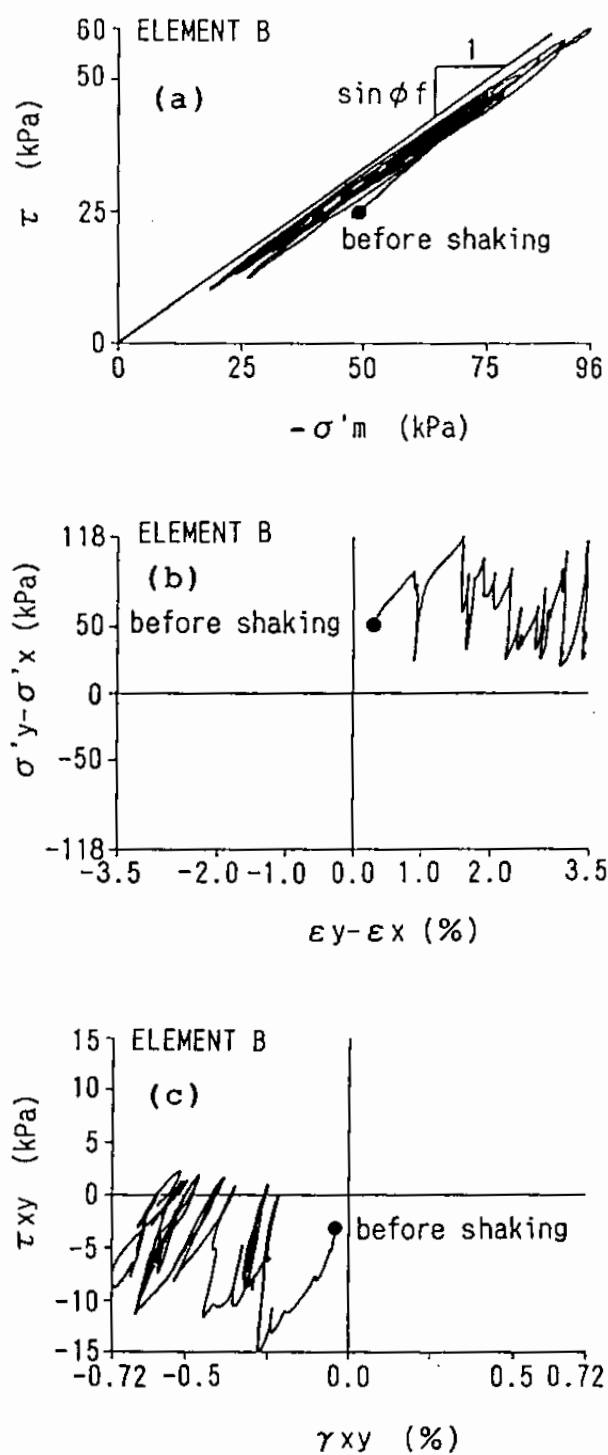


Fig. 5.43 Stress and strain of soil in front of sheet pile;  
 (a) stress path, (b) stress strain relation in axial mode  
 and (c) stress strain relation in simple shear mode

dilatancy of the sand but the effective confining pressure rapidly decreases back to the initial value as shown in the same figure and continues the fluctuation around the initial value.

As indicated by the positive axial stress difference in Fig. 5.43(b), the soil initially undergoes passive earth pressure. In accordance with the aforementioned stress path, the axial strain difference gradually increases as shown in Fig. 5.43(b). This corresponds to the wedge-like deformation of the soil mass in front of the sheet pile.

The shear strain  $\gamma_{xy}$ , which is negative before the shaking, also gradually increases in the negative direction in accordance with the deformation of the sheet pile as shown in (c) in the same figure.

The directions of principal stress and strain are easily identified in Fig. 5.44. The shaking mainly causes cyclic fluctuation in the axial stress difference as shown in Fig. 5.44(a). In accordance with this stress path, the principal shear strain is gradually induced toward the direction of the initial principal stress as shown in Fig. 5.44(b).

### 5.5.2 Stress and Strain behind Sheet Pile

Behind the sheet pile quay wall at the soil element D in Fig. 5.33, the effective confining pressure rapidly decreases as soon as the shaking starts as shown in Fig. 5.45(a) and converges on a certain limiting stress path close to the origin.

As indicated in the negative axial stress difference in Fig. 5.45(b), the soil initially undergoes active earth pressure. The shaking causes release in the initial axial stress difference and

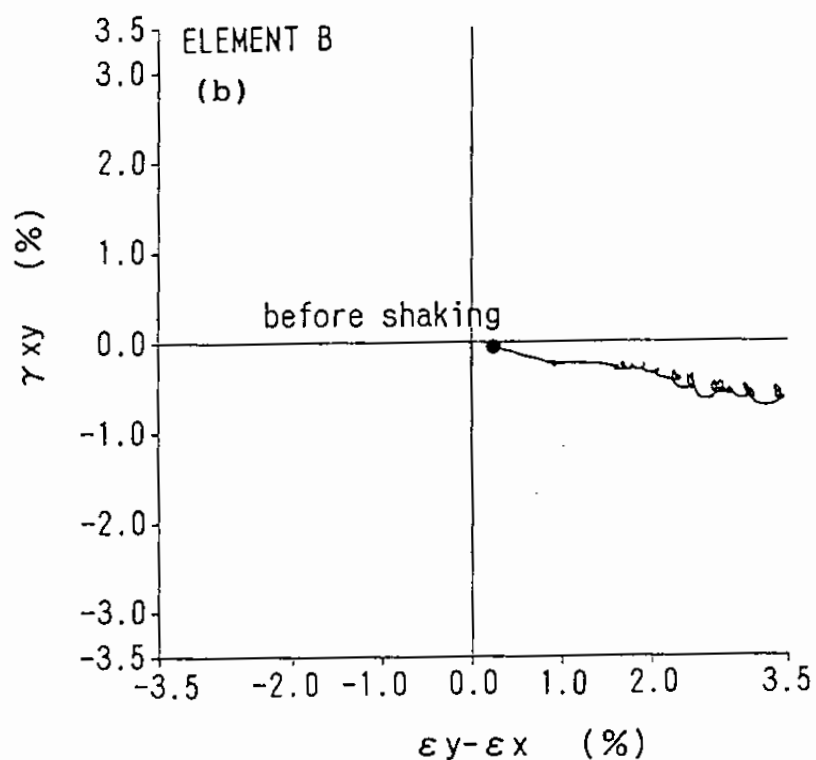
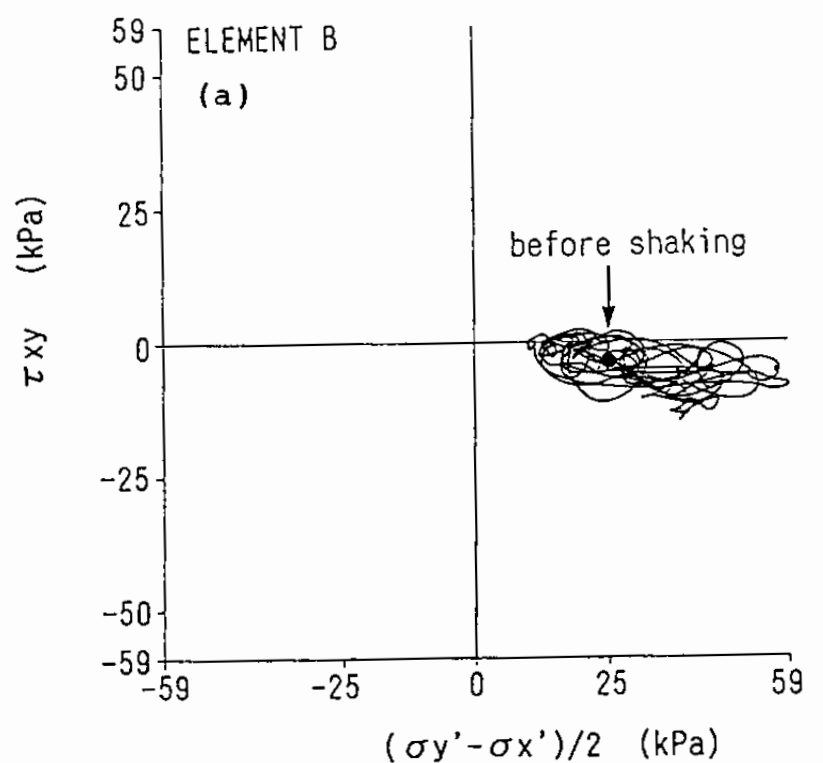


Fig. 5.44 Principal stress and strain directions of soil in front of sheet pile; (a) stress direction and (b) strain direction

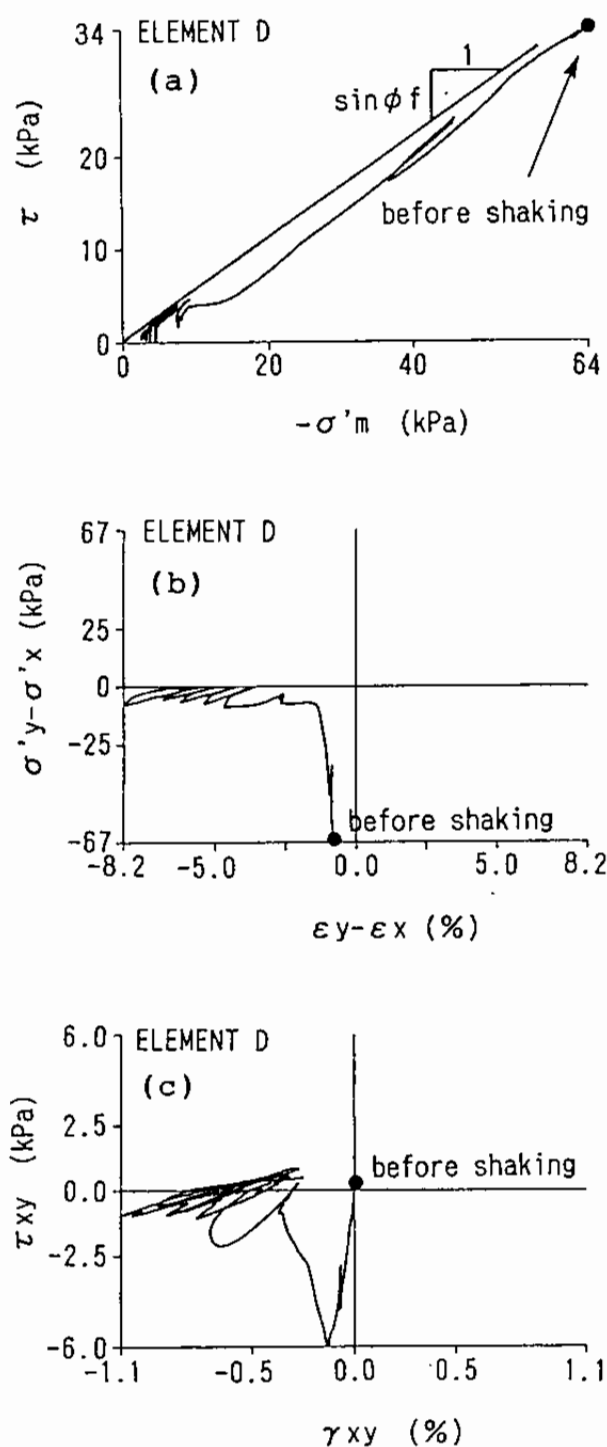


Fig. 5.45 Stress and strain of soil behind sheet pile; (a) stress path, (b) stress strain relation in axial mode and (c) stress strain relation in simple shear mode

further induces axial strain difference in the manner of "crawling"; i.e. increasing stress induces increase in strain but reducing stress induces decrease in strain in a lesser degree and repetition of this process accumulates the considerable amount of residual strain.

The shear strain  $\gamma_{xy}$  is also induced as shown in Fig. 5.45(c) but the order-of-magnitude is very small due to the confining effect of the sheet pile. Thus the main cause for the progress of the cyclic mobility in the soil behind the sheet pile is the shear work generated by the axial stress and strain differences rather than the one generated by the simple shear stress and strain in the horizontal direction.

The shaking causes cyclic axial loading in the horizontal direction as shown in Fig. 5.46(a) but this rapidly diminishes due to the rapid progress of the cyclic mobility. Direction of principal strain axes is, again, similar to that of initial principal stress axes as shown in Fig. 5.46(b).

### 5.5.3 Stress and Strain in the middle of the Ground

#### (1) Backfill soil

In the middle part of the ground between the sheet pile and the anchor at the backfill soil element F in Fig. 5.33, the initially  $K_0$  consolidated soil rapidly loses the mean effective stress as shown in Fig. 5.47(a). Axial strain difference rapidly grows with release in axial stress difference as shown in Fig. 5.47(b). Shear stress in the simple shear mode fluctuates with the shaking and induces the large shear strain in the simple shear mode.

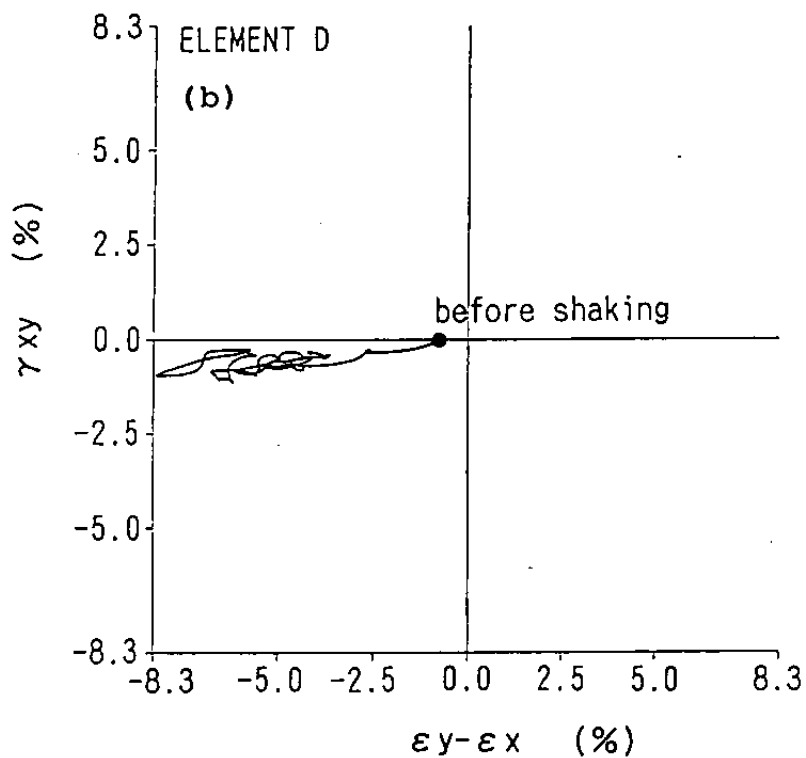
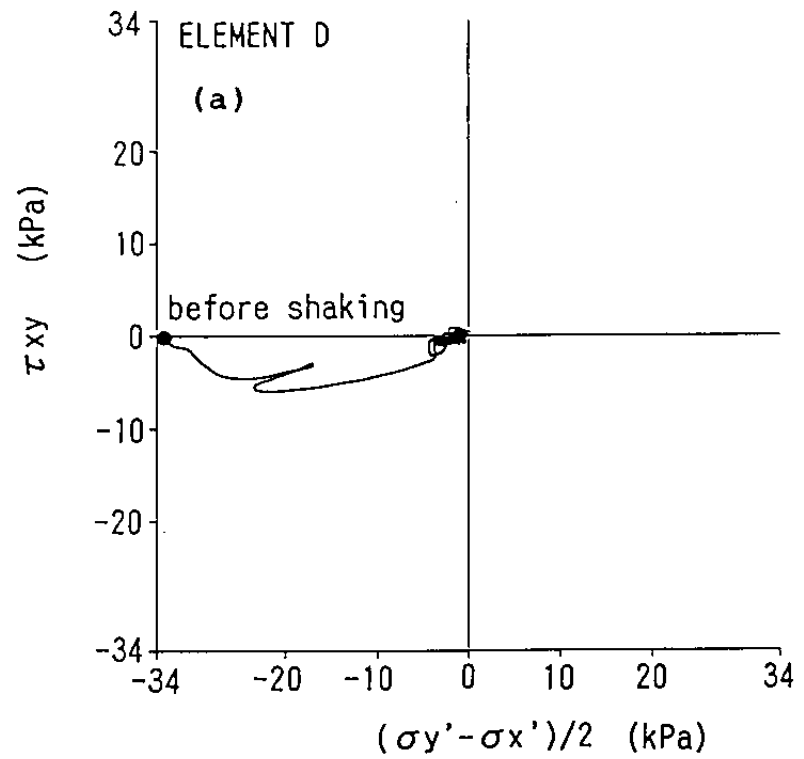


Fig. 5.46 Principal stress and strain directions of soil behind sheet pile; (a) stress direction and (b) strain direction

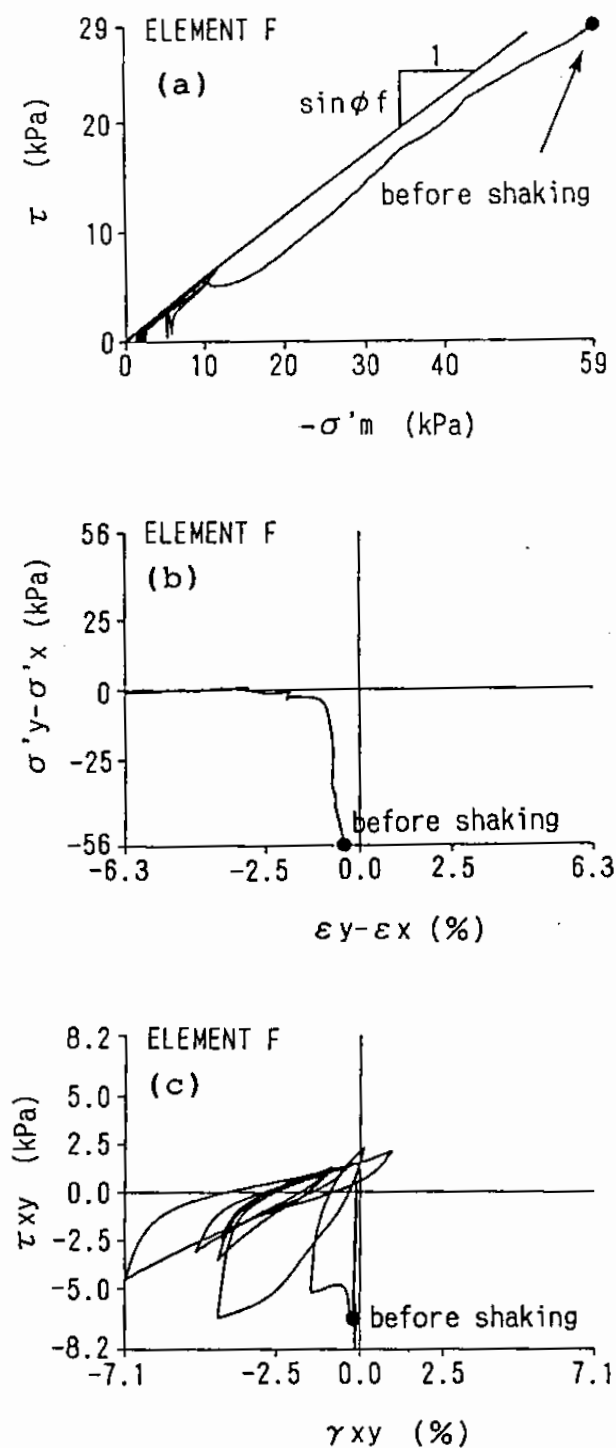


Fig. 5.47 Stress and strain in the middle of the liquefiable ground; (a) stress path, (b) stress strain relation in axial mode and (c) stress strain relation in simple shear mode



The principal strain is again gradually induced in the initial principal stress direction as shown in Fig. 5.48. Thus, basic behavior of this soil element is similar to that of the element D behind the sheet pile except for the large shear strain amplitude in the simple shear mode.

## (2) Firm ground

In the middle part of the ground between the sheet pile and the anchor at the firm ground element G in Fig. 5.33, the initially  $K_0$  consolidated soil does not lose the mean effective stress as shown in Fig. 5.49(a). In contrast to the case of horizontally layered ground in which bulging is constrained, initial deviatoric stress is kept almost constant throughout the process of the cyclic mobility, gradually inducing axial strain difference as shown in Fig. 5.49(b).

Though cyclic shear stress acts in the simple shear mode as well as axial compression mode as shown in Fig. 5.50(a), the strain generated by the cyclic shear stress is predominant in the direction of compression shear as shown in Fig. 5.50(b). This is similar to the behavior of initially anisotropically consolidated soil without constraint on the bulging seen in Chapter 3, in which settlement is associated with bulging in the horizontal direction. Direction of principal strain axes is, again, similar to that of initial principal stress axes.

### 5.5.4 Stress and Strain in front of Anchor

In front of the anchor at the soil element H in Fig. 5.33, the effective mean stress again gradually decreases as shown in Fig. 5.51(a). The deformation mode, as shown in Fig. 5.51(b) and

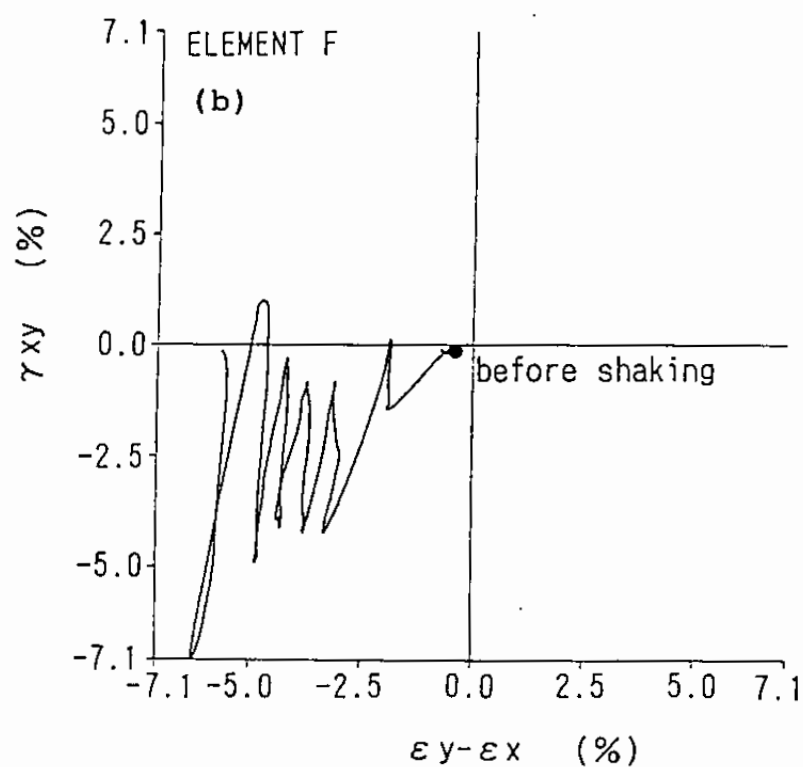
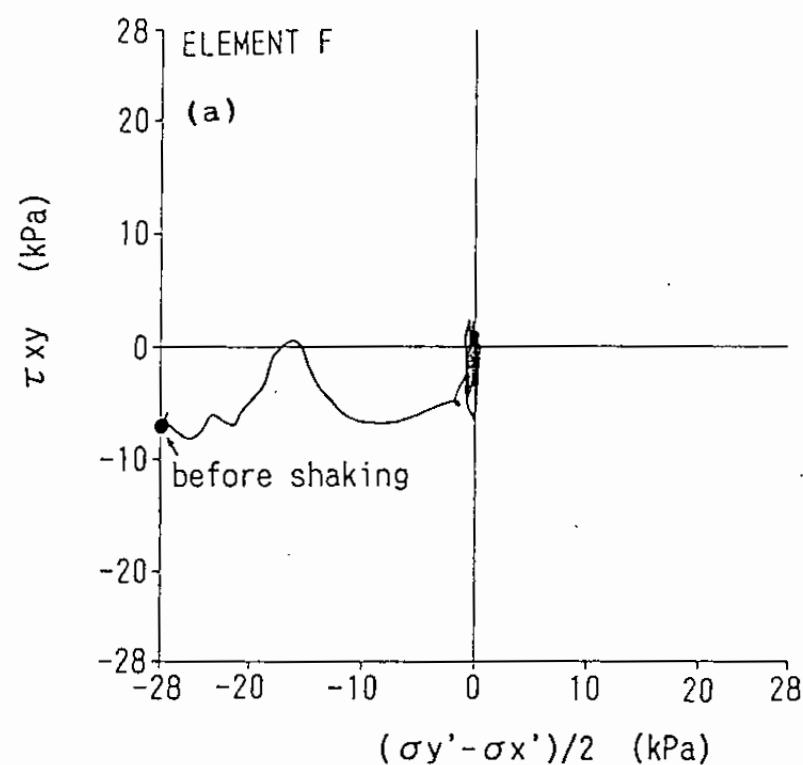


Fig. 5.48 Principal stress and strain directions of soil in the middle of the liquefiable ground; (a) stress direction and (b) strain direction

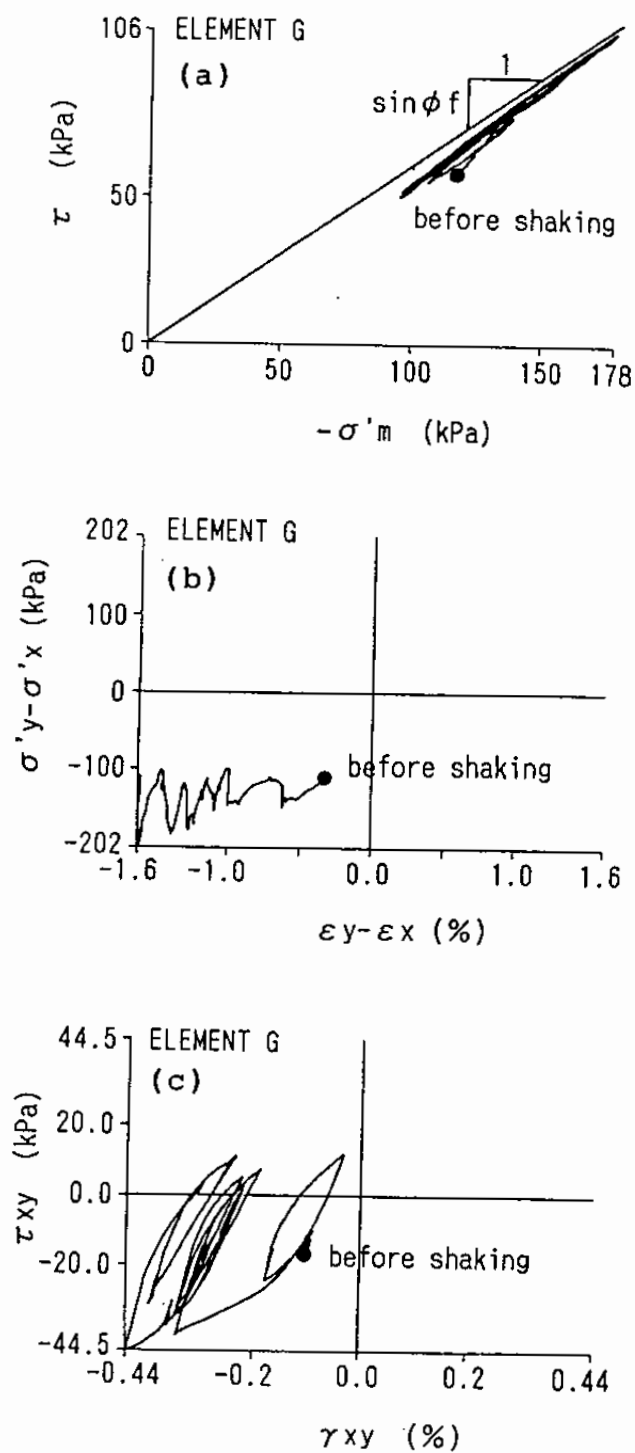


Fig. 5.49 Stress and strain in the middle of the non-liquefiable ground; (a) stress path, (b) stress strain relation in axial mode and (c) stress strain relation in simple shear mode

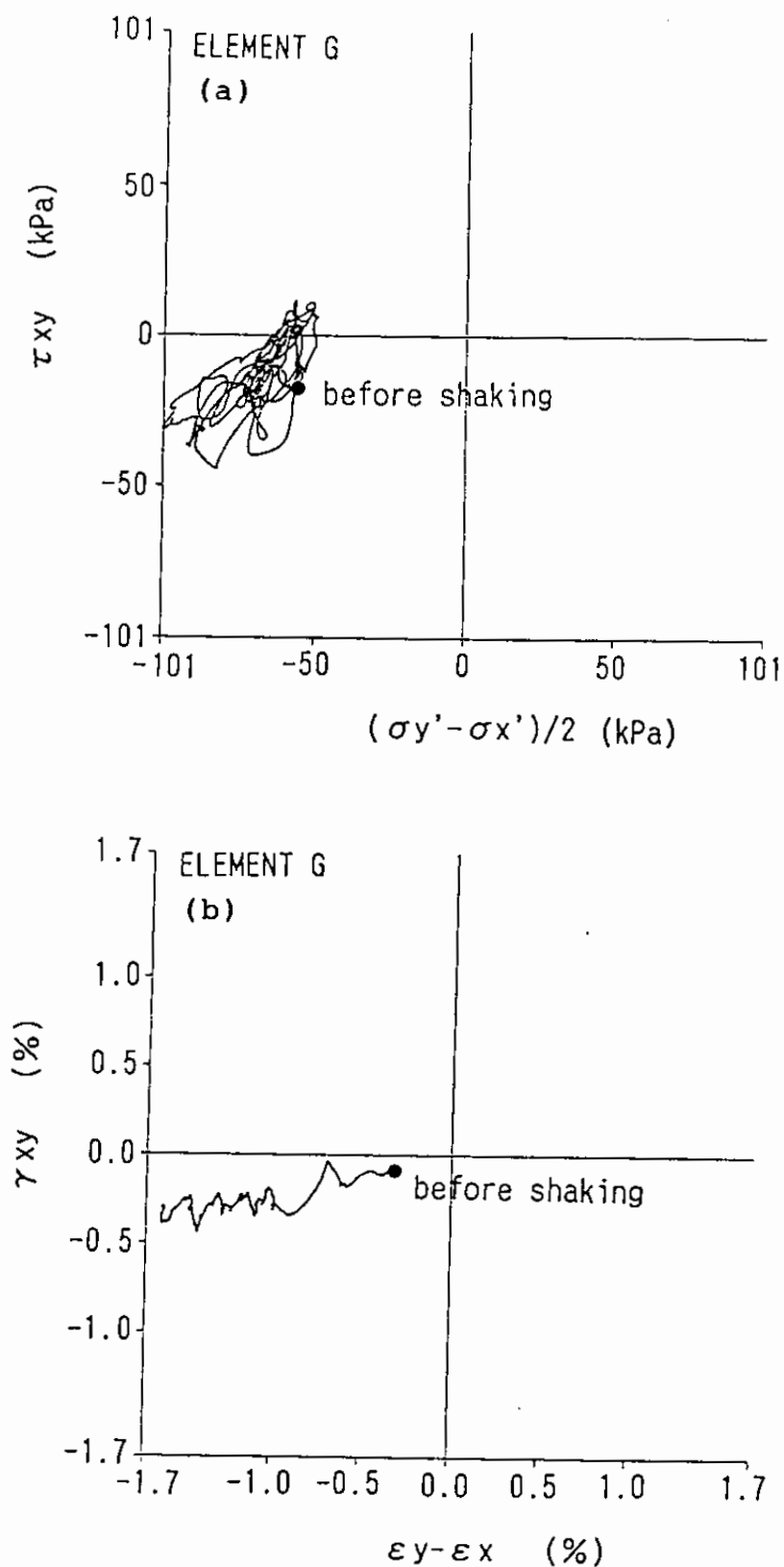


Fig. 5.50 Principal stress and strain directions of soil in the middle of the non-liquefiable ground; (a) stress direction and (b) strain direction

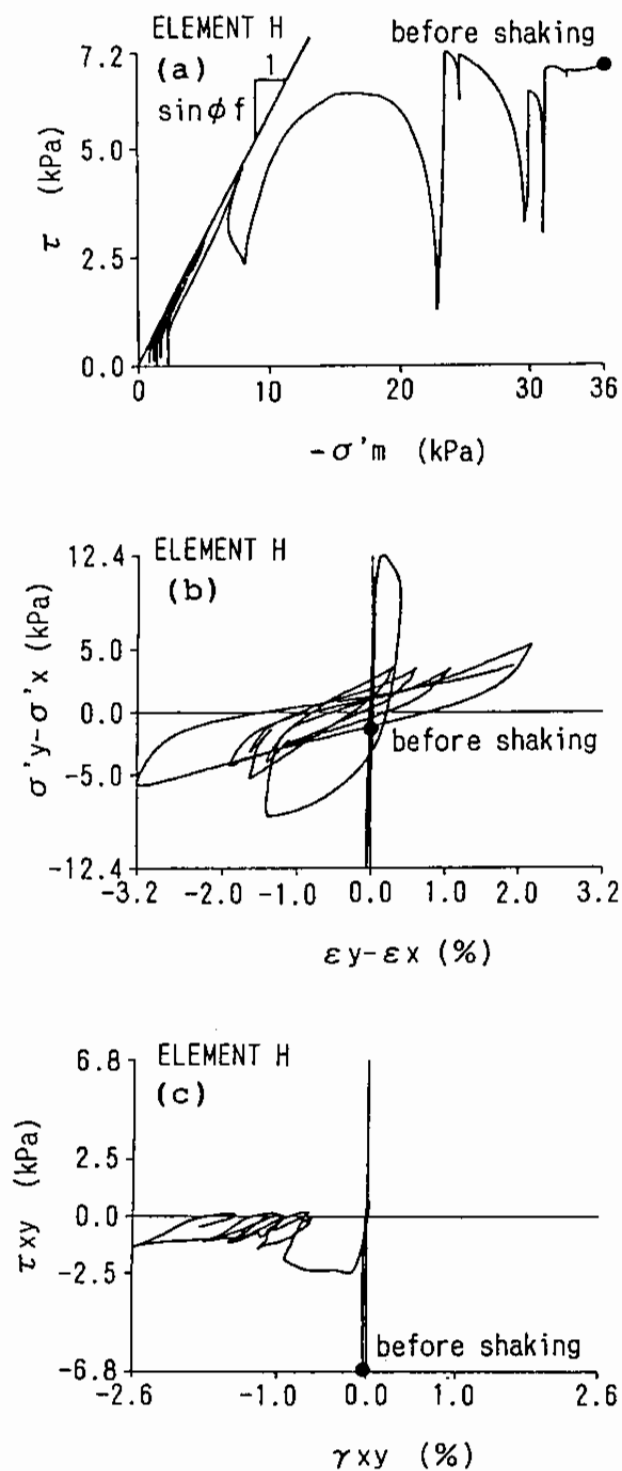


Fig. 5.51 Stress and strain of soil in front of anchor; (a) stress path, (b) stress strain relation in axial mode and (c) stress strain relation in simple shear mode

(c), is different from that at the soil B in front of the sheet pile. As shown in Fig. 5.52(a), initial stress is predominant in horizontal simple shear mode due to the deformation of the anchor; axial stress difference is close to zero supposedly due to cancellation of  $K_0$  consolidation effect with the effect of passive earth pressure. The shaking causes rotation in the principal stress axes as shown in the same figure. This is considered due to the Rayleigh wave generated by the soil-structure interaction as seen in Fig. 5.34. This affects the strain, mainly resulting in the rotational behavior with accumulating simple shear strain as shown in Fig. 5.52(b).

#### 5.5.5 Initial Stress and Residual Deformation

The foregoing effective stress analysis of an anchored sheet pile quay wall reveals the following four types of initial stress release resulting in the residual deformation of the quay wall due to cyclic mobility:

- (1) Soil in front of sheet pile, which was initially in nearly passive failure state, shows gradual deformation with cyclic extension shear.
- (2) Soil behind the sheet pile, which was initially in nearly active failure state, shows rapid stress release in compression shear mode.
- (3) Soil between sheet pile and anchor, which was initially in  $K_0$  consolidated state, shows cyclic simple shear behavior in horizontal direction with unconstrained bulging.
- (4) Soil in front of the anchor, which was initially sheared in

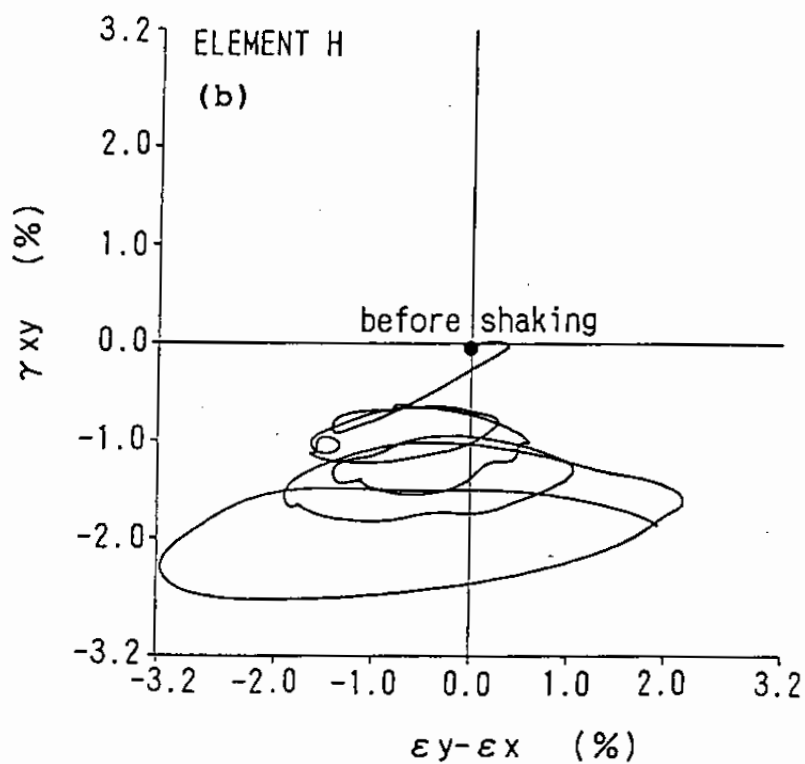
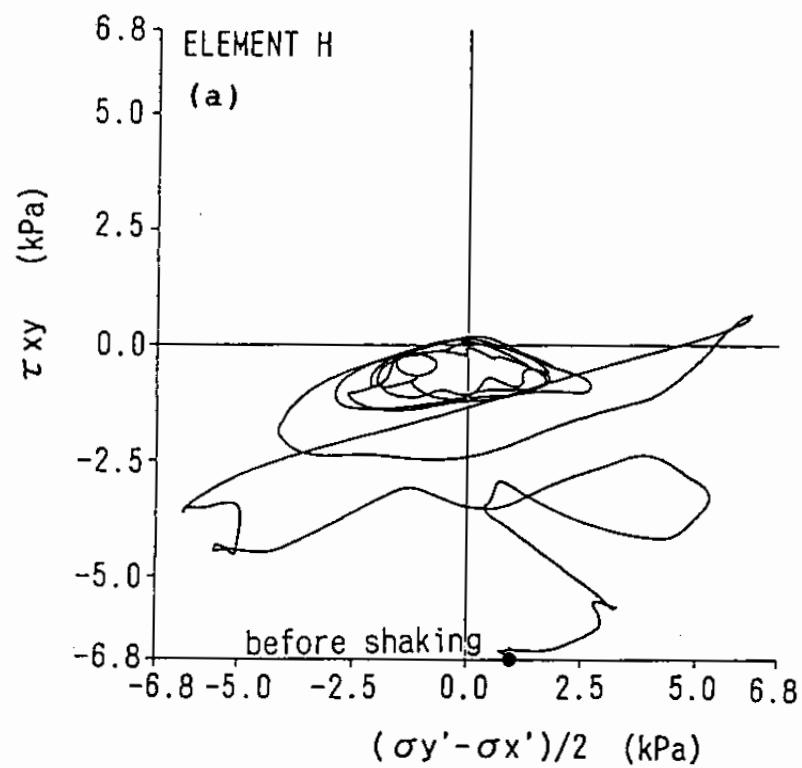


Fig. 5.52 Principal stress and strain directions of soil in front of anchor; (a) stress direction and (b) strain direction

the horizontal direction, shows rotation of principal stress axes due to Rayleigh wave possibly generated by the soil-structure interaction.

In addition and the most important, the analysis reveals the following mechanism:

- (5) Principal strains are gradually produced mainly in the direction of initial principal stress axes.

The mechanism of the deformation of the sheet pile is thus quite naturally understood through the present approach and this is considered as one of the support for the applicability of the present approach.

## 5.6 Analysis of a Quay Wall without Damage

### 5.6.1 Earthquake Response and Deformation

The numerical simulation of the quay wall, after 14 seconds of shaking, results in the deformation shown in Fig. 5.53 at the Ohama No.1 Wharf; deformation towards sea are mainly recognized at the soil wedge behind the sheet pile.

Instantaneous directions of the response accelerations, shown in Fig. 5.54, show slight indication of rotational waves but it is not very remarkable in these figures.

The maximum acceleration at the top of the quay wall is about 270 Gals as shown in Fig. 5.55, much higher than in the case of the Ohama No.2 Wharf, but the horizontal displacement, as shown in Fig. 5.56, is only about 15 cm. The backfill soil behind the sheet gradually settles as shown in lower two rows in



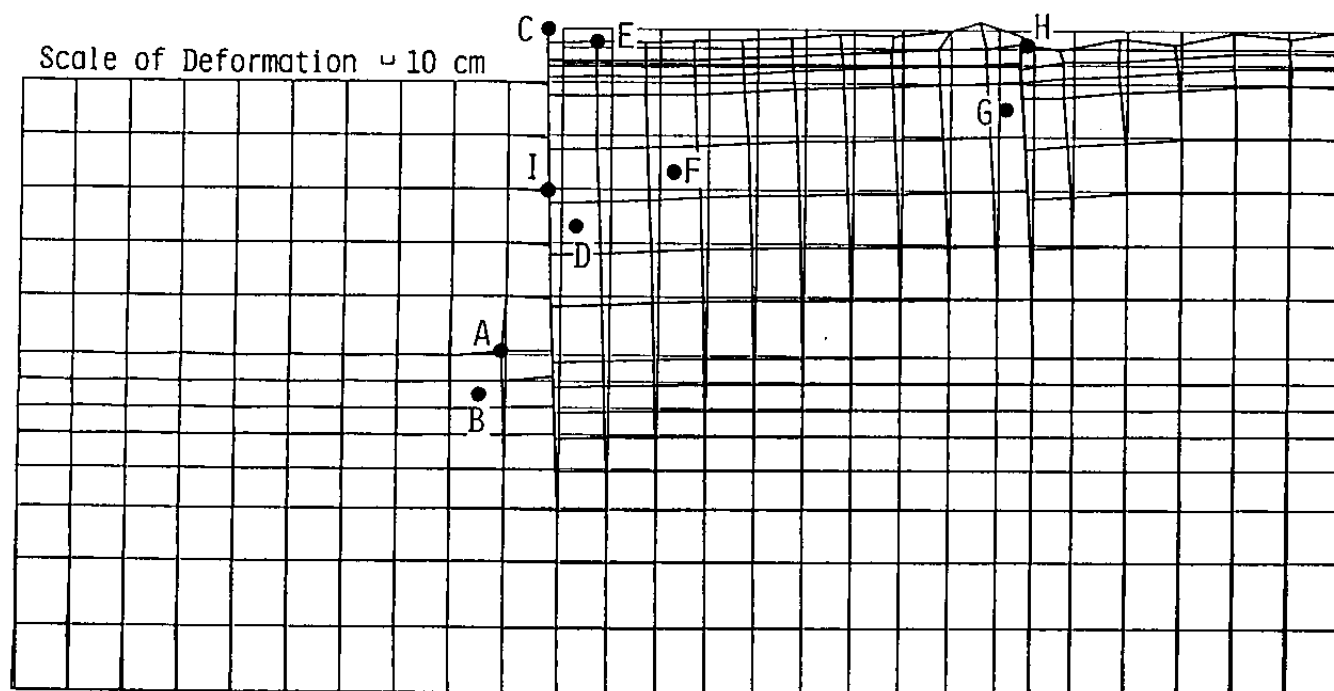


Fig. 5.53 Computed deformation of quay wall at Ohama No.1 Wharf  
at the end of computation (14 seconds)

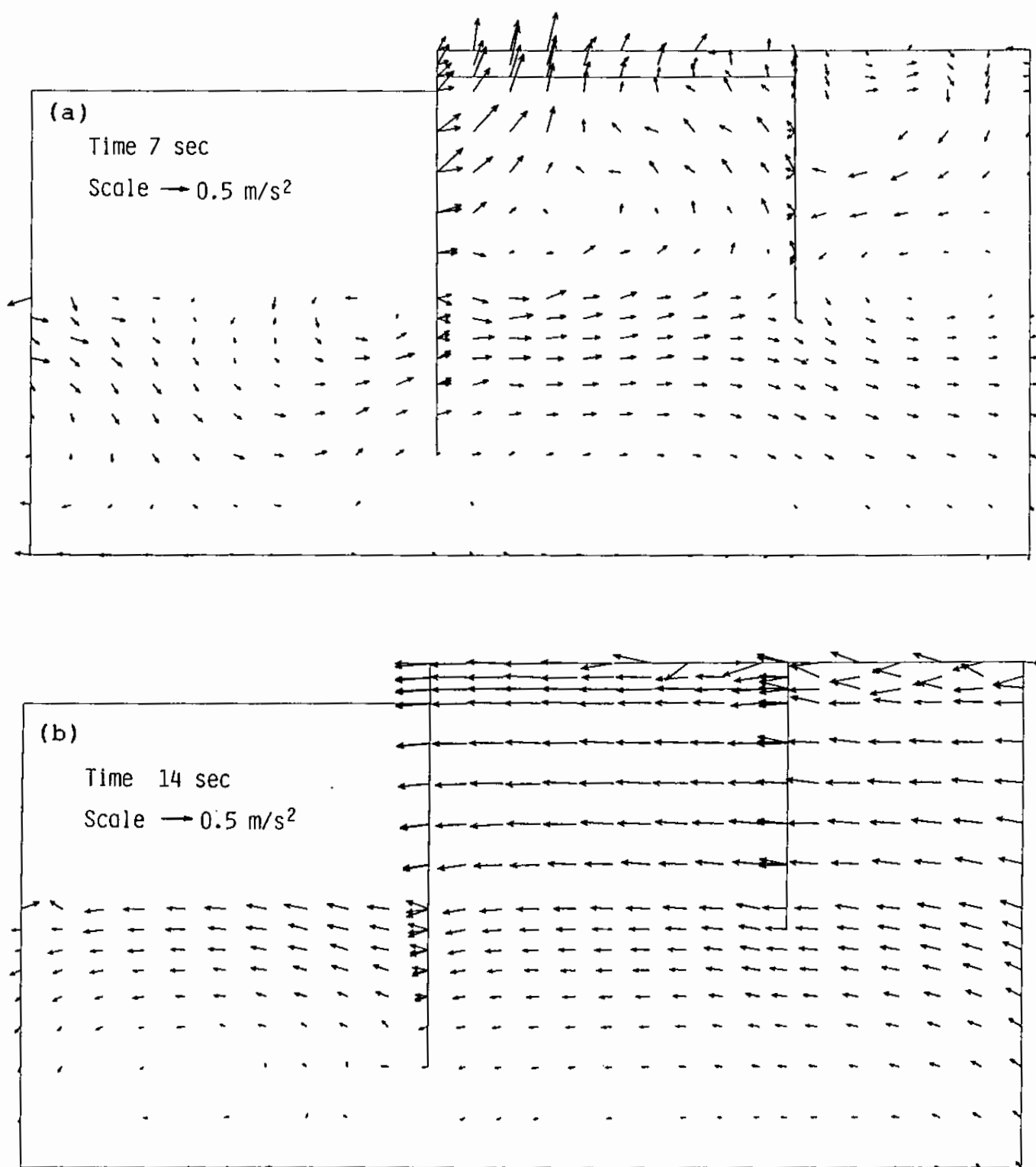


Fig. 5.54 Computed distribution of accelerations at Ohama No.1 Wharf; (a) at 7 seconds and (b) at 14 seconds

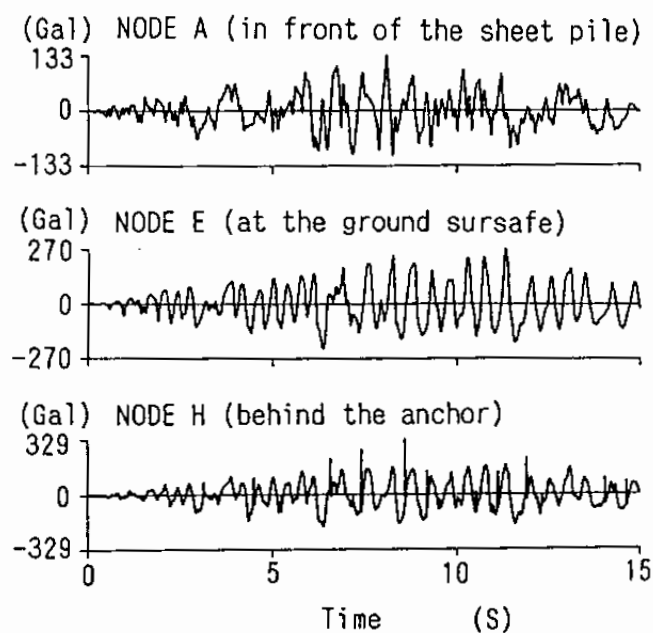


Fig. 5.55 Horizontal response acceleration at Ohama No.1 Wharf

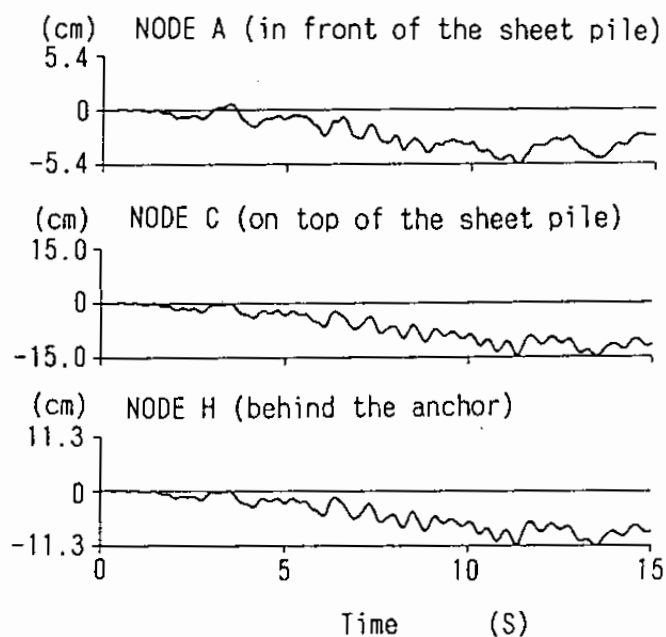


Fig. 5.56 Horizontal response displacement at Ohama No.1 Wharf

Fig. 5.57 where as the sea bed in front of the sheet pile gradually swells as shown in the same figure but the order-of-magnitude is again very small.

The horizontal displacement at the sheet pile is computed as 0.15 meters at the end of the shaking whereas the observed displacement is reportedly zero, indicating the computed displacement slightly errs on the safe side. The same applies to the settlement behind the sheet pile. The author thinks this amount of error is small enough to be admissible in practice for differentiating very large deformation (i.e. damage) from very small deformation (i.e. non damage).

#### 5.6.2 Earth Pressure and Bending Moment

The earth pressures, i.e. the normal total stresses (= the normal effective stresses + the excess pore water pressures), acting on the sheet pile after 15 seconds of shaking, shown in Fig. 5.58, become greater than those before the shaking. The earth pressures behind the sheet pile at 15 seconds of shaking become close to that of  $K_0 = 1.0$  condition from the ground surface to the elevation of -5 meters below the water level.

In accordance with those changes in the normal total stress, the bending moment of the sheet pile changes as shown in Fig. 5.59. In particular, the bending moment at the level of 6 meters below the water level gradually increases as shown in Fig. 5.60.

The maximum stress due to bending is computed as 260000 kPa as shown in Fig. 5.59 whereas the failure strength of the steel sheet pile is 300000 kPa, indicating that the observed

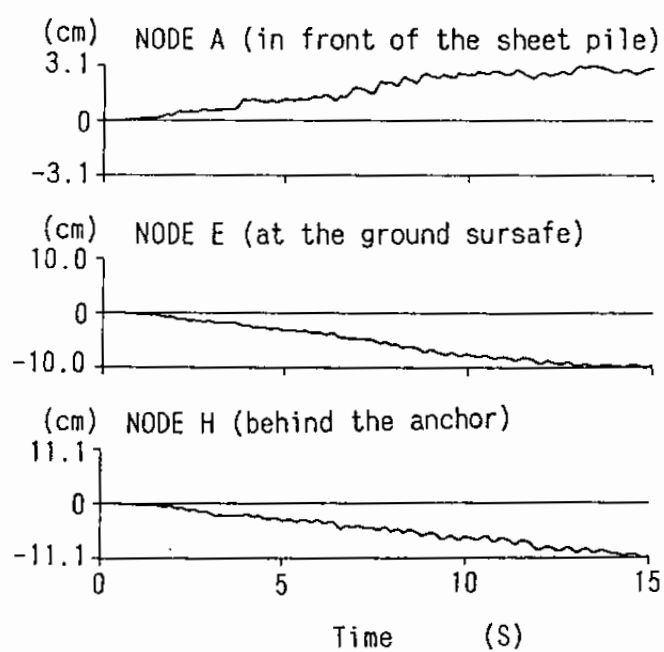


Fig. 5.57 Vertical response displacement at Ohama No.1 Wharf

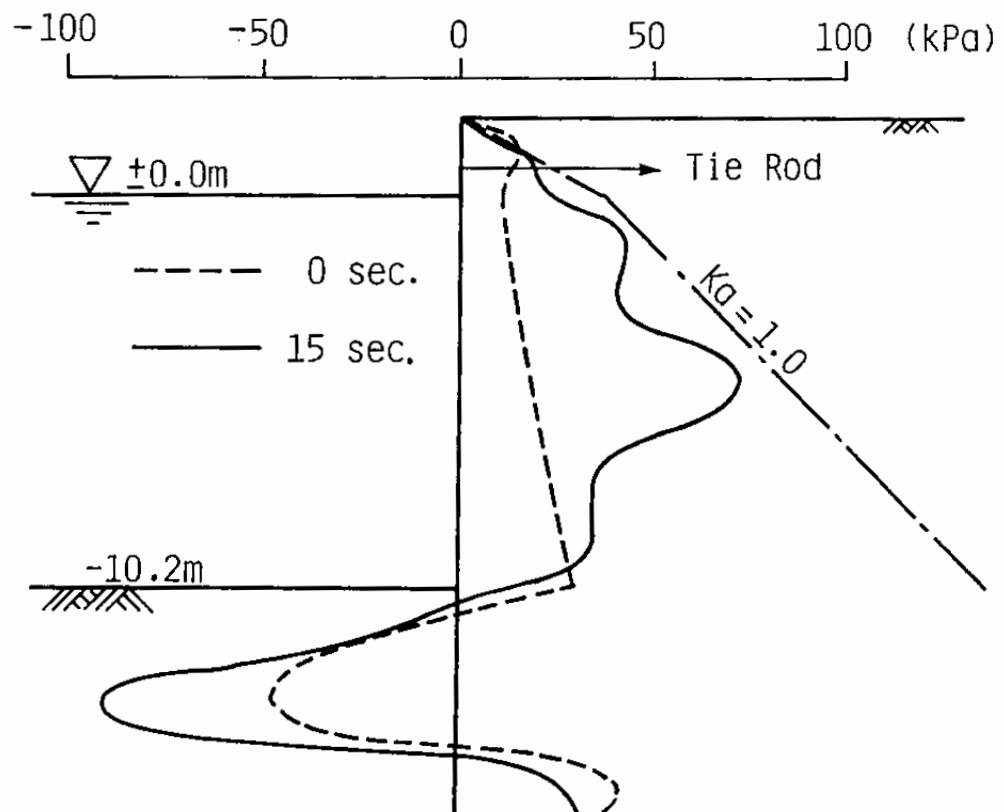


Fig. 5.58 Normal stresses on sheet pile before and after the earthquake at Ohama No.1 Wharf

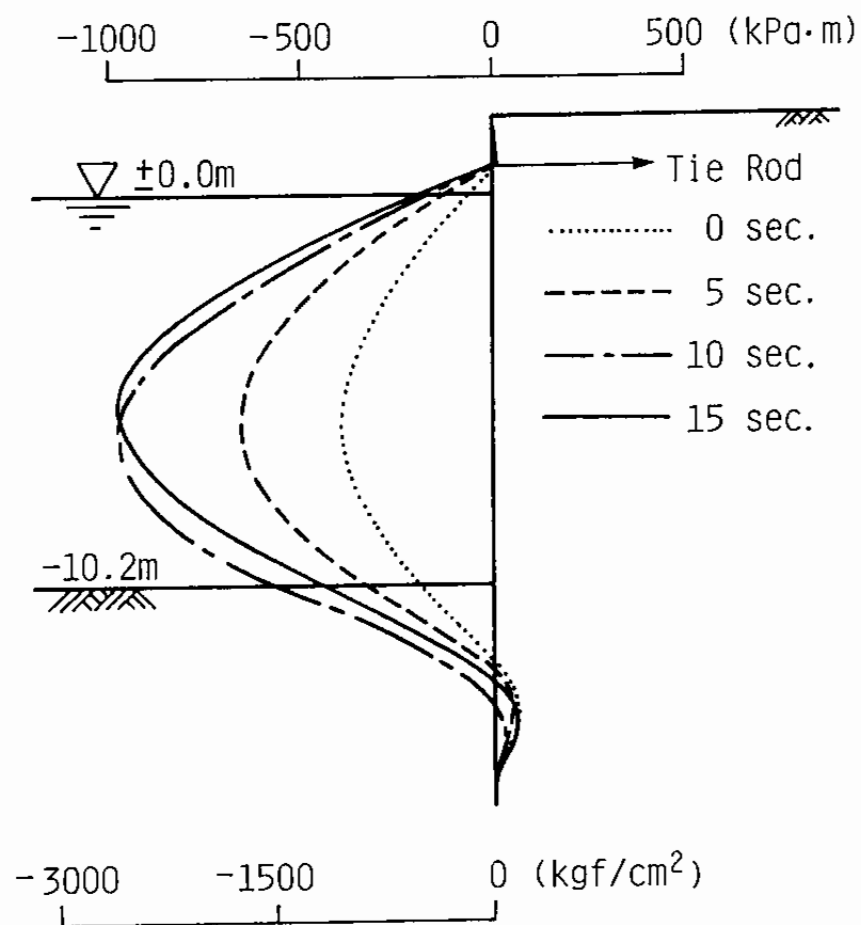


Fig. 5.59 Bending moment (shown in upper scale) and bending stress (shown in lower scale) before and after the earthquake at Ohama No.1 Wharf

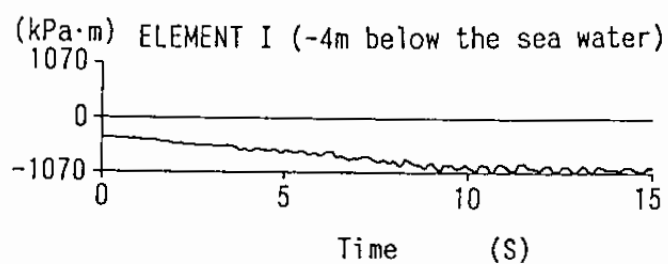


Fig. 5.60 Time history of bending moment at the elevation of  
- 6 m at Ohama No.1 Wharf

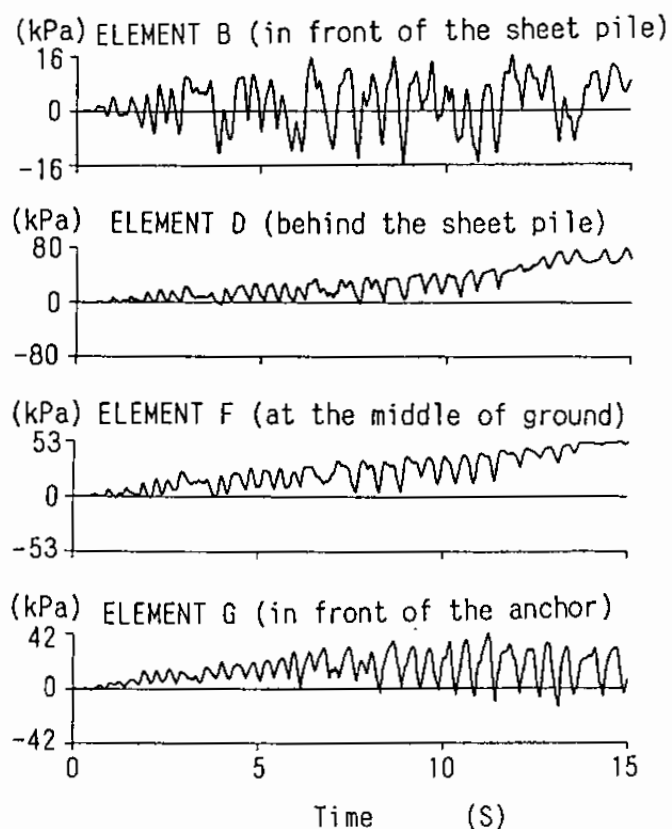


Fig. 5.61 Excess pore water pressures at Ohama No.1 Wharf



phenomenon, i.e. no damage to the sheet pile, is well explained by the analysis.

Excess pore water pressures in the soils in front of and behind the sheet pile are computed as shown in Fig. 5.61. The excess pore water pressures gradually increase behind the sheet pile as the shaking continues, but never so remarkably as in the case of the Ohama No.2 Wharf. The excess pore water pressures in front of the sheet pile, however, fluctuates around the value of zero.

#### 5.6.3 Comparison between Observed and Computed Results

The results of the analysis of the quay wall at the Ohama No.1 Wharf indicate that the results of the analysis are not contradictory to many of the observed phenomena relevant to the deformation of the sheet pile quay wall. It is concluded that the approach taken in the present analysis is capable of representing the essential features of the observed performance of the sheet pile quay wall during the earthquake.

#### 5.7 Applicability to Quay Wall Analysis

In this chapter, two dimensional analysis is conducted on the behavior of sheet pile quay walls. The results of the analysis are consistent with the observed deformation and the observed yielding of the sheet pile. In particular, the present model demonstrates the ability to differentiate the seriously large deformation (i.e. damage) from the negligibly small deformation (i.e. non damage) in the similar type of sheet pile

quay walls.

In the present analysis, major deformations are recognized in the soil wedges in front of and behind the sheet pile. In both of the soil wedges, the strains are gradually induced due to the existence of the initial stresses and its release in accordance with the cyclic mobility. In particular, principal strains are gradually induced mainly in the initial principal axes direction.

With the reasonable mechanisms available for explaining the deformation of sheet pile quay walls, the author concludes that the present approach is capable of representing the essential features in the performance of sheet pile quay walls during earthquakes.

As an example of the application of the present approach, effect of the liquefaction resistance of backfill sand is studied in relation to the maximum bending moment of the sheet pile induced by the earthquake shaking. The quay wall at Ohama No.2 Wharf is taken as an example. The liquefaction resistances of the backfill sand are varied as shown in Fig. 5.62. The maximum bending moment, which exceeded the yield point when the backfill sand was very loose as in the earthquake, becomes smaller if the liquefaction resistance of the backfill sand is increased as shown in Fig. 5.63. This type of analysis could be useful in design when the backfill sand should be improved as a measure against liquefaction.

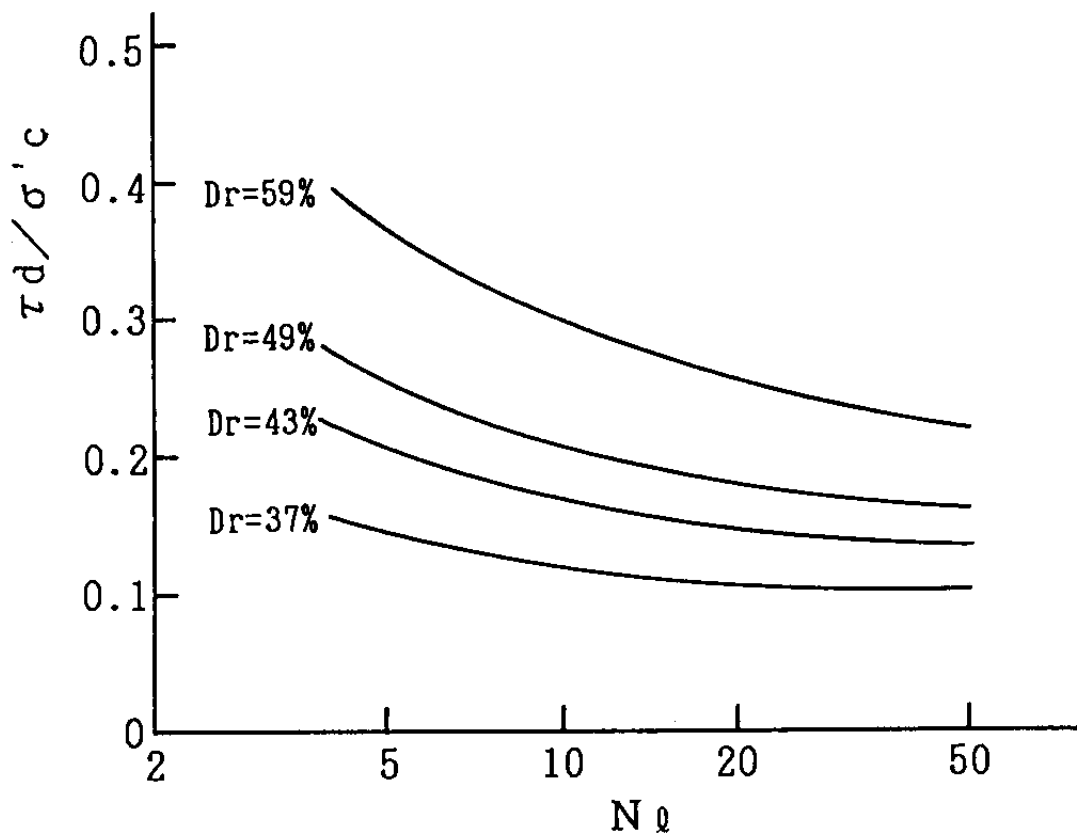


Fig. 5.62 Varied liquefaction resistance of backfill soil

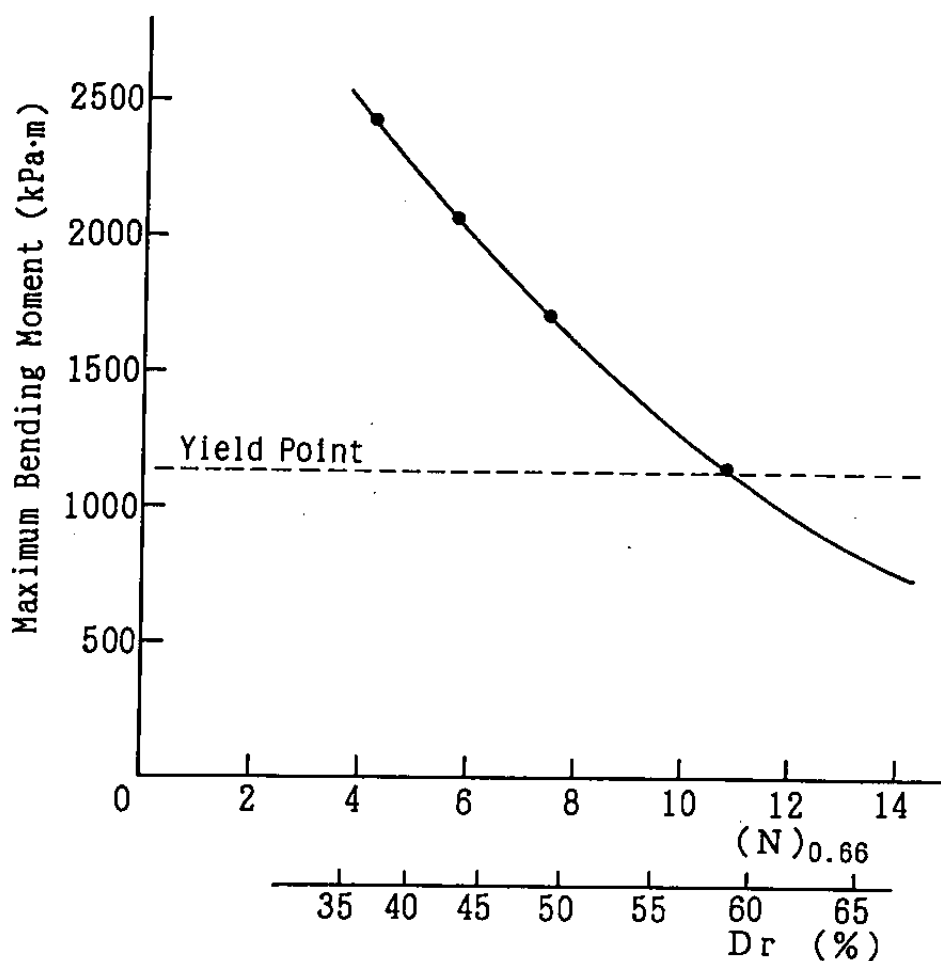


Fig. 5.63 Relation between the maximum bending moment of sheet pile and the relative density of backfill soil at Ohama No.2 Wharf

## References

- (1) Arai, H. and Yokoi, T. (1965) : "Model vibration tests of anchored sheet-pile walls in dry sand," Report of the Port and Harbour Research Institute, pp.1-57 (in Japanese)
- (2) Hinton, E. and Owen, D.R.J (1977) : Finite Element Programming, Academic Press, p.305
- (3) Iai, S., Kurata, E. and Tsuchida, H. (1978) : "Digitization and correction of strong-motion accelerograms," Technical Note of the Port and Harbour Research Institute, No.286, 56p. (in Japanese)
- (4) Iai, S., Tsuchida, H. and Koizumi, K. (1989) : "A liquefaction criterion based on field performances around seismograph stations," Soils and Foundations, Vol.29, No.2, pp.52-68
- (5) Kano, T. (1965) : "On the topography and quaternary geology in the north area of Akita City, Akita Prefecture, Northeast Honshu," Report of the Research Institute of Underground Resources, Mining College, Akita University, No.33, pp.1-12 (in Japanese)
- (6) Kurata, E., Fukuhara, T. and Nod, S. (1983) : "Strong-motion earthquake records on the 1983 Nipponkai-Chubu Earthquake in port areas," Technical Note of the Port and Harbour Research Institute, No.458, 372p.
- (7) Seed, H.B., Tokimatsu, K., Harder, L.F. and Chung, R.M. (1985) : "Influence of SPT procedures in soil liquefaction resistance evaluations," Journal of Geotechnical Engineering Division, ASCE, Vol.111, No.12, pp.1425-1445

- (8) Tokimatsu, K. and Yoshimi, Y. (1983) : "Empirical correlation of soil liquefaction based on SPT N-value and fines content," *Soils and Foundations*, Vol.23, No.4, pp.56-74
- (9) Tsuchida, H. (1968) : "Earth pressure due to liquefied soil," *Tsuchi-to-Kiso*, Vol.16, No.5, pp.3-10 (in Japanese)
- (10) Tsuchida, H., Noda, S., Inatomi, T., Uwabe, T., Iai, S., Oneda, H. and Toyama, S. (1985) : "Damage to port structures by the 1983 Nipponkai-Chubu Earthquake," *Technical Note of the Port and Harbour Research Institute* No.511, p.447 (in Japanese)
- (11) Zienkiewicz, O.C. (1977) : *The Finite Element Method*, 3rd edition, McGraw-Hill Book Co.
- (12) Zienkiewicz, O.C. and Bettess, P. (1982) : "Soils and other saturated media under transient, dynamic conditions," *Soil Mechanics-Transient and Cyclic Loads*. (Pande and Zienkiewicz eds.) John Wiley and Sons, pp.1-16

## CHAPTER 6

### CONCLUSIONS

An attempt is made in the present study for modeling the cyclic mobility of saturated cohesionless soil. The conclusions obtained from the present study are as follows;

- (1) The proposed concept for modeling of cyclic mobility is of a generalized plasticity type defined in the strain space. Concept of multiple mechanism is used as a vehicle for decomposing the complex mechanism into a set of simple mechanisms defined in one dimensional space. Each virtual simple shear mechanism is assumed to follow a hyperbolic relation in the virtual stress and strain space. The hysteresis is given by modified Masing's rule.
- (2) Difficulty is known to exist in the numerical analysis of the cyclic mobility when the effective stress path becomes very close to the failure line. In order to overcome the difficulty, a simple scheme is proposed; modeling of cyclic mobility, not as a yielding process, but as a process in which the scale of the shear strain is gradually enlarged as the effective stress path approaches the failure line.
- (3) To define the "distance" to the failure line, the concept of "liquefaction front" is introduced in the effective stress space as an envelope of current stress points. The liquefaction front, originating from the envelope of initial effective stress points, gradually approaches the failure line as the cyclic mobility proceeds.
- (4) Incremental as well as integrated constitutive relations

are obtained. In particular, the tangent stiffness matrix in the incremental relation becomes symmetric, ensuring the efficiency in the numerical analysis, whereas the integrated constitutive relation serves as a guide, ensuring the convergence on the physically feasible stress strain relation.

- (5) The single soil element analysis indicates that the present model is capable of representing the rapid as well as gradual increases in the shear strain amplitude greater than several percent in the manner consistent with the laboratory data of undrained cyclic torsion shear tests.
- (6) According to the present approach, the effect of the anisotropic consolidation, when the bulging of soil is constrained as in the level ground, does not have a significant influence on the virtual simple shear mechanisms oriented close to horizontal direction whereas these virtual mechanisms are the main mechanisms being mobilized during the cyclic loading in the simple shear test. Thus the behavior of soil under the cyclic simple shear loading is not affected by the initial anisotropic consolidation conditions if the initial mean effective stress is kept the same. This is consistent with the previous laboratory findings.
- (7) When the bulging of the soil is not constrained, the results of the single element analysis show the limit in decreasing value of the effective mean stress and the gradual settlement with bulging in the soil element, suggesting reasonable applicability in the two dimensional

analysis of soil structures and foundations.

- (8) The effect of initial confining pressure is also consistent with the laboratory results; if the same shear stress ratio is used for the cyclic loading, the initial confining pressure does not affect the effective stress path whereas it does affect the shear strain amplitude to be proportional to the square root of the initial confining pressure.
- (9) One dimensional analysis of level ground indicates that the present approach is basically capable of representing essential features of the cyclic mobility in the level ground during sinusoidal as well as earthquake excitations.
- (10) Two dimensional analysis of sheet pile quay walls indicates that the present approach is capable of representing essential features of deformation due to the cyclic mobility and is capable of differentiating seriously large deformation (i.e. damage) from negligibly small deformation (i.e. non damage).
- (11) Though the two dimensional analysis shows, in each soil element, complex stress paths involving rotation of principal stress axes, the fundamental mechanism inducing residual deformation is the existence of initial stress and its release in accordance with the cyclic mobility. In particular, principal strains are gradually induced mainly in the principal axes directions of initial stresses.



## APPENDIX A

### EXTENSION TO THREE DIMENSIONS

The present model, essentially represented by Eqs.(2.32) through (2.35), idealizes the two dimensional shear mechanism around the  $z$  axis. The present model is extended into three dimensions by superposing the two dimensional virtual shear mechanisms around axes of arbitrary orientations. The extension is reduced to a series of manipulations with coordinate transformation as follows.

#### A.1 Coordinate Transformation

To begin with, the effective stress and the strain vectors are written in the three dimensional space by

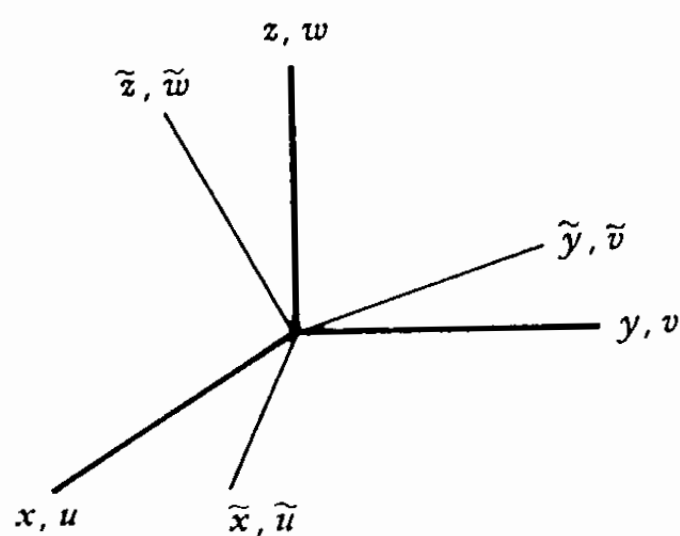
$$\{\sigma'\} = \{\sigma_x' \ \sigma_y' \ \sigma_z' \ \tau_{xy} \ \tau_{yz} \ \tau_{zx}\} \quad (\text{A.1})$$

$$\{\epsilon\} = \{\epsilon_x \ \epsilon_y \ \epsilon_z \ \gamma_{xy} \ \gamma_{yz} \ \gamma_{zx}\} \quad (\text{A.2})$$

in which  $\gamma_{xy}$ , etc. are shear strains in engineering definition such as shown in Eq.(2.12).

Strain transformations are essentially transformations of displacement derivatives (e.g. Cook, 1981). For example, from Fig. A.1, displacement  $\tilde{u}$  in the transformed direction  $\{\tilde{x}\}^T = \{a_1 \ b_1 \ c_1\}$  can be written in terms of displacements in the original directions as

$$\tilde{u} = a_1 u + b_1 v + c_1 w \quad (\text{A.3})$$



	$x$	$y$	$z$
$\tilde{x}$	$a_1$	$b_1$	$c_1$
$\tilde{y}$	$a_2$	$b_2$	$c_2$
$\tilde{z}$	$a_3$	$b_3$	$c_3$

Fig. A.1 Cartesian coordinate systems  $xyz$  and  $\tilde{x}\tilde{y}\tilde{z}$  with table of direction cosines between axes

By chain rule differentiation, in which ",", denotes partial differentiation with respect to the variable after the ",", one obtains

$$\tilde{u}_{,\tilde{x}} = \tilde{u}_{,x}x_{,\tilde{x}} + \tilde{u}_{,y}y_{,\tilde{x}} + \tilde{u}_{,z}z_{,\tilde{x}} \quad (\text{A.4})$$

in which

$$\tilde{u}_{,x} = a_1 u_{,x} + b_1 v_{,x} + c_1 w_{,x} \quad \text{etc.} \quad (\text{A.5})$$

$$x_{,\tilde{x}} = a_1 \quad y_{,\tilde{x}} = b_1 \quad z_{,\tilde{x}} = c_1 \quad (\text{A.6})$$

By this process one finds

$$\{\tilde{u}_{,\tilde{x}} \tilde{u}_{,\tilde{y}} \tilde{u}_{,\tilde{z}} \dots \tilde{w}_{,\tilde{z}}\}^T = [\tilde{T}]\{u_{,x} u_{,y} u_{,z} \dots w_{,z}\}^T \quad (\text{A.7})$$

in which

$$[\tilde{T}] = \begin{bmatrix} a_1 \tilde{T}_c & b_1 \tilde{T}_c & c_1 \tilde{T}_c \\ a_2 \tilde{T}_c & b_2 \tilde{T}_c & c_2 \tilde{T}_c \\ a_3 \tilde{T}_c & b_3 \tilde{T}_c & c_3 \tilde{T}_c \end{bmatrix} \quad (\text{A.8})$$

$$[\tilde{T}_c] = \begin{bmatrix} a_1 & b_1 & c_1 \\ a_2 & b_2 & c_2 \\ a_3 & b_3 & c_3 \end{bmatrix} \quad (\text{A.9})$$

The matrix  $[\tilde{T}]$  is orthogonal; i.e.  $[\tilde{T}]^{-1} = [\tilde{T}]^T$ . Therefore the inverse relation of Eq. (A.7) involves simply  $[\tilde{T}]^T$ .

From Eq. (A.7) and the strain-displacement relations such as Eq.(2.12), the relation is written between strains in  $\tilde{x}\tilde{y}\tilde{z}$

coordinates and the strains expressed in xyz coordinates as

$$\{\tilde{\epsilon}\} = [\tilde{T}_\epsilon]\{\epsilon\}, \quad \{\epsilon\} = [\tilde{T}_\epsilon]^{-1}\{\tilde{\epsilon}\} \quad (\text{A.10})$$

in which

$$[\tilde{T}_\epsilon] = \begin{bmatrix} a_1^2 & b_1^2 & c_1^2 & a_1b_1 & b_1c_1 & c_1a_1 \\ a_2^2 & b_2^2 & c_2^2 & a_2b_2 & b_2c_2 & c_2a_2 \\ a_3^2 & b_3^2 & c_3^2 & a_3b_3 & b_3c_3 & c_3a_3 \\ 2a_1a_2 & 2b_1b_2 & 2c_1c_2 & (a_1b_2+a_2b_1) & (b_1c_2+b_2c_1) & (c_1a_2+c_2a_1) \\ 2a_2a_3 & 2b_2b_3 & 2c_2c_3 & (a_2b_3+a_3b_2) & (b_2c_3+b_3c_2) & (c_2a_3+c_3a_2) \\ 2a_3a_1 & 2b_3b_1 & 2c_3c_1 & (a_3b_1+a_1b_3) & (b_3c_1+b_1c_3) & (c_3a_1+c_1a_3) \end{bmatrix} \quad (\text{A.11})$$

By partitioning  $[\tilde{T}_\epsilon]$  into 3-by-3 submatrices as

$$[\tilde{T}_\epsilon] = \begin{bmatrix} \tilde{T}_Q & \tilde{T}_R \\ \tilde{T}_S & \tilde{T}_T \end{bmatrix} \quad (\text{A.12})$$

let us define a new matrix  $[\tilde{T}_\sigma]$  from it as

$$[\tilde{T}_\sigma] = \begin{bmatrix} \tilde{T}_Q & 2\tilde{T}_R \\ (1/2)\tilde{T}_S & \tilde{T}_T \end{bmatrix} \quad (\text{A.13})$$

It is to be noted that

$$[\tilde{T}_\epsilon]^{-1} = [\tilde{T}_\sigma]^T, \quad [\tilde{T}_\sigma]^{-1} = [\tilde{T}_\epsilon]^T \quad (\text{A.14})$$

The stress transformation is derived by considering the equilibrium of a differential element. As shown in various elasticity text books,

$$\{\tilde{\sigma}'\} = [\tilde{T}_\theta]\{\sigma'\}, \quad \{\sigma'\} = [\tilde{T}_\theta]^{-1}\{\tilde{\sigma}'\} \quad (A.15)$$

## A.2 Virtual Two Dimensional Shear Mechanisms

Let us define the direction of the axes, around which the virtual shear mechanisms of two dimensional nature are idealized, with the angles  $\psi$  and  $\zeta$  of a spherical coordinates shown in Fig. A.2. The components of the new set of axes  $\tilde{x}\tilde{y}\tilde{z}$  are given by

$$\{\tilde{x}\}^T = \{\cos\psi\cos\zeta \quad \sin\psi\cos\zeta \quad -\sin\zeta\} = \{a_1 \ b_1 \ c_1\} \quad (A.16)$$

$$\{\tilde{y}\}^T = \{-\sin\psi \quad \cos\psi \quad 0\} = \{a_2 \ b_2 \ c_2\} \quad (A.17)$$

$$\{\tilde{z}\}^T = \{\cos\psi\sin\zeta \quad \sin\psi\sin\zeta \quad \cos\zeta\} = \{a_3 \ b_3 \ c_3\} \quad (A.18)$$

In the present approach, the complex shear behavior of soil in the three dimensional space will be decomposed into  $J = 1, \dots, j$  sets of virtual shear mechanisms of the two dimensional nature presented in Chapter 2. The sphere in Fig. A.2 is divided into  $J$  sets of sub-planes of which unit normal vector is defined by  $\{\tilde{z}^{(j)}\}^T$ .

From Eqs. (A.10) and (A.15), two dimensional virtual stress and virtual strain vectors around the axis  $\{\tilde{z}^{(j)}\}$  will be given as

$$\{\tilde{\sigma}^{(j)}\}^T = \{\sigma_{\tilde{x}}^{(j)} \quad \sigma_{\tilde{y}}^{(j)} \quad \tau_{\tilde{xy}}^{(j)}\} \quad (A.19)$$

$$\{\tilde{\epsilon}^{(j)}\}^T = \{\epsilon_{\tilde{x}}^{(j)} \quad \epsilon_{\tilde{y}}^{(j)} \quad \gamma_{\tilde{xy}}^{(j)}\} \quad (A.20)$$

It is obviously noted that the transformed stress and strain vectors given by Eqs.(A.10) and (A.15) are shrunk into 3

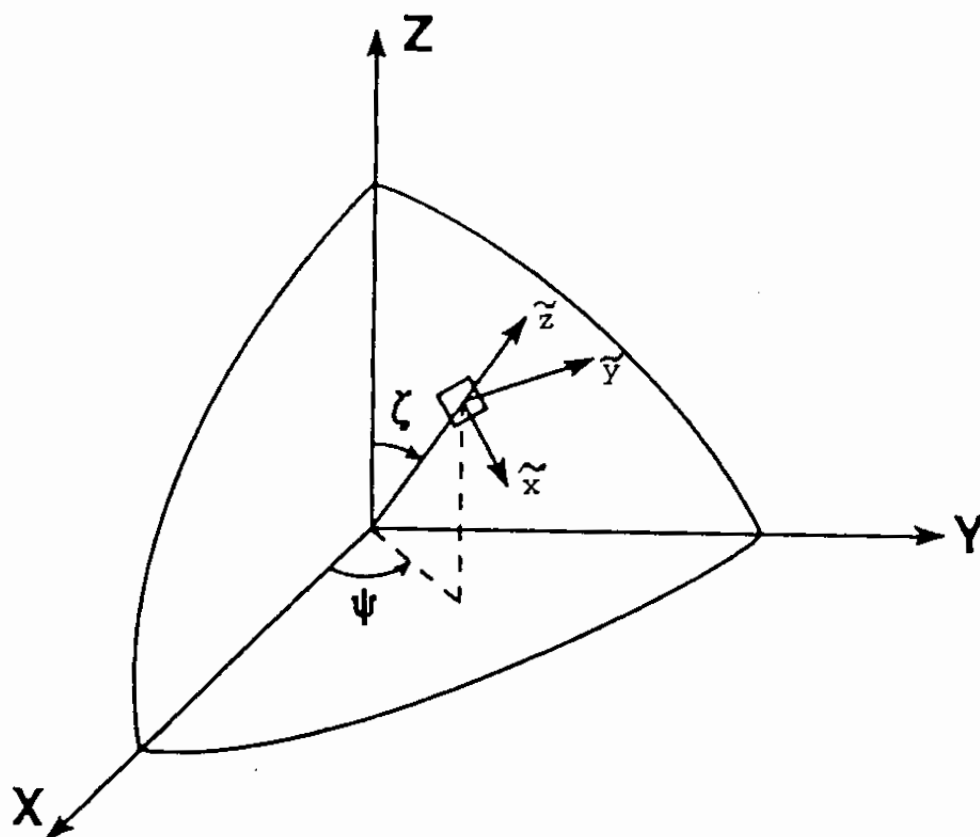


Fig. A.2 Spherical polar coordinate system

component vectors in the above equations.

In the manner similar to the formulation in Eq.(2.32), the virtual shear stress of  $j$ -th virtual shear mechanism of two dimensional nature is given by

$$\{\tilde{d\sigma}^{(j)}\} = \sum_{i=1}^I R_{L/U}^{(ij)} \{n^{(i)}\} \{n^{(i)}\}^T \{\tilde{d\epsilon}^{(j)}\} \quad (A.21)$$

in which  $\{n^{(i)}\}$  is given by Eq.(2.35).

### A.3 Incremental Constitutive Equation in Three Dimensions

The rest is to expand the stress vector of 3 components given by the above equation back to the stress vector of 6 components by appropriately filling the corresponding stress components, to transform back to the original coordinate by Eq.(A.15), and to do the summation with respect to  $j = 1, \dots, J$ .

Thus, with the obvious modification in the direction vectors for volumetric mechanism  $i = 0$ , the three dimensional relation between the stress and strain is given by

$$\begin{aligned} \{d\sigma'\} = & K\{m^{(0)}\}\{m^{(0)}\}^T(\{d\epsilon\} - \{d\epsilon_p\}) \\ & + \sum_{i,j=1}^{I,J} R_{L/U}^{(ij)} [\tilde{T}_\epsilon^{(j)}]^T [T_E] [n^{(i)}] \{n^{(i)}\}^T [T_E]^T [\tilde{T}_\epsilon^{(j)}] \{d\epsilon\} \end{aligned} \quad (A.22)$$

in which

$$\{m^{(0)}\}^T = \{ 1 \ 1 \ 1 \ 0 \ 0 \ 0 \} \quad (A.23)$$

$$\{n^{(i)}\}^T = \{ \cos\theta_i \ -\cos\theta_i \ \sin\theta_i \} \text{ (for } i = 1, \dots, I) \quad (A.24)$$

and  $[T_E]$  is a matrix for the expansion of the stress vector, being defined as

$$[T_E]^T = \begin{bmatrix} 1 & 0 & 0 & 0 & 0 & 0 \\ 0 & 1 & 0 & 0 & 0 & 0 \\ 0 & 0 & 0 & 1 & 0 & 0 \end{bmatrix} \quad (A.25)$$

If one defines the direction vectors by writing

$$\{m^{(ij)}\} = [\tilde{T}_\epsilon^{(j)}]^T [T_E] \{n^{(i)}\} \quad (A.26)$$

then Eq.(A.22) can be simply rewritten as

$$\{d\sigma'\} = K\{m^{(0)}\}\{m^{(0)}\}^T (\{d\epsilon\} - \{d\epsilon_p\}) + \sum_{i,j=1}^{I,J} R_{L/0}^{(ij)} \{m^{(ij)}\} \{m^{(ij)}\}^T \{d\epsilon\} \quad (A.27)$$

The factor  $R_{L/0}^{(ij)}$  is given as a function of the virtual simple shear strain  $\{m^{(ij)}\}^T \{d\epsilon\}$  and of its history.

The constitutive equation in Eq.(A.27) can be rewritten, by noting that  $\{m^{(ij)}\}^T \{d\epsilon_p\} = 0$ , as

$$\{d\sigma'\} = [D] (\{d\epsilon\} - \{d\epsilon_p\}) \quad (A.28)$$

in which

$$[D] = K\{m^{(0)}\}\{m^{(0)}\}^T + \sum_{i,j=1}^{I,J} R_{L/0}^{(ij)} \{m^{(ij)}\} \{m^{(ij)}\}^T \quad (A.29)$$



The incremental stress strain relation extended for three dimensions is very similar to that defined in two dimensions. In particular, the stiffness matrix is symmetric, giving an advantage in efficient solution.

The additional volumetric strain of plastic nature  $\{\epsilon_p\}$  is given by summing up the contributions  $\epsilon_p^{(j)}$  generated by the  $j$ -th two dimensional mechanism, such that

$$\{\epsilon_p\}^T = \{(1/3)\epsilon_p \quad (1/3)\epsilon_p \quad (1/3)\epsilon_p \quad 0 \quad 0 \quad 0\} \quad (A.30)$$

in which  $\epsilon_p$  is given by

$$\epsilon_p = \sum_{j=1}^J \epsilon_p^{(j)} \Delta\Omega \quad (A.31)$$

and  $\Delta\Omega = \sin\zeta\Delta\psi\Delta\zeta$  denotes solid angle for the  $J$  sets of sub-planes.

Integration of the incremental relation in Eq. (A.28) can also be done in the same manner as shown in Chapter 2.

In the three dimensional model, distinction should be made between the mean effective stresses in two dimensions and three dimensions. The mean effective stress in two dimensions is defined by

$$\sigma_m^{(j)} = (\sigma_x^{(j)} + \sigma_y^{(j)})/2 \quad (A.32)$$

and this is used in defining the shear mechanism such as in Eqs. (2.65), (2.153), etc. The virtual simple shear mechanisms defined in this way promise to take into account the effect of

intermediate principal stress. The mean effective stress in three dimensions is defined in the usual manner by

$$\sigma_m' = (\sigma_x' + \sigma_y' + \sigma_z')/3 \quad (\text{A.33})$$

and this is used in defining the volumetric mechanism such as in Eqs. (2.27), (2.58), etc.

#### A.4 Objectivity

Objectivity is one of the fundamental requirements for physically feasible constitutive models as discussed by Yatomi and Nishihara (1984). In the vector-matrix notation of the stress strain relation, objectivity of constitutive equations is expressed as follows. To begin with, let  $[R_\sigma]$  be the transformation matrix associated with the rotation of the reference coordinate to give the stress vector  $\{\sigma'^*\}$  in the transformed coordinate, such that

$$\{\sigma'^*\} = [R_\sigma]\{\sigma'\} \quad (\text{A.34})$$

The components of  $[R_\sigma]$  is given similarly to Eq.(A.13). Let  $[R_\epsilon]$  be the corresponding transformation matrix for the strain vector, such that

$$\{\epsilon^*\} = [R_\epsilon]\{\epsilon\} \quad (\text{A.35})$$

The components of  $[R_\epsilon]$  is given similarly to Eq.(A.11). It is to

be noted, from Eq.(A.14), that

$$[R_\epsilon]^{-1} = [R_0]^T, \quad [R_0]^{-1} = [R_\epsilon]^T \quad (A.36)$$

Let  $[D^*]$  be the stiffness matrix expressed in the transformed coordinate as

$$\{d\sigma^*\} = [D^*](\{d\epsilon^*\} - \{d\epsilon_p^*\}) \quad (A.37)$$

in which

$$[D^*] = K^* \{m^{(0)*}\} \{m^{(0)*}\}^T + \sum_{i,j=1}^{I,J} R_{L/0}^{(ij)*} \{m^{(ij)*}\} \{m^{(ij)*}\}^T \quad (A.38)$$

The objectivity of the constitutive equation requires that Eq.(A.37) should represent the same behavior of soil as Eq.(A.28). This demands, from Eqs.(A.34) and (A.35), that

$$[D^*] = [R_0][D][R_\epsilon]^{-1} \quad (A.39)$$

Substituting Eq.(A.36) into this, one obtains

$$[D^*] = [R_0][D][R_0]^T \quad (A.40)$$

This is the requirement for the objectivity of the constitutive equation expressed in the vector-matrix notation.

The requirement for the objectivity in Eq.(A.40) is easily seen to be satisfied by the present model. To begin with, the

vectors  $\{m^{(0)}\}$  and  $\{m^{(ij)}\}$  in Eq.(A.28) are the direction vectors for specifying the stress increment for each mechanism so that they are transformed in the same manner as the stress vector; i.e.

$$\{m^{(0)*}\} = [R_0]\{m^{(0)}\} \quad (A.41)$$

$$\{m^{(ij)*}\} = [R_0]\{m^{(ij)}\} \quad (A.42)$$

It should be noted, from the definition of the components of  $[R_0]$  similar to those shown in Eq.(A.13), that

$$\{m^{(0)*}\} = \{m^{(0)}\} \quad (A.43)$$

From Eqs.(A.41) and (A.42), the right hand side of Eq.(A.40) becomes

$$[R_0][D][R_0]^T = K\{m^{(0)*}\}\{m^{(0)*}\}^T + \sum_{i,j=1}^{I,J} R_{L/U}^{(ij)}\{m^{(ij)*}\}\{m^{(ij)*}\}^T \quad (A.44)$$

The rest is to examine that scalars  $K$  and  $R_{L/U}^{(ij)}$  are not affected by the transformation. The scalar function  $K$  is a function of effective mean stress  $\{m^{(0)}\}^T\{\sigma'\}$ . One obtains, from Eqs.(A.34), (A.41) and (A.43), that

$$\{m^{(0)*}\}^T\{\sigma',*\} = \{m^{(0)}\}^T[R_0]\{\sigma'\} = \{m^{(0)}\}^T\{\sigma'\} \quad (A.45)$$

Equivalently, the scalar function  $K$  is actually a function of elastic volumetric strain  $\{m^{(0)}\}^T(\{\epsilon\}-\{\epsilon_p\})$  as seen in Eq.(2.45). One obtains, from Eqs. (A.35), (A.36) and (A.41), that

$$\begin{aligned}\{\mathbf{m}^{(0)*}\}^T(\{\epsilon^*\}-\{\epsilon_p^*\}) &= \{\mathbf{m}^{(0)}\}^T[\mathbf{R}_\sigma]^T[\mathbf{R}_\epsilon](\{\epsilon\}-\{\epsilon_p\}) \\ &= \{\mathbf{m}^{(0)}\}^T(\{\epsilon\}-\{\epsilon_p\})\end{aligned}\quad (\text{A.46})$$

Either by Eq.(A.45) or (A.46), one obtains

$$\mathbf{K}^* = \mathbf{K} \quad (\text{A.47})$$

Similarly the scalar functions  $R_{L/U}^{(ij)}$  are functions of  $\{\mathbf{m}^{(ij)}\}^T\{\epsilon\}$  and of its history. One obtains, from Eqs.(A.35), (A.36) and (A.42), that

$$\{\mathbf{m}^{(ij)*}\}^T\{\epsilon^*\} = \{\mathbf{m}^{(ij)}\}^T[\mathbf{R}_\sigma]^T[\mathbf{R}_\epsilon]\{\epsilon\} = \{\mathbf{m}^{(ij)}\}^T\{\epsilon\} \quad (\text{A.48})$$

This leads to

$$R_{L/U}^{(ij)*} = R_{L/U}^{(ij)} \quad (\text{A.49})$$

Substitution of Eqs.(A.47) and (A.49) into Eq.(A.44) yields

$$[\mathbf{R}_\sigma][\mathbf{D}][\mathbf{R}_\sigma]^T = \mathbf{K}^*\{\mathbf{m}^{(0)*}\}\{\mathbf{m}^{(0)*}\}^T + \sum_{i,j=1}^{I,J} R_{L/U}^{(ij)*}\{\mathbf{m}^{(ij)*}\}\{\mathbf{m}^{(ij)*}\}^T \quad (\text{A.50})$$

From the definition of  $[\mathbf{D}^*]$  in Eq.(A.38), one obtains

$$[\mathbf{R}_\sigma][\mathbf{D}][\mathbf{R}_\sigma]^T = [\mathbf{D}^*] \quad (\text{A.51})$$

This proves the objectivity of the present model as stated in

Eq.(A.40). Obviously the same proof applies to the two dimensional model in the present study.

In the present model inherent anisotropy is readily introduced through the definition of  $R_{L/U}^{(ij)}$  as a function of the direction dependent variable  $\{m^{(ij)}\}^T \{\epsilon\}$  as seen in Eq.(2.76). Inherent isotropy is achieved simply by dropping off the superscript (ij) from the soil parameters as seen in Eq.(2.77). Stress induced anisotropy is indicated by retaining the superscript (ij) for  $Q$  and  $R_{L/U}$  as seen in Eqs.(2.77) and (2.78).

#### A.5 Relation among One, Two and Three Dimensional Models

If number of the virtual shear mechanisms  $J$  of two dimensional nature is reduced to one, the three dimensional model is reduced to the two dimensional model studied in the present study. Similarly, if number of the virtual shear mechanisms  $I$  as well as  $J$  is reduced to one, the three dimensional model is reduced to the one dimensional model often used for level ground analysis. The author believes that number of the virtual mechanisms can thus be reduced in accordance with the type of the boundary value problems for ensuring efficiency in computation.

Obviously decreasing number of the virtual mechanisms results in deterioration in accuracy and narrower limit in applicability. For example, if both numbers  $I$  and  $J$  are reduced to one, isotropy of the model cannot be satisfied and rotation of the principal stress axes cannot be properly taken into account. This, however, does not necessarily mean that the model is inadequate or useless. As seen in the previous studies on the

one dimension analysis of level ground (e.g. Finn et al, 1977), appropriately chosen coordinates and accordingly modified parameters have given quite satisfactory results in practice. Thus, it is quite probable that practically satisfactory results can be efficiently obtained with decreasing number of the virtual mechanisms with appropriately chosen coordinates and accordingly adjusted model parameters. An instance of this is the application of the two dimensional model (i.e.  $J = 1$ ) to the boundary value problems under plane strain condition as seen in the present study.

#### Notation for the Appendix A

$[D]$  : tangential stiffness matrix

$J$  : number of virtual two dimensional shear mechanisms

$K$  : elastic tangent bulk modulus of soil skeleton

$\{m^{(0)}\}$  : direction vector for the volumetric mechanism

$\{m^{(ij)}\}$  : direction vector for the  $ij$ -th virtual simple shear mechanism

$\{n^{(i)}\}$  : direction vector for the  $i$ -th virtual simple shear mechanism in the two dimensional mechanism

$[R_\epsilon]$  :  $6 \times 6$  transformation matrix for strain; to be used for examining objectivity

$[R_\sigma]$  :  $6 \times 6$  transformation matrix for stress; to be used for examining objectivity

$R_{L/U}^{(ij)}$  : tangential stiffness modulus for mechanism  $ij$  at loading and unloading

$\tilde{[T]}$  :  $9 \times 9$  transformation matrix for displacement gradient

$[\widetilde{T}_c]$  : 3 x 3 transformation matrix for displacement

$[T_E]$  : 6 x 3 matrix for extracting three components of stress from six components

$[\widetilde{T}_\epsilon]$  : 6 x 6 transformation matrix for strain

$[\widetilde{T}_\epsilon^{(j)}]$  : 6 x 6 transformation matrix for strain represented in the coordinates for j-th virtual mechanism

$[\widetilde{T}_\sigma]$  : 6 x 6 transformation matrix for stress

u, v and w : displacements in x, y and z coordinates

$\widetilde{u}$ ,  $\widetilde{v}$  and  $\widetilde{w}$  : displacements in  $\widetilde{x}$ ,  $\widetilde{y}$  and  $\widetilde{z}$  coordinates

$\{\widetilde{x}\}^T = \{a_1, b_1, c_1\}$ , etc : direction vector of x axis, etc., represented in the original coordinates

$\{\widetilde{z}^{(j)}\}$  : direction of z axis normal to the j-th sub-plane

x, y and z : original coordinates

$\widetilde{x}$ ,  $\widetilde{y}$  and  $\widetilde{z}$  : transformed coordinates

$\{\epsilon\}^T = \{\epsilon_x, \epsilon_y, \epsilon_z, \gamma_{xy}, \gamma_{yz}, \gamma_{zx}\}$  : strain vector

$\{\widetilde{\epsilon}\}$  : strain vector represented in the transformed coordinate

$\epsilon_p$  : volumetric strain of plastic nature

$\epsilon_p^{(ij)}$  : volumetric strain of plastic nature generated by j-th mechanism

$\{\epsilon_p\}$  : volumetric strain vector of plastic nature

$\{\widetilde{\epsilon}^{(j)}\}^T = \{\epsilon_{\widetilde{x}}^{(j)}, \epsilon_{\widetilde{y}}^{(j)}, \gamma_{\widetilde{xy}}^{(j)}\}$  : strain vector of j-th virtual mechanism of two dimensional nature

$\zeta$  and  $\psi$  : angles for specifying spherical polar coordinate system

$\{\sigma'\}^T = \{\sigma_x', \sigma_y', \sigma_z', \tau_{xy}, \tau_{yz}, \tau_{zx}\}$  : effective stress vector

$\{\widetilde{\sigma}'\}$  : stress vector represented in the transformed coordinate to be used for defining the virtual two dimensional mechanism

$\{\widetilde{\sigma}'^{(j)}\} = \{\sigma_{\widetilde{x}}'^{(j)}, \sigma_{\widetilde{y}}'^{(j)}, \tau_{\widetilde{xy}}'^{(j)}\}$  : effective stress vector of j-th



virtual mechanism of two dimensional nature

$\sigma_m'$  : mean effective stress in the three dimensions

$\sigma_m'^{(j)}$  : mean effective stress for j-th two dimensional mechanism

superscript "\*" : scalars, vectors and matrices in the transformed space for examining objectivity

subscript "x", etc. : partial differentiation with respect to x, etc.

## References

- (1) Cook, R.D. (1981) : Concepts and Applications of Finite Element Analysis, Second Edition, John Wiley & Sons
- (2) Finn, W.D.L., Lee, K.W. and Martin, G.R. (1977) : "An effective stress model for liquefaction," Journal of the Geotechnical Engineering Division, ASCE, Vol.103, No.GT6, pp.517-533
- (3) Yatomi, C. and Nishihara, A. (1984) : " Principles for constitutive equations and expressions of anisotropy in soil materials," Soils and Foundations, Vol.24, No.3, pp.15-26

## APPENDIX B

### COMPARISON WITH THE STRESS DILATANCY RELATION

Stress dilatancy relations are extensively studied in the discipline of soil mechanics. The relations specify the dilatancy (i.e. the ratio of plastic volumetric strain increment over plastic shear strain increment) as a function of relevant stress ratios. Pradhan and Tatsuoka (1989) offer a good review on them. In the simple shear test as in the present study, there are three representative equations.

#### (1) Sliding Block Theory

The sliding block theory (e.g. Tokue, 1978) assumes the simple shear deformation of two dimensional blocks in contact. The stress dilatancy relation in simple shear is given by

$$\frac{de_p}{d\gamma_{xy}^p} = - \frac{\tan\phi'_p - \tau_{xy}/\sigma'_y}{1 + \tan\phi'_p \cdot \tau_{xy}/\sigma'_y} \quad (\text{B.1})$$

in which  $\gamma_{xy}^p$ : plastic shear strain in the horizontal direction.

#### (2) Rowe's Stress Dilatancy Relation

Rowe (1969) assumes that the energy increment ratio of input over output is constant. Rowe's stress dilatancy relation in simple shear is given by

$$\frac{de_p}{d\gamma_{xy}^p} = \frac{\sigma'_1/\sigma'_3 - K}{\sigma'_1/\sigma'_3 + K} \quad (\text{B.2})$$

#### (3) Energy Dissipation Theory

Taylor (1948) derived a stress dilatancy relation based on energy dissipation theory. The stress dilatancy relation based

on the energy dissipation theory is given for simple shear by

$$\frac{d\epsilon_p}{d\gamma_{xy}^p} = -\sin\phi'_p + \frac{\tau_{xy}}{\sigma'_y} \quad (\text{B.3})$$

All of these equations represent a straight line or a similar line in the plane with coordinates of the dilatancy and the stress ratio in Fig. B.1.

In the present study, the plastic volumetric strain is generated as a function of plastic shear work and the shear stress ratio as shown in Chapter 2. The author attempts, in the present appendix, to examine if the present approach gives consistent stress dilatancy relation with the above mentioned relations.

First of all, approximating the undrained condition with  $\epsilon_x + \epsilon_y = 0$ , one obtains a relation between plastic volumetric strain increment and the effective mean stress from the volumetric mechanism in Eq. (2.43) as

$$d\sigma'_m = K(-d\epsilon_p) \quad (\text{B.4})$$

From this and such definition of the state parameter  $S$  as  $S = \sigma'_m / \sigma'_{m0}$ , one obtains

$$d\epsilon_p = (-\sigma'_{m0}/K)dS \quad (\text{B.5})$$

Since the plastic shear strain increment  $d\gamma_{xy}^p$  generates the plastic shear work increment  $dW_s$  during simple shear process as

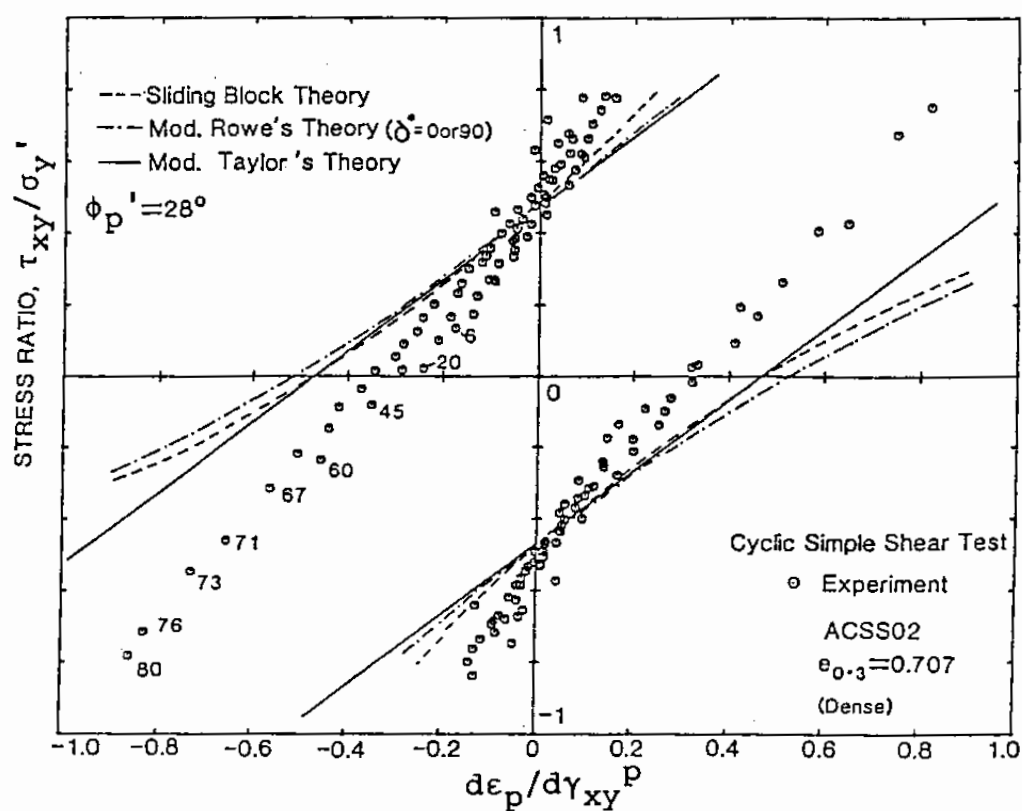


Fig. B.1 Stress dilatancy relation by the previous studies  
 (After Pradhan and Tatsuoka, 1989)

$$dW_s = \tau_{xy} d\gamma_{xy}^p \quad (B.6)$$

one obtains

$$d\gamma_{xy}^p = (1/\tau_{xy}) dW_s \quad (B.7)$$

From this, one obtains

$$\frac{de_p}{d\gamma_{xy}^p} = \tau_{xy} \frac{de_p}{dW_s} \quad (B.8)$$

Substitution of Eq.(B.5) into this yields

$$\frac{de_p}{d\gamma_{xy}^p} = \tau_{xy} \frac{(-\sigma'_{mo})}{K} \frac{dS}{dW_s} \quad (B.9)$$

As shown in Eq.(2.59), when the effective stress is in contractive zone (i.e. when the shear stress ratio is low so that  $r < r_3$ ),  $S$  is the same as the liquefaction parameter  $S_0$  defined as a function of normalized plastic shear work  $w = W_s/W_0$  as shown in Eq. (2.68). Definition of normalizing factor  $W_0$  is given in Eq.(2.64). From Eq.(2.68), one obtains

$$\frac{dS_0}{dW_s} = -0.6 \frac{p_1}{W_n W_1} \left( \frac{w}{w_1} \right)^{p_1-1} \quad (B.10)$$

Similarly, when the effective stress is in dilative zone or in transition zone from contractive zone, one obtains

$$\frac{dS}{dW_s} = \frac{dS_2}{dW_s} + \frac{d}{dW_s} \left[ \sqrt{(S_0 - S_2)^2 + ((r - r_3)/m_1)^2} \right] \quad (B.11)$$

From Eqs. (2.60) through (2.62), one can find that the term  $S_2$ ,  $(S_0 - S_2)$  and  $(r - r_3)$  are all expressed by  $S_0$  and  $r$ . After some manipulation, one can rewrite Eq.(B.11) into

$$\begin{aligned} \frac{dS}{dW_s} = & \left(1 - \frac{m_2 - m_3}{m_1}\right) \frac{dS_0}{dW_s} \\ & + \frac{1}{\sqrt{(S_0 - S_2)^2 + ((r - r_3)/m_1)^2}} \left[ \left(\frac{m_2 - m_3}{m_1}\right)^2 \frac{dS_0}{dW_s} + \frac{r - r_3}{m_1^2} \left( \frac{dr}{dW_s} - m_3 \frac{dS_0}{dW_s} \right) \right] \quad (\text{B.12}) \end{aligned}$$

in which  $dS_0/dW_s$  is given by Eq.(B.10).

To summarize, one obtains the stress dilatancy relation for the present model as

$$\frac{de_p}{d\gamma_{xy}^p} = \tau_{xy} \frac{(-\sigma'_{m0})}{K} \frac{dS_0}{dW_s} \quad (\text{B.13})$$

for contractive zone ( i.e. if  $r < r_3$ ) and

$$\begin{aligned} \frac{de_p}{d\gamma_{xy}^p} = & \tau_{xy} \frac{(-\sigma'_{m0})}{K} \left(1 - \frac{m_2 - m_3}{m_1}\right) \frac{dS_0}{dW_s} \\ & + \frac{\tau_{xy} (\sigma'_{m0})}{K \sqrt{(S_0 - S_2)^2 + ((r - r_3)/m_1)^2}} \left[ \left(\frac{m_2 - m_3}{m_1}\right)^2 \frac{dS_0}{dW_s} + \frac{r - r_3}{m_1^2} \left( \frac{dr}{dW_s} - m_3 \frac{dS_0}{dW_s} \right) \right] \quad (\text{B.14}) \end{aligned}$$

for dilative or transition zone (i.e. if  $r > r_3$ ) in which  $dS_0/dW_s$  is given by Eq.(B.10). The author, however, found it difficult to obtain analytical form of  $dr/dW_s$  in Eq.(B.14).

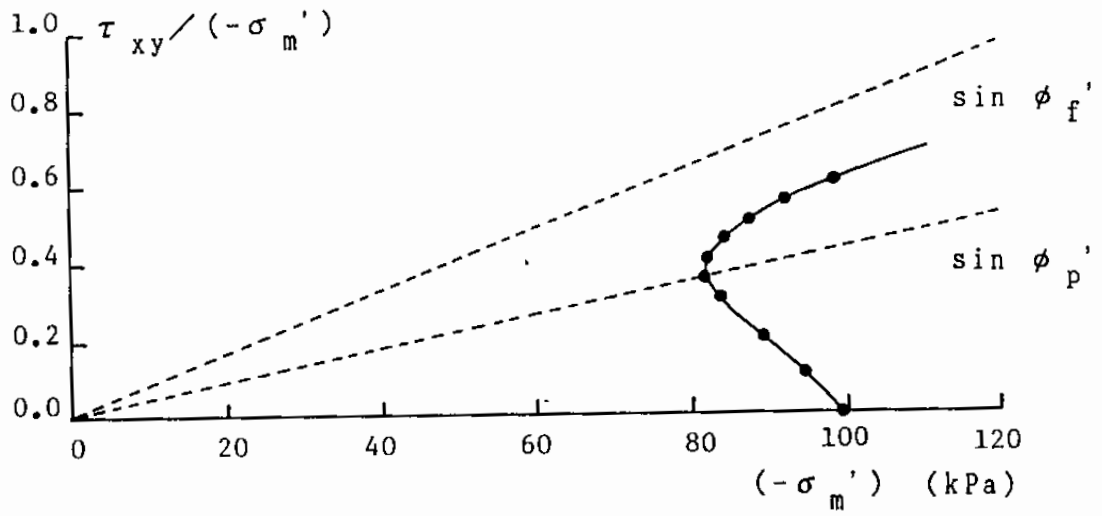
As an example, the stress dilatancy relation for the present model is computed for the initial loading path out of the stress path shown in Fig. 3.5(b). The parameters of the model used for

the computation is given on the right hand side in Table 3.1. The result, shown in Fig. B.2 in which horizontal axis is equivalent to  $K(d\epsilon_p/d\gamma_{xy}^P)$ , is basically consistent with the previous studies in such a sense that the stress dilatancy relation can be approximated by a straight line.

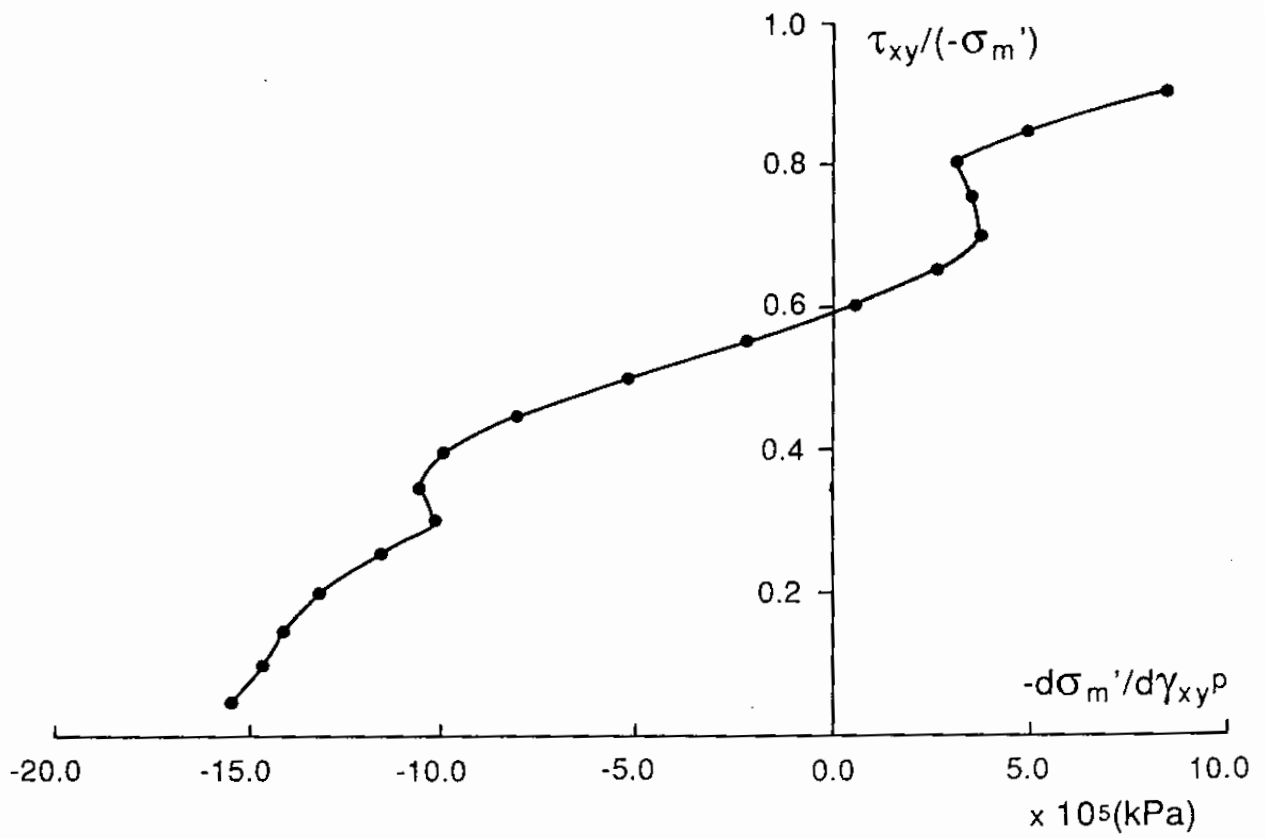
Though the certain consistency is thus observed between the stress dilatancy relation by the present study and those by the previous studies, there are differences between them. The stress dilatancy relations by the previous studies are, as mentioned earlier, quite basic and can be one of the principles in the mechanics of granular materials. Though the relations hold true both in drained and undrained conditions, it is more closely related to the soil test in drained condition.

The present approach, on the contrary, is based directly on the undrained stress path. It assures the physically feasible performance in the undrained analysis because all the modeling and the parameter determination are done in reference to the undrained cyclic loading test. In contrast to the stress dilatancy relation which focuses on the strain increment, the present model puts an emphasis on cumulative effect. This assures stable performance of the model in the overall sense.

The author concludes from these observations that, if one intends to acquire a deeper understanding of the mechanics of granular materials, a further study might be necessary on the aspect of the stress dilatancy relation. If one needs a useful tool in the practice of soil dynamics and earthquake engineering, the present model can be quite dependable, stable and efficient in the numerical analysis.



(a) Stress path



(b) Stress dilatancy relation

Fig. B.2 Stress dilatancy relation by the present model



## References

- (1) Pradhan, T.B.S. and Tatsuoka, F. (1989) : "On stress-dilatancy equations of sand subjected to cyclic loading," Soils and Foundations, Vol.29, No.1, pp.65-81
- (2) Rowe, P.W. (1969) : "The relation between the shear strength of sands in triaxial compression, plane strain and direct shear," Geotechnique, Vol.19, No.1, pp.75-86
- (3) Taylor, D.W. (1948) : Fundamentals of Soil Mechanics, John Wiley and Sons
- (4) Tokue, T. (1978) : "A consideration about Rowe's minimum energy ratio principle and a new concept of shear mechanism," Soils and Foundations, Vol.18, No.1, pp.1-10